MACROSCOPIC PROPERTIES OF ELECTRICALLY INTERACTING SUSPENSIONS

Thesis by

Roger Temor Bonnecaze

In Partial Fulfillment of the Requirements

for the Degree of

Doctor of Philosophy

California Institute of Technology

Pasadena, California

1991

(Defended February 26, 1991)

To my father and mother

ACKNOWLEDGEMENTS

I have been fortunate to have met many special people who have contributed to my education, both scientifically and otherwise, and deserve my heartfelt thanks.

First and foremost, of course, is my research advisor, John Brady. He has shown constant interest and support throughout my studies. Our many discussions on science and other topics have broadend my education and sharpened my thinking. I have learned so much from John, and for that, I am extremely grateful. I also appreciate his understanding when I felt it necessary to leave Caltech for a while and his enthusiasm when I returned to finish my degree.

During the latter part of my thesis work, I had the benefit of working with Dr. Andrew Kraynik of Sandia National Laboratories, who was like a second research advisor. In addition to teaching much about rheology, I also have a new appreciation for birds.

Because of my leave of absence from Caltech, I have two generations of Caltech graduate students to thank for their friendship and help in my thesis work. During the first half of my tenure, Jim Stoos, Ed Ascoli, Dave Dandy, Lou Durlofsky, Julia Lester and, of course, Howard Stone, were great friends and taught me a lot about fluid mechanics. Special thanks go to my friends and bridge partners, Mike Creed, Dan Laughlin, and Sue Miner. For the second half of my stay at Caltech, I have been fortunate to have special friends and teachers in John Bauer, Thanh Phung, Ivan Claeys, Phil Lovalenti, Jeff Morris, Matt Gursky, and Shaun Sellers. Also, to all my other friends at Caltech, thank you.

I am indebted to my many friends in Northern California for their support and helping me keep my perspective. My visits with Gustavo Arboleda, Pedro Castillo, and Victor Salazar were always an enjoyable and welcome break from my studies.

Finally, special thanks and appreciation goes to Alicia Isaac-Cura. Her friendship, support, and love were ever constant throughout my studies, and I cannot begin to say how grateful I am for that. I shall be fortunate if I can give only fraction of it back to her.

ABSTRACT

Several bulk or macroscopic properties of electrically interacting suspensions –or at least electrically interacting by mathematical analogy– are studied using simulation methods. These bulk properties include the effective conductivity, percolation transitions, effective reaction rates, and the effective viscosity of an electrorheological fluid. In order to compute these properties, the detailed potential field in the suspension is not required, but rather only the linear relationship between the charge and dipole moments of the particles to their potentials and the applied electric field is needed. A method is developed to compute this relationship accurately and efficiently for arbitrary particle configuration and shape. The method includes both the many-body far-field and near-field particle interactions and properly accounts for the long-ranged interactions common to electrostatic problems.

The method is applied as part of a simulation to determine the effective conductivity of spherical particles. The simulation accurately reproduces the known values of the conductivity for cubic lattices of spheres for any volume fraction and particle-matrix conductivity ratio providing confidence in the method. It is then applied to determine the conductivity of mono-disperse, random hard-sphere suspensions for a variety of conductivity ratios of up to sixty volume percent particles. This is the first rigorous theoretical determination of the effective conductivity at such large volume fractions. The method is also used to study the percolation behavior of highly conducting spherical particles in close contact. It is found that such a system does exhibit a percolation transition, but only when the near-field effects are extremely large compared to the far-field interactions. This indicates that such a condition is a necessity for modeling a suspension as a percolating system.

The diffusion-limited reaction rate of a highly mobile reactant with spherical traps is also computed using the simulation method. Here the average "charge" on the particle is the effective consumption of the reactant by the spherical particle. The results are quite good up to a volume fraction of 30%, but then unphysically deviate from the expected increasing reaction rate with volume fraction and show

a maximum rate at forty volume percent. The deviation is explained and serves as an example of the limitations of the method developed earlier. Using the effective conductivity results, however, a self-consistent Brinkman medium-like theory is developed that predicts the effective reaction rate quite accurately.

The method is finally applied to the dynamic simulation of electrorheological (ER) fluids –suspensions of dielectric particles with electric field tunable effective viscosities. Using the method developed in earlier chapters, the electrostatic interparticle forces in the ER suspension can be determined accurately and efficiently for arbitrary particle configurations, especially in capturing the strong near-field interactions. Coupled with Stokesian dynamics to account for the hydrodynamic interactions among the particles, the dynamics of the microstructure and its rheology can be determined. Dynamic simulations of an unbounded monolayer for a variety of electric field strengths and shear rates reproduce qualitatively and quantitatively experimental behavior. From the correlation of the dynamics and rheology, a theory for the dynamic yield stress observed in the suspensions is proposed and then successfully tested with the dynamic simulation. From the theory a simple model of the dynamic yield stress is created to predict its dependence on the volume fraction and the particle to fluid dielectric constant. The power of simulations to provide insight into the physics of multiphase materials and then to allow the testing of theories is particularly well illustrated with the study on ER fluids.

TABLE OF CONTENTS

CHAPTER 1

INTRODUCTION

As we approach the twenty-first century, more and more man-made multiphase materials will be invented for specialized applications. Graphite composite materials have already revolutionized the aerospace industry by allowing the construction of strong yet light weight aircraft components, and the computer industry has long benefited from magnetic memory medium synthesized from suspensions of magnetizable particles. From the beginning of the development of man-made materials, it was recognized that we need to know how the microstructure, the distribution of one or several phases in another, effects the bulk properties to guide us in the invention of new materials. In addition we would like to predict a material's bulk properties in advance of its synthesis, making preliminary design decisions via relatively inexpensive simulations, thus reducing both the time and production costs of creating a new material.

In this thesis we shall provide the beginnings of solutions to both these problems for suspensions of particles that interact electrically, or at least by mathematical analogy appear to interact electrically. In particular we shall develop molecular-dynamics-like simulation methods that allow the direct computation of the bulk properties of these suspensions. The methods effeciently and accurately account for the many-body far-field and near-field interactions, allowing the simulations to be confidently used for the complete range of volume fractions and arbitrary particle configurations. From these simulation methods, the relationship between the bulk properties of the suspension and its microstructure can be determined directly and thus provide insight into the physics of the multiphase material. Several bulk properties are examined in the thesis:

In Chapter 2 we develop a method for the determination of the effective conductivity of an arbitrary (ordered or disordered), statistically homogeneous suspension of particles. By mathematical analogy, this includes the effective electrical and thermal conductivities, diffusion coefficient, dielectric constant, and magnetic permeability. The method follows closely that of the "Stokesian dynamics" method of Durlofsky,

Brady, and Bossis (1987), and captures both far- and near-field particle interactions, and the convergence difficulties typical of these systems with their long-ranged interactions is also completely resolved. This is accomplished by forming a capacitance matrix, the electrostatic analog of the low-Reynolds-number resistance matrix, which relates the monopole (charge), dipole, and quadrupole of the particles to the potential field of the system. A far-field approximation to the capacitance matrix is formed via a moment expansion of the integral equation for the potential. The capacitance matrix of the infinite system is limited to a finite number of equations by using periodic boundary conditions, and the Ewald method is used to form rapidly converging lattice sums of particle interactions. To include near-field effects, exact two-body interactions are added to the far-field approximation of the capacitance matrix. The particle dipoles are then calculated directly to determine the effective conductivity of the system. The effective conductivities of spherical particles in cubic arrays are calculated for a variety of particle-to-matrix conductivity ratios. In all cases the results are in excellent agreement with the known results of Sangani & Acrivos (1982).

In Chapter 3 the effective conductivity of a random, mono-disperse, hard-sphere suspension is determined with the method for several conductivity ratios up to a volume fraction of sixty percent. This provides the first accurate and rigorously correct, in principle, effective conductivities for such a range of volume fractions. The results are also consistent with the previous theoretical work of Jeffrey (1973), the bounds computed by Torquato & Lado (1986), and the random walker simulations of Kim & Torquato (1990) that appeared after this work was completed. Our calculated conductivities also compare extremely well with those of experiments.

In Chapter 4 percolation-like numerical experiments are performed on periodically replicated cubic lattices of nearly touching, perfectly conducting spheres, where the effective conductivity was computed as spheres were removed one by one from the lattice. Under suitable normalization of the conductivity and volume fraction, it is found that the initial volume fraction must be extremely close to maximum packing in order to observe a percolation transition, indicating that the near-field effects must be very large relative to far-field effects. The percolation transitions occur at

the accepted values for simple, body-centered, and face-centered cubic lattices. Also, the vulnerability of the lattices computed are exactly thoses of previous investigators. Unfortunately, due to the limited data just above the percolation threshold, we could not correlate the conductivity with a power law near the threshold; however, it can be correlated with a power law for large normalized volume fractions.

In Chapter 5 the effective reaction rate for a random or regular array of reactive, stationary spherical traps in a medium containing a mobile reactant is calculated using the method, taking advantage of its mathematical analogy to perfectly conducting spheres at zero potential in a non-zero bulk potential. It is found here that the direct addition of the two-body interactions has a negligible effect on the effective reaction rate computed, in contrast to the case of the effective conductivity. Since the potential matrix is only formed up to the quadrupole level, our results closely match the "correct" random walker simulation results of Lee, Kim, Miller, and Torquato (1989) up to only thirty volume percent, after which they underpredict the effective reaction rate. To accurately compute the effective reaction rate at high volume fractions, higher order many-body multipole interactions are required. The failure of the method at high volume fractions is explained and serves as an example of the limitations of method developed in Chapter 2.

The remainder of this thesis is concerned with predicting and understanding the rheological properties of electrorheological (ER) fluids. These novel suspensions exhibit Bingham plastic-like behavior with an apparent yield stress that grows with the square of the applied electric field. Thus, one has a fluid whose effective viscosity can be tuned over several orders of magnitude by varying the field. Applications of these fluids include electromechanical clutches, vibration dampers, and valves. These suspensions of particles interact electrically, as well as hydrodynamically, due to the mismatch of particle and fluid dielectric constants to give rise to their interesting rheological behavior.

In Chapter 6 we describe how the ideas developed earlier can be combined with Stokesian dynamics to dynamically simulate an ER suspension. The Stokesian dynamics method allows the efficient and accurate computation of the evolving mi-

crostructure and the rheology of the suspension given the bulk shear rate and electrostatic interparticle forces. These complex, many-body, conservative interparticle forces are determined from the energy of the suspension which can be computed from the capacitance matrix developed in Chapter 2. We then apply the total simulation to an unbounded monolayer of dielectric spheres with an areal fraction of forty percent for a variety of shear rates and electric field strengths. The effective viscosities computed in the simulation match experimental measurements qualitatively and quantitatively. Observation of the microstructure indicates that suspension undergoes repeated episodes of slow solid-body like deformations followed by rapid reconfigurations at high electric field strengths relative to the shear rates. These dynamics are correlated with the onset of the yield stress behavior and dramatic changes in the electrostatic energy of the suspension and impel us to propose a connection between the dynamic yield stress and electrostatic energy.

In Chapter 7 we describe and determine the static and dynamic or Bingham yield stresses in an ER fluid from a microstructural point of view. In particular, both descriptions relate these yield stresses to the electrostatic energy determined with the suspension capacitance matrix. The static yield stress is determined from the non-linear elastic stress-strain relationship of the ER suspension derived from the energy of the system for a variety of volume fractions and particle-to-fluid dielectric constant ratios. The connection between the dynamic yield stress and the energy jumps observed in the dynamic simulation are derived from a total energy balance. The dynamic yield stress is indeed found to be equal to the product of the energy jumps and their frequency. The theory is then successfully tested using the dynamic simulation. Using this theory of the dynamic yield stress, a simple model is developed that predicts the effects of volume fraction and particle-to-fluid dielectric constant ratio on the dynamic yield stress. We find that the yield stress increases strongly with the dielectric constant ratio, and there is a predicted maximum for a volume fraction of 40% particles as is observed experimentally.

CHAPTER 2

A METHOD FOR DETERMINING THE EFFECTIVE CONDUCTIVITY OF DISPERSIONS OF PARTICLES

2.1. Introduction

Predicting the effective conductivity of two-phase media has occupied engineers and physicists for the last one hundred and twenty years. This long interest has been fueled by the proliferation of man-made composite materials and the need to predict their bulk properties, such as effective conductivity. We take the approach that the problem of predicting the effective conductivity (indeed, any bulk property) of a suspension can be reduced to understanding the transport processes on the scale of the heterogeneous inclusions followed by an appropriate averaging. These inclusions are assumed to be large enough so that the following continuum equations of conduction are applicable in each phase:

$$\nabla \cdot \mathbf{F} = \rho(\mathbf{x}), \tag{2.1}$$

$$\mathbf{F} = -\mathbf{\Lambda} \cdot \nabla\phi. \tag{2.2}$$

The first equation is a conservation equation that accounts for sources and sinks, $\rho(\mathbf{x})$, within one of the phases. The second equation is a constitutive diffusive-type equation that relates the flux of the conservable quantity (heat, mass, or charge), $\mathbf{F}$, to the potential gradient (temperature or concentration gradient or the electric field), $\nabla\phi$, by a transport coefficient tensor, $\mathbf{\Lambda}$. Typically, $\mathbf{\Lambda}$ is isotropic for a single phase and is representable by a scalar quantity (*i.e.*, $\mathbf{\Lambda} = \lambda\mathbf{I}$). Table 2.I lists some of the fluxes, gradients, and transport coefficients represented by such differential equations.

Table 2.I Conductive-type Transport Phenomena

Material Flux $\mathbf{F}$	Gradient $\nabla\phi$	Transport Coefficient
Heat Flux	Temperature Gradient	Thermal Conductivity
Mass Flux	Concentration Gradient	Diffusion Coefficient
Electric Current	Electric Field	Electrical Conductivity
Electric Displacement	Electric Field	Dielectric Constant
Magnetic Induction	Magnetic Field	Magnetic Permeability

As seen in Table I, the prediction of the effective conductivity of a two-phase medium spans many fields, and a great deal of effort has been devoted to its resolution. Therefore, we cannot possibly summarize even a small fraction of the previous investigations on the subject. For a detailed review of the subject, the interested reader is referred to the article by Batchelor (1974). Here, we shall give a brief account of those papers of direct relevance to our work.

Maxwell (1873) was the first to consider conduction through a suspension of particles. He recognized that the change in conductivity due to the presence of particles in the matrix was related to the average particle dipole. Maxwell then applied this result to a dilute suspension of spheres; so dilute that interactions among the particles were negligible. By calculating the dipole of an isolated sphere subject to a potential gradient, Maxwell derived an expression for the effective conductivity correct to $O(c)$ for random or regular dispersions of spheres, where c is the volume fraction of spheres in the suspension.

Following Maxwell, Rayleigh (1892) calculated the effective conductivity correct to $O(c^2)$ for a simple-cubic array of spheres. Rayleigh's approach was to consider particle moments up to the octupole and determine their effect on the particle dipoles. Because the dipole-dipole interactions are long-ranged (*i.e.*, $O(1/r^3)$), and the suspension is infinite, Rayleigh formed a conditionally convergent sum of dipole-dipole interactions. Rayleigh noted the conditional convergence of the sum and performed the summation in a particular order with no justification. As later shown by McPhedran & McKenzie (1978) and O'Brien (1979), Rayleigh fortunately performed the sum correctly.

Meredith & Tobias (1960), McPhedran & McKenzie (1978), and McKenzie, McPhedran, & Derrick (1978) extended Rayleigh's method to include the complete range of volume fractions and conductivity ratios for cubic lattices. Zuzovski & Brenner (1977) developed an alternate method that takes advantage of the periodicity of the potential field in cubic arrays, and in so doing, circumvents the convergence difficulties of Rayleigh's method. Sangani & Acrivos (1982) modified Zuzovski & Brenner's method by taking advantage of the symmetry of spherical

particles and calculated the effective conductivity for cubic arrays of spheres at all volume fractions and conductivity ratios. Sangani & Acrivos's results are in excellent agreement with those of McPhedran & McKenzie and McKenzie, *et al.*

Jeffrey (1973) was the first to calculate the effective conductivity correct to $O(c^2)$ for a random dispersion of spheres. However, in order to deal with the conditional convergence of his ensemble average of two-sphere dipole interactions, Jeffrey had to form a "*renormalization quantity.*" The renormalization quantity was first proposed by Batchelor (1972) and was used to calculate the $O(c^2)$ correction for the effective viscosity of a suspension of spheres by Batchelor & Green (1972) and the effective bulk modulus of spherical inclusions in an elastic matrix by Chen & Acrivos (1978). Chen & Acrivos noted, however, that it is not always obvious which renormalization quantity to choose since there is apparently more than one choice. O'Brien (1979) formulated an unambiguous method to determine the renormalization quantity, and hence the effective transport coefficients. The method is based on correctly assessing the importance of the macroscopic bounding integral that surrounds particles in the integral formulation of the transport equations. With O'Brien's method, the renormalization quantity arises quite naturally so there is no ambiguity in choosing its correct form.

While there has been no further work extending Jeffrey's result to higher orders in concentration, progress has been made in determining the effective conductivity for densely packed dispersions of highly conductive spheres. The method here employs the reasonable physical assumption that the flux of heat or charge occurs entirely in the region where particles are in near contact. Thus, the effective conductivity is determined with the asymptotic form for the flux between two spheres, which is logarithmically singular in gap width and justifies the assumption. Keller (1963) solved this problem correct to $O(\ln\epsilon)$, where ϵ is the dimensionless gap width, for a densely packed simple-cubic array of spheres. Batchelor & O'Brien (1977) extended Keller's work to include touching spheres and near-perfect conductors and calculated the effective conductivity for cubic arrays of spheres. (Note, the exact results for cubic arrays near maximum packing for perfect conductors, which were

published after the results of Keller and Batchelor & O'Brien, are consistent with these asymptotic results.) Using these asymptotic results, Batchelor & O'Brien estimated the effective conductivity for random densely packed spheres, based on experimentally determined average sphere coordination numbers.

In lieu of an exact solution for a random dispersion of particles, many investigators have derived upper and lower bounds on the effective conductivity. Hashin & Shtrikman (1962) used a variational technique to establish the most restrictive bounds upon the effective conductivity of a dispersion of spheres. Recent work by Torquato & Lado (1986) provides more accurate bounds on the effective conductivity for a dispersion of spheres. Their work does this by including microstructural information beyond the volume fraction of spheres, such as two-point correlation functions. However, for moderate concentrations of highly conducting spheres (relative to the matrix) the upper and lower bounds differ by a factor of 5 to 10, and for perfect conductors, no upper bound exists (a consequence of the logarithmic singularity of the flux). Thus, no accurate prediction is available for the effective conductivity of moderate-to-highly concentrated random dispersions of spheres.

In this paper a general method is developed to predict the effective conductivity of an arbitrary configuration of an infinite suspension of particles. For the sake of clarity, the paper is divided into the following subsections:

In §2.2 we develop the suspension transport equations for a statistically homogeneous medium. These macroscopic transport equations are derived from spatial averages of the local transport equations for conduction, namely (2.1) and (2.2). The macroscopic transport equations explicitly relate the effective conductivity of the medium to the average particle dipole and the intrinsic dipole. This result serves as a motivation to determine the particle dipoles directly in our calculation scheme. The suspension transport equations are also used in formulating the method.

In §2.3 for pedagogical reasons, we develop a method for determining the individual dipoles for a finite number of particles in a matrix of infinite extent. In the case of finite particles, there are no conditional convergence problems, so we may concentrate on a key element of the method: including both far- and near-field

particle interactions. We follow, by analogy, the "Stokesian dynamics" method of Durlofsky, Brady, & Bossis (1987). The integral equations of the conductive-type transport are expanded into a sum of particle moments (*i.e.*, the charge, dipole, quadrupole, etc.). The individual particle potentials and the potential gradient are related to the sum of particle moments with Faxén laws to generate a "potential" matrix (the electrostatic analog of the low-Reynolds-number mobility matrix). Inverting this potential matrix forms the capacitance matrix (the electrostatic analog of the low-Reynolds-number resistance matrix). The potential invert produces the many-body reflections of the particle moments that were included in its formulation. Thus, the potential invert captures the far-field interactions of the particles. To include near-field interactions, exact two-body interactions not already counted are added to the potential invert to form a more accurate capacitance matrix. The capacitance matrix formed includes both far- and near-field particle interactions. In the case of particles with a given charge subject to an external electric field, the dipoles of the particles can now be calculated directly. Although no simulations were done with a finite number of particles, it should be noted that this method could be used for calculating electrostatic forces on a finite group of charged particles in an ionic solution or on dielectric particles in a fluid.

In §2.4 the method is extended to infinite suspensions of particles. In the case of an infinite suspension, the potential matrix containing the far-field particle interactions must be carefully formed to avoid convergence difficulties. The starting point is again the integral form of the transport equations; however, the bounding integral on a surface at infinity does not vanish as in the case of a finite number of particles. Also, it is not possible to have a statistically homogeneous medium if the average charge density for the medium is nonzero. Therefore, in the most general case where there is a net average particle charge, there must be a balancing charge density in the form of an integral distributed throughout the medium to ensure a zero average charge density. With the bounding integral written following the method of O'Brien and the balancing charge density integral, absolutely convergent sums of particle moments are formed. It will be seen that these integrals give rise

to the "renormalization quantity" for this problem.

Since there is an infinite dispersion of particles, the above formulation generates an infinite number of equations. In §2.5 we invoke periodic boundary conditions to reduce the system to a finite number of linear equations. To accelerate the formation of the potential matrix, and to take advantage of the periodic replication of space filling cells of particles, the method of Ewald is employed to form rapidly converging lattice sums. In forming the lattice sums, the convergence problem and solution become clear. The lattice sums have singularities at the zero wave vector; however, these singularities cancel exactly with terms from the bounding integral at infinity, producing convergent sums. After the potential matrix is formed with the lattice sums, it is inverted and the two-body interactions are added as before in §2.3 to form the capacitance matrix of the system. There are no convergence difficulties with the addition of two-body interactions, since they are short-ranged, as will be shown.

In §2.6 as an example and a test for accuracy, the method is used to calculate the Madelung constant of cohesive energy for ionic crystals and to determine the effective conductivity for cubic arrays of spheres with particle-to-matrix conductivity ratios of infinity, 10, and 0.01. The effective conductivity results of the simulation are compared to those of Sangani & Acrivos.

Finally, in §2.7 we provide a concluding discussion of the strengths and weaknesses of the method. In addition, we outline future work using the method to determine the conductivities of random suspensions (Chapter 3) and to determine the effective reaction rate coefficients in diffusion-limited reactions between large particles and a reactant (Chapter 5). Also with the use of "Stokesian dynamics," the method can be used for the dynamic simulation of electro- and magneto-rheological fluids (Chapters 7 & 8). It should be noted that the method is also applicable to the statistical mechanical and molecular dynamical simulation of dipolar fluids. Indeed, in the Monte Carlo simulation of a Stockmayer fluid, De Leeuw, Perram, and Smith (1983) faced conditional convergence difficulties which were dealt in an ad hoc manner. These difficulties are rigorously and completely resolved with our

method.

2.2 Suspension Transport Equations

Consider an infinite suspension of particles with conductivity λ_p dispersed in a matrix of conductivity λ. Each particle has a specified charge distribution, $\rho(\mathbf{x})$, and the suspension is subject to a macroscopic or volume-averaged potential gradient, $\mathbf{G}$. To determine the effective conductivity, we must relate the volume-averaged flux to the volume-averaged potential gradient in this two-phase medium. To do so, we follow the formalism discussed by Batchelor (1974) for generating the suspension or macroscopic transport equations.

The average potential gradient, $\mathbf{G}$, and the average flux, $\langle \mathbf{F} \rangle$, are defined by,

$$\mathbf{G} = \frac{1}{V} \int_V \nabla \phi dV, \tag{2.3}$$

$$\langle \mathbf{F} \rangle = \frac{1}{V} \int_V \mathbf{F} dV, \tag{2.4}$$

where the volume, V, is large enough to include many particles. Note that both $\mathbf{G}$ and $\langle \mathbf{F} \rangle$ are suspension averages – averages over both matrix and particle phases. Making use of the constitutive law for the matrix, the volume-averaged flux in equation (2.4) can be written as,

$$\langle \mathbf{F} \rangle = -\frac{1}{V} \int_V \lambda \nabla \phi dV + \frac{1}{V} \sum_\beta \int_{V_\beta} (\lambda \nabla \phi + \mathbf{F}) dV, \tag{2.5}$$

or,

$$\langle \mathbf{F} \rangle = -\lambda \mathbf{G} + \frac{1}{V} \sum_\beta \int_{V_\beta} [\nabla \cdot (\lambda \phi \mathbf{I} + \mathbf{F}\mathbf{x}) - \mathbf{x} \nabla \cdot \mathbf{F}] dV, \tag{2.6}$$

where the sum is over all the particles, which are labeled by the index β. Inside the particles, $\nabla \cdot \mathbf{F} = \rho(\mathbf{x})$, where $\rho(\mathbf{x})$ is the specified charge density within the particle. Thus (2.6) becomes,

$$\langle \mathbf{F} \rangle = -\lambda \mathbf{G} + n \langle \mathbf{S} \rangle - n \langle \mathbf{P} \rangle \tag{2.7}$$

where

$$\mathbf{S} = \int_{\partial \Omega_\beta} (\mathbf{x}\mathbf{F} + \lambda \phi \mathbf{I}) \cdot \mathbf{n} dS, \tag{2.8}$$

and

$$\mathbf{P} = \int_{V_\beta} \rho(\mathbf{x})\mathbf{x}dV. \tag{2.9}$$

The quantity $\langle \mathbf{S} \rangle$ is the average particle dipole, the quantity $\langle \mathbf{P} \rangle$ is the average intrinsic dipole, and n is the number density of particles. In (2.8) and (2.9) $\mathbf{x}$ is a point within the particle relative to a reference point inside the particle. Equation (2.7) is the suspension transport equation for a two-phase medium.

For a statistically homogeneous medium with zero-charge particles where the local transport equations, (2.1) and (2.2), are linear, we can write

$$\langle \mathbf{F} \rangle = -\mathbf{\Lambda}_{eff} \cdot \mathbf{G}, \tag{2.10}$$

where $\mathbf{\Lambda}_{eff}$ is the effective conductivity tensor of the medium. For zero-charge particles, $\langle \mathbf{P} \rangle = 0$, and $\langle \mathbf{S} \rangle$ is a linear function of $\mathbf{G}$ (*i.e.* $\langle \mathbf{S} \rangle = \mathbf{C} \cdot \mathbf{G}$, where $\mathbf{C}$ is some 3 by 3 matrix). Thus, we see that the effective conductivity defined by (2.10) is determined by the average particle dipole. Also for a statistically homogeneous medium, the average charge density in the medium is zero, so performing a similar average on $\nabla \cdot \mathbf{F}$ yields,

$$\nabla \cdot \langle \mathbf{F} \rangle = 0. \tag{2.11}$$

Note that the form of the average flux in (2.7) is a special case of the average flux in a structured continuum. As shown by Russakoff (1970) and Dahler & Scriven (1963), the general average flux includes the divergences of all the higher particle moments such as quadrupoles, hexadecupoles, etc. The form of equation (2.7) assumes a statistically homogeneous medium with no sources or sinks of higher particle moments because of the choice of the averaging function used in (2.3) and (2.4). The averaging function inherently assumes that the exact size of the volume is not important as long as V is large enough to include many particles. This is only true if the medium is statistically homogeneous.

As shown above, the calculation of the effective conductivity of an infinite dispersion of particles is reduced to the calculation of the average particle dipole. In the next section, we will outline the method for determining the individual particle dipoles for a finite number of particles in an arbitrary configuration.

2.3. Method for a Finite Number of Particles

In this section we shall consider the problem of a finite number of particles in a matrix of infinite extent. This will allow a clear explanation of the method for capturing both far- and near-field interactions, without the complicating convergence problems of infinite systems. These convergence difficulties will be addressed in the next section.

2.3.1 Calculation of Far-Field Interactions

Consider a suspension of N particles of conductivity λ_p in an unbounded matrix of conductivity λ. The particles have a specified internal charge distribution, and the charge density within the matrix is zero. The integral form of Laplace's equation is,

$$\phi(\mathbf{x}) - \phi^E(\mathbf{x}) = \frac{1}{4\pi}\sum_\beta \int_{\partial\Omega_\beta} (\mathbf{F}\frac{1}{\lambda r} + \phi\nabla_y\frac{1}{r}) \cdot \mathbf{n}dS, \tag{2.12}$$

where $\phi(\mathbf{x})$ is the potential field at $\mathbf{x}$, $\phi^E(\mathbf{x})$ is the imposed or external potential field at $\mathbf{x}$ in the absence of any particles, and the integral is over the surface of the β particle. The distance $r = |\mathbf{x} - \mathbf{y}|$ and $\nabla_y = \partial/\partial(\mathbf{y} - \mathbf{x})$. The normal, $\mathbf{n}$, points out of the particle. The particle moments are defined as,

$$q_\beta = \int_{\partial\Omega_\beta} \mathbf{F} \cdot \mathbf{n}dS, \tag{2.13a}$$

$$\mathbf{S}_\beta = \int_{\partial\Omega_\beta} (\mathbf{x}\mathbf{F} + \lambda\nabla\phi) \cdot \mathbf{n}dS, \tag{2.13b}$$

$$\mathbf{Q}_\beta = \int_{\partial\Omega_\beta} \left(\left[\mathbf{x}\mathbf{x} - \frac{1}{3}(\mathbf{x}\cdot\mathbf{x})\mathbf{I}\right]\mathbf{F}\cdot\mathbf{n} + \left[\mathbf{x}\mathbf{n} + \mathbf{n}\mathbf{x} - \frac{2}{3}(\mathbf{n}\cdot\mathbf{x})\mathbf{I}\right]\lambda\phi \right) dS\,, \tag{2.13c}$$

which are the charge (monopole), dipole, and quadrupole, respectively, and where the position $\mathbf{x}$ in the moment definitions is defined relative to some reference point in the particle. For a sphere, the reference point is taken as the center of the sphere. Note that the quadrupole is symmetric and traceless. Expanding the integral in (2.12) in terms of the particle moments yields,

$$\phi(\mathbf{x}) - \phi^E(\mathbf{x}) = \frac{1}{4\pi\lambda}\sum_\beta (q_\beta\frac{1}{r} + \mathbf{S}_\beta\cdot\nabla_y\frac{1}{r} + \frac{1}{2}\mathbf{Q}_\beta : \nabla_y\nabla_y\frac{1}{r} + \cdots), \tag{2.14}$$

where the expansion has been truncated at the quadrupole level and the moment propagators $(\frac{1}{r}, \nabla_y \frac{1}{r}, \nabla_y \nabla_y \frac{1}{r})$ are evaluated at $\mathbf{x} - \mathbf{R}_\beta$, where $\mathbf{R}_\beta$ is the reference point inside particle β, such as the center of a spherical particle.

However, we are not interested in the matrix potential, but rather the potential of a particle. To determine a particle potential, we use a Faxén-type law, which relates the particle potential, at a specific point, to its charge and the potential at that point in the particle's absence. For spherical particles in a charge free matrix, the Faxén-type law takes on the simple form (see Appendix 2.I),

$$\phi(\mathbf{R}_\alpha) - \phi'(\mathbf{R}_\alpha) = \frac{q_\alpha}{4\pi\lambda a}[1 + h(\rho)], \tag{2.15}$$

where $\phi(\mathbf{R}_\alpha)$ is the potential of particle α at its center and $\phi'(\mathbf{R}_\alpha)$ is the potential at $\mathbf{R}_\alpha$ due to the external potential and the other particles. The dimensionless function $h(\rho)$ varies with the prescribed charge distribution within the particle. For a constant distribution of charge, $h(\rho) = \frac{1}{2}\gamma^{-1}$ where $\gamma = \lambda_p/\lambda$. For a perfect conductor $h(\rho) = 0$. The potential, $\phi'(\mathbf{R}_\alpha)$, due to the external potential and the other particles is, in fact, $\phi(\mathbf{x})$ given by (2.14) evaluated at $\mathbf{R}_\alpha$. Combining (2.14) and (2.15) we have,

$$\phi(\mathbf{R}_\alpha) - \phi^E(\mathbf{R}_\alpha) = \frac{q_\alpha}{4\pi\lambda a}[1 + h(\rho)] + \frac{1}{4\pi\lambda}\sum_{\substack{\beta \\ \beta \neq \alpha}} (q_\beta \frac{1}{r} + \mathbf{S}_\beta \cdot \nabla_y \frac{1}{r} + \frac{1}{2}\mathbf{Q}_\beta : \nabla_y \nabla_y \frac{1}{r}), \tag{2.16}$$

where the moment propagators are evaluated at $\mathbf{R}_\alpha - \mathbf{R}_\beta$. We can now relate the potentials of the N particles to the N particle charges, dipoles, and quadrupoles and to the external potential field. We need to develop equations similar to (2.16) to relate the gradient, $\mathbf{G}^E$, and the gradient of the gradient, $\nabla\mathbf{G}^E$, of the external potential field to the N particles' moments.

To this end we operate on (2.12) with ∇ and $\nabla\nabla$ and expand the integrals in terms of particle moments to form,

$$\nabla\phi(\mathbf{x}) - \mathbf{G}^E \cong -\frac{1}{4\pi\lambda}\sum_\beta (q_\beta \nabla_y \frac{1}{r} + \mathbf{S}_\beta \cdot \nabla_y \nabla_y \frac{1}{r} + \frac{1}{2}\mathbf{Q}_\beta : \nabla_y \nabla_y \nabla_y \frac{1}{r}), \tag{2.17}$$

$$\nabla\nabla\phi(\mathbf{x}) - \nabla\mathbf{G}^E \cong \frac{1}{4\pi\lambda}\sum_{\beta}(q_\beta\nabla_y\nabla_y\frac{1}{r} + \mathbf{S}_\beta\cdot\nabla_y\nabla_y\nabla_y\frac{1}{r} + \frac{1}{2}\mathbf{Q}_\beta : \nabla_y\nabla_y\nabla_y\nabla_y\frac{1}{r}). \tag{2.18}$$

As before, the moment expansion is truncated at the quadrupole level. For spheres, the Faxén laws for the particle dipole and quadrupole are (see Appendix 2.I),

$$\nabla\phi'(\mathbf{R}_\alpha) = -\frac{\mathbf{S}_\alpha}{4\pi a^3\delta\lambda}, \tag{2.19}$$

$$\nabla\nabla\phi'(\mathbf{R}_\alpha) = -\frac{3\mathbf{Q}_\alpha}{4\pi\lambda a^5}, \tag{2.20}$$

respectively, where $\delta = (\gamma\text{-}1)/(\gamma+2)$, and $\nabla\phi'(\mathbf{R}_\alpha)$ and $\nabla\nabla\phi'(\mathbf{R}_\alpha)$ are the gradient and the gradient of the gradient, respectively, of the potential at $\mathbf{R}_\alpha$ due to the external potential and the presence of the other particles. The $\nabla\phi'(\mathbf{R}_\alpha)$ and $\nabla\nabla\phi'(\mathbf{R}_\alpha)$ are given by (2.17) and (2.18) evaluated at $\mathbf{R}_\alpha$. Note, the Faxén law for the quadrupole assumes the sphere is a perfect conductor, *i.e.* $\lambda/\lambda_p = 0$. A non-perfect conductor Faxén law would merely alter the RHS of (2.20) by a constant multiple and would not change the subsequent analysis. Combining (2.19) and (2.20) with (2.17) and (2.18) we have,

$$-\mathbf{G}^E = \frac{\mathbf{S}_\alpha}{4\pi a^3\delta\lambda} - \frac{1}{4\pi\lambda}\sum_{\substack{\beta\\ \beta\neq\alpha}}(q_\beta\nabla_y\frac{1}{r} + \mathbf{S}_\beta\cdot\nabla_y\nabla_y\frac{1}{r} + \frac{1}{2}\mathbf{Q}_\beta : \nabla_y\nabla_y\nabla_y\frac{1}{r}), \tag{2.21}$$

$$-\nabla\mathbf{G}^E = \frac{3\mathbf{Q}_\alpha}{4\pi\lambda a^5} + \frac{1}{4\pi\lambda}\sum_{\substack{\beta\\ \beta\neq\alpha}}(q_\beta\nabla_y\nabla_y\frac{1}{r} + \mathbf{S}_\beta\cdot\nabla_y\nabla_y\nabla_y\frac{1}{r} + \frac{1}{2}\mathbf{Q}_\beta : \nabla_y\nabla_y\nabla_y\nabla_y\frac{1}{r}). \tag{2.22}$$

In equation (2.22) the gradient of the external potential gradient, $\nabla\mathbf{G}^E$, is zero in the medium we consider here because it is inconsistent to have an imposed quadratic potential field without boundaries, and the direct contribution from the boundaries is actually more important than several of the terms in (2.16), (2.21), and (2.22).

Equations (2.16), (2.21), and (2.22) can be written for all the N particles in the system, and the resulting equation set may be conveniently written in the following

form of a matrix of tensors:

$$\begin{pmatrix} \mathbf{\Phi} \\ -\mathbf{G}^E \\ \mathbf{O} \end{pmatrix} = \begin{pmatrix} \hat{\mathbf{M}}_{\Phi q} & \hat{\mathbf{M}}_{\Phi \mathbf{S}} & \hat{\mathbf{M}}_{\Phi \mathbf{Q}} \\ \hat{\mathbf{M}}_{\mathbf{G}q} & \hat{\mathbf{M}}_{\mathbf{GS}} & \hat{\mathbf{M}}_{\mathbf{GQ}} \\ \hat{\mathbf{M}}_{\nabla q} & \hat{\mathbf{M}}_{\nabla \mathbf{S}} & \hat{\mathbf{M}}_{\nabla \mathbf{Q}} \end{pmatrix} \cdot \begin{pmatrix} \mathbf{q} \\ \mathbf{S} \\ \mathbf{Q} \end{pmatrix}, \tag{2.23}$$

where $\mathbf{\Phi}$ is the vector of particle potentials less the external potential field evaluated at the particle centers, $\phi(\mathbf{R}_\beta) - \phi^E(\mathbf{R}_\beta)$, and $\mathbf{q}$, $\mathbf{S}$, and $\mathbf{Q}$ are the vectors of the particle moments. Because a particle quadrupole is symmetric and traceless, only five of its components are needed. Equation (2.23) defines the "potential" matrix relating the charge, dipole, and quadrupole to the potential, the potential gradient, etc. There are 9 unknowns for each particle; one charge, 3 dipole and 5 quadrupole. The submatrices are the couplings between potential and charge, gradient and dipoles, etc. The matrix in (2.23) is called the grand potential matrix, $\hat{\mathcal{M}}$, in electrostatics. It is analogous to the grand mobility matrix in low-Reynolds-number fluid mechanics introduced by Brenner (1964*a*). The symbols $\hat{\mathcal{M}}$ and the $\hat{\mathbf{M}}'s$ are used because of that analogy. The grand potential matrix is a function of the particle positions only; it is determined uniquely by the geometry of the suspension. Since $\nabla \mathbf{G}^E$ is zero, $\mathbf{Q}$ may be written in terms of the charges and dipoles, and the grand potential matrix, $\hat{\mathcal{M}}$, reduces to the potential matrix, $\mathbf{M}$:

$$\begin{pmatrix} \mathbf{\Phi} \\ -\mathbf{G}^E \end{pmatrix} = \begin{pmatrix} \mathbf{M}_{\Phi q} & \mathbf{M}_{\Phi \mathbf{S}} \\ \mathbf{M}_{\mathbf{G}q} & \mathbf{M}_{\mathbf{GS}} \end{pmatrix} \cdot \begin{pmatrix} \mathbf{q} \\ \mathbf{S} \end{pmatrix}, \tag{2.24}$$

where the new couplings contain the quadrupole contributions.

The moment expansion of the particle integral in (2.12) could have been continued beyond the quadrupoles to include octupoles, hexadecupoles, etc., along with the higher order derivatives of the gradient. Again, all higher derivatives of the gradient must be zero to be consistent with the absence of the boundaries in the medium. Thus, all the higher moments can be expressed in terms of the particle charges and dipoles, as was done for the quadrupoles, resulting in a matrix identical in form to (2.24). The accuracy of (2.24) depends upon the number of moments included in the integral equation expansion. When the particles are far from each other, including the moments up to the dipoles or quadrupoles is adequate. However, in the case of near-perfect conductors, as the particles come nearer to each

other, the two-particle near-field interactions are expected to become important. Physically, the conservable quantity, be it charge, heat, etc., prefers to flow through the highly conducting particles. Thus, to minimize resistance the conservable quantity flows though the small gap between the two closely spaced particles. The charge or dipole between two perfect conductors at different potentials is logarithmically singular in the separation distance between particle surfaces, which is indicative of the preferred conduction path. The singularity is called a lubrication singularity by analogy to the fluid mechanic case. To include the lubrication interaction between particles near contact from the potential formulation, many (indeed all) of the higher moments must be included. Clearly, to include many moments would be computationally expensive since the number of equations to be solved would increase by p^2, and the computation time would increase by p^6, where p is the level of the particle moments retained in the formulation of the potential matrix. In the following subsection we will describe a computationally efficient method of including exact two-body interactions to describe concentrated systems of particles. In the case of non-perfectly conducting particles, it is not immediately clear how important two-particle interactions are in determining the effective conductivity. As will be demonstrated in §5, two-particle interactions for non-perfectly conducting particles are not important; hence, the potential matrix formulation provides an adequate description for determining the effective conductivity of such suspensions.

2.3.2 Addition of Two-Body Effects to Calculate Near-Field Interactions

There exists the exact relationship

$$\begin{pmatrix} \mathbf{q} \\ \mathbf{S} \end{pmatrix} = \begin{pmatrix} \mathbf{C}_{q\Phi} & \mathbf{C}_{q\mathbf{G}} \\ \mathbf{C}_{\mathbf{S}\Phi} & \mathbf{C}_{\mathbf{SG}} \end{pmatrix} \cdot \begin{pmatrix} \mathbf{\Phi} \\ -\mathbf{G}^E \end{pmatrix} \tag{2.25}$$

among the $\mathbf{q}$ and $\mathbf{S}$ moments and the potential vectors $\mathbf{\Phi}$ and $\mathbf{G}^E$. The matrix in (2.25) is called the capacitance matrix, $\mathbf{C}$, in electrostatics. The sub-matrices of the capacitance matrix are couplings between charge and potential, charge and gradient, etc. Now, the inversion of $\mathbf{M}$ produces the many-body reflections of the interactions among the particle charges, dipoles, and higher moments that were included in the formulation of the potential matrix in (2.24). If $\mathbf{M}$ were exact, then its invert would

be equal to the capacitance matrix, $\mathbf{C}$. As stated before, the accuracy of $\mathbf{M}$, and subsequently the accuracy of $\mathbf{M}^{-1}$, depends upon the number of moments included in the original potential formulation and the concentration of the suspension. The highest moment we will retain is the dipole or quadrupole. To approximate the exact multi-body capacitance matrix, which would contain information on all the moments of each particle, we will add to the potential matrix invert a capacitance matrix containing exact two-body interactions between all the particles less two-body far-field interactions between particles. Thus, the approximate capacitance matrix is

$$\mathbf{C} \approx \mathbf{M}^{-1} + \mathbf{C}_{2b} - \mathbf{C}_{2b}^{\infty}. \tag{2.26}$$

The matrix $\mathbf{C}_{2b}$ contains the exact two-body interactions between all pairs of particles. That is, $\mathbf{C}_{2b}$ contains the $\mathbf{q} - \mathbf{S}$ capacitance matrix for particles α and β alone in the medium, *i.e.* ignoring particles δ, γ, etc. Similarly, $\mathbf{C}_{2b}^{\infty}$ contains the two-body interactions between particles formed by inverting the two-body potential matrix that includes terms up to the same order as in $\mathbf{M}$. The latter term is subtracted since it was already included in the potential inverse of (2.24). The exact two-body capacitance matrix for spheres can be constructed from the solutions of Jeffrey (1973, 1978) and Davis (1974) for two perfect spherical conductors immersed in a linear potential gradient.

For dilute dispersions, the two-body capacitance matrices' difference will not contribute to $\mathbf{C}$, and the particle interactions are accurately described by $\mathbf{M}^{-1}$. For concentrated suspensions of perfect conductors the two-body interactions will capture the lubrication singularities between particles. Because the limits of dilute and concentrated suspensions are well-described by $\mathbf{C}$, moderately concentrated suspensions are also expected to be well described. Durlofsky, *et al.* (1987) use an analogous approximation to form the Stokesian dynamics grand resistance tensor. Their successful results, along with those for the effective conductivities of periodic arrays of spheres presented in §6, validate the method. As mentioned previously, the addition of two-body interactions is not necessary for non-perfect conductors since there is no lubrication singularity between particles near contact.

With this approximation to C, the particle dipoles are determined by specifying a zero-charge on each particle and imposing an external potential gradient. Solving the matrix equation yields,

$$\mathbf{S} = (\mathbf{C_{S\Phi}} \cdot \mathbf{C_{q\Phi}}^{-1} \cdot \mathbf{C_{qG}} - \mathbf{C_{SG}}) \cdot \mathbf{G}^E. \tag{2.27}$$

The dipoles of each particle can be calculated and averaged, or the matrix coupling $\mathbf{S}$ to $\mathbf{G}^E$ can be averaged to produce a coupling between $\langle \mathbf{S} \rangle$ and $\mathbf{G}^E$. Thus, the effective conductivity, at least locally in the region of particles, is given by

$$\mathbf{\Lambda}_{eff} = \lambda \mathbf{I} - n\langle \mathbf{C_{S\Phi}} \cdot \mathbf{C_{q\Phi}}^{-1} \cdot \mathbf{C_{qG}} - \mathbf{C_{SG}} \rangle, \tag{2.28}$$

where here $\langle\ \rangle$ denotes an average over all particles.

Up to now the potential matrix has been formed for a finite number of particles. To calculate the effective conductivity of an infinite medium, we could form the approximate capacitance matrix for M particles and calculate the average dipole for N particles in the middle of the suspension. If $M \gg N \gg 1$, we expect the effective conductivity to be the same as that of an infinite medium of spheres in a matrix. However, we would have $9(M - N)$ extra components in the unknown vector in (2.23). In the next two sections we will present an exact, unambiguous method for forming the potential matrix for an infinite suspension and use periodic boundary conditions to retain a finite number of unknowns.

2.4. Potential Matrix Formulation for Infinite Systems of Particles

In the previous section we considered a finite collection of particles in a matrix of infinite extent. The form of (2.12) assumes that far from the collection of particles, the flux and the potential approach those given by the external field. That is to say, the effect of the presence of the particles dies away far from the particles. This is not the case, however, for an infinite collection of particles. For example, a test particle a distance r from a particle with charge q will experience a potential of $O(q/r)$. If the test particle is in a system of size R where the number density of other particles with charge q is n, then the interaction potential experienced by the test particle is $O(nqR^2)$; the interaction potential grows as R^2. Particle-particle interactions growing with system size occur for all long-ranged interactions, *i.e.* those that decay as $O(1/r^3)$ or slower. Thus, as the system size goes to infinity, $R \to \infty$, the interactions seem to diverge. The same argument for charge applies to the dipoles and quadrupoles as well. Following the same line of reasoning reveals that the interaction potential for a test particle is $O(n\langle \mathbf{S} \rangle R)$ and $O(n\langle \mathbf{Q} \rangle lnR)$ due to the long-ranged interactions of the dipoles and quadrupoles, respectively.

Therefore, we must carefully reconsider our formulation of the problem for infinite systems. First, for a statistically homogeneous medium the average charge density in the *entire* medium must be zero. If it were not, as for example if one assumed a nonzero average particle charge without a compensating charge distribution in the matrix, the average potential would grow quadratically with position. This would necessitate an origin for reference measurement and thus violate the assumed homogeneity. In the physical context of heat transfer, the temperature distribution would be determined by the boundaries necessary to remove the growing (unbounded) source of heat. Similarly, since the particle dipoles are proportional to the potential gradient, which now must vary linearly rather than be a constant, the average particle dipole will also grow linearly with position. This also clearly violates the assumption of statistical homogeneity.

Even if the average particle charge is zero (and there is no charge distribution in the matrix), we may proceed only up to the potential formulation. The full potential

matrix cannot be inverted to form the capacitance matrix because the system of equations is overspecified by requiring $\langle q \rangle = 0$. To complete the capacitance matrix, the potential matrix must be formed for the most general case of a nonzero average particle charge. After all, the capacitance matrix is a geometric quantity completely determined by the particle configuration, which cannot "know" the value of the charge vector. To allow for the most general case of a completely unspecified $\mathbf{q}$, and still have a statistically homogeneous medium, requires the average particle charge density, $n\langle q \rangle$, to be balanced by an opposite charge density distributed throughout the medium, such that the average charge density in the entire medium is zero and $\nabla \cdot \langle \mathbf{F} \rangle = 0$. Here we will present the result for a constant average charge density, $-n\langle q \rangle$, distributed uniformly throughout the entire medium. The method can, however, be extended to other balancing charge distributions (Chapter 5).

Note, these problems do not arise in the analogous low-Reynolds-number hydrodynamic problem (Brady, Phillips, Lester, & Bossis 1988). There, it is possible to have a nonzero average force on an infinite collection of particles with no specified balancing force distribution and still have a statistically homogeneous medium. The hydrodynamic equations allow a linearly growing stress field because the pressure gradient precisely balances the average force exerted by the particles on the fluid. In the electrostatic case there is no equivalent pressure term, so a balancing charge density is required in the problem statement.

To correctly account for long-ranged interactions, we must begin with the exact integral representation of Laplace's equation, which is given by,

$$\begin{aligned}\phi(\mathbf{x}) = \frac{1}{4\pi}\sum_{\beta}\int_{\partial\Omega_\beta}(\mathbf{F}\frac{1}{\lambda r} + \phi\nabla_y\frac{1}{r})\cdot\mathbf{n}\, ds + \frac{1}{4\pi}\int_{S'_\infty}(\mathbf{F}\frac{1}{\lambda r} + \phi\nabla_y\frac{1}{r})\cdot\mathbf{n} dS \\ - \frac{1}{4\pi\lambda}\int_{V'} n\langle q\rangle\frac{1}{r}dV.\end{aligned} \tag{2.29}$$

The surface S'_∞ is a distant closed surface that surrounds $\mathbf{x}$ and does not intersect particles, but rather stays in the matrix following particle boundaries to avoid intersection, as illustrated in Figure 2.1. The volume integral represents the decrease in potential due to the constant charge distributed in the volume enclosed by S'_∞.

The normal, $\mathbf{n}$, points into the matrix. In a finite suspension of particles where there is no balancing charge density over all space, the volume integral vanishes, and the integral over S'_∞ vanishes as S'_∞ grows if $\mathbf{F}$ and ϕ are written in disturbance variables, and we recover (2.12). For an infinite system the integral over S'_∞ cannot be neglected. This integral, as O'Brien (1979) astutely pointed out, will give rise to the average potential and render the interactions convergent.

To see this, let us transform the surface integral over S'_∞ to one over S_∞ that cuts through the particles that S'_∞ went around. We can rewrite the integral over S'_∞ as a surface integral over S_∞ and a sum of integrals over the N_s particles' partial volumes lying between S'_∞ and S_∞:

$$\begin{aligned}\frac{1}{4\pi}\int_{S'_\infty}(\mathbf{F}\frac{1}{\lambda r}+\phi\nabla_y\frac{1}{r})\cdot\mathbf{n}dS = \frac{1}{4\pi}\int_{S_\infty}(\mathbf{F}\frac{1}{\lambda r}+\phi\nabla_y\frac{1}{r})\cdot\mathbf{n}dS \\ \pm\frac{1}{4\pi}\sum_{i=1}^{N_s}\int_{V_i}\nabla\cdot(\mathbf{F}\frac{1}{\lambda r}+\phi\nabla_y\frac{1}{r})dV.\end{aligned} \tag{2.30}$$

The plus and minus correspond to the particles whose centers lie inside or outside S_∞, respectively. Following O'Brien, to evaluate the first integral on the RHS of (2.30), we make the assumption that $\mathbf{F}$ and ϕ can be replaced by their suspension averages, $\langle\mathbf{F}\rangle$ and $\langle\phi\rangle$. This assumption is reasonable because $\frac{1}{r}$ and $\nabla_y\frac{1}{r}$ are approximately constant over a large enough section of S_∞ to perform an average of $\mathbf{F}$ and ϕ. With the use of the divergence theorem, the integral over S_∞ becomes,

$$\begin{aligned}\frac{1}{4\pi}\int_{S_\infty}(\langle\mathbf{F}\rangle\frac{1}{\lambda r}+\langle\phi\rangle\nabla_y\frac{1}{r})\cdot\mathbf{n}dS = -\frac{1}{4\pi\lambda}\int_{V-V_\epsilon}(\langle\mathbf{F}\rangle+\lambda\nabla\langle\phi\rangle)\cdot\nabla_y\frac{1}{r}dV \\ -\frac{1}{4\pi}\int_{S_\epsilon}(\langle\mathbf{F}\rangle\frac{1}{\lambda r}+\langle\phi\rangle\nabla_y\frac{1}{r})\cdot\mathbf{n}dS,\end{aligned} \tag{2.31}$$

where S_ϵ is the surface of a sphere of radius ϵ surrounding $\mathbf{x}$ and V_ϵ is the corresponding volume. Note that $\mathbf{n}$ points out of S_ϵ for the surface integral on the RHS of (2.31). The surface integral over S_ϵ may be resolved by writing $\langle\mathbf{F}\rangle$ and $\langle\phi\rangle$ in their Taylor series expansion, and evaluating the integral term by term and letting ϵ go to zero. Using the suspension transport equation (2.7), (2.31) now becomes,

$$\frac{1}{4\pi}\int_{S_\infty}(\langle\mathbf{F}\rangle\frac{1}{\lambda r}+\langle\phi\rangle\nabla_y\frac{1}{r})\cdot\mathbf{n}dS = -\frac{1}{4\pi\lambda}\int_V(n\langle\mathbf{S}\rangle-n\langle\mathbf{P}\rangle)\cdot dV+\langle\phi(\mathbf{x})\rangle. \tag{2.32}$$

The sum of partial particle volume integrals is evaluated following a procedure similar to that of Glenndinning & Russel (1982) giving,

$$\pm\frac{1}{4\pi}\sum_{i=1}^{N_s}\int_{V_i}\nabla\cdot(\mathbf{F}\frac{1}{\lambda r}+\phi\nabla_y\frac{1}{r})dV=\frac{na^2\langle q\rangle}{6\lambda}$$
$$-\frac{1}{4\pi\lambda}\int_V(n\langle\mathbf{P}\rangle\cdot\nabla_y\frac{1}{r}+n\frac{1}{2}\langle\mathbf{Q}\rangle:\nabla_y\nabla_y\frac{1}{r})dV. \tag{2.33}$$

Here we have assumed the particles to be spheres of radius a, although the method can be extended to include other particle shapes. Inserting (2.32) and (2.33) into (2.30) and combining it with the moment expansion of the particle surface integrals in (2.29) yields,

$$\phi(\mathbf{x})-\langle\phi(\mathbf{x})\rangle=\frac{na^2\langle q\rangle}{6\lambda}+\frac{1}{4\pi\lambda}\sum_\beta(q_\beta\frac{1}{r}+\mathbf{S}_\beta\cdot\nabla_y\frac{1}{r}+\frac{1}{2}\mathbf{Q}_\beta:\nabla_y\nabla_y\frac{1}{r})$$
$$-\frac{1}{4\pi\lambda}\int_V(n\langle q\rangle\frac{1}{r}+n\langle\mathbf{S}\rangle\cdot\nabla_y\frac{1}{r}+\frac{1}{2}n\langle\mathbf{Q}\rangle:\nabla_y\nabla_y\frac{1}{r})dV, \tag{2.34}$$

where V is the volume enclosed by S_∞. The integral of the average charge density over V' in (2.29) is replaced by the volume integral of the charge density over V in (2.34); they are equivalent by applying the considerations of Glenndinning & Russel used for the partial particle volume integrals. Again, the moment expansion has been truncated after the quadrupoles. The particle volume integrals arising from changing the surface S'_∞ to S_∞ provide the average particle quadrupole term and the additional average charge term. Higher moments are absolutely convergent and can be added to (2.34) without difficulty.

From equation (2.34) we see the influences of the "macroscopic" boundary integral. For example, in a spherical volume of radius R, the dipole propagator decays as $1/r^2$, but there are nR^3 dipoles within the volume. Therefore, the potential grows as $n\langle\mathbf{S}\rangle$R from the particle dipole contribution. However, the integral over V grows as $-n\langle\mathbf{S}\rangle$R; thus, the growing terms cancel leaving a finite contribution to $\phi(\mathbf{x})$ due to the dipoles. The dipole sum and the average dipole integral together form an absolutely convergent expression. The integral of the average dipole is a naturally

arising "renormalization quantity." Physically, a continuous dipole distribution exists throughout the two-phase medium, which balances the particle dipoles. Similar arguments can be used to show absolute convergence for the charge and quadrupole interactions. For all other higher moments, the interactions are short-ranged and there are no convergence difficulties.

Note that the partial particle volume integrals also generate an intrinsic dipole term that cancels with the intrinsic dipole in (2.32). Hence, the average intrinsic polarization of the suspension does not effect the potential anywhere inside the suspension, although it does effect the conductivity or flux of the suspension as shown in (2.7). This is to be expected if we consider the example of a dielectric inserted in a capacitor attached to a battery. (Recall, a model for a dielectric is a material containing permanent dipoles, such as an intrinsic dipole.) The potential remains the same across the capacitor, whether the dielectric is present or not. However, the electric displacement (the flux in this case) changes due to the dielectric. Thus, the cancellation of the intrinsic dipole terms is to be expected.

Following the procedure outlined in §3 to develop equations for the potential gradient and the gradient of the potential gradient in terms similar to (2.34), we operate on (2.29) with ∇ and $\nabla\nabla$, and perform operations analogous to those we did on (2.29). The results are

$$\begin{aligned}\nabla\phi(\mathbf{x}) = \mathbf{G} &- \frac{n\langle\mathbf{S}\rangle}{3\lambda} \\ &- \frac{1}{4\pi\lambda}\sum_{\beta}(q_\beta\nabla_y\frac{1}{r} + \mathbf{S}_\beta\cdot\nabla_y\nabla_y\frac{1}{r} + \frac{1}{2}\mathbf{Q}_\beta : \nabla_y\nabla_y\nabla_y\frac{1}{r}) \\ &+ \frac{1}{4\pi\lambda}\int_V n\langle q\rangle\nabla_y\frac{1}{r}dV + \frac{1}{4\pi\lambda}\int_{V-V_\epsilon} n\langle\mathbf{S}\rangle\cdot\nabla_y\nabla_y\frac{1}{r}dV \\ &+ \frac{1}{4\pi\lambda}\int_{S_\infty}\frac{1}{2}n\langle\mathbf{Q}\rangle : \nabla_y\nabla_y\frac{1}{r}\cdot\mathbf{n}dS,\end{aligned} \tag{2.35}$$

$$\begin{aligned}\nabla\nabla\phi(\mathbf{x}) = \nabla\mathbf{G} &+ \frac{n\langle q\rangle}{3\lambda}\mathbf{I} \\ &+ \frac{1}{4\pi\lambda}\sum_{\beta}(q_\beta\nabla_y\nabla_y\frac{1}{r} + \mathbf{S}_\beta\cdot\nabla_y\nabla_y\nabla_y\frac{1}{r} + \frac{1}{2}\mathbf{Q}_\beta : \nabla_y\nabla_y\nabla_y\nabla_y\frac{1}{r}) \\ &- \frac{1}{4\pi\lambda}\int_{V-V_\epsilon} n\langle q\rangle\nabla_y\nabla_y\frac{1}{r}dV \\ &+ \frac{1}{4\pi\lambda}\int_{S_\infty}(n\langle\mathbf{S}\rangle\cdot\nabla_y\nabla_y\frac{1}{r} + \frac{1}{2}n\langle\mathbf{Q}\rangle : \nabla_y\nabla_y\nabla_y\frac{1}{r})\cdot\mathbf{n}dS,\end{aligned} \tag{2.36}$$

Note that in both (2.35) and (2.36) there are $\langle\mathbf{P}\rangle$ terms from the integral over S_∞ that cancel with equal but opposite terms arising from the partial particle volume integrals, just as in the case for the potential. Also, although the integrals over S_ϵ were evaluated by letting ϵ vanish, the V_ϵ portion of the dipole volume integral in (2.35) still makes a non-zero contribution due to the nature of the singularity in the integrand; indeed, those integrals are independent of the size of the volume V_ϵ. In the next section the volume integrals over real space are transformed into Fourier space, requiring the explicit evaluation of the V_ϵ integrals. These evaluated integrals cancel with the $n\langle\mathbf{S}\rangle/3\lambda$ and $n\langle q\rangle\mathbf{I}/3\lambda$ terms in (2.35) and (2.36), respectively. Observe that V_ϵ portion of the quadrupole volume integral in (2.34) produces the trace of the quadrupole which is zero. The volume integral of the charge is converted into the volume integral over $V-V_\epsilon$ and $n\langle q\rangle/3\lambda$ to show clearly that the charge distribution in space is $-n\langle q\rangle$, the trace of $-\lambda\nabla\nabla\phi(\mathbf{x})$.

Further simplifications of (2.35) and (2.36) can be made by noting the behavior of the integrals over S_∞. For a spherical shell of radius R, the integral over S_∞ in (2.35) containing $\langle\mathbf{Q}\rangle$ decays as 1/R, while the integrals in (2.36) containing $\langle\mathbf{S}\rangle$ and $\langle\mathbf{Q}\rangle$ over S_∞ decay as 1/R and $1/R^2$, respectively. Thus, these integrals do not contribute to the gradient and the gradient of the potential gradient at $\mathbf{x}$ as S_∞ approaches infinity. A similar analysis shows that integrals of average moments higher than the quadrupole also make no contribution.

To generate equations similar to (2.16), (2.21), and (2.22), we use the Faxén laws of (2.15), (2.19), and (2.20), noting that now we must include an additional $na^2\langle q\rangle/6\lambda$ term in the charge Faxén law for a constant charge density distributed

throughout the medium (see Appendix 2.I). Applying them to (2.34)-(2.36), we generate the following infinite set of equations:

$$\begin{aligned}\phi(\mathbf{R}_\alpha) - \langle\phi(\mathbf{R}_\alpha)\rangle &= \frac{q_\alpha}{4\pi\lambda a}\left[1+h(\rho)\right] + \frac{na^2\langle q\rangle}{3\lambda} \\ &+ \frac{1}{4\pi\lambda}\sum_{\substack{\beta\\ \beta\neq\alpha}}\left(q_\beta\frac{1}{r} + \mathbf{S}_\beta\cdot\nabla_y\frac{1}{r} + \frac{1}{2}\mathbf{Q}_\beta : \nabla_y\nabla_y\frac{1}{r}\right) \\ &- \frac{1}{4\pi\lambda}\int_V\left(n\langle q\rangle\frac{1}{r} + n\langle\mathbf{S}\rangle\cdot\nabla_y\frac{1}{r} + \frac{1}{2}n\langle\mathbf{Q}\rangle : \nabla_y\nabla_y\frac{1}{r}\right)dV,\end{aligned} \tag{2.37}$$

$$\begin{aligned}-\mathbf{G} &= \frac{\mathbf{S}_\alpha}{4\pi a^3\delta\lambda} - \frac{n\langle\mathbf{S}\rangle}{3\lambda} \\ &- \frac{1}{4\pi\lambda}\sum_{\substack{\beta\\ \beta\neq\alpha}}\left(q_\beta\nabla_y\frac{1}{r} + \mathbf{S}_\beta\cdot\nabla_y\nabla_y\frac{1}{r} + \frac{1}{2}\mathbf{Q}_\beta : \nabla_y\nabla_y\nabla_y\frac{1}{r}\right) \\ &+ \frac{1}{4\pi\lambda}\int_V n\langle q\rangle\nabla_y\frac{1}{r}dV + \frac{1}{4\pi\lambda}\int_{V-V_\epsilon} n\langle\mathbf{S}\rangle\cdot\nabla_y\nabla_y\frac{1}{r}dV,\end{aligned} \tag{2.38}$$

$$\begin{aligned}-\nabla\mathbf{G} &= \frac{3\mathbf{Q}_\alpha}{4\pi\lambda a^5} + \frac{n\langle q\rangle}{3\lambda}\mathbf{I} \\ &+ \frac{1}{4\pi\lambda}\sum_{\substack{\beta\\ \beta\neq\alpha}}\left(q_\beta\nabla_y\nabla_y\frac{1}{r} + \mathbf{S}_\beta\cdot\nabla_y\nabla_y\nabla_y\frac{1}{r} + \frac{1}{2}\mathbf{Q}_\beta : \nabla_y\nabla_y\nabla_y\nabla_y\frac{1}{r}\right) \\ &- \frac{1}{4\pi\lambda}\int_{V-V_\epsilon} n\langle q\rangle\nabla_y\nabla_y\frac{1}{r}dV.\end{aligned} \tag{2.39}$$

Equations (2.37)-(2.39) relate the particle moments to the particle potentials and the average gradient for an infinite suspension of particles. The above equations also form an infinite set, since there are an infinite number of particles.

It should also be noted that the particle integrals did not have to be expanded in terms of the particle moments to ensure convergence. If the particle integrals had been left unaltered, the method would still result in absolutely converging terms as outlined by O'Brien (1979). The choice of doing a moments expansion was purely for convenience in forming the potential matrix. Equations (2.37)-(2.39) contain no approximation other than expressing the particles in terms of a finite number of moments and assuming spherical Faxén laws. These equations are correct for random or non-random systems. Computationally, we cannot contend with an infinite system of equations. Also, since we truncated the moment expansion at

the quadrupole level, the above equations cannot account for the near-field effects discussed in §3. In the next section we shall apply periodic boundary conditions and the method of Ewald to form a finite set of linear equations. In addition we will show that the method outlined in §3.2 is still applicable for capturing near-field effects.

2.5. Application of Basic Equations with Periodic Boundary Boundary Conditions and Ewald Sums

For an infinite medium, the equations (2.37)-(2.39) lead to an infinite number of equations. To make the system of equations finite, we will use periodic boundary conditions on a cell of volume V_c containing N particles to model the infinite medium. The cell is primitive, generally called a Wigner-Seitz cell, and is periodically replicated to fill all space. The sums over the infinite particles are replaced by double sums over the N particles in the l^{th} cell of the system and over all the replicated cells.

In periodic systems, sums that are slowly convergent can be made rapidly convergent by the method of Ewald (1921). In fact Ewald used his method to recast the charge sum of (2.37), with the condition that the net charge in the cell is zero, into a rapidly converging sum over real and reciprocal space. Nijboer & De Wette (1957) generalized Ewald's method for any lattice sum. To demonstrate the method, the charge sum in (2.37) will be converted into an Ewald sum.

First, we rewrite the sum over all particles as a sum over all cells and particles within the cell. The charge sum becomes,

$$\begin{aligned}\frac{1}{4\pi\lambda}\sum_{\substack{\beta\\ \beta\neq\alpha}} q_\beta \frac{1}{r} = \frac{1}{4\pi\lambda}\sum_{l}\sum_{\substack{\beta\\ \beta_l\neq\alpha_0}} q_{\beta_l}\frac{1}{2}\nabla^2 r\,\mathrm{erfc}(\xi r) \\ + \frac{1}{4\pi\lambda}\sum_{l}\sum_{\beta} q_{\beta_l}\frac{1}{2}\nabla^2 r\,\mathrm{erf}(\xi r) - \frac{1}{4\pi\lambda} q_{\beta_l}\frac{1}{2}\nabla^2 r\,\mathrm{erf}(\xi r)|_{r=0},\end{aligned} \tag{2.40}$$

where $\frac{1}{r}$ has been replaced by its identity $\frac{1}{2}\nabla^2(r\mathrm{erfc}(\xi r) + r\mathrm{erf}(\xi r))$. Note ξ is an arbitrary positive constant; later, we will see that ξ affects the rate of convergence of the Ewald sums.

The first sum on the RHS of (2.40) converges rapidly, and the second sum can be made rapidly converging by transforming the outer sum from a sum over the cells to a sum over reciprocal space using the Poisson summation formula. The last term of (2.40) is also evaluated by rewriting it as the inverse Fourier transform of its Fourier transform, letting r go to zero, and evaluating the integral explicitly.

Combining these results, (2.40) becomes

$$\begin{aligned}\frac{1}{4\pi\lambda}\sum_{\substack{\beta\\ \beta\neq\alpha}} q_\beta \frac{1}{r} &= -\frac{q_{\alpha_0}}{4\pi\lambda a} 6\xi a\pi^{-\frac{1}{2}} \\ &+ \frac{1}{4\pi\lambda}\sum_{l}\sum_{\substack{\beta\\ \beta_l\neq\alpha_0}} q_{\beta_l} M_{\Phi q}^{(r)} + \frac{1}{4\pi\lambda}\frac{1}{V_c}\sum_{\mathbf{k}}\sum_{\beta} q_{\beta_l} M_{\Phi q}^{(k)},\end{aligned} \tag{2.41}$$

where,

$$M_{\Phi q}^{(r)} = \Big[(2\xi^3 r^2 - 4\xi)\frac{e^{-\xi^2 r^2}}{\sqrt{\pi}} + \frac{\operatorname{erfc}(\xi r)}{r}\Big], \tag{2.42}$$

$$M_{\Phi q}^{(k)} = \frac{4\pi}{k^2}\Big[1 + \frac{1}{4}\big(\frac{k}{\xi}\big)^2 + \frac{1}{8}\big(\frac{k}{\xi}\big)^4\Big] e^{-(k^2/4\xi^2)} \cos\big[\mathbf{k}\cdot(\mathbf{R}_\alpha - \mathbf{R}_\beta)\big]. \tag{2.43}$$

In summary, l is the cell index number, β is the particle index number, $\mathbf{R}_{\alpha 0}$ is the position of particle α in the zeroth cell, $\mathbf{R}_{\beta_l}$ is the position of the particle β in the l^{th} cell, $\mathbf{k}$ is the periodic cell reciprocal or wave vector, k is its magnitude, $r = |\mathbf{R}_{\alpha 0} - \mathbf{R}_{\beta_l}|$, and $\mathbf{R}_\alpha - \mathbf{R}_\beta$ is the position vector difference between particles α and β within a cell. The arbitrary number ξ regulates the speed of convergence for the sums and is typically chosen to be $1/V_c{}^{\frac{1}{3}}$. Each sum converges exponentially fast.

The convergence difficulties of the sum are betrayed by the singularity of $M_{\Phi q}^{(k)}$ for the zero wave vector. Ewald's original problem demanded that the net particle charge in the cell be zero, so the singularity disappears. However, with the inclusion of a balancing charge distribution, it is not necessary to require that the average particle charge be zero because the Fourier representation of the volume integral proportional to the average particle charge in (2.37) cancels out the singularity at $\mathbf{k} = 0$ in (2.41), namely,

$$-\frac{1}{4\pi\lambda}\int_V n\langle q\rangle \frac{1}{r} dV = -\frac{n\langle q\rangle}{4\pi\lambda}\int_V \frac{1}{(2\pi)^3}\int_{\mathbf{k}} FT_3\big(\frac{1}{r}\big) e^{-i\mathbf{k}\cdot\mathbf{r}} d^3\mathbf{k} dV, \tag{2.44}$$

where $FT_3(\cdot)$ corresponds to the 3-dimensional Fourier transform and the inner integral is over all wave vector space. Evaluating $FT_3(\frac{1}{r})$, inserting the result into

the RHS of (2.44), and exchanging the order of integration yields,

$$\begin{aligned} -\frac{1}{4\pi\lambda}\int_V n\langle q\rangle\frac{1}{r}dV &= -\frac{n\langle q\rangle}{4\pi\lambda}\int_{\mathbf{k}}\left(\int_{\mathbf{V}}\frac{1}{(2\pi)^3}e^{-i\mathbf{k}\cdot\mathbf{r}}dV\right)\frac{4\pi}{k^2}d^3\mathbf{k}, \\ &= -\frac{n\langle q\rangle}{4\pi\lambda}\int_{\mathbf{k}}\delta(\mathbf{k})\frac{4\pi}{k^2}d^3\mathbf{k}, \end{aligned} \tag{2.45}$$

where $\delta(\mathbf{k})$ is the 3-dimensional delta function. So finally,

$$-\frac{1}{4\pi\lambda}\int_V n\langle q\rangle\frac{1}{r}dV = -\lim_{k\to 0}\frac{n\langle q\rangle}{4\pi\lambda}\frac{4\pi}{k^2}, \tag{2.46}$$

which exactly cancels with the zero wave vector singularity in (2.41). Now the second double sum in (2.41) is over all wave vectors except the zero wave vector. Thus, the sum in (2.41) is absolutely convergent. Physically, the sum over real space represents nearby particle interactions, and the sum over reciprocal space represents particle interactions "from infinity." The other non-absolutely convergent sums and their corresponding integrals can be converted into rapidly, absolutely convergent sums over real and reciprocal space in a similar manner. For example, the macroscopic boundary integral gives rise to reciprocal space singularities that cancel with the reciprocal space singularites of the dipole and quadrupole sums in (2.37). The Ewald sum forms for these and the other particle moments in (2.37)-(2.39) can be found in Appendix 2.II.

We can now form the approximate grand potential matrix for a periodically replicated group of N particles. The grand potential matrix has the same form as (2.23), but the $\hat{\mathbf{M}}_{\Phi q}$, $\hat{\mathbf{M}}_{\Phi\mathbf{S}}$, $\hat{\mathbf{M}}_{\Phi\mathbf{Q}}$, $\hat{\mathbf{M}}_{\mathbf{G}q}$, $\hat{\mathbf{M}}_{\mathbf{GS}}$, and $\hat{\mathbf{M}}_{\nabla q}$ couplings are formed with Ewald sums. As we did in §3.1, the grand potential matrix can be converted to the potential matrix, $\mathbf{M}$, because $\nabla\mathbf{G} = 0$ in the statistically homogeneous medium.

There are no convergence difficulties with adding the two-body capacitance matrices' difference to the Ewald sum formulation of the potential invert because $\mathbf{C}_{2b} - \mathbf{C}_{2b}^{\infty}$ interactions are all short-range, (of $O(1/r^8)$), if the potential matrix formulation includes quadrupoles. The highest order term neglected in the two-body far-field capacitance matrix is the octupole of particle α induced by the charge on particle β. The charge from β propagates as $O(1/r)$ inducing an octupole on α of

$O(1/r^4)$. The correction to the potential on particle β due to the induced octupole on particle α is $O(1/r^8)$. The exact two-body capacitance matrix contains all orders of interaction, hence the capacitance matrices' difference must be $O(1/r^8)$. Using a similar analysis, if only moments up to dipoles were included in the formation of the potential matrix, the $\mathbf{C}_{2b} - \mathbf{C}_{2b}^{\infty}$ interactions are still short-range, but now of $O(1/r^6)$.

With the Ewald sum method to form the potential matrix and the addition of exact near-field particle interactions, the potentials, dipoles, and effective conductivity may be predicted for an arbitrary configuration of spheres in an infinite medium subject to a macroscopic potential gradient.

2.6. Results

2.6.1 Madelung Constants

As mentioned earlier, the method of Ewald sums was first developed to calculate the cohesive energy of ionic crystals, where the ions are assumed to experience coulombic interaction only. The ionic crystal is composed of points of equal and alternating positive and negative charge. For example, the NaCl crystal lattice is modelled as a simple cubic lattice composed of alternating positive and negative point charges of magnitude unity (although the ion pairs are in a face-centered cubic arrangement, and hence NaCl is considered a face-centered cubic crystal, geometrically, the individual ions are in a simple cubic lattice). The cohesive energy per charge pair, E_c, for such an ionic crystal model is given by,

$$E_c = \frac{1}{4\pi\lambda} \sum_{\substack{\beta \\ \beta \neq \alpha}} \frac{q_\alpha q_\beta}{|\mathbf{R}_\alpha - \mathbf{R}_\beta|}, \tag{2.47}$$

where q_α and q_β are the charges on ions α and β, and their positions are given by $\mathbf{R}_\alpha$ and $\mathbf{R}_\beta$, respectively. Here λ is the permittivity of vacuum. For a neutral ionic crystal, $|q_\alpha| = |q_\beta| = q$. Therefore, we may rewrite E_c as,

$$E_c = \frac{q^2}{4\pi\lambda} \sum_{\substack{\beta \\ \beta \neq \alpha}} \frac{q_{\alpha\beta}}{|\mathbf{R}_\alpha - \mathbf{R}_\beta|}, \tag{2.48}$$

where $q_{\alpha\beta}$ is an alternating ± 1, depending upon whether the charge β is positive or negative. The Madelung constant, M_c, is defined as (Kittel 1976),

$$M_c = \frac{4\pi\lambda r_l}{q^2} E_c = r_l \sum_{\substack{\beta \\ \beta \neq \alpha}} \frac{q_{\alpha\beta}}{|\mathbf{R}_\alpha - \mathbf{R}_\beta|}. \tag{2.49}$$

The factor r_l is the nearest neighbor distance between a cation and an anion in the ionic crystal. Apart from a constant multiple, the sum in (2.49) is the charge sum described in the previous section, namely equation (2.40), with the particle radius, a, set to zero (recall, we are modelling the crystal as a collection of point charges). Equation (2.49) was evaluated for simple cubic and body-centered cubic lattices, and the Madelung constants were determined to be 1.7476 and 1.7627,

respectively. These results are correct to four decimal places (Kittel 1976). The agreement between our results and the accepted values confirm that the potential-charge interactions were correctly accounted for in our method.

2.6.2 Effective Conductivity of Cubic Arrays of Spheres

To test the method for forming the capacitance matrix, the effective conductivity calculated via the simulation is compared to the known effective conductivity of cubic arrays of spheres. Sangani & Acrivos (1982) have determined the effective conductivity for simple cubic, body-centered cubic, and face-centered cubic arrays of spheres from dilute to near densest-packed volume for any particle-to-matrix conductivity ratio. Unlike the method developed here, Sangani & Acrivos developed their solution based upon an infinite set of spherical harmonics and took advantage of lattice symmetries. Thus, their work provides an independent check on our method.

To calculate the effective conductivity, the potential matrix, $\mathbf{M}$, was formed directly without including quadrupoles. Due to the symmetry properties of cubic arrays, the potential and capacitance matrices have certain properties that make the formation of $\mathbf{M}$ equally accurate whether quadrupoles are included or not. The couplings $\hat{\mathbf{M}}_{\Phi\mathbf{S}}$, $\hat{\mathbf{M}}_{\mathbf{G}q}$, $\hat{\mathbf{M}}_{\Phi\mathbf{Q}}$, $\hat{\mathbf{M}}_{\nabla q}$, $\hat{\mathbf{M}}_{\mathbf{GQ}}$, and $\hat{\mathbf{M}}_{\nabla\mathbf{S}}$ are zero for cubic arrays. Therefore, the grand potential matrix in (2.23) becomes,

$$\begin{pmatrix} \mathbf{\Phi} \\ -\mathbf{G} \\ \mathbf{O} \end{pmatrix} = \begin{pmatrix} \hat{\mathbf{M}}_{\Phi q} & \mathbf{0} & \hat{\mathbf{M}}_{\Phi\mathbf{Q}} \\ \mathbf{0} & \hat{\mathbf{M}}_{\mathbf{GS}} & \mathbf{0} \\ \hat{\mathbf{M}}_{\nabla q} & \mathbf{0} & \hat{\mathbf{M}}_{\nabla\mathbf{Q}} \end{pmatrix} \cdot \begin{pmatrix} \mathbf{q} \\ \mathbf{S} \\ \mathbf{Q} \end{pmatrix}. \tag{2.50}$$

Upon inspection it is evident that the particle charges and quadrupoles make no contribution to the gradient-dipole coupling. Also, if the particles have zero net charge, the particle quadrupoles are zero. Thus, for zero-charge particles in a cubic array, the potential matrix, $\mathbf{M}$, is as accurate as the grand potential matrix.

The approximate capacitance matrix has the same form as the potential matrix, which for cubic arrays is

$$\begin{pmatrix} \mathbf{q} \\ \mathbf{S} \end{pmatrix} = \begin{pmatrix} \mathbf{C}_{q\Phi} & \mathbf{0} \\ \mathbf{0} & \mathbf{C}_{\mathbf{SG}} \end{pmatrix} \cdot \begin{pmatrix} \mathbf{\Phi} \\ -\mathbf{G} \end{pmatrix}. \tag{2.51}$$

For periodic arrays all particles are equivalent, and hence the average particle dipole is the same as the dipole for a single sphere in the periodic cell. The effective conductivity given by equation (2.28) then becomes

$$\mathbf{\Lambda}_{eff} = \lambda \mathbf{I} + n\mathbf{C}_{\mathbf{SG}}. \tag{2.52}$$

The coupling $\mathbf{C}_{\mathbf{SG}}$ is isotropic for cubic arrays, so the effective conductivity is isotropic and representable by a scalar, λ_{eff}.

Figures 2.2($a-b$) and 2.3 and Tables II-IV compare the results of the simulation method to those of Sangani & Acrivos. The effective conductivity was calculated for simple cubic, body-centered, and face-centered cubic arrays, from dilute to near closest packing, with particle-to-matrix conductivity ratios of infinity, 10, and 0.01. Overall, the simulation does quite well in predicting the effective conductivity of the cubic arrays.

Figures 2.2($a-b$) present the relative effective conductivities versus the sphere volume fraction for a simple cubic array. Results for body- and face-centered cubic arrays are similar as Tables III-IV show. For perfect conductors, $\lambda_p/\lambda = \infty$, the initially slow increase in relative effective conductivity with sphere volume fraction is followed by a rapid increase as the volume fraction approaches densest-packing $c_{\max}$ (recall, $c_{\max}$ for sc, bcc, and fcc arrays are $\pi/6$, $\sqrt{3}\pi/8$, and $\pi/3\sqrt{2}$, respectively). Near densest-packing, lubrication or near-field interactions between spheres dominate, resulting in this rapid increase in the relative effective conductivity. The relative effective conductivity approaches infinity asymptotically at $c_{\max}$ for the arrays of perfect conductors due to the lubrication singularity. For dense suspensions of perfect conductors, the importance of the lubrication is readily apparent. The simulation, however, noticeably over predicts the relative effective conductivity for the moderately concentrated regime. In fact the overprediction increases as the sphere coordination number increases (sc = 6, bcc = 8, fcc = 12). The maximum errors are 4%, 14%, and 28% for sc, bcc, and fcc cubic arrays, respectively. Interestingly, the maximum errors all occur at a volume fraction of about eighty-percent of densest-packing for each cubic array.

The maximum errors occur in these regimes since the suspensions are not dilute and the lubrication singularities do not dominate. In these concentration regimes, fixing up the potential matrix invert with an exact three-body capacitance matrix rather than just a two-body capacitance matrix might improve the accuracy, since the former would capture two- and three-body interactions. The other source of error is the addition of $\mathbf{C}_{2b}$ to the potential matrix. For a periodic array, the individual zero-charge particle quadrupoles must be zero. However, the quadrupoles included in the exact two-body interactions, $\mathbf{C}_{2b}$, are not zero. The non-zero quadrupole will change the accuracy of the capacitance matrix in the moderately and highly concentrated regimes. Adding an exact three- or even four-body capacitance matrix might improve the accuracy, but only if such matrices reduce the effect of the quadrupoles on the dipoles.

The relative effective conductivity calculated from just the invert of $\mathbf{M}_{\mathbf{GS}}$ is also presented for all the cubic arrays in Tables II-IV. The invert of $\mathbf{M}_{\mathbf{GS}}$ accurately predicts the effective conductivity from the dilute to the moderately concentrated regime. As expected, the invert of $\mathbf{M}_{\mathbf{GS}}$ does not capture the lubrication singularity (the predicted effective conductivity is constant at $c_{\max}$) since only the dipole moment was used in its formation.

As mentioned earlier, the rapid increase in the effective conductivity near densest-packing for each cubic array is due to the lubrication or "short-circuiting" of material flux (heat, charge, etc.) between the particles. From lubrication theory, Batchelor & O'Brien (1973) showed that the relative effective conductivity near densest-packing will follow the relation,

$$\lambda_{eff}/\lambda = -K_1 \ln(\epsilon) + K_2, \tag{2.53}$$

where K_1 and K_2 are constants particular to the array, and epsilon is one half the gap width nondimensionalized with sphere radius, which is $\epsilon = 1 - (c/c_{\max})^{1/3}$. Batchelor & O'Brien showed that K_1 depends upon the average coordination number of a sphere, which for cubic lattices are constants. They found K_1 to be $\pi/2$, $\sqrt{3}\pi/2$, and $\sqrt{2}\pi$ for sc, bcc, and fcc lattices, respectively. Figure 2.3 shows the

relative effective conductivity versus the logarithm of the gap width for the simple cubic lattice. For all the cubic arrays, the relation is a straight line, as expected, since the lubrication interaction is logarithmically singular with the gap width. The simulation predicts the correct slope because it correctly adjusts for the sphere coordination number. However, we see the simulation overpredicts K_2, and subsequently λ_{eff}/λ. This is true for all the cubic arrays. To form the two-body capacitance matrix for the lubrication regime, the simulation uses a matched asymptotic expansion developed by Jeffrey (1978). The logarithmic singularity is based only upon the geometry of the particle areas close to contact. However, Jeffrey's $O(1)$ correction, which contributes to K_2, relies on the outer geometry, which in his case for only two spheres is an unbounded medium. Obviously, this is not the outer geometry for the cubic arrays. The higher the sphere coordination number the less the outer geometry resembles that for two spheres, and the less accurate is the $O(1)$ correction and K_2. Near densest packing, however, the singularity will overwhelm the approximate value of K_2, albeit slowly since the singularity is only logarithmic, and accurately predict λ_{eff}/λ. Also, properly accounting for the non-zero particle quadrupoles in $\mathbf{C}_{2b}$ will contribute to the accuracy of K_2 for the reasons already mentioned.

In the case of non-perfect conductors with a conductivity ratio of 10, it was found that using only the potential matrix invert to form the capacitance matrix was fairly accurate for almost the entire range of volume fractions, except near closest packing. As seen in Figure 2.2*b* and Tables II-IV, the simulation results compare well to those of Sangani & Acrivos. For conductivity ratio 10, the simulation without the addition of near-field interactions underpredicts the correct results, with the error increasing as $c_{\max}$ is approached. Although the spheres are not perfect conductors, there is some lubrication-like behavior near closest packing that is not captured with only the potential invert. With the addition of two-body interactions for this conductivity ratio, the simulation results compare extremely well to the conductivities of Sangani & Acrivos.

For a sphere-to-matrix conductivity ratio of 0.01, the agreement between the

simulation and the results of Sangani & Acrivos was excellent. Because the spheres are insulators relative to the matrix, the effective conductivity decreases with increasing volume fraction. The error was found to increase slightly as the sphere volume fraction approached densest packing. It appears in the case of insulating particles, the dipole description is quite accurate in describing the particles. Evidently, the negative particle dipoles of insulating particles create a potential field that effectively confines the flux of the conservable quantity to the "channels" of the cubic arrays, as would be expected in the case of insulators. Since these "channels" exist even at maximum packing, the effective conductivity never vanishes for cubic arrays of near perfect insulators, which is observed in the results.

2.7. Conclusions/Applications

In this paper we have outlined a method for determining the effective conductivity of an infinite suspension of particles. The method treats an infinite number of particles without any of the convergence difficulties encountered by previous investigators. The method includes both far- and near-field particle interactions, and thus is applicable at all volume fractions. As shown in the results section, the simulation method's predictions of effective conductivities are quite good compared to the known results for cubic arrays from dilute to near closest packing and for a variety of conductivity ratios.

In Chapter 3 we use the method to determine the effective conductivity of random suspensions of spherical particles. To date there has been no determination of the effective conductivity of high volume fraction random suspensions of spheres. In this study a Monte Carlo-type method is used to generate random particle configurations, and the effective conductivity of the dispersions is calculated according to equation (2.28). These results provide a fundamental data-base for comparison with future theoretical and experimental work. In the analogous hydrodynamic problem, Phillips, Brady, & Bossis (1988) found the effective suspension viscosities to be in excellent agreement with experiment.

In addition to determining the effective conductivity of dispersions of particles, the method can be used to study problems associated with diffusion-limited reactions between large particles and solute molecules. Highly reactive particles are simulated, assuming perfectly conducting spheres with zero potential, and determining the charge on the spheres with a constant average potential in the media. Because the charge is equal to the flux of material reacted on the sphere, the effective reaction rate coefficient for the media can be calculated, for both random and non-random systems, and is done in Chapter 5.

Coupled with "Stokesian dynamics," the simulation method described here will be used for the dynamic simulation of electrorheological fluids in Chapters 7 and 8. Electrorheological fluids are fluid suspensions of colloidal, dielectric particles that exhibit interesting rheological behavior when subjected to an electric field.

The forces on the individual particles of the suspension can be determined via the induced dipoles calculated from the present method. These interparticle forces combined with the hydrodynamic shearing forces in Stokesian dynamics allow one to dynamically simulate the motions of the particles, as well as determine the effective viscosity of the suspension. When combined, the two simulation methods provide an excellent tool for understanding the interplay between the shear and electric fields in the development of suspension microstructure and its resulting macroscopic properties.

Finally, the simulation method developed here is also applicable to the molecular dynamics simulation of dipolar fluids. For example, in the simulation of a Stockmayer fluid by De Leeuw, Perram, & Smith (1983), they include ad hoc reaction and external potential fields, arising from an assumed medium surrounding the simulated particles, to address the long-range conditionally convergent dipole-dipole interactions. As in the case of electrorheological fluids, the forces on the dipolar fluid particles can be calculated from the dipoles determined in the simulation method outlined in this paper. The dipoles are determined rigorously and completely from the fundamental equations of electrostatics, without any ad hoc assumptions. Indeed, while Ewald sums have often been used in the simulation of dipolar or ionic fluids, questions have repeatedly arisen concerning the validity of the Ewald method. The formulation presented here, which includes the effects of the macroscopic boundary S_∞, shows clearly that the Ewald summation corresponds to an infinite statistically homogeneous medium. The present analysis can be viewed as a justification of this often-used method.

Appendix 2.I. Faxén Laws

Faxén originally developed his laws to explicitly relate the force and torque on a sphere due to the velocity field and its derivatives evaluated at the center of the sphere for zero-Reynolds-number flow fields. In the same spirit, the various electrostatic particle moments can be related to the potential field and its derivatives evaluated at the center of the sphere. Because of their simplicity, we have used electrostatic Faxén laws for spheres. However, it should be noted that the Faxén laws can be developed for non-spherical particles as done by Brenner (1964*b*) for the force and torque on ellipses subject to a zero-Reynolds-number flow field. Below we outline the derivation for the Faxén laws for the charge and the quadrupole. The interested reader is referred to O'Brien (1979), who derived the Faxén law for dipoles.

Charge Faxén Law

The potential on the surface of a single particle α in any external potential field is given by,

$$\phi(\mathbf{x}) - \phi'(\mathbf{x}) = \frac{1}{2\pi}\int_{\partial\Omega_{\alpha_y}} (\mathbf{F}\frac{1}{\lambda r} + \phi\nabla_y\frac{1}{r})\cdot\mathbf{n}dS_y, \qquad (2.I.1)$$

where $\phi(\mathbf{x})$ is the potential at a point $\mathbf{x}$ on the surface of the particle, $\phi'(\mathbf{x})$ is the external potential in the absence of the particle, and $r = |\mathbf{y} - \mathbf{x}|$. The other terms are as defined in the main body of the paper. Now let us integrate both sides of (2.I.1) over the surface of the sphere with respect to the variable $\mathbf{x}$ to give,

$$\int_{\partial\Omega_{\alpha_x}} [\phi(\mathbf{x}) - \phi'(\mathbf{x})]dS_x = \frac{1}{2\pi}\int_{\partial\Omega_{\alpha_x}}\int_{\partial\Omega_{\alpha_y}} (\mathbf{F}\frac{1}{\lambda r} + \phi\nabla_y\frac{1}{r})\cdot\mathbf{n}dS_y dS_x. \qquad (2.I.2)$$

The RHS of (2.I.2) can be evaluated by switching the order of integration and evaluating the integral with respect to $\mathbf{x}$ first and then with respect to $\mathbf{y}$. The result is,

$$\int_{\partial\Omega_{\alpha_x}} [\phi(\mathbf{x}) - \phi'(\mathbf{x})]dS_x = \frac{q_\alpha a}{\lambda}. \qquad (2.I.3)$$

Given the charge distributions in the particle and in the matrix we may expand $\phi(\mathbf{x})$ and $\phi'(\mathbf{x})$ in their Taylor series about the center of the sphere and integrate

to evaluate the LHS of (2.I.3). Let us assume a constant charge distribution for the matrix in the immediate vicinity of the sphere such that $\nabla^2\phi'(\mathbf{R}_\alpha) = n\langle q\rangle/\lambda$, and all higher terms in the Taylor series expansion of $\phi'(\mathbf{R}_\alpha)$ vanish. Then (2.I.3) becomes,

$$(1+\frac{a^2}{6}\nabla^2+\frac{a^4}{120}\nabla^4+\cdots)\phi(\mathbf{R}_\alpha)-\phi'(\mathbf{R}_\alpha)=\frac{q_\alpha}{4\pi\lambda a}+\frac{na^2\langle q\rangle}{6\lambda}, \qquad (2.I.4)$$

where the operation on ϕ is evaluated at the center of the sphere, $\mathbf{R}_\alpha$. In general the relation can be written as,

$$\phi(\mathbf{R}_\alpha)-\phi'(\mathbf{R}_\alpha)=\frac{q_\alpha}{4\pi\lambda a}(1+h(\rho))+\frac{na^2\langle q\rangle}{6\lambda}, \qquad (2.I.5)$$

where $h(\rho)$ is a dimensionless function of the charge distribution within the particle defined by,

$$h(\rho)=\frac{-4\pi\lambda a}{q_\alpha}[(\frac{a^2}{6}\nabla^2+\frac{a^4}{120}\nabla^4+\cdots)\phi(\mathbf{R}_\alpha)]. \qquad (2.I.6)$$

For a perfect conductor, $h(\rho)=0$ because $\nabla^2\phi(\mathbf{R}_\alpha)$, $\nabla^4\phi(\mathbf{R}_\alpha)$, etc. are zero. For a particle with constant charge ρ, $h(\rho)=\frac{1}{2}\gamma^{-1}$ where $\gamma=\lambda_p/\lambda$. If there is no charge distribution in the matrix, the last term in (2.I.5) vanishes.

Quadrupole Faxén Law

For a perfect conductor, the potential on the surface of the particle is given by,

$$\phi(\mathbf{x})-\phi'(\mathbf{x})=\frac{1}{4\pi\lambda}\int_{\partial\Omega_{\alpha_y}}\frac{1}{r}\mathbf{F}\cdot\mathbf{n}dS_y. \qquad (2.I.7)$$

We begin by multiplying both sides by $(\mathbf{xx}-\frac{a^2}{3}\mathbf{I})$ and integrating over the surface of the sphere with respect to $\mathbf{x}$ to yield,

$$\int_{\partial\Omega_{\alpha_x}}(\mathbf{xx}-\frac{a^2}{3}\mathbf{I})(\phi(\mathbf{x})-\phi'(\mathbf{x}))dS_x=\frac{1}{4\pi\lambda}\int_{\partial\Omega_{\alpha_x}}\int_{\partial\Omega_{\alpha_y}}(\mathbf{xx}-\frac{a^2}{3}\mathbf{I})\frac{1}{r}\mathbf{F}\cdot\mathbf{n}dS_ydS_x \qquad (2.I.8)$$

Interchanging the order of integration on the RHS of (2.I.8) and integrating with respect to $\mathbf{x}$, (2.I.7) then becomes,

$$\int_{\partial\Omega_{\alpha_x}}(\mathbf{xx}-\frac{a^2}{3}\mathbf{I})(\phi(\mathbf{x})-\phi'(\mathbf{x}))dS_x=\frac{a}{5\lambda}\int_{\partial\Omega_{\alpha_y}}(\mathbf{yy}-\frac{a^2}{3}\mathbf{I})\mathbf{F}\cdot\mathbf{n}dS_y \qquad (2.I.9)$$

Note that the RHS of (2.I.9) is just the definition of a quadrupole for a perfectly conducting sphere. The terms on the LHS of (2.I.9) containing $\phi(\mathbf{x})$ sum to zero for a perfectly conducting sphere since $\phi(\mathbf{x})$ is constant over the sphere surface. Expanding the external potential, $\phi'(\mathbf{x})$, in its Taylor series about the center of the sphere, and integrating the LHS of (2.I.10) yields,

$$-\frac{4\pi a^6}{15}\nabla\nabla\phi'(\mathbf{R}_\alpha) = \frac{a}{5\lambda}\int_{\partial\Omega_{\alpha_y}} (\mathbf{yy} - \frac{a^2}{3}\mathbf{I})\mathbf{F}\cdot\mathbf{n}dS_y = \frac{a}{5\lambda}\mathbf{Q}_\alpha, \qquad (2.I.10)$$

or

$$\nabla\nabla\phi'(\mathbf{R}_\alpha) = -\frac{3\mathbf{Q}_\alpha}{4\pi\lambda a^5} \qquad (2.I.11)$$

which is our Faxén law for the quadrupole of a perfectly conducting sphere.

APPENDIX 2.II. Ewald Sums of Potential Sub-Matrices

Here we list the remaining Ewald sums of the particle moments. All the sums below were determined in the manner described in §5.

$$\frac{1}{4\pi\lambda}\sum_{\substack{\beta\\ \beta\neq\alpha}}\mathbf{S}_\beta\cdot\nabla_y\frac{1}{r}-\frac{1}{4\pi\lambda}\int_V n\langle\mathbf{S}\rangle\cdot\nabla_y\frac{1}{r}dV=$$

$$\frac{1}{4\pi\lambda}\sum_l\sum_{\substack{\beta\\ \beta_l\neq\alpha_0}}\mathbf{S}_{\beta_l}\cdot\mathbf{M}^{(r)}_{\Phi\mathbf{S}}+\frac{1}{4\pi\lambda}\frac{1}{V_c}\sum_{\substack{\mathbf{k}\\ \mathbf{k}\neq\mathbf{0}}}\sum_\beta\mathbf{S}_{\beta_l}\cdot\mathbf{M}^{(k)}_{\Phi\mathbf{S}}, \tag{2.II.1}$$

$$\frac{1}{4\pi\lambda}\sum_{\substack{\beta\\ \beta\neq\alpha}}\frac{1}{2}\mathbf{Q}_\beta:\nabla_y\nabla_y\frac{1}{r}-\frac{1}{4\pi\lambda}\int_V\frac{n}{2}\langle\mathbf{Q}\rangle:\nabla_y\nabla_y\frac{1}{r}dV=$$

$$\frac{1}{4\pi\lambda}\sum_l\sum_{\substack{\beta\\ \beta_l\neq\alpha_0}}\mathbf{Q}_{\beta_l}:\mathbf{M}^{(r)}_{\Phi\mathbf{Q}}+\frac{1}{4\pi\lambda}\frac{1}{V_c}\sum_{\substack{\mathbf{k}\\ \mathbf{k}\neq\mathbf{0}}}\sum_\beta\mathbf{Q}_{\beta_l}:\mathbf{M}^{(k)}_{\Phi\mathbf{Q}}, \tag{2.II.2}$$

$$\frac{1}{4\pi\lambda}\sum_{\substack{\beta\\ \beta\neq\alpha}}q_\beta\nabla_y\frac{1}{r}-\frac{1}{4\pi\lambda}\int_V n\langle q\rangle\nabla_y\frac{1}{r}dV=$$

$$\frac{1}{4\pi\lambda}\sum_l\sum_{\substack{\beta\\ \beta_l\neq\alpha_0}}q_{\beta_l}\mathbf{M}^{(r)}_{\mathbf{G}q}+\frac{1}{4\pi\lambda}\frac{1}{V_c}\sum_{\substack{\mathbf{k}\\ \mathbf{k}\neq\mathbf{0}}}\sum_\beta q_{\beta_l}\mathbf{M}^{(k)}_{\mathbf{G}q}, \tag{2.II.3}$$

$$\frac{n\langle\mathbf{S}\rangle}{3\lambda}+\frac{1}{4\pi\lambda}\sum_{\substack{\beta\\ \beta\neq\alpha}}\mathbf{S}_\beta\cdot\nabla_y\nabla_y\frac{1}{r}-\frac{1}{4\pi\lambda}\int_{V-V_\epsilon}n\langle\mathbf{S}\rangle\cdot\nabla_y\nabla_y\frac{1}{r}dV=$$

$$\frac{\mathbf{S}_{\alpha_0}}{4\pi\lambda}\frac{40}{3}\xi^3\pi^{-\frac{1}{2}}+\frac{1}{4\pi\lambda}\sum_l\sum_{\substack{\beta\\ \beta_l\neq\alpha_0}}\mathbf{S}_{\beta_l}\cdot\mathbf{M}^{(r)}_{\mathbf{GS}}+\frac{1}{4\pi\lambda}\frac{1}{V_c}\sum_{\substack{\mathbf{k}\\ \mathbf{k}\neq\mathbf{0}}}\sum_\beta\mathbf{S}_{\beta_l}\cdot\mathbf{M}^{(k)}_{\mathbf{GS}}, \tag{2.II.4}$$

$$\frac{n\langle q\rangle}{3\lambda}+\frac{1}{4\pi\lambda}\sum_{\substack{\beta\\ \beta\neq\alpha}}q_\beta\nabla_y\nabla_y\frac{1}{r}-\frac{1}{4\pi\lambda}\int_{V-V_\epsilon}n\langle q\rangle\nabla_y\nabla_y\frac{1}{r}dV=$$

$$\frac{1}{4\pi\lambda}\sum_l\sum_{\substack{\beta\\ \beta_l\neq\alpha_0}}q_{\beta_l}\mathbf{M}^{(r)}_{\nabla q}+\frac{1}{4\pi\lambda}\frac{1}{V_c}\sum_{\substack{\mathbf{k}\\ \mathbf{k}\neq\mathbf{0}}}\sum_\beta q_{\beta_l}\mathbf{M}^{(k)}_{\nabla q}, \tag{2.II.5}$$

where,

$$\mathbf{M}^{(r)}_{\Phi\mathbf{S}}=\mathbf{M}^{(r)}_{\mathbf{G}q}=\left[(4\xi^5r^3-12\xi^3r+2\xi r^{-1})\frac{e^{-\xi^2r^2}}{\sqrt{\pi}}+\frac{\operatorname{erfc}(\xi r)}{r^2}\right]\frac{(\mathbf{R}_{\alpha0}-\mathbf{R}_{\beta_l})}{r}, \tag{2.II.6}$$

$$\mathbf{M}^{(k)}_{\mathbf{\Phi S}} = \mathbf{M}^{(k)}_{\mathbf{G}q} = \frac{4\pi}{k^2}\left[1 + \frac{1}{4}\left(\frac{k}{\xi}\right)^2 + \frac{1}{8}\left(\frac{k}{\xi}\right)^4\right] e^{-(k^2/4\xi^2)} \sin\left[\mathbf{k}\cdot(\mathbf{R}_\alpha - \mathbf{R}_\beta)\right]\mathbf{k}, \quad (2.II.7)$$

$$\mathbf{M}^{(r)}_{\mathbf{\Phi Q}} = \mathbf{M}^{(r)}_{\mathbf{GS}} = \mathbf{M}^{(r)}_{\nabla q} =$$

$$\left[(8\xi^7 r^4 - 36\xi^5 r^2 + 16\xi^3 + 4\xi r^{-2})\frac{e^{-\xi^2 r^2}}{\sqrt{\pi}} + \frac{2\mathrm{erfc}(\xi r)}{r^3}\right]\frac{(\mathbf{R}_{\alpha 0} - \mathbf{R}_{\beta_l})(\mathbf{R}_{\alpha 0} - \mathbf{R}_{\beta_l})}{r^2}$$

$$+ \left[(4\xi^5 r^3 - 12\xi^3 r + 2\xi r^{-1})\frac{e^{-\xi^2 r^2}}{\sqrt{\pi}} + \frac{\mathrm{erfc}(\xi r)}{r^2}\right]\left[\frac{(\mathbf{R}_{\alpha 0} - \mathbf{R}_{\beta_l})(\mathbf{R}_{\alpha 0} - \mathbf{R}_{\beta_l})}{r^3} - \frac{\mathbf{I}}{r}\right], \quad (2.II.8)$$

and

$$\mathbf{M}^{(k)}_{\mathbf{\Phi Q}} = \mathbf{M}^{(k)}_{\mathbf{GS}} = \mathbf{M}^{(k)}_{\nabla q} =$$

$$\frac{4\pi}{k^2}\left[1 + \frac{1}{4}\left(\frac{k}{\xi}\right)^2 + \frac{1}{8}\left(\frac{k}{\xi}\right)^4\right] e^{-(k^2/4\xi^2)} \cos\left[\mathbf{k}\cdot(\mathbf{R}_\alpha - \mathbf{R}_\beta)\right]\mathbf{kk}. \quad (2.II.9)$$

Table 2.II

Effective Conductivity of Simple Cubic Lattice

	$\lambda_p/\lambda = \infty$			$\lambda_p/\lambda = 10.0$			$\lambda_p/\lambda = 0.01$	
c	$\mathbf{M_{GS}^{-1}}$	$\mathbf{C_{SG}}$	**S & A**	$\mathbf{M_{GS}^{-1}}$	$\mathbf{C_{SG}}$	**S & A**	$\mathbf{M_{GS}^{-1}}$	**S & A**
0.00	1.000	1.000	1.000	1.000	1.000	1.000	1.000	1.000
0.05	1.158	1.158	1.158	1.117	1.117	1.117	0.928	0.928
0.10	1.333	1.333	1.333	1.243	1.243	1.243	0.859	0.859
0.15	1.529	1.533	1.531	1.380	1.381	1.381	0.794	0.794
0.20	1.750	1.762	1.756	1.529	1.533	1.532	0.731	0.730
0.25	2.000	2.031	2.018	1.692	1.701	1.699	0.671	0.670
0.30	2.286	2.357	2.333	1.871	1.890	1.888	0.614	0.611
0.35	2.615	2.771	2.727	2.068	2.109	2.105	0.559	0.554
0.40	3.000	3.332	3.250	2.286	2.368	2.362	0.506	0.497
0.45	3.455	4.190	4.040	2.528	2.685	2.679	0.456	0.441
0.50	4.000	6.099	5.880	2.800	3.100	3.090	0.407	0.385
0.51				2.858	3.207	3.187	0.398	0.373
0.52				2.918	3.345	3.255	0.388	0.360
0.523	4.289	12.123	11.675					
0.5231	4.291	12.412	11.962					
0.5232	4.292	12.765	12.314					
0.5233	4.293	13.221	12.767					
0.5234	4.295	13.865	13.408					

$\mathbf{M_{GS}^{-1}}$:Simulation with $\mathbf{M_{GS}^{-1}}$ only.

$\mathbf{C_{SG}}$:Simulation with $\mathbf{M_{GS}^{-1}}$ and lubrication.

S & A :Results of Sangani & Acrivos (1982).

Table 2.III

Effective Conductivity of Body-Centered Cubic Lattice

	$\lambda_p/\lambda = \infty$			$\lambda_p/\lambda = 10.0$			$\lambda_p/\lambda = 0.01$	
c	$\mathbf{M_{GS}^{-1}}$	$\mathbf{C_{SG}}$	**S & A**	$\mathbf{M_{GS}^{-1}}$	$\mathbf{C_{SG}}$	**S & A**	$\mathbf{M_{GS}^{-1}}$	**S & A**
0.00	1.000	1.000	1.000	1.000	1.000	1.000	1.000	1.000
0.05	1.158	1.158	1.158	1.117	1.117	1.117	0.928	0.928
0.10	1.333	1.333	1.333	1.243	1.243	1.243	0.859	0.859
0.15	1.529	1.532	1.530	1.380	1.381	1.381	0.794	0.793
0.20	1.750	1.757	1.751	1.529	1.532	1.530	0.731	0.731
0.25	2.000	2.018	2.002	1.692	1.700	1.693	0.671	0.671
0.30	2.286	2.326	2.292	1.871	1.885	1.873	0.614	0.613
0.35	2.615	2.696	2.631	2.068	2.088	2.073	0.559	0.556
0.40	3.000	3.151	3.035	2.286	2.310	2.297	0.506	0.505
0.45	3.455	3.728	3.530	2.528	2.565	2.551	0.456	0.453
0.50	4.000	4.487	4.157	2.800	2.863	2.843	0.407	0.403
0.55	4.667	5.541	4.900	3.106	3.200	3.187	0.361	0.354
0.60	5.500	7.151	6.294	3.454	3.629	3.601	0.316	0.306
0.65	6.572	10.368	9.024	3.853	4.147	4.117	0.272	0.259
0.67	7.091	13.439	12.009	4.029	4.400	4.363	0.256	0.240
0.68	7.375	24.763	23.080	4.121	4.551	4.496	0.247	0.231
0.68011	7.378	27.513	25.781					
0.68012	7.379	27.983	26.237					
0.68013	7.379	28.551	26.786					
0.68014	7.379	29.271	27.474					
0.68015	7.379	30.251	28.397					

$\mathbf{M_{GS}^{-1}}$:Simulation with $\mathbf{M_{GS}^{-1}}$ only.

$\mathbf{C_{SG}}$:Simulation with $\mathbf{M_{GS}^{-1}}$ and lubrication.

S & A :Results of Sangani & Acrivos (1982).

Table 2.IV

Effective Conductivity of Face-Centered Cubic Lattice

	$\lambda_p/\lambda = \infty$			$\lambda_p/\lambda = 10.0$			$\lambda_p/\lambda = 0.01$	
c	$\mathbf{M_{GS}^{-1}}$	$\mathbf{C_{SG}}$	**S & A**	$\mathbf{M_{GS}^{-1}}$	$\mathbf{C_{SG}}$	**S & A**	$\mathbf{M_{GS}^{-1}}$	**S & A**
0.00	1.000	1.000	1.000	1.000	1.000	1.000	1.000	1.000
0.05	1.158	1.158	1.158	1.117	1.117	1.117	0.928	0.928
0.10	1.333	1.333	1.333	1.243	1.243	1.243	0.859	0.859
0.15	1.529	1.532	1.530	1.380	1.381	1.380	0.794	0.794
0.20	1.750	1.757	1.751	1.529	1.532	1.530	0.731	0.731
0.25	2.000	2.018	2.002	1.692	1.700	1.693	0.671	0.671
0.30	2.286	2.326	2.292	1.871	1.880	1.872	0.614	0.614
0.35	2.615	2.694	2.631	2.068	2.080	2.070	0.559	0.559
0.40	3.000	3.145	3.035	2.286	2.300	2.290	0.506	0.506
0.45	3.455	3.712	3.530	2.528	2.549	2.537	0.456	0.455
0.50	4.000	4.440	4.157	2.800	2.830	2.816	0.407	0.405
0.55	4.667	5.430	4.900	3.106	3.154	3.134	0.361	0.358
0.60	5.500	6.824	6.294	3.454	3.552	3.502	0.316	0.312
0.65	6.572	8.984	9.024	3.853	4.000	3.935	0.272	0.267
0.70	8.000	13.028	10.611	4.316	4.556	4.454	0.231	0.223
0.71	8.345	14.538	11.893					
0.72	8.714	16.122	13.680					
0.73	9.111	19.385	16.677	4.630	4.929	4.818	0.207	0.197
0.74	9.539	33.436	30.392	4.742	5.100	4.951	0.199	0.189
0.7401	9.543	34.482	31.429					
0.7402	9.547	35.850	32.783					
0.7403	9.552	37.833	34.743					

$\mathbf{M_{GS}^{-1}}$:Simulation with $\mathbf{M_{GS}^{-1}}$ only.

$\mathbf{C_{SG}}$:Simulation with $\mathbf{M_{GS}^{-1}}$ and lubrication.

S & A :Results of Sangani & Acrivos (1982).

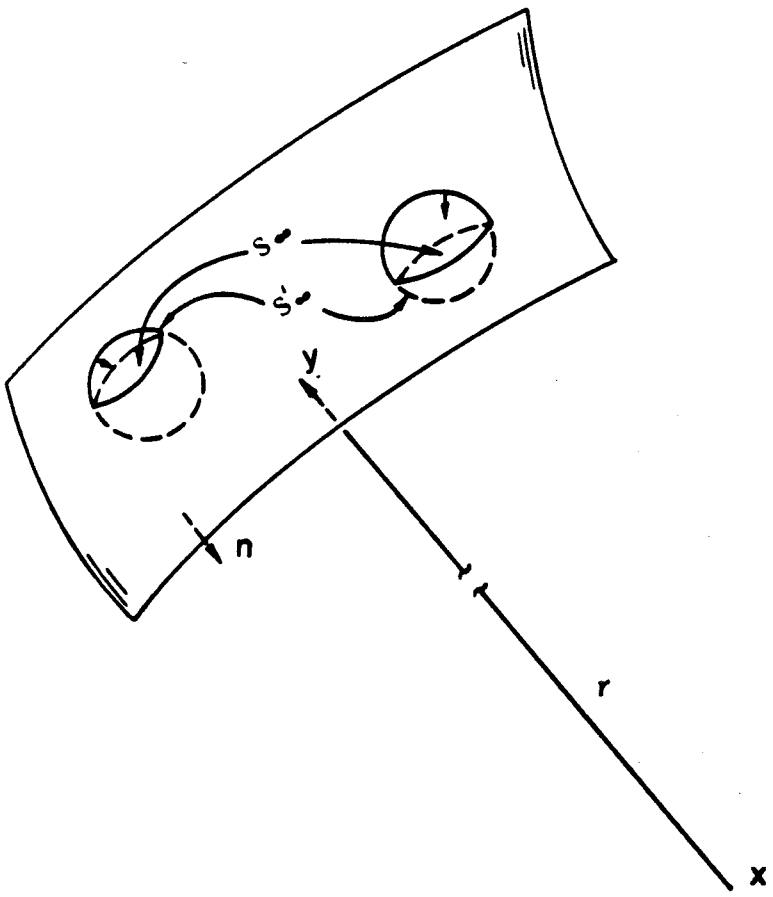

Figure 2.1. Sketch of sections of the distant boundary surfaces, S'_∞ and S_∞, which surround **x**. The surface S'_∞ passes only though the matrix and does not intersect particles. The surface S_∞ cuts through both the particles and the matrix.

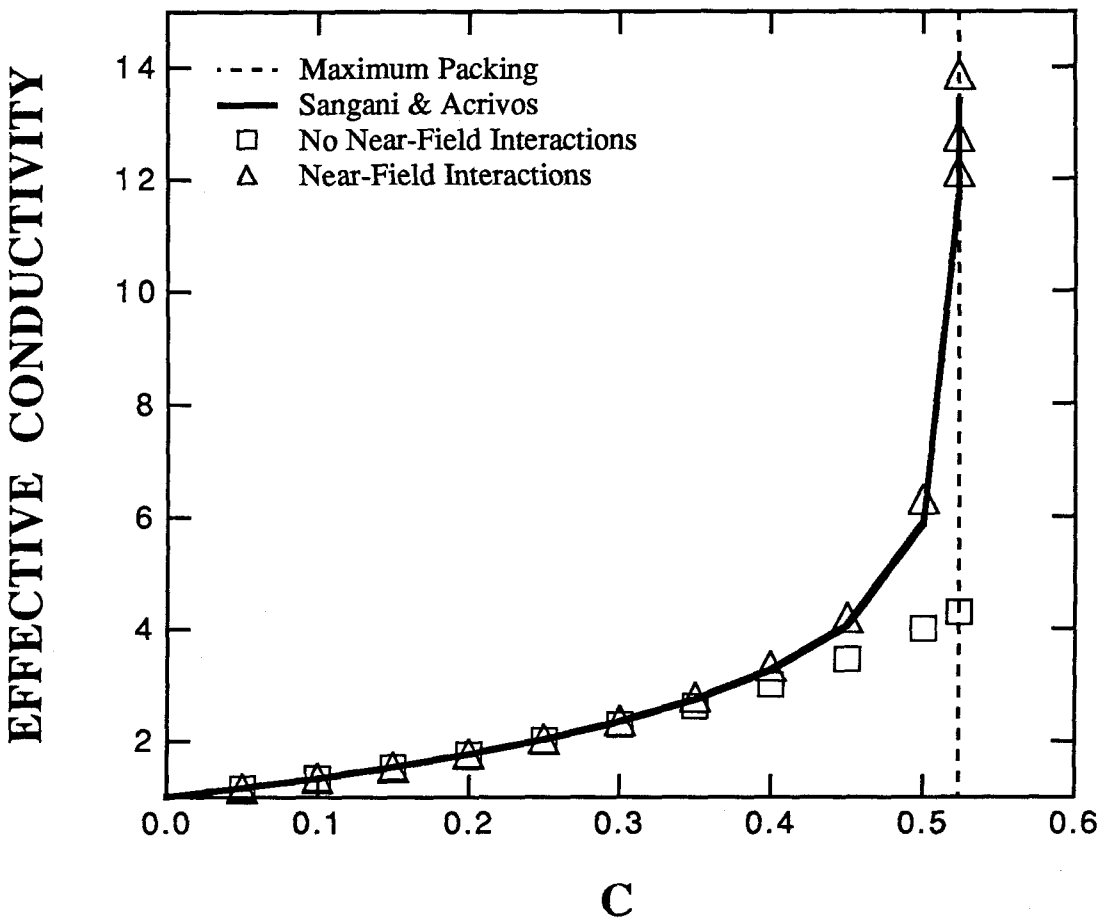

Figure 2.2*a*. Effective conductivity versus volume fraction for a simple cubic lattice with sphere-to-matrix conductivity ratio of $\infty(a)$ and 10.0 and $0.01(b)$. The open symbols are results of the simulation method with and without near-field interactions, and the solid lines are the analytical results of Sangani & Acrivos. Results for body- and face-centered cubic lattices are similar.

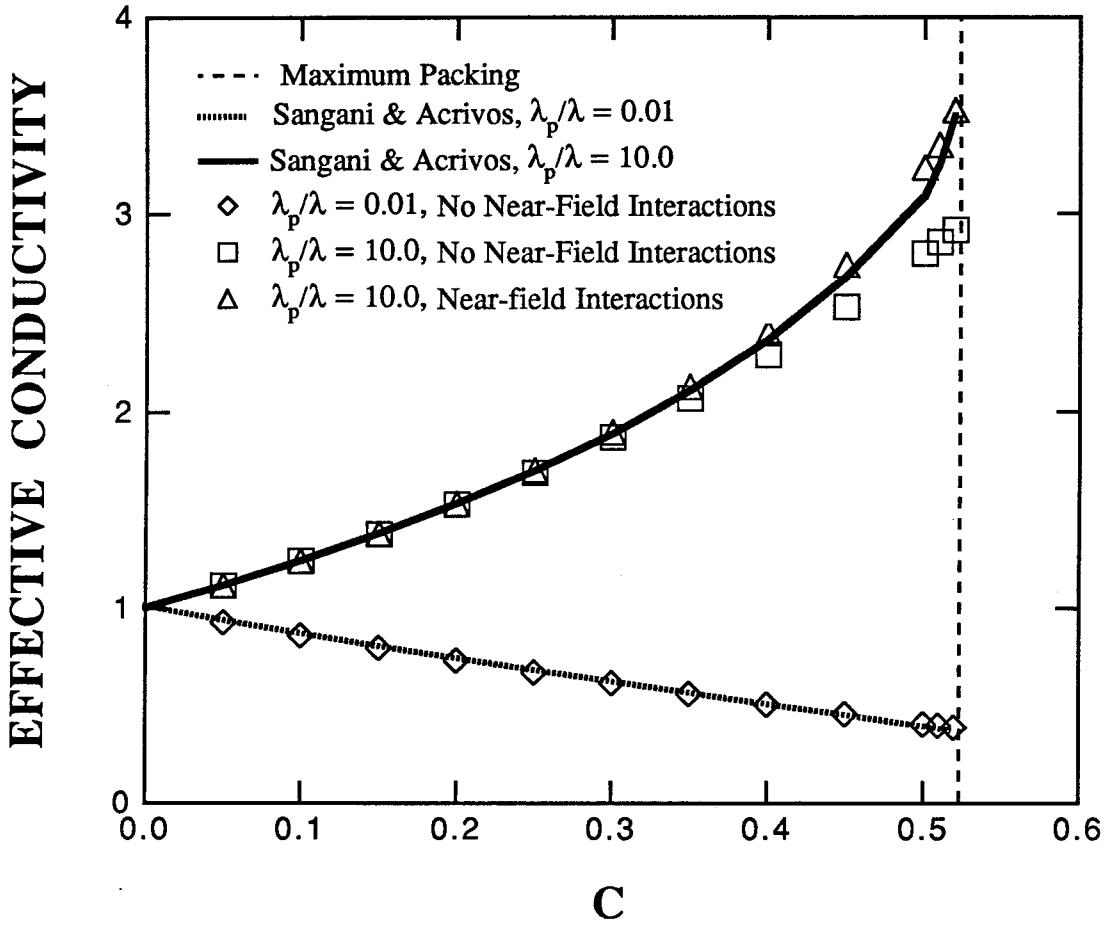

Figure 2.2*b*. See figure caption 2.2*a*.

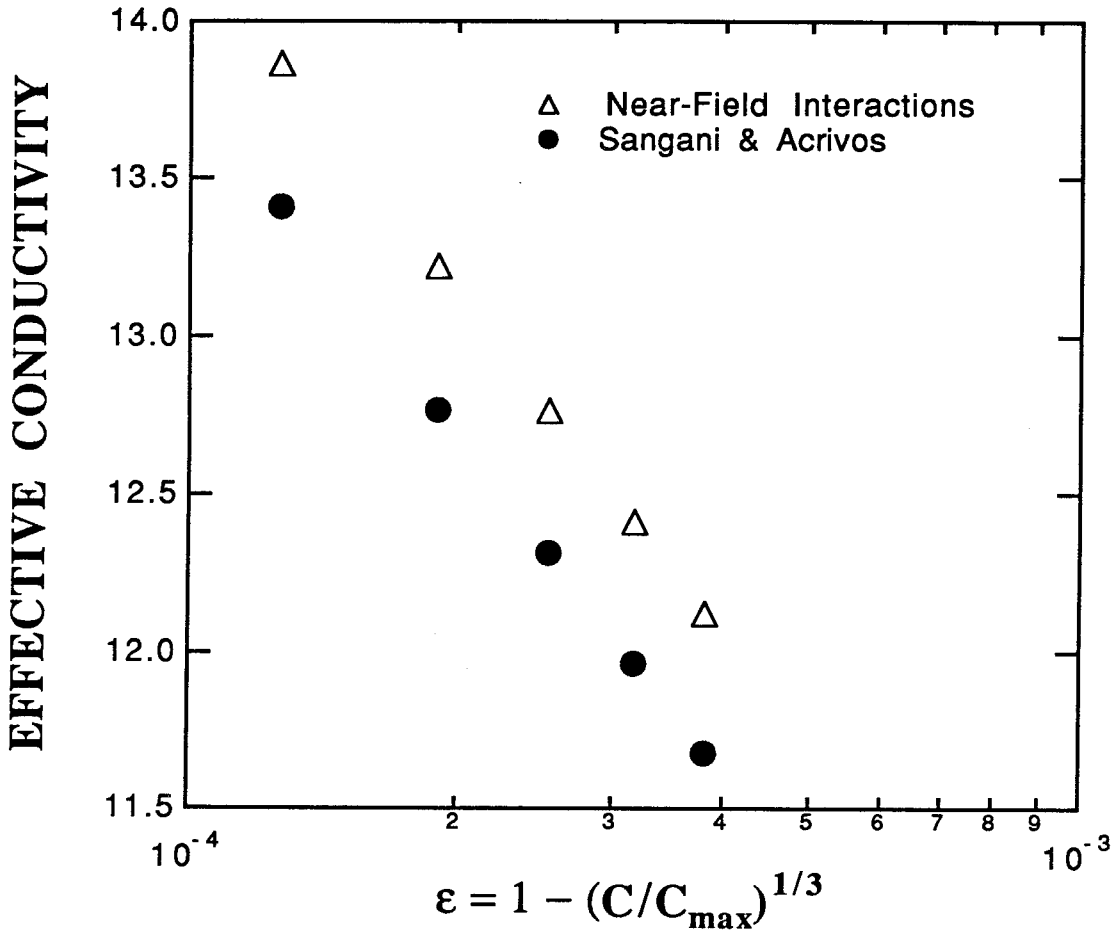

Figure 2.3. Effective conductivity near closest packing for a simple cubic lattice of perfectly conducting spheres. The open symbols are the simulation results with near-field interactions, and the closed symbols are the analytical results of Sangani & Acrivos. Note the logarithmic behavior of the conductivity with the gap width as predicted by asymptotic analysis.

CHAPTER 3

EFFECTIVE CONDUCTIVITY OF RANDOM HARD-SPHERE SUSPENSIONS

3.1. Introduction

In the previous chapter we outlined a simulation method for determining the effective conductivity of an arbitrary configuration of particles. We successfully verified the method by comparing our simulation results to the known analytical results of Sangani & Acrivos (1982) for cubic arrays. In this chapter we shall apply the method to determine the effective conductivity of a random hard-sphere dispersion over nearly the entire volume fraction range. As mentioned earlier, Maxwell (1873) first began work on this problem 120 years ago by calculating the $O(c)$ correction to the conductivity. Until now, the best theoretical calculation of the effective conductivity is the $O(c^2)$ result of Jeffrey (1973). Here, we shall extend the database up to sixty volume percent and bring this long-standing problem to a close.

In §3.2 we briefly review the method and its application to the problem of determining the effective conductivity of random suspensions. The method and the results will be discussed in the context of charge transport or electrical conductivity, but by mathematical analogy, they apply to thermal and mass transport, electric displacement, and magnetic induction. In addition we describe how a random infinite suspension of spherical particles is generated with a Monte Carlo method and periodic boundary conditions. In §3.3 the results of the simulations are compared to the theoretical work of Jeffrey and the bounds of Torquato & Lado. These simulation results are also compared to the physical measurements of Meredith & Tobias (1960) on the electrical conductivity of emulsions and to those of Turner (1976) on the electrical conductance of spherical resins fluidized in aqueous salt solutions.

3.2. Simulation Method

The method for determining the effective conductivity of a random dispersion of particles is explained in detail in Chapter 2. Here we briefly describe the method and discuss how we model random suspensions of spherical particles with a Monte

Carlo scheme and periodic boundary conditions.

Calculation of the Effective Conductivity of Suspensions

Consider an infinite, statistically homogeneous suspension of particles with conductivity λ_p immersed in a matrix of conductivity λ with a particle volume fraction c. Within each phase the continuum equations of conductive transport,

$$\nabla \cdot \mathbf{F} = 0, \tag{3.1}$$

$$\mathbf{F} = -\lambda_{(p)} \nabla \phi, \tag{3.2}$$

are satisfied. The first equation indicates there is no charge source or sink in either phase, and the second equation is a Fick's law constitutive equation that relates the electric current or flux, $\mathbf{F}$, to the potential gradient, $\nabla\phi$, with $\lambda_{(p)}$ taking on the value λ or λ_p in the matrix or particle phase, respectively.

The suspension is subject to a macroscopic or volume average potential gradient, $\mathbf{G} = \langle \nabla \phi \rangle$, producing an average flux $\langle \mathbf{F} \rangle$. Because the transport equations (3.1) and (3.2) are linear, the average flux is linearly related to the average gradient by,

$$\langle \mathbf{F} \rangle = -\Lambda_{eff} \cdot \mathbf{G}, \tag{3.3}$$

where Λ_{eff} is the effective conductivity tensor. As shown by Batchelor (1974) the average flux for a statistically homogeneous medium of charge-free particles is also given by,

$$\langle \mathbf{F} \rangle = -\lambda \mathbf{G} + n \langle \mathbf{S} \rangle, \tag{3.4}$$

where

$$\mathbf{S} = \int_{\partial \Omega_\beta} (\mathbf{x}\mathbf{F} + \lambda \phi \mathbf{I}) \cdot \mathbf{n} dS. \tag{3.5}$$

The quantity $\langle \mathbf{S} \rangle$ is the average particle dipole and n is the particle number density. Note in (3.5) $\mathbf{x}$ is a point on the particle surface relative to a reference point within the particle.

The calculation of the effective conductivity reduces to the determination of the relationship between the average dipole and the average potential gradient. Again

due to the linear nature of the problem, there exists the exact relationship,

$$\begin{pmatrix} \mathbf{q} \\ \mathbf{S} \end{pmatrix} = \begin{pmatrix} \mathbf{C}_{q\Phi} & \mathbf{C}_{q\mathbf{G}} \\ \mathbf{C}_{\mathbf{S}\Phi} & \mathbf{C}_{\mathbf{SG}} \end{pmatrix} \cdot \begin{pmatrix} \mathbf{\Phi} \\ -\mathbf{G} \end{pmatrix} \tag{3.6}$$

among N particles. The vectors $\mathbf{q}, \mathbf{S}, \mathbf{\Phi}$, and $\mathbf{G}$ contain the N particle charges, the $3N$ components of the particle dipoles, the N relative particle potentials at each particle reference point, $\mathbf{R}_\beta$ $(\phi(\mathbf{R}_\beta) - \langle\phi(\mathbf{R}_\beta)\rangle)$, and $3N$ components of the average potential gradient, respectively. The matrix in (3.6) is called the capacitance matrix, $\mathbf{C}$, in electrostatics. Its submatrices relate the charge to the potential, $\mathbf{C}_{q\Phi}$, the charge to the gradient, $\mathbf{C}_{q\mathbf{G}}$, etc. Solving the matrix equation for zero-charge particles and averaging over the N of them yields,

$$\langle \mathbf{S} \rangle = \langle \mathbf{C}_{\mathbf{S}\Phi} \cdot {\mathbf{C}_{q\Phi}}^{-1} \cdot \mathbf{C}_{q\mathbf{G}} - \mathbf{C}_{\mathbf{SG}} \rangle \cdot \mathbf{G}, \tag{3.7}$$

and combining it with (3.3) and (3.4) gives

$$\mathbf{\Lambda}_{eff} = \lambda \mathbf{I} - n\langle \mathbf{C}_{\mathbf{S}\Phi} \cdot {\mathbf{C}_{q\Phi}}^{-1} \cdot \mathbf{C}_{q\mathbf{G}} - \mathbf{C}_{\mathbf{SG}} \rangle, \tag{3.8}$$

for the effective conductivity tensor. The capacitance matrix and its submatrices are purely geometric quantities completely determined by the configuration of the particles. Thus, the effective conductivity depends entirely upon the details of the suspension microstructure, and the problem reduces to one of determining the N-body capacitance matrix.

The capacitance matrix is approximated by,

$$\mathbf{C} \approx \mathbf{M}^{-1} + \mathbf{C}_{2b} - \mathbf{C}_{2b}^{\infty}. \tag{3.9}$$

The mobility or "potential" matrix, $\mathbf{M}$, in its *exact* form is the inverse of the capacitance matrix. Here, the potential matrix is approximately formed from a moment expansion about each particle derived from the integral equation representation of (3.1) and (3.2). The moment expansion can be carried out to any level. The accuracy of the potential matrix and, hence, the potential invert depends on the number of terms retained in the expansion. In this present paper we will consider moment

expansions through both the dipole and quadrupole levels. The inversion of this potential matrix accurately captures the many-body far-field particle interactions since the inversion is equivalent to a many-body method of reflections solution. Note, care must be taken in forming the potential matrix in this way for an infinite suspension because the particle interactions are long-ranged, giving rise to convergence difficulties. The reader is referred to Chapter 2 for a detailed description of the formation of the potential matrix for a finite or infinite suspension of particles.

As mentioned in the introduction, perfectly conducting particles near contact at different potentials, say due to a macroscopic electric field, will have a logarithmically singular charge flux between them. This charge flux will be localized at nearly a point, so from equation (3.5) we see that the particles' dipoles are logarithmically singular as well. (Indeed the essence of this argument combined with equations (3.3) and (3.4) gives the logarithmic singularity for the effective conductivity noted by Batchelor & O'Brien (1977).) Although the potential invert captures the far-field interactions, it does not capture these near-field interactions, particularly those singularities in the charge flux and the dipole for particles near contact. An infinite number of moments would be required in the potential matrix formulation to capture these singularities. To include these near-field effects, exact two-body interactions $\mathbf{C}_{2b}$, less the far-field two-body interactions up to dipoles or quadrupoles depending upon the number of moments included in the potential matrix $\mathbf{C}_{2b}^{\infty}$, are added to the approximate potential invert. The two-body capacitance matrix contains the interactions between particles α and β, ignoring particles δ, γ, etc., and the interactions between particles α and δ, ignoring particles β, γ, etc., and so on. The far-field two-body interactions are subtracted since they were already included in the potential invert. The two-body capacitance matrix for perfectly conducting spheres can be constructed from the solutions of Jeffrey (1973, 1978) and Davis (1964) for two spherical conductors in a linear potential gradient. The method's results compare extremely well to those of Sangani & Acrivos (1982) for the effective conductivity of perfectly conducting particles in cubic arrays as was shown in our earlier paper. It was also discovered that for modest conductivity ratios of about 10

or less, the far-field interactions in the potential invert were sufficient to accurately determine the effective conductivity.

Generation of a Random Hard-Sphere Dispersion

To use the capacitance matrix to calculate the dipoles for an infinite suspension, we apply periodic boundary conditions on N spheres in a cubic cell to model an infinite suspension. An infinite random suspension was modeled by randomly placing the N spheres in the periodic cell using the following steps: First, the spheres are placed on an initial simple cubic, body-centered cubic, or face-centered cubic lattice superimposed on the cubic periodic cell, whose size is chosen to satisfy a given sphere volume fraction c. Note for some choices of N, initial lattice-type, and c, the lattice is only partially filled, which presents no difficulty to the method described below, and some other choices are not possible. After choosing only realizable combinations, the spheres are moved about the periodic cell with a Monte Carlo method. That is, the spheres, one by one, are moved a small distance d in some random direction, and the cycle is repeated a large number of times. Care is taken so that spheres leaving on one side of the periodic cell reappear on the opposite side, and that spheres do not overlap and are not in contact with others in the cell or in the neighboring periodic cells. This method has been employed by others (Lee & Torquato 1988) to generate hard-sphere dispersions.

After each m cycles, the effective conductivity is calculated for the particular realization and the average position statistics are updated. The average position statistics at the end of the run are used to generate a simulation hard-sphere distribution function, $g(r)$. If the simulation distribution function compares well with the known distribution function, we are confident then that the average effective conductivity computed is that of a random dispersion of hard-spheres.

Figures $3.1(a-c)$ illustrate the distribution functions calculated for 32 spheres in a cubic periodic cell initially placed on a face-centered cubic lattice for $c = 0.4, 0.5$, and 0.6. The Monte Carlo step size, d, and the cycles between samples, m, are listed in Table I. In each case 200 realizations were used to compute the $g(r)$s presented here. For $c = 0.4$ the average $g(r)$ of the simulation is identical to a hard-sphere ra-

dial distribution up to a distance of about 6.9 (non-dimensionalized with the sphere radius). (The exact hard-sphere distribution is calculated from the Percus-Yevick analytical solution given by Smith & Henderson (1970) for $r \leq 10$ and the large r solution given by Perry & Throop (1972).) Beyond this distance there are small negative deviations in the distribution function and isolated large positive "spikes." The cell size for this system is 6.95 indicating that the periodic boundary conditions do influence $g(r)$. Indeed these isolated spikes correspond to each particle's image in the surrounding periodic cells. For lower volume fractions the comparisons of the simulation $g(r)$ and that for true hard-spheres are qualitatively similar. While we conclude that periodic boundary conditions do not truly generate a random suspension far from a spheres center for finite N, the spheres within these spike regions contribute negligibly to each sphere's dipole compared to the contribution of the nearer particles. Because the near-field $g(r)$ is reproduced faithfully in the simulations, we are confident that we are measuring the effective conductivity of a random suspension for $c \leq 0.4$. Note that for large N, the range of agreement between the simulation and exact $g(r)$ will increase since the cell size increases with N. The spikes are moved further away from the sphere center since each sphere's periodic images are further away. The effect of cell size on the effective conductivity is discussed in §3.3.

Figures 3.1($b-c$) compare the simulation $g(r)$ to the exact $g(r)$ for $c = 0.5$ and 0.6, respectively. The theoretical $g(r)$s shown in Figures 3.1($b-c$) are for the continuation of the fluid phase into the two-phase region. A hard-sphere system undergoes a phase transition from a disordered fluid to an fcc crystal for $c > 0.494$. The two-phases coexist for $0.494 < c < 0.55$, and the fcc lattice is the equilibrium phase above $c = 0.55$. For both volume fractions at large r, the Monte Carlo $g(r)$ has peaks corresponding to an fcc lattice structure as well as to each sphere's periodic image. However, the near-field $g(r)$ for $c = 0.5$ is very close to the exact value up to $r \approx 5.0$, so we have confidence that the effective conductivity for this volume fraction is close to that of a random hard-sphere dispersion, especially in light of forthcoming comparisons to experimental systems that probably approximate hard-

sphere dispersions. The simulation $g(r)$ for $c = 0.6$ appears only correct up to a $r \approx 3$, with deviations from the exact value thereafter even larger than those for $c = 0.5$. It is not known how much these deviations effect the calculated effective conductivity. We report the conductivity for $c = 0.6$ but with the reservation that it may not be that of a random hard-sphere dispersion. Note, we also performed a simulation at $c = 0.6$ for 99 spheres per cell and found no change in the effective conductivity or the distribution function, except that the spikes were further away from the sphere center for 99 versus 32 spheres.

For $c \geq 0.6$ the simulated distribution function represents more perturbations to a face centered-cubic lattice, the initial lattice, than a random hard-sphere distribution. We have been unsuccessful with using this Monte Carlo scheme to generate a random suspension that even reproduces the near-field $g(r)$, so we report here only conductivities for $c \leq 0.6$.

Increasing the number of cycles between samples and/or the number of samples in the Monte Carlo procedure will not alter the $g(r)$s for $c \geq 0.5$, because of the phase transition between randomly dispersed and fcc crystalline structures for hard-sphere suspensions. As far as we know, no method has been developed to generate a periodically replicated, densely packed, random hard-sphere dispersion.

Finally, note that any system for the formation of the particle configurations could be used for the simulation. A real suspension is most likely formed by hydrodynamic flows or some other processes. We have chosen the Monte Carlo method because it is well defined, easily reproducible by other workers, the configurations it generates conform to those of past theoretical studies, and it seems to model experimental conditions well.

3.3. Effective Conductivity Results

The method outlined in the previous section was applied to determine the effective conductivity for a random suspension of spheres for $c \leq 0.6$ and particle-matrix conductivity ratios, λ_p/λ, of ∞, 10, and 0.01. The bulk of the simulations were performed for 32 particles initially placed in a face-centered cubic lattice superimposed on a simple cubic periodic cell. The simulation conditions including the Monte Carlo step size, number of cycles between sampling, and the number of realizations for the bulk of the data are summarized in Table I. Using the quadrupole formulation of the potential matrix requires an additional matrix inversion, substantially increasing the execution time, so fewer realizations are sampled. Simulations were also done for 27 particles initially placed in a simple cubic lattice for $c = 0.1$ and 0.3 and showed no differences in $g(r)$ or the average effective conductivity. Although the simulation computes the tensorial effective conductivity, $\mathbf{\Lambda}_{\text{eff}}$, a random hard-sphere dispersion is isotropic *on average*, and $\mathbf{\Lambda}_{\text{eff}}$ averaged over a number of realizations can be represented by $\lambda_{eff}\mathbf{I}$, where λ_{eff} is the scalar effective conductivity. All conductivities reported here are relative to that of the matrix. These average effective conductivities computed with the simulation are listed in Table II and plotted in Figures $3.4(a-c)$.

Table II lists the effective conductivity using the dipole formulation for the three conductivity ratios. The effective conductivity for $\lambda_p/\lambda = \infty$ and 10 was calculated with and without the near-field two-body interactions. The addition of two-body interactions contributes substantially at large volume fractions, especially for the infinite conductivity ratio. For $\lambda_p/\lambda = 0.01$, no two-body interactions were added to the potential invert. From the results for cubic arrays, it was found that this was quite accurate, though at large volume fractions the effective conductivities were slightly overestimated. Table II also lists the 95% confidence limits computed from the realizations sampled. In general the variation increases with increasing volume fraction and particle-matrix conductivity ratio. As the particles are moved about the cell in the Monte Carlo randomization, particle clusters are formed that provide locally (in)efficient paths of conduction for λ_p/λ $(\leq)$ ≥ 1 since the charge

prefers the path of least resistance. As mentioned earlier, this fact is reflected in the logarithmic singularity observed in the charge flux and the dipoles of perfectly conducting particles near contact. In general we may consider the effect of clustering in terms of induced dipoles. For conductivity ratios greater than one, particles nearby induce even greater individual dipoles due to their interactions, so clusters will increase the conductivity relative to a "well-separated" suspension by increasing the average particle dipoles. Similar arguments show that for conductivity ratios less than one, the clusters will decrease the conductivity relative to a well-separated suspension. The number and length of the clusters varies from realization to realization sampled, so a variation in the effective conductivity is observed. However, the largest variation is only about 7% of the average effective conductivity, which is a consequence of the weakness of the logarithmic singularity. Also, for perfectly conducting particles, the effective conductivity is expected to approach infinity as c approaches closest-packing, about 0.63 for a hard-sphere dispersion. Figure 3.4a indicates that the rate of change in the effective conductivity increases as c increases, which is, at least in appearance, consistent with an infinite conductivity at closest-packing. Note also, though, that along with the rapid rise in the conductivity there should be an increase in its variance with increasing volume fraction. At $c = 0.6$ and $\lambda_p/\lambda = \infty$, the effective conductivity confidence limits actually decrease, probably due to the inadequacies in the the Monte Carlo method. This indicates that caution must be used in assigning this conductivity to that of a random hard-sphere dispersion.

Also included in Figures 3.4$(a - b)$ are the results using the quadrupole formulation for conductivity ratios of ∞ and 10. The results using quadrupoles for the conductivity ratio 0.01 are hardly distinguishable from the dipole results and so are not plotted. The most noticeable change is for $\lambda_p/\lambda = \infty$. The effective conductivity is lower using the quadrupole formulation than using the dipole formulation for $c \geq 0.4$, particularly at $c = 0.6$ where there is also a noticeable change in conductivity for $\lambda_p/\lambda = 10$. This is best explained by considering the change in the effective conductivity for regular lattices with the quadrupole formulation.

For any regular lattice, the sphere quadrupole is zero for charge-free spheres; hence, the addition of quadrupole terms will not improve the accuracy of the potential invert. However, the $\mathbf{C}_{2b}^{\infty}$ matrix includes the far-field two-body, in general, *non-zero* quadrupole term. When subtracting $\mathbf{C}_{2b}^{\infty}$ from $\mathbf{M}^{-1}$, we have subtracted a quadrupole piece not present in the potential invert. The effect is to reduce the absolute average in (3.7) and hence reduce the effective conductivity. Note that as the volume fraction approaches maximum packing, the lubrication singularity will dominate and the conductivity will be independent of the formulation. Unfortunately, since the singularity is weak, the particles must be extremely close together for this to occur.

As discussed earlier the $g(r)$ at $c = 0.6$ indicates a perturbed fcc structure, close to a cubic lattice, so as explained above the effect of the quadrupole is practically zero for the potential invert, but the subtraction of $\mathbf{C}_{2b}^{\infty}$ will reduce the effective conductivity relative to the dipole formulation. The differences at $c = 0.4$ and 0.5 are slight and may be due either to the less ordered nature of the suspension at these volume fractions or to the quadrupole formulation simply giving a better result.

From Chapter 2 (1990) it was found that the dipole formulation for infinite conductivity ratios overpredicted the effective conductivity for cubic arrays compared to the results of Sangani & Acrivos (1982). Using the quadrupole formulation, it was found that the effective conductivities for all the cubic lattices were reduced compared to the results from the dipole formulation for high volume fractions. This reduction is entirely due to the modified two-body interactions which now include the quadrupoles, since for cubic lattices there is no coupling between the quadrupoles and the dipoles. It turns out that when using the quadrupoles, and comparing the method to the results of Sangani & Acrivos, it now *underpredicts* the effective conductivity for simple cubic lattices, still overpredicts the effective conductivity for face-centered cubic lattices, and now only very slightly overpredicts the effective conductivity for body-centered cubic lattices. Recall that the coordination number for a body-centered cubic lattice is 8 and the estimated coordination number is 6 to 7 for a random array, so using the quadrupole formulation probably

underpredicts the effective conductivity of random arrays. Indeed, as will be shown later, the computed results do straddle one set of experimental results.

The effects of periodic cell size on the effective conductivity were tested by varying the number of particles per cell for $c = 0.4$ and $\lambda_p/\lambda = \infty$. For 4 to 65 particles per cell, the minimum, maximum, and average effective conductivities were found to reach a constant value at about 32 particles per cell, as displayed in Figure 3.2. The variation in the maximum and minimum was largest for the least number of particles per cell because it is more likely to have a small number of particles either form a cluster, an efficient path for conduction, or be completely unconnected, the least efficient configuration for conduction. Based on these simulations we are confident with our results for other volume fractions with only 32 particles per periodic cell. Note that in the analogous hydrodynamic problem of determining the effective viscosity of a suspension of spheres, Phillip, Brady, & Bossis (1988) have shown that 27 particles are sufficient to give a good average value.

Figure 3.3 presents the current average (the average of the three eigenvalues of $\mathbf{\Lambda}_{\text{eff}}$) and the running average of the effective conductivity for $c = 0.4$ and 32 particles for 200 realizations, as well as the current maximum and minimum eigenvalues of the effective conductivity matrix. The data we report in Table 3.II are averaged over 150 to 200 realizations for the sake of thoroughness, however, from Figure 3.3 it appears 10 to 40 realizations would be sufficient to calculate an accurate effective conductivity. Plots for other volume fractions are qualitatively similar, except for increasing fluctuations with increasing volume fraction and conductivity ratio.

The results of the simulation compare quite well to previous theoretical work and experimental measurements. Table II also lists the effective conductivities computed with Jeffrey's $O(c^2)$ correction. His results closely follow those of the simulations up to a volume fraction of 0.2 for $\lambda_p/\lambda = \infty$, 0.3 for $\lambda_p/\lambda = 10.0$, and 0.5 for $\lambda_p/\lambda = 0.01$. This provides a check on our simulation as well as defining the limits of Jeffrey's results. In addition the results of the Clausius-Mosotti equation

are listed in Table II. The Clausius-Mosotti equation is

$$\lambda_{eff} = (1 + 2\beta c)/(1 - c), \tag{3.10}$$

where

$$\beta = (\lambda_p/\lambda - 1)/(\lambda_p/\lambda + 2). \tag{3.11}$$

It is derived by assuming that the effective electric field experienced by a particle is the applied field plus that induced by an average over the particle dipoles. Further, it is assumed that each particle's dipole is the average particle dipole; hence, the formulation is a self-consistent mean-field theory. Exact details of the derivation are given by Jackson (1975). As shown in Table II, the Clausius-Mosotti equation predicts conductivities within 10% of our method for $\lambda_p/\lambda = 10.0$ and 3% for $\lambda_p/\lambda = 0.01$, indeed far better than Jeffrey's $O(c^2)$ result for the former case. It is not as successful for an infinite conductivity ratio for fairly concentrated suspensions, indicating the importance of the near-field interactions for high-conductivity ratio materials. As we shall see in the next section on percolation experiments, these near-field interactions often dominate and are the essential basis for the behavior of suspensions of particles near contact.

Figures 3.4$(a - c)$ illustrate the simulation results along with the upper and lower bounds derived by Torquato & Lado (1986). There is no upper bound for an infinite conductivity ratio because the microstructural information included in the problem formulation does not preclude the formation of an infinite percolating cluster, which would result in an infinite effective conductivity. The simulation results lie on the lower bound for volume fractions less than 0.2, and above it for all higher volume fractions. For a conductivity ratio of 10.0, the simulation results lie along the lower bound up to about a volume fraction of 0.4, after which the simulation results using the dipole formulation lie slightly above it. Using the quadrupole formulation, the effective conductivity predicted by the simulation lies along the lower bound up to a volume fraction of 0.5, though the bound is still higher for $c = 0.6$. For a conductivity ratio of 0.01 the simulation results lie precisely along the upper bound, except for $c \geq 0.5$. No two-body interactions were

added, which in this case tend to slightly overestimate the effective conductivity at large volume fractions, a result also seen with comparisons to cubic arrays. Since the deviations were small in those comparisons, it is reasonable to conclude that for particle-matrix conductivity ratios less than one, the upper bounds are the true effective conductivity.

Meredith & Tobias (1961) experimentally measured the electrical conductivity of well-mixed, water-propylenecarbonate emulsions of narrow size distribution in aqueous KCl solutions for volume fractions ranging up to 0.5. By varying the salt concentration, they varied the emulsion droplet-solution conductivity ratio from 101 to 0.172. From their experiments they developed an accurate correlation, based loosely upon the theory of Fricke (1924), which is an extension of the Clausius-Mosotti equation, for their effective conductivity data, namely,

$$\lambda_{eff} = \left(\frac{2+2\beta c}{2-\beta c}\right)\left(\frac{2+(2\beta-1)c}{2-(\beta+1)c}\right), \tag{3.12}$$

Their correlation is plotted in Figure 3.4*a* for an infinite conductivity ratio, and the simulation results for the dipole formulation agree perfectly up to a volume fraction of 0.5. The disagreement at higher conductivity ratios is probably due to the limited range of the correlation. At volume fractions higher than 0.5, the singularity in charge flux becomes more important as more particles are in near contact. Meredith & Tobias's correlation can in no way capture the expected rapid rise in the effective conductivity near maximum packing of a random suspension. Note also that the quadrupole result at $c = 0.6$ is below the correlation curve, which is consistent with arguments made earlier about the quadrupole slightly underpredicting the effective conductivity. The simulation results also agree quite well with their correlation for the other conductivity ratios as shown in Figures 3.4($b-c$).

Finally, the electrical conductivities of ion-exchange and non-sulphonated resins fluidized in aqueous NaCl solutions for conductivity ratios of 14400, 10, and 0 measured by Turner (1976) are plotted in Figures 3.4($a-c$). Turner's results for an infinite conductivity ratio are far above those of the simulation. From the information provided in Turner's paper we have no explanation for the large discrepancies

between his data and the simulation results and the data of Meredith & Tobias. However, for the more modest conductivity ratio of 10.0 and 0.01 the simulation results agree extremely well with those of Turner, even up to a volume fraction of 0.6. This indicates that the discrepancies at high conductivity ratios are probably not due to differences in particle configurations but rather to an unaccounted for physicochemical phenomena for charge transport associated with the extremely high conductivity ratio in Turner's experiment.

Note that in our comparison to experimental measurements, we assume that the experimental systems studied are random hard-sphere dispersions. There is, however, no necessity that this be true. The flow fields used in both experiments to disperse the particles do not guarantee random hard-sphere dispersions and could in fact create a different suspension microstructure. The excellent agreement between the simulations and the experiments indicates that either the experimental microstructures are random hard-sphere dispersions or the results up to the volume fractions reported here are rather insensitive to the exact suspension configurations. Examining the conductivities for cubic lattices reported in Chapter 2, we find that around volume fractions of 0.3 to 0.5, the sc lattice is substantially more conductive than either the bcc or fcc lattice, the latter two of which are almost equally conductive in this volume fraction range and whose particles are fairly well-spaced compared to the sc lattice. Since the bcc and fcc lattices have widely different coordination numbers and the random arrays should have a coordination number a bit less than the bcc lattice, it is reasonable to conclude that the experimental microstructure may not be exactly a hard-sphere dispersion, but is probably well-dispersed so the conductivities in either configuration are equivalent.

After this work was completed and in press, we learned that Kim & Torquato (1990) have recently developed a method to determine the effective conductivity of a random suspension from numerical simulations of random walkers. The random walkers or tracers are released in a Monte Carlo-generated random hard-sphere suspension. The tracers walk more quickly in the higher conductivity medium, and the times and mean-square displacements are recorded in the simulation. From this

information, an effective diffusivity or analogous conductivity can be determined. Our results are found to compare extremely well to those of Kim & Torquato, and in fact they use our results as a check of their method.

3.4. Conclusions

We have presented computational simulation results for the effective conductivity for random hard-sphere dispersions for particle-to-matrix conductivity ratios of $\infty, 10$, and 0.01 for volume fractions up to 0.6. These results compare extremely well to the past theoretical work of Jeffrey (1973) and Torquato & Lado (1986) as well to experimental measurements of Meredith & Tobias (1960) and Turner (1976). It is also found that the Clausius-Mosotti equation is quite accurate for conductivity ratios of 10 or less and, based on our results, it is of comparable accuracy to Jeffrey's calculations. The numerical results are representative of random hard-sphere suspensions based upon the computed radial distribution functions for the simulations. However, no effective conductivities for volume fractions near closest packing could be computed because we were unable to generate a close-pack random suspension with the Monte Carlo method. Of course, the effective conductivity of random hard-sphere dispersions near closest packing generated by other means could also be calculated with the simulation method. In fact, although we selected Monte Carlo methods for generating each realization, the effective conductivity could be calculated from configurations generated by hydrodynamic forces or any other processes. These configurations, and hence the effective conductivity, would include microstructural features arising from the particular process, which is an example of the relation of macroscopic properties of a dispersion to its past processing environment.

Table I

Summary of Simulation Conditions

c	*Monte Carlo step size, d*	*Cycles between sampling, m*	*Total number of samples*
0.05	0.25	1000	200(20)
0.10	0.25	1000	150(20)
0.20	0.15	2000	150(20)
0.30	0.10	2000	200(20)
0.40	0.10	3000	200(20)
0.50	0.02	5000	200(20)
0.60	0.01	20000	200(20)

All simulations reported here are for 32 spheres. The parenthetical values are the total number of samples using the quadrupole formulation.

Table II

Effective Conductivity - Random Dispersion of Spheres

(Dipole Formulation Only)

$\lambda_p/\lambda = \infty$

c	$\mathbf{M}^{-1}$ *only* λ_{eff}/λ ($\pm$95% *conf.*)	$\mathbf{C}$ λ_{eff}/λ ($\pm$95% *conf.*)	*Jeffrey's* $O(c^2)$ *result*	*Clausius–Mosotti Eqn.*
0.00	1.000	1.000	1.000	1.000
0.05	1.160 ± 0.009	1.162 ± 0.010	1.161	1.158
0.10	1.341 ± 0.024	1.352 ± 0.030	1.345	1.333
0.20	1.772 ± 0.053	1.821 ± 0.081	1.780	1.750
0.30	2.341 ± 0.095	2.529 ± 0.168	2.306	2.286
0.40	3.079 ± 0.120	3.590 ± 0.230	2.923	3.000
0.50	4.065 ± 0.128	4.967 ± 0.339	3.628	4.000
0.60	5.100 ± 0.098	8.853 ± 0.524	4.424	5.500

$\lambda_p/\lambda = 10$

c	$\mathbf{M}^{-1}$ *only* λ_{eff}/λ ($\pm$95% *conf.*)	$\mathbf{C}$ λ_{eff}/λ ($\pm$95% *conf.*)	*Jeffrey's* $O(c^2)$ *result*	*Clausius–Mosotti Eqn.*
0.00	1.000	1.000	1.000	1.000
0.10	1.246 ± 0.011	1.247 ± 0.011	1.240	1.243
0.20	1.540 ± 0.028	1.545 ± 0.028	1.511	1.529
0.30	1.889 ± 0.046	1.944 ± 0.046	1.812	1.871
0.40	2.300 ± 0.046	2.443 ± 0.046	2.144	2.286
0.50	2.817 ± 0.049	3.080 ± 0.053	2.507	2.800
0.60	3.589 ± 0.026	3.966 ± 0.041	2.900	3.455

Table II (continued)

Effective Conductivity - Random Dispersion of Spheres

(Dipole Formulation Only)

$\lambda_p/\lambda = 0.01$

c	$\mathbf{M}^{-1}$ *only* λ_{eff}/λ ($\pm$95% *conf.*)	*Jeffrey's* $O(c^2)$ *result*	*Clausius–Mosotti Eqn.*
0.00	1.000	1.000	1.000
0.10	0.859 ± 0.004	0.858	0.859
0.20	0.729 ± 0.005	0.727	0.731
0.30	0.600 ± 0.007	0.608	0.614
0.40	0.504 ± 0.010	0.501	0.506
0.50	0.406 ± 0.012	0.455	0.407
0.60	0.308 ± 0.005	0.297	0.316

$\mathbf{M}^{-1}$ indicates only the potential matrix invert (dipole formulation) was used for the calculation of the particle dipoles, while **C** indicates that the two-body interactions (also dipole formulation) were also included.

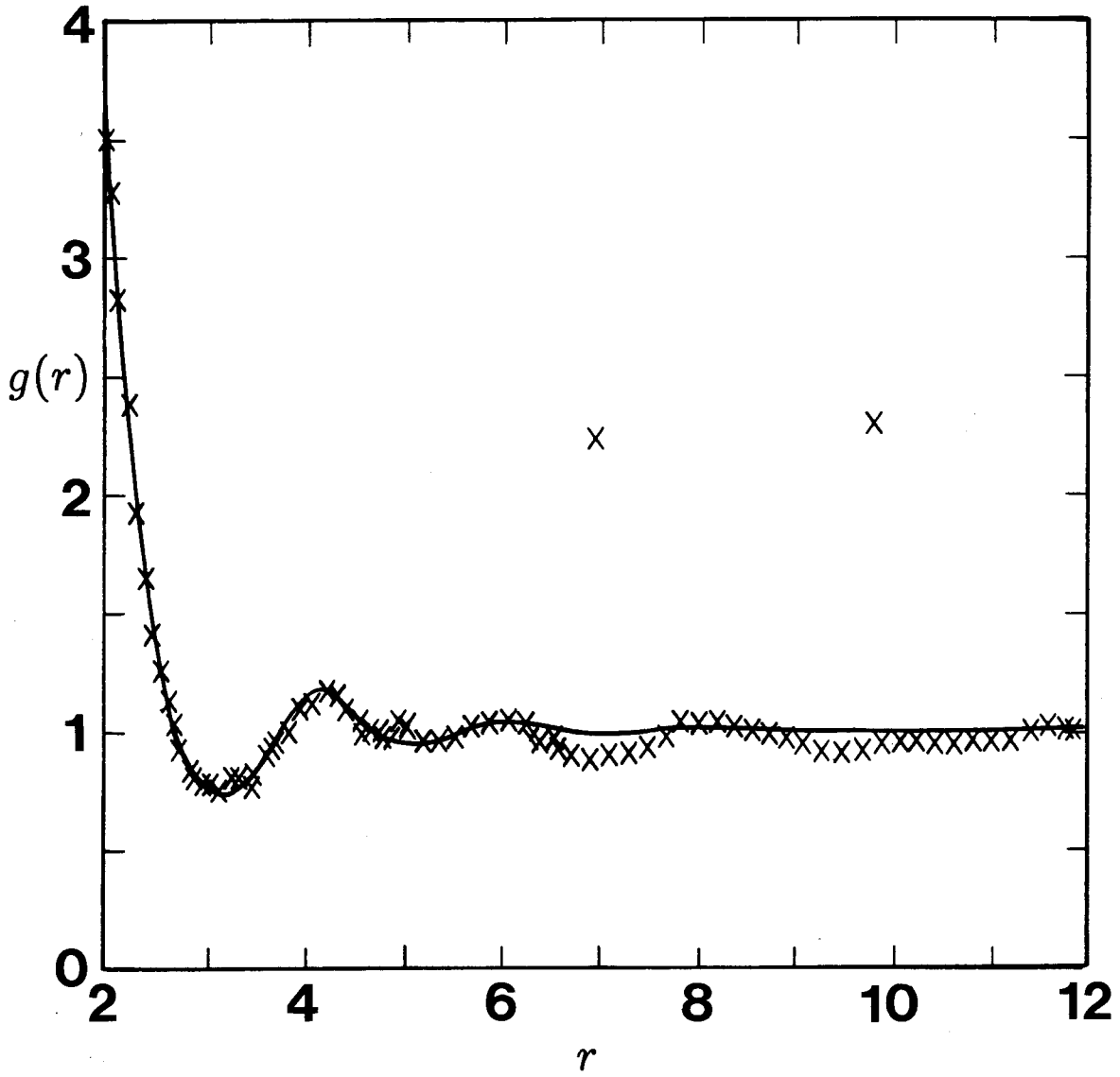

Figure 3.1*a* The exact (——) and simulation (×) radial distribution function, $g(r)$, for (*a*) $c = 0.4$, (*b*) $c = 0.5$, and (*c*) $c = 0.6$. The simulation $g(r)$ is the average of 30 realizations for 32 particles per cubic cell in an initial fcc lattice. Other details are in the text and Table I. The isolated "spikes" correspond to each sphere's periodic image, and the large, smooth deviations observed at large r for $c = 0.5$ and 0.6 correspond to the sphere positions of the initial fcc lattice.

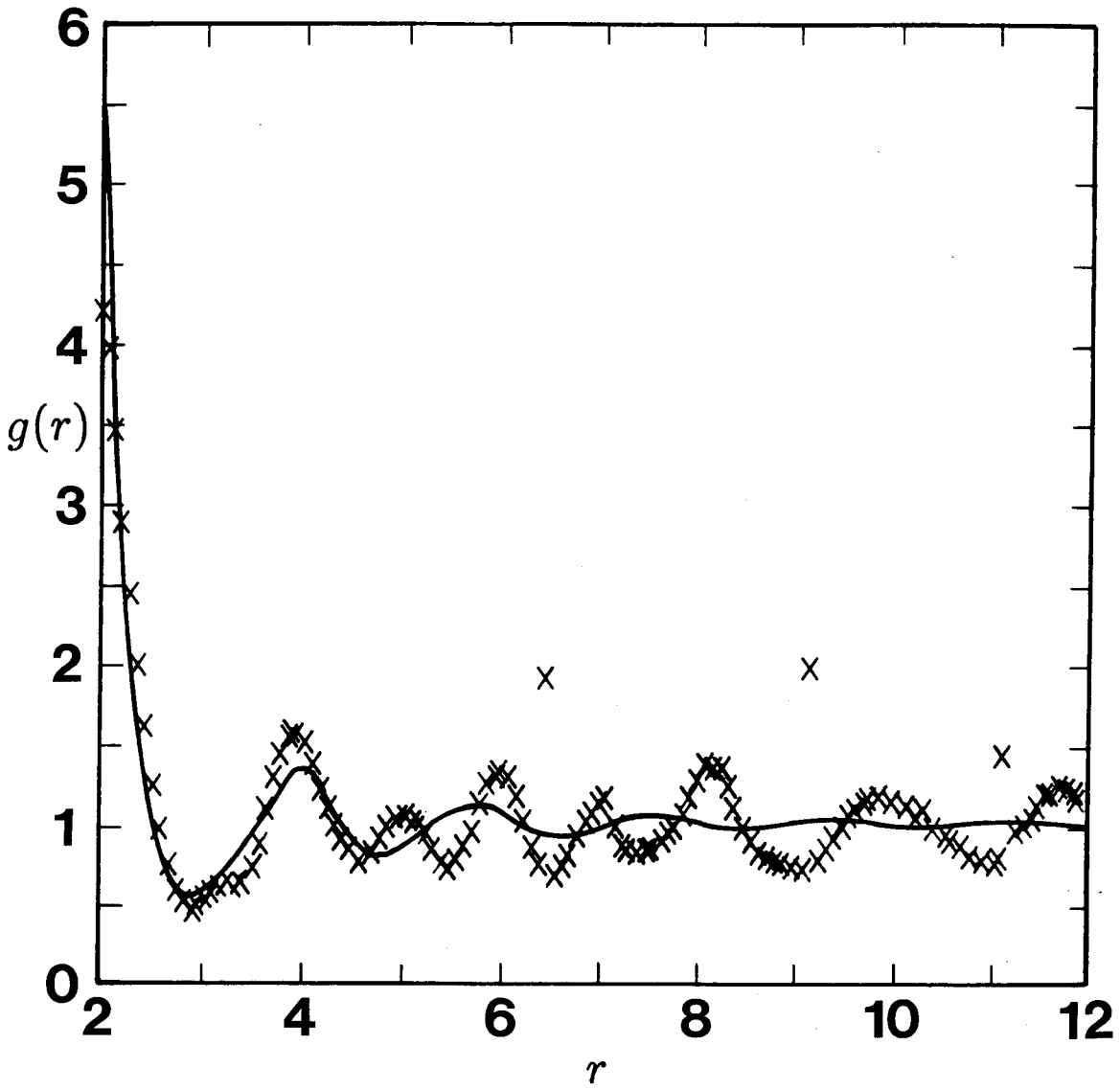

Figure 3.1*b* See previous caption.

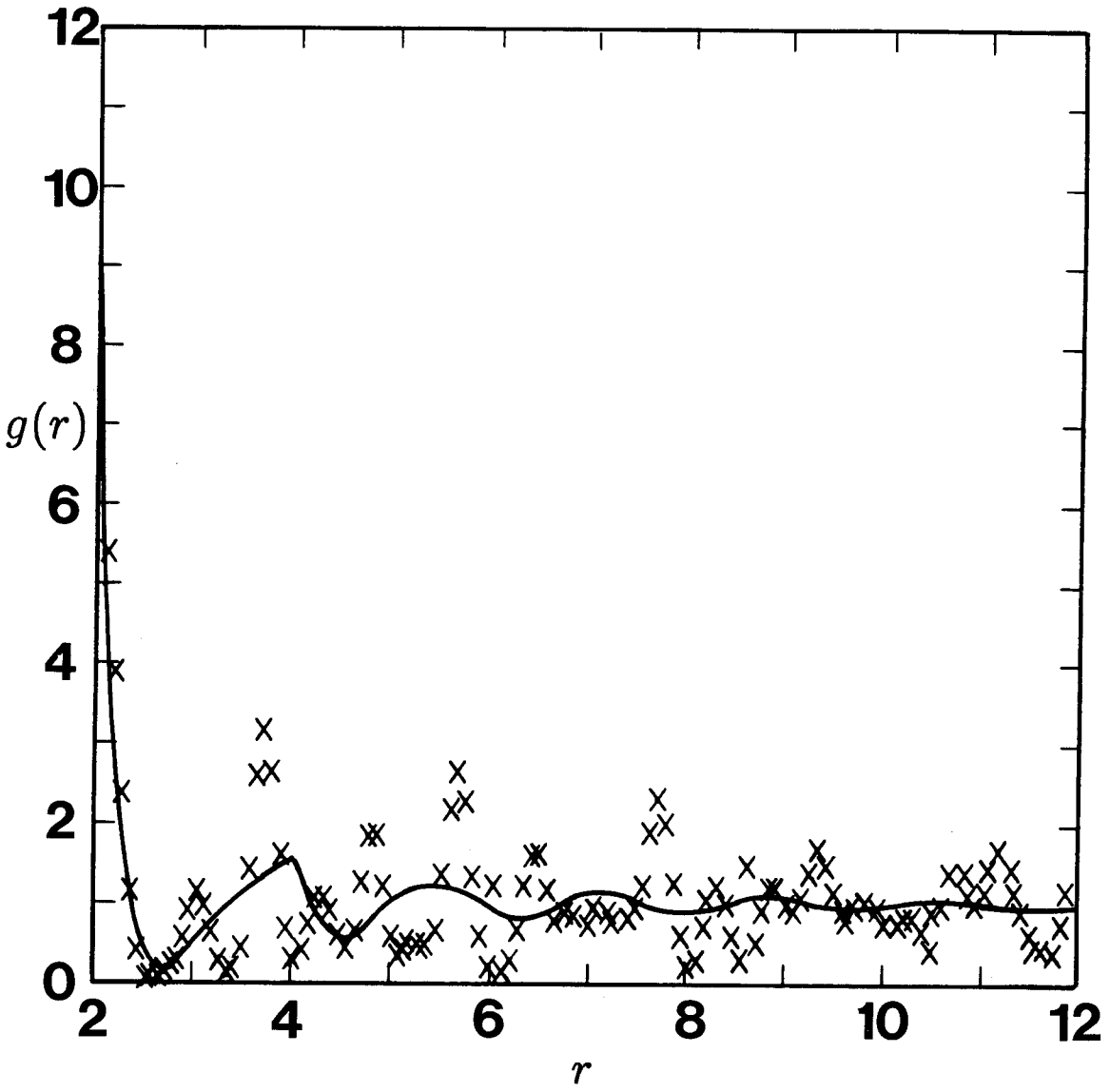

Figure 3.1*c* See previous caption.

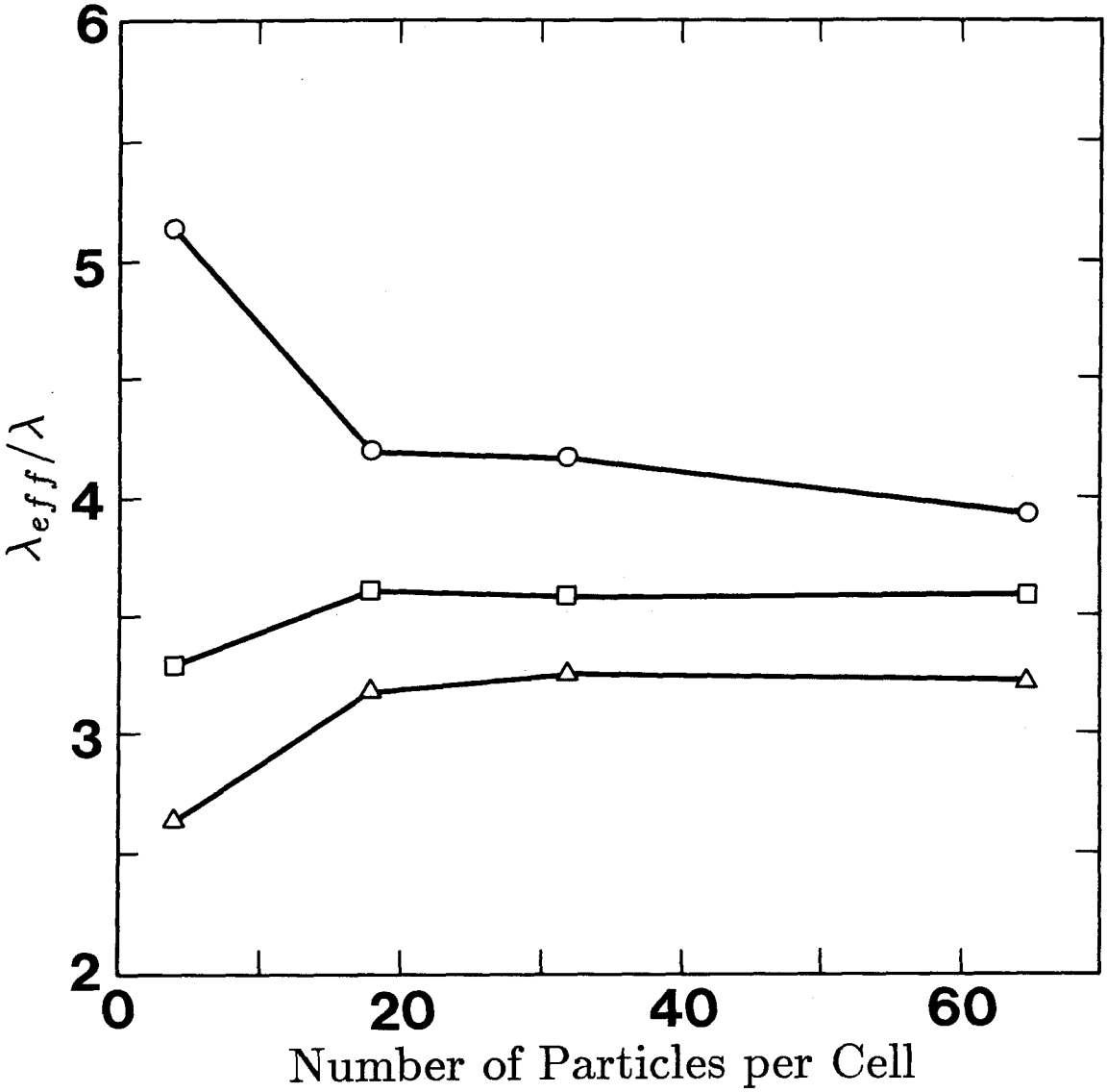

Figure 3.2 The average maximum (○) and minimum (△) and average (□) effective conductivities versus number of particles per periodic cell for $c = 0.4$. Note the effective conductivity is independent of the number of particles per cell for $N \geq 20$.

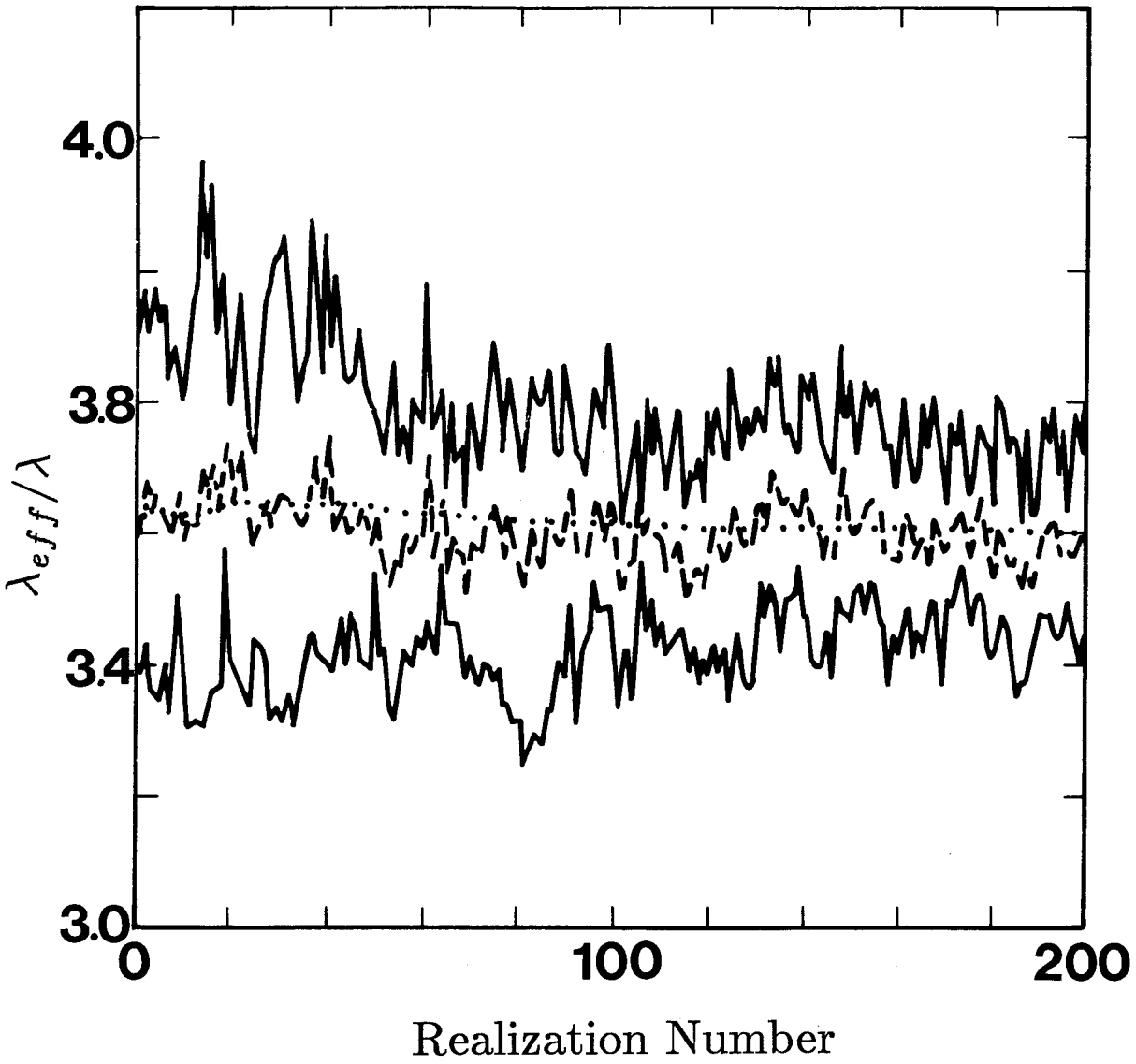

Figure 3.3 The effective conductivity versus realization number for $c = 0.4$: running (·····), current (– – –), maximum (upper ——), and minimum (lower ——) average conductivities.

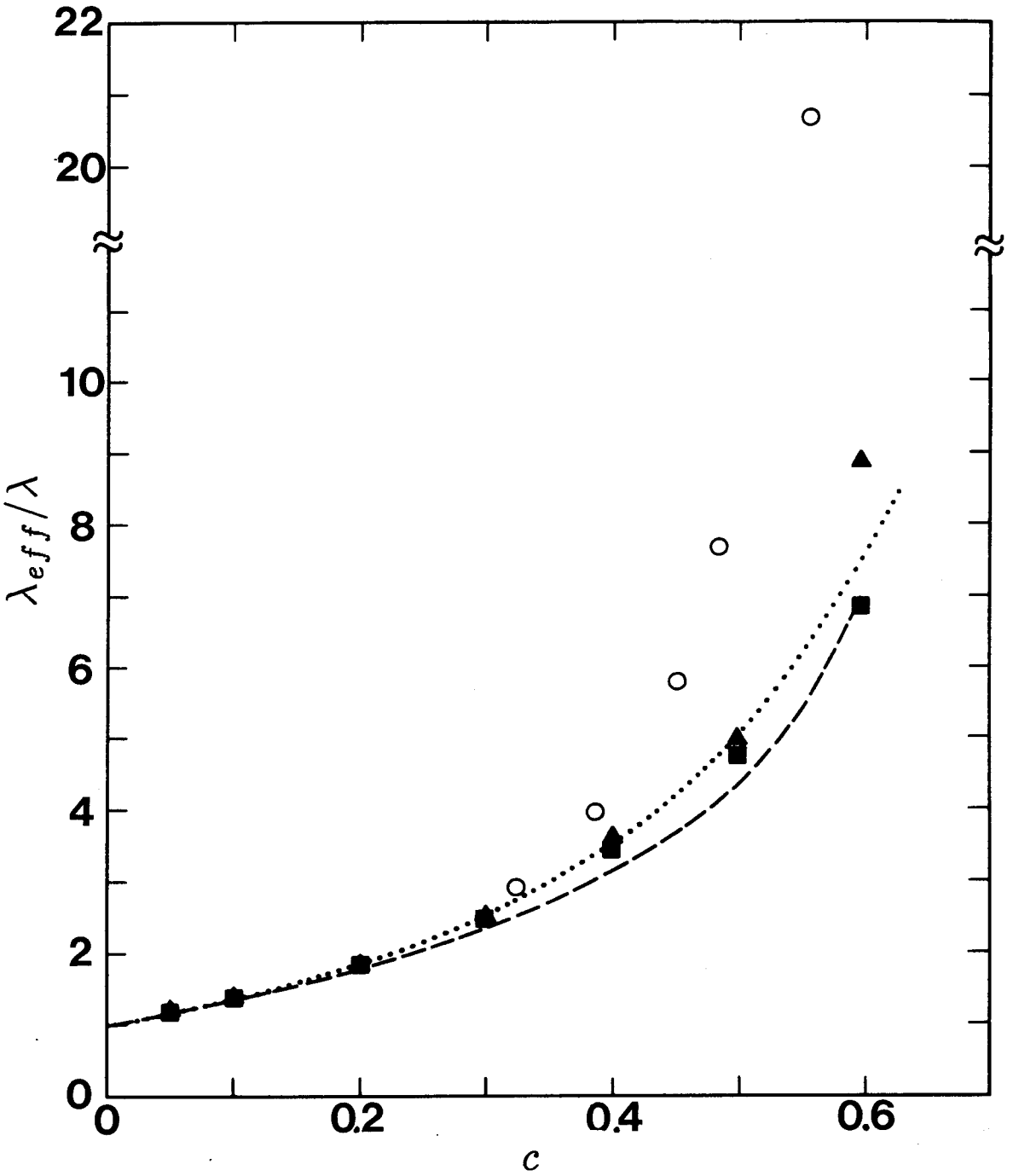

Figure 3.4*a* See next caption.

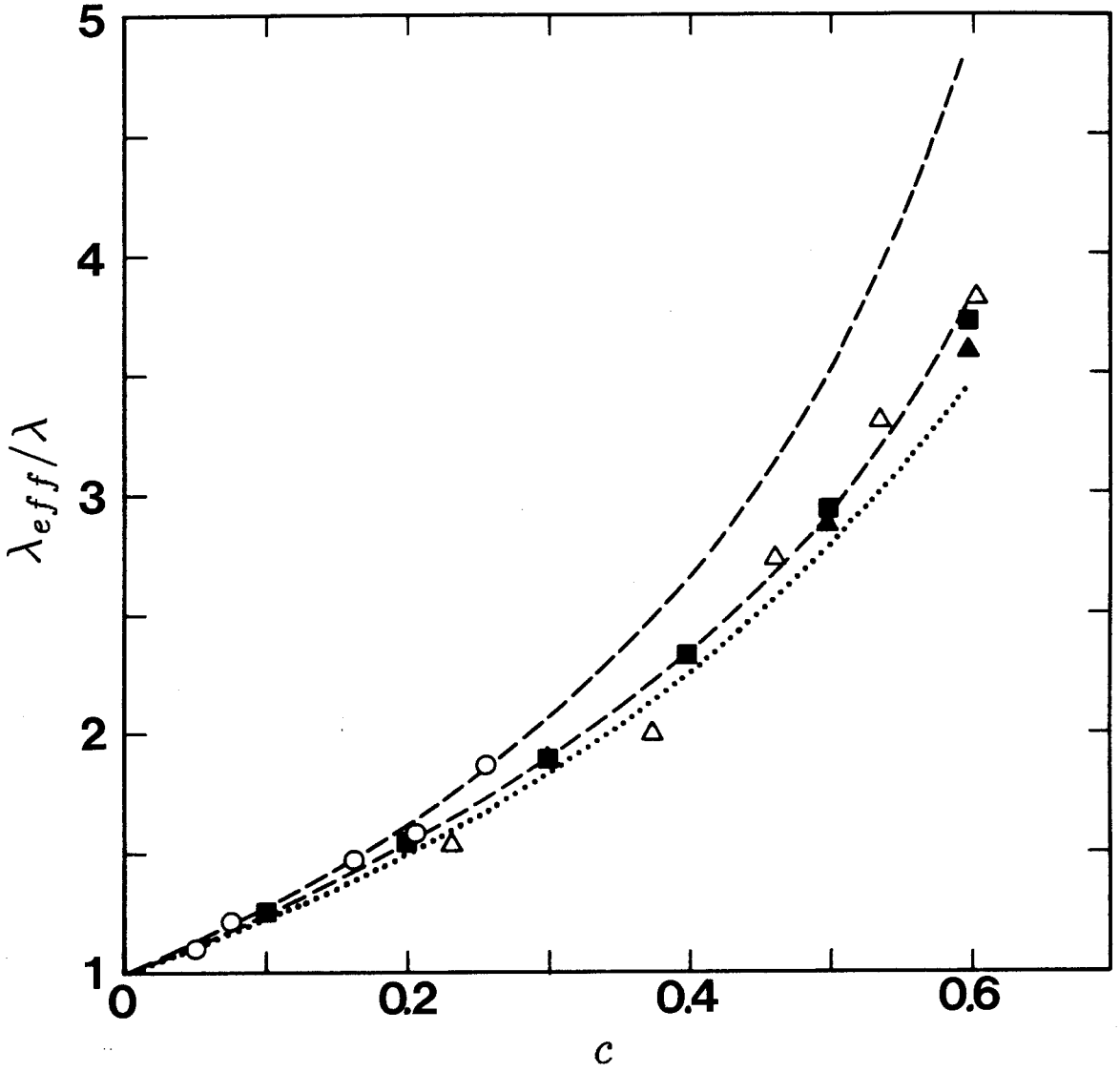

Figure 3.4*b* The effective conductivity versus volume fraction for $\lambda_p/\lambda = (a)\ \infty$, (b) 10, and (c) 0.01. In addition to the dipole ($\triangle$) and quadrupole ($\sqcup$) simulation results within this suite of figures, the upper and lower bounds on the conductivity computed by Torquato & Lado (– – – –) are shown as well as the experimental correlation of Meridith & Tobias (• • • •) and the data of Turner. The Turner data are for $\lambda_p/\lambda = 14400$ ($\circ$) in 4(a), 10.0 ($\circ$) and 10.8 ($\triangle$) in 4(b), and 0.0 ($\circ$) in 4(c). Note the break in the conductivity coordinate in figure 4(a).

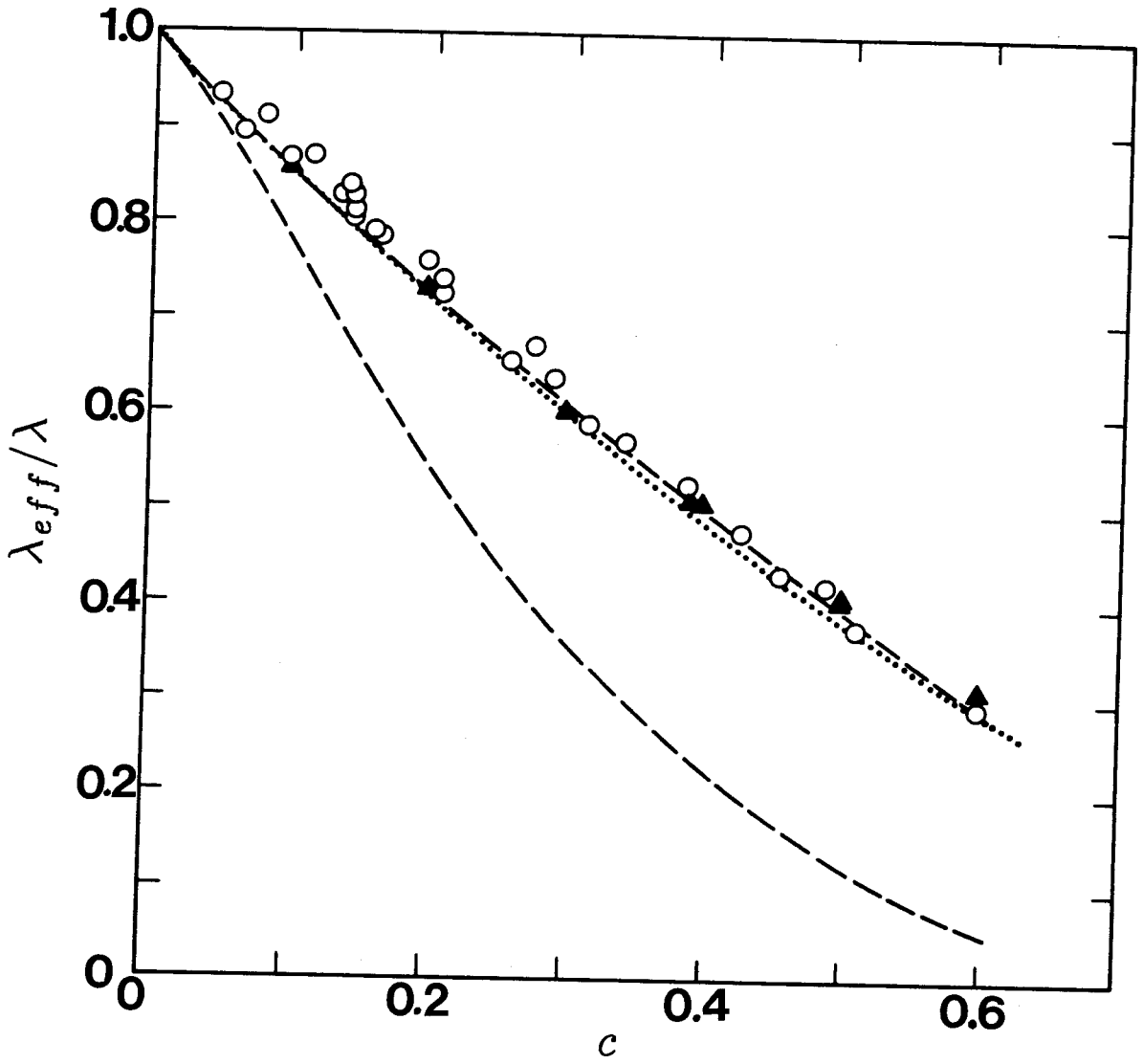

Figure 3.4c See previous caption.

CHAPTER 4

PERCOLATION OF NEARLY TOUCHING SPHERES

4.1. Introduction

Imagine a very large lattice, say simple cubic, inserted between two conducting plates each at a different potential. Initially, all the sites are occupied by insulating cubes, and one by one sites are chosen at random and replaced by a cube of finite conductivity. There will be no conduction across the gap between the plates until the percolation threshold has been reached, namely the condition when there exists one spanning or percolating cluster of conducting cubes connecting one plate to the other. For 3-D lattices filled with cubes the typical percolating threshold is at a volume fraction of about 0.29 (Scher & Zallen 1970). After this percolating threshold has been reached, the conductivity, normalized with that of a conducting cube, increases to one at a unit volume fraction of conductors. This is called a site percolation problem, since sites are either conducting or insulating. The conductivity for these numerical experiments is found to scale as $(c - c_c)^{\mu}$ when c is near the percolation threshold c_c. Previous numerical experiments have established μ at about 2.0 for three-dimensional lattices (Stauffer 1985). Reversing the procedure – starting with all conductors and replacing them by insulators – results in a retracing of the conductivity curve mentioned above–the conductivity becomes zero as the last connecting path is broken.

There are a number of variations on this experiment. One possibility is to begin with finite conductors everywhere in the lattice, and replace the sites randomly with superconductors. In this case the conductivity across the plates begins at unity and increases toward infinity as the percolation threshold is approached. Another possibility is to connect each site by the appropriate number of bonds for the lattice type where each bond is either a superconductor or conductor. This is called bond percolation. The salient features about percolation phenomena are that the conductivities change dramatically at the percolation threshold and are successfully described by power laws near this threshold.

In this brief chapter, we apply the simulation method developed in Chapter 2 to perform percolation-like experiments on cubic arrays of nearly touching, perfect conductors. Unlike the classical or "pure" percolation experiments described above, here the spherical particles are imbedded in a matrix of relatively small, but finite conductivity, so the matrix always carries some charge. From our experiments we wish to determine if continuum percolation exists without the need of artificial sites or bonds. Also, we expect the singularity in near-field effects to give rise to the percolation phenomena, but it is unclear how the many-body far-field interactions affect the percolation.

4.2 Method/Results

A simulation begins with a given lattice-type containing N spheres near but not quite at the lattice closest packing. The collection of spheres was periodically replicated throughout all space. Then, one by one, a sphere, as well as all its periodic images, was removed at random from the lattice of the cell. After each sphere removal, the conductivity of the system was computed according to equation (3.8). Note that this procedure is equivalent to adding spheres one by one at random to a lattice site and to its periodic images.

These percolation-like simulations were performed for a variety of lattice types, number of particles per unit cell, and initial volume fractions. We found that the initial volume fractions needed to be extremely close to maximum packing in order to observe percolation behavior. Indeed, gap widths, ϵ, of 10^{-10} to 10^{-99} are required to observe a rapid increase in the conductivity at the percolation threshold (recall that $\epsilon = 1 - (c/c_{max})^{\frac{1}{3}}$). These very small initial separations give very large initial effective conductivities up to approximately 1008 for $\epsilon = 10^{-99}$, because of the logarithmic singularity. Before presenting the results for these extremely small separations, we present the results for those simulations with more modest separations and discuss their qualitative features. We do this because the percolating and non-percolating systems do share many common qualitative features and any "real" system will probably have these more reasonable gap widths.

In Figure 4.1 the average effective conductivity is plotted versus the volume fraction for three simulations on a face-centered cubic lattice of 108 spheres with initial volume fractions of 0.7404, 0.7403, and 0.7400, which correspond to $\epsilon = 3.6 \times 10^{-5}, 3.1 \times 10^{-5}$, and 2.2×10^{-4}, respectively. Recall that the densest packing volume fraction for spheres in an fcc lattice is $\sqrt{2}\pi/6 \approx 0.7405$. There is always a relative effective conductivity of at least one since the matrix has a finite conductivity. Higher initial sphere volume fractions have higher initial effective conductivities since the spheres are nearer closest packing. As the volume fraction decreases, the effective conductivity decreases, but not along the curve of the effective conductivity of a regular fcc lattice. Until a volume fraction of about 0.1, the conductivity of

each simulation is greater than that of the regular fcc lattice.

This last observation is explained by considering how the volume fraction is varied for the two configurations. For the regular fcc lattice, the volume fraction is decreased by increasing the lattice size, moving each sphere apart from one another, thus decreasing the dipole moment of each sphere and the effective conductivity of the medium. For the percolation experiments, the volume fraction is decreased by removing one sphere from the lattice, after which there still remains many spheres near-closest packing with large dipoles. The decrease in the effective conductivity for the percolation experiments, as will be shown, is due to the loss of approximately two sphere dipoles per sphere removed rather than a decrease in all the dipoles. From another point of view, the expansion of the regular fcc lattice ruptures all the efficient conduction paths simultaneously, while the one by one sphere removal in the percolation experiments leaves some of these efficient paths intact. Thus, the percolation experiments decrease in conductivity less rapidly than a fcc lattice with decreasing volume fraction. The conductivities of the two configurations are equal below a volume fraction of 0.1 since the conductivity is independent of configuration at small volume fractions.

For volume fractions between 0.1 and about 0.5, the conductivity fluctuates as it decreases with volume fraction. These fluctuations are attributed to the fact that there are a finite number of particles in the experiments. The removal of one sphere can destroy an efficient conductivity path created by a cluster of spheres, decreasing the conductivity significantly. However, the dangling end or dead branch of a cluster or an isolated sphere might be eliminated by the removal of a sphere, which would cause a relatively small decrease in the conductivity. So, when a sphere is removed, or the volume fraction is decreased, the conductivity will decrease by a large or a small amount depending upon which sphere is chosen, resulting in fluctuations. The magnitude of these fluctuations will increase with decreasing number of particles in a cell, since the average sphere dipole is more sensitive to a loss of sphere when there are few spheres in the cell initially. This is illustrated in Figure 4.2 for 32, 108, and 256 spheres all with initial volume fractions of 0.7400. Note that the

conductivities match closely for volume fractions exceeding 0.5. Also note that the effective conductivity decreases slightly with increasing N in the range of 0.2 to 0.5 volume fraction. This result is more pronounced when we examine the more severe gap widths.

The curves in Figure 4.1 appear self-similar, at least at large volume fractions. This fact suggests normalizing the effective conductivity and volume fraction by,

$$\lambda_n = \frac{\lambda_{eff} - 1}{\lambda_i - 1} \tag{4.1}$$

and

$$c_n = c/c_{max}, \tag{4.2}$$

respectively. Here, λ_i is the effective conductivity at the initial volume fraction and c_{max} is the closest packing sphere volume fraction. The normalized conductivity and volume fraction span the interval [0,1] typical of the percolation experiments described in the beginning of this section.

Figure 4.3*a* is a plot of the normalized conductivity versus volume fraction for ϵ ranging from 10^{-4} to 10^{-99} for 108 particles in an fcc lattice. The curves plotted are the averages of three simulations for each gap width. The inset more clearly shows the definite transition in the rate of increase in the conductivity with volume fraction at $c_n \approx 0.2$ for $\epsilon \leq 10^{-10}$, which is very close to the accepted value of 0.195 for an fcc lattice (Stauffer 1985, Scher & Zallen 1970). For greater values of the gap width no similar transition is observed. Figure 4.3*b* is the log-log plot of the data in Figure 4.3*a*. It even more clearly shows the transition at $c_n = 0.2$ for $\epsilon = 10^{-10}$ and 10^{-99}, but not for 2.2×10^{-4}. Note also that the data in Figures $4.3(a - b)$ collapse onto a single line for all $c_n \geq 0.6$. The results for simple and body-centered cubic lattices, although not shown here, exhibit qualitatively similar behavior, except that the transition occurs near the accepted normalized volume fractions of 0.31 and 0.24 for sc and bcc lattices, respectively.

Even for the normalized volume fractions less than the percolation threshold value, the normalized conductivity is non-zero. This is due to the fact that even

an isolated sphere or cluster of spheres contributes its dipole to the effective conductivity since the matrix conductivity is non-zero. Realize also that these isolated spheres or clusters also influence the dipoles of other clusters and the percolating cluster or clusters due to the long-range nature of their interactions. So although we do not observe a vanishing conductivity as in "pure" percolation experiments, we note that the contribution of the dangling ends and clusters does not remove the percolative behavior, at sufficiently small gap widths, indicated by the abrupt change in rate of increase in the conductivity at the percolation threshold. Similar types of percolation have been observed by Kirkpatrick (1971) who performed percolation experiments on networks of resistors. Instead of changing the resistors to perfect insulators one by one, he changed the resistivity of each resistor one at a time. Kirkpatrick observed no percolation transition until a resistance ratio (the ratio of the "insulating" resistance to the "conducting" resistance) of 10^{-2}, where he also considered an abrupt change in the rate of increase of conductivity as an indication of percolation. In fact our simulations are quite similar to those of Kirkpatrick. Although the spheres are perfect conductors, they do not touch each other, so an occupied site is really a perfectly conducting sphere imbedded in a cube of finite conductivity. The removal of a sphere from a site can be thought of as replacing a low-resistance material with a much higher resistance material. Arguably from Figures 4.3$(a-b)$, the percolation transition no longer occurs for $\epsilon \geq 10^{-10}$ which corresponds to a matrix-to-fcc lattice conductivity ratio of 1/98.2 or about 10^{-2}.

The slope of the normalized conductivity or the rate of its increase at $c_n = 1$ is called the *vulnerability*, (Blanc & Guyon 1983). We measured vulnerabilities of 2.47, 2.30, and 2.22 for simple, body-centered and face-centered cubic lattices, respectively. Ottavi, *et al.* (1983) found the correlation

$$K = \frac{2z-2}{z-2} \tag{4.3}$$

to fit the vulnerability computed from numerical percolation experiments (using resistors and insulators) in two and three dimensions for a number of different lattice

types. Here z is the coordination number of the lattice. From this correlation the vulnerability is expected to be 2.50, 2.33, and 2.20 for $z = 6$, 8, and 12 for sc, bcc, and fcc lattices, respectively, indicating the vulnerability decreases with coordination number. Our results appear to match their correlation quite well. In the percolation experiments the loss of a neighboring sphere means the loss of one of the conduction paths. The more nearest neighbors a sphere has the less vulnerable it is to the loss of a path.

In Figure 4.4 we plot the normalized conductivity for fcc lattices at initial gap widths of $\epsilon = 10^{-99}$ for three percolation experiments with 108 spheres initially and a single experiment for 256 spheres in the initial lattice. In all the lattices, the conductivity decreases with increasing system size for normalized volume fractions in the range $c_c < c_n < 2.5c_c$. Unfortunately, additional percolation experiments with larger system sizes were not attempted because the computations became prohibitively time consuming (the execution time grows as N^3), so it is not known if the shape of the conductivity curve around the percolation threshold remains constant above some value of the system size. In fact Stauffer (1985) notes that the conductivity *at* the percolation threshold scales as approximately $L^{-2.2}$, where L is the distance between electrodes in the classical percolation experiments, so the effect may persist beyond the percolation threshold, though not for normalized volume fractions near unity.

As mentioned earlier, previous numerical percolation experiments have shown that the normalized conductivity can be fit by a power law of the form $\lambda_n = A(c_n - c_c)^\mu$ near the percolation threshold. Due to the our limited system size, there is not enough data to determine the power law exponent near the percolation threshold. As Figure 4.3*b* shows, however, the conductivity can be fit with a power law near $c_n = 1$. Knowing the vulnerability and that $\lambda_n = 1$ at $c_n = 1$, we find the exponent,

$$\mu = K(1 - c_c) \tag{4.4}$$

and the premultiplier

$$A = 1/(1 - c_c)^\mu. \tag{4.5}$$

Using the values of K and c_c quoted earlier, μ and A are 1.70 and 1.88 for the sc lattice, 1.75 and 1.62 for the bcc lattice, and 1.79 and 1.47 for the fcc lattice, respectively. In Figure 4.4 we plot the normalized conductivity for the fcc lattice with the just derived premultipliers and exponents in the power law equation. For all lattice types the power law formula appears to correlate the data well for normalized volume fractions exceeding 0.5, where the number of particles per periodic cell is not important, however the comparison is not so good near the percolation threshold. The power law formula results lie somewhere between the percolation data for 108 and 256 spheres near the percolation threshold. Since the vulnerability and the normalized conductivity near a normalized volume fraction of unity are not system size dependent, but the conductivity around the percolation threshold appears to be system size dependent, it does not appear that a single power law can accurately correlate all the conductivity data above the percolation threshold.

4.3. Conclusions

In closing, since no boundaries are necessary in observing the percolation, it can be concluded that percolation is a true material property. One should also note that the percolation can be obtained using the standard "definition" of effective conductivity given by (3.8), which is the traditional starting point for effective medium theories; no "special" approach is necessary. The observation of percolation depends, however, on the relative importance of near to far-field interactions and on the "connectivity" of the microstructure. The connectivity comes through the formation of the capacitance matrix and the near-field lubrication-like singularities. For the conducting problem examined here the near-field effects scale as $\ln\epsilon$ which is a very weak singularity, hence requiring very small gap widths for percolative behavior to occur. These gap widths are probably not physically reasonable since sintering of the particles, local melting, etc. may occur, changing the microstructure of the two-phase material. Also the effects of particle roughness probably become important on these length scales and possibly change the nature of the singularity for the near-field interactions. Percolation behavior, however, can be obtained at more reasonable gap widths for systems with long-range particle interactions, but with stronger near-field singularities. In hydrodynamics, for example, the stress transmission scales as $1/\epsilon$, so we may estimate that gap widths of only about 10^{-3} are necessary to observe percolation-like behavior. In general the more singular the nature of the near-field interaction, the more the system behavior will be dominated by percolation phenomena.

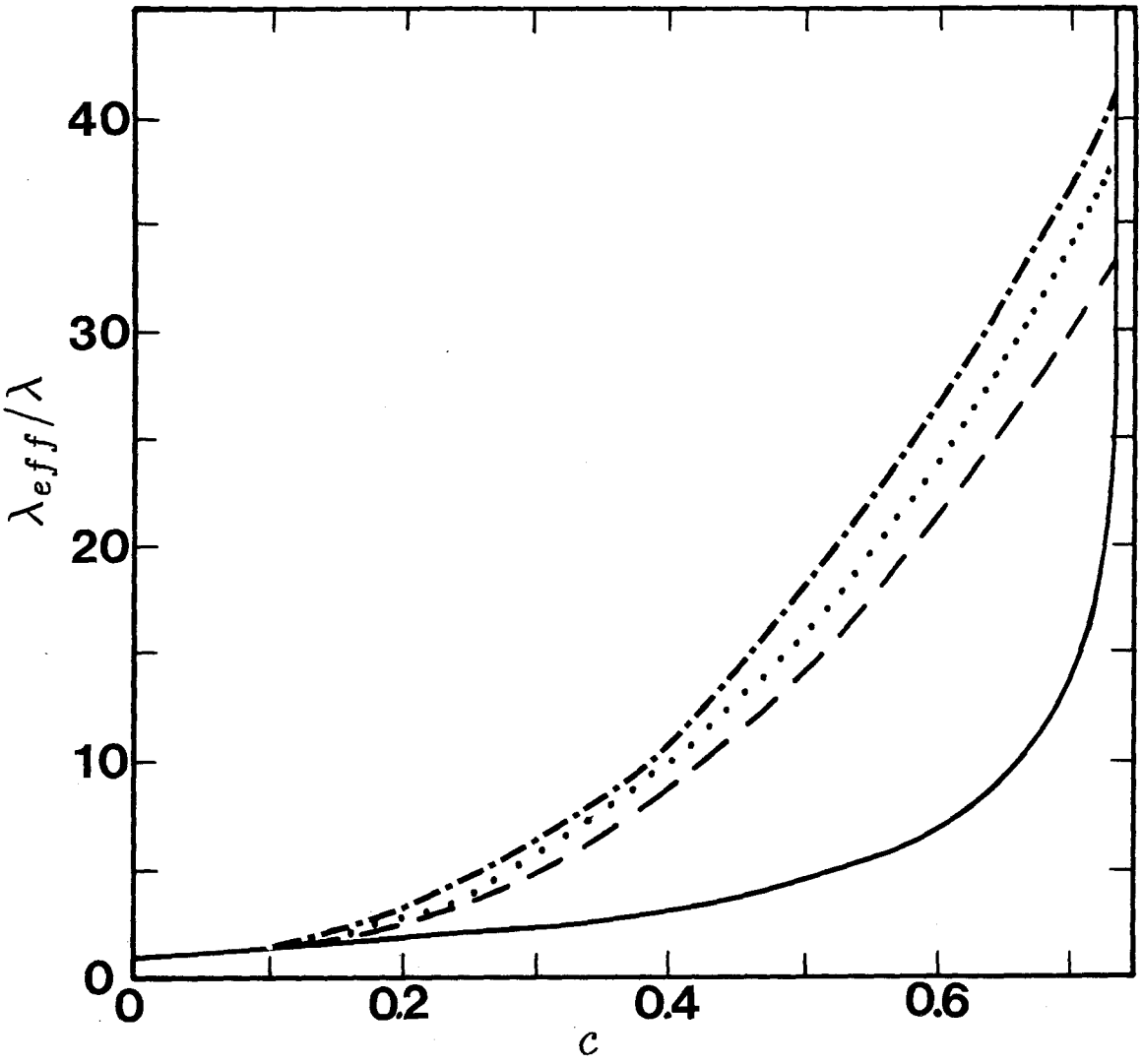

Figure 4 .1 The effective conductivities versus volume fraction for the percolation-like experiments for a face-centered cubic lattice with originally 108 spheres and c_i = 0.7404 (— · —), 0.7403 (· · · ·), and 0.7400 (– – –). The computed conductivity of a regular fcc lattice (———) is also illustrated.

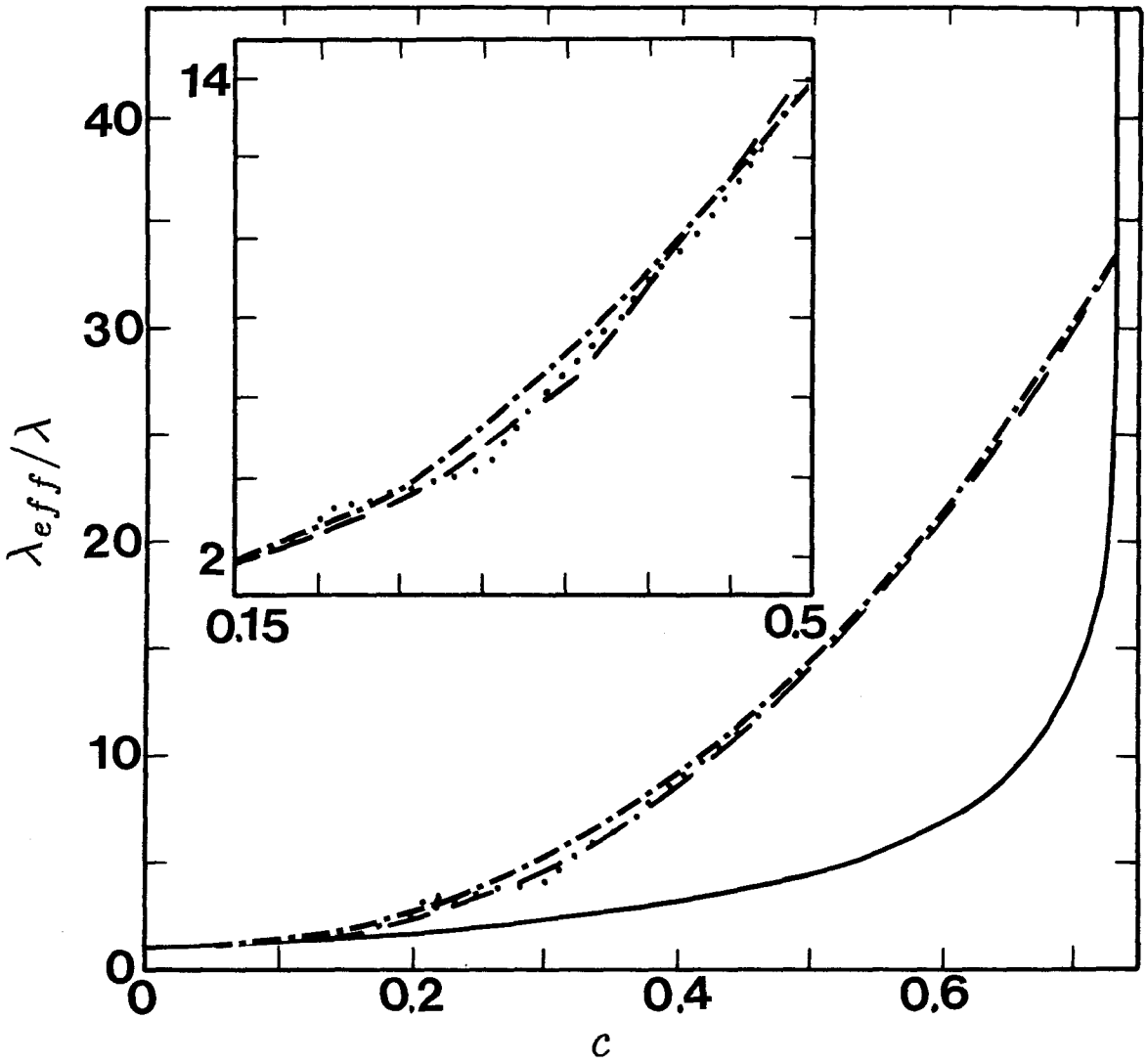

Figure 4.2 The effective conductivity versus volume fraction for $c_i = 0.7400$ and $N = 32$ (· · · · ·), 108 (- - - -), and 256 (— · —). The inset magnifies the region of fluctuations between $c = 0.15$ and 0.5. The fluctuations appear more pronounced the fewer the number of particles per cell. The computed conductivity of a regular fcc lattice (———) is also illustrated.

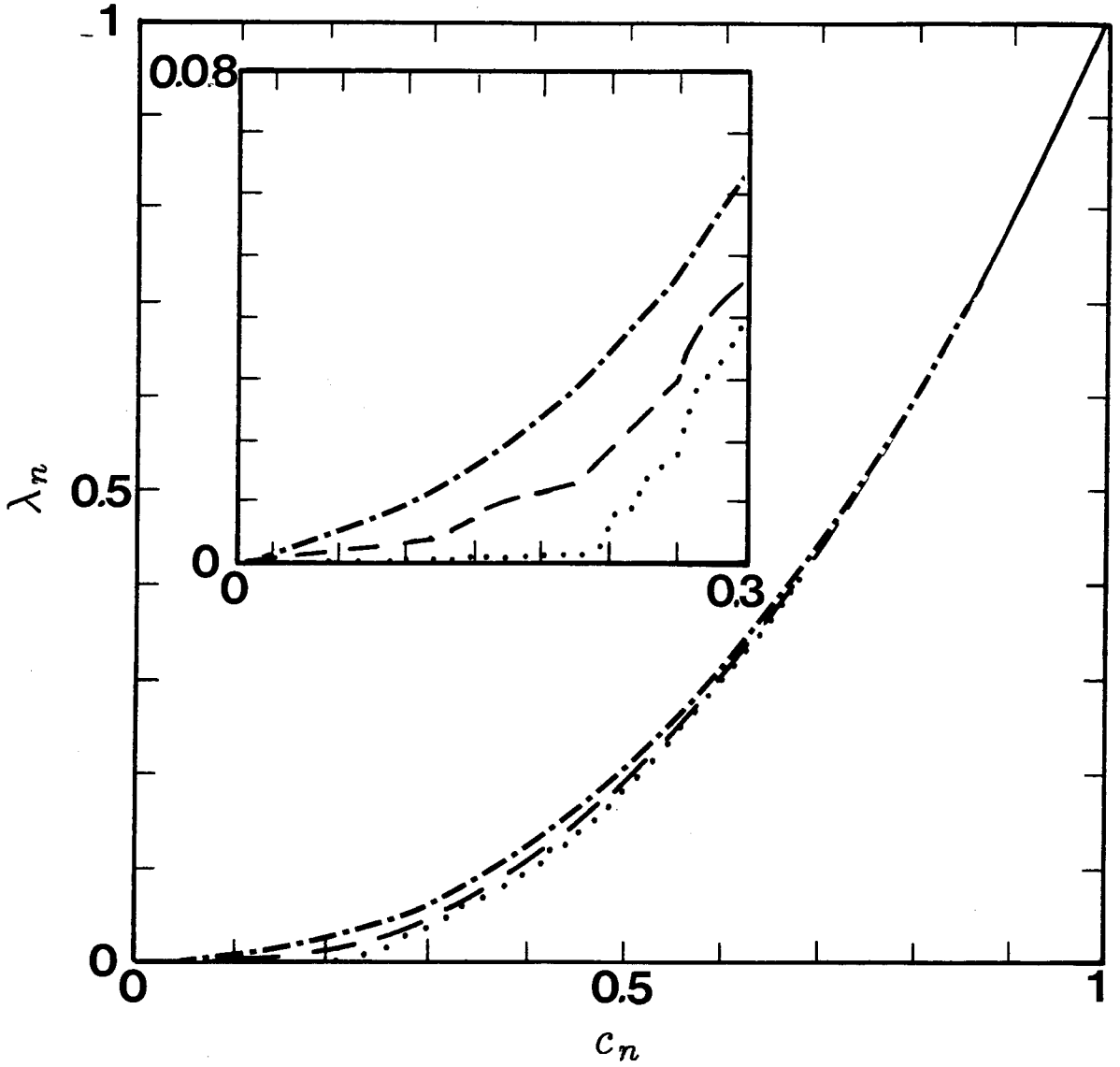

Figure 4.3*a* A linear (*a*) and log-log (*b*) plot of the normalized effective conductivity versus the normalized volume fraction as defined in equations (12) and (13) for an fcc lattice of 108 particles per cell and gap widths $\epsilon = 10^{-4}(\text{—·—}, \circ), 10^{-10}(\text{– – –}, \triangle)$, and $10^{-99}(\cdots\cdots, \square)$. The log-log plot clearly shows the percolative transition for $\epsilon \leq 10^{-10}$.

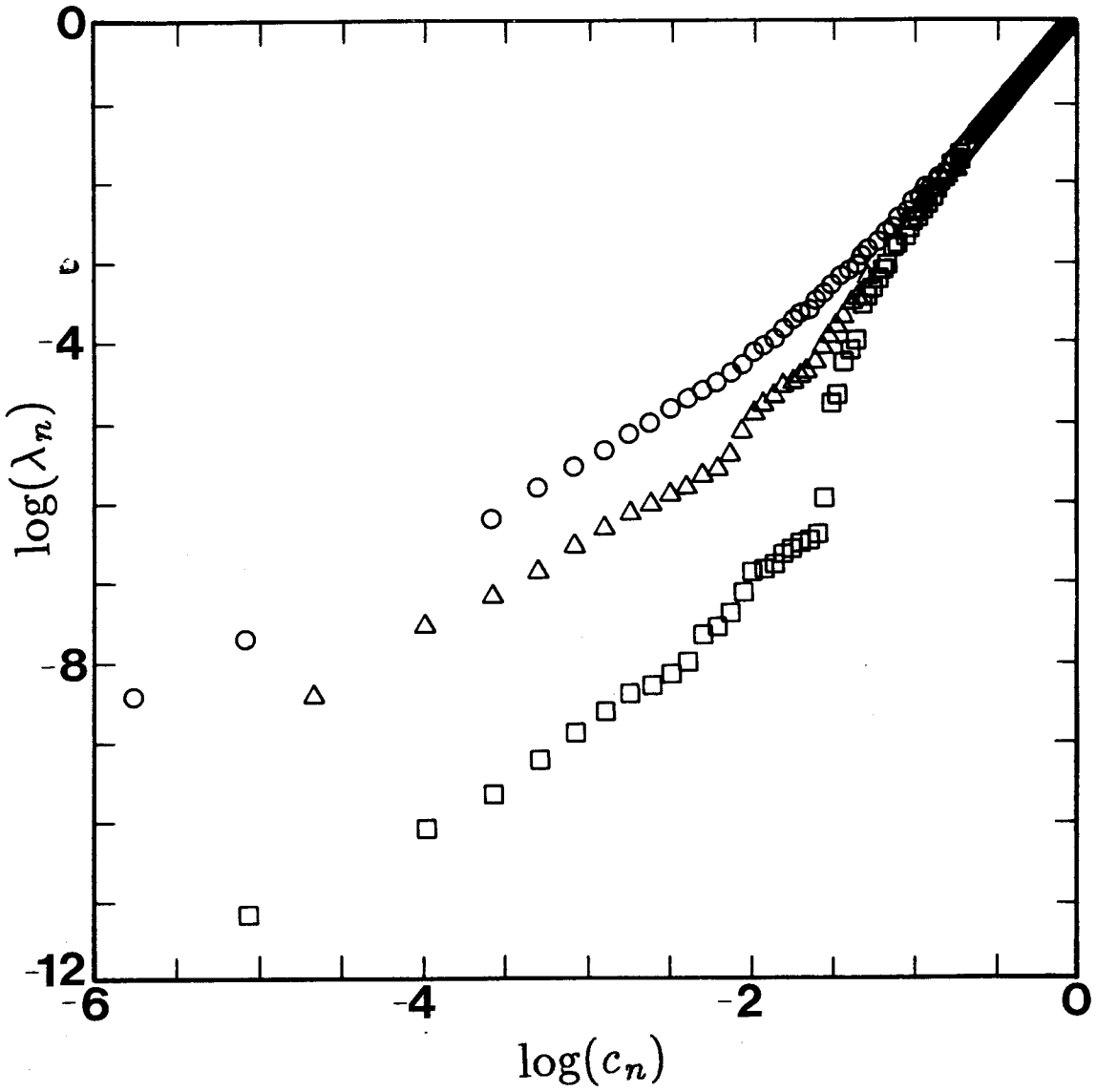

Figure 4.3*b* See previous caption.

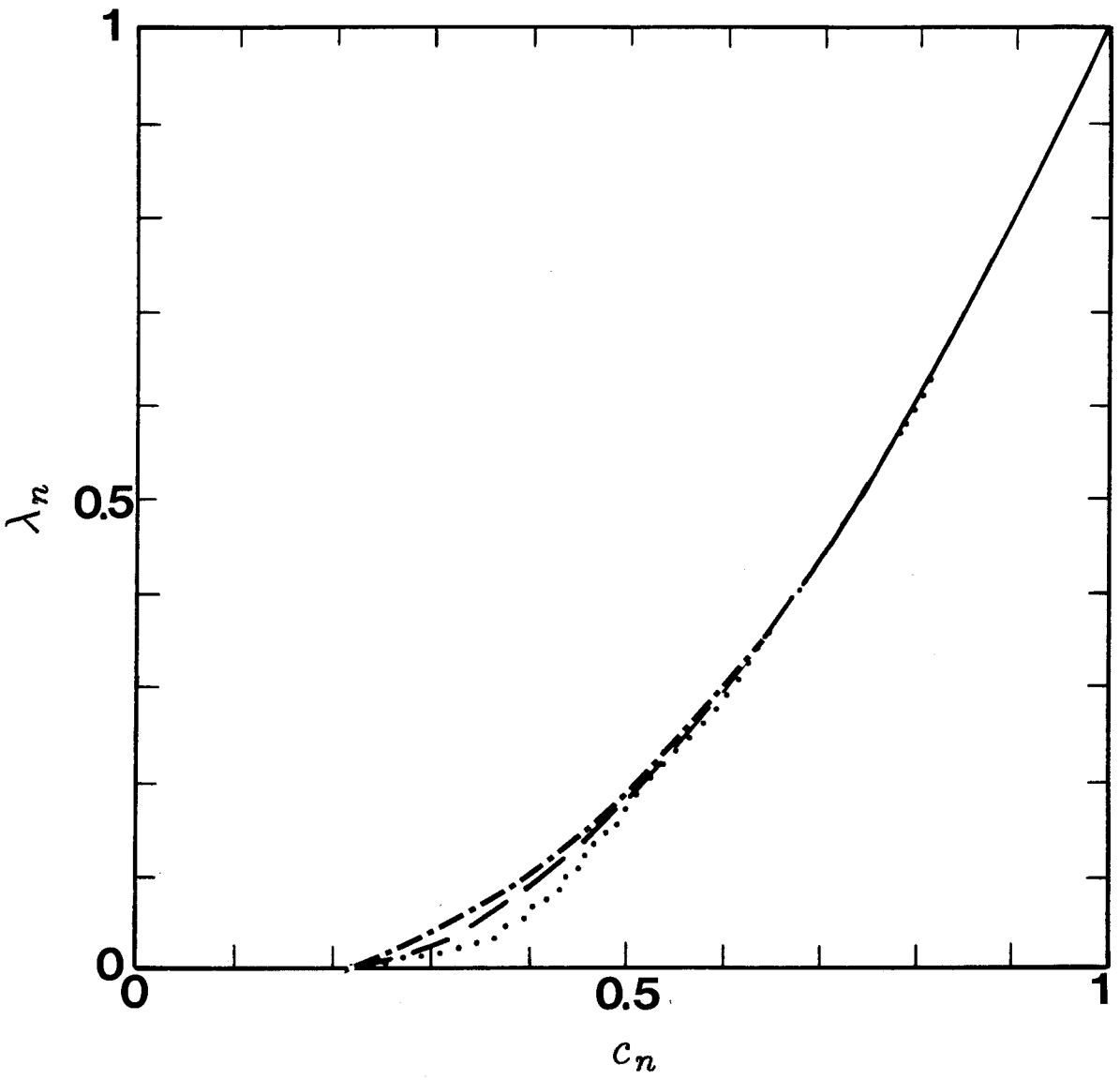

Figure 4.4 The normalized effective conductivity versus the normalized volume fraction for fcc lattices with 108 (—• —) and 256 (• • • •) spheres initially per periodic cell. In both cases $\epsilon = 10^{-99}$. The data for 108 spheres is an average of three percolation simulations and the data for 256 spheres is from a single simulation. The power law (— — —) and its parameters are described in the text.

CHAPTER 5

EFFECTIVE REACTION RATE IN A SUSPENSION OF SPHERICAL TRAPS

5.1 Introduction

Diffusion-limited reactions are common to many kinetic systems including suspension polymerization, growth of aerosol or colloidal particles, and the combustion of liquid drops, to name only a few. In these systems, the effective reaction rate is essentially determined by the time scale for the reacting species to diffuse to one another, rather than the time scale for the species to overcome an activation energy barrier. Typically, one of the reacting species is much larger and less mobile than the other reactant, for example, as in the case of the suspended polymer and reactive monomer. In these situations one of the reactants is effectively a static trap, and the time scale is determined by the mobile reactant diffusion coefficient. The concentration of the traps, however, also influences the effective reaction rate because of the competition among them for the mobile reactant. It is our aim to determine the effective reaction rate for spherical traps over a wide range of sphere volume fractions for random and periodic systems.

To determine the effective reaction rate one needs the relationship (ratio) of the average flux into a trap to the average mobile reactant concentration. The method developed in Chapter 2 allows us to directly determine this relationship in the context of electrostatic, which is mathematically analogous to the problem at hand. The method is based upon multipole scattering and properly handling the long-ranged, conditionally convergent interactions among an infinite collection of particles. The method can be used for both random and non-random dispersions.

Smoluchowski (1916) first computed the infinite dilution or non-interacting traps effective reaction rate by considering a single spherical particle in an unbounded fluid. In the last 15 years a great deal of effort has been devoted to include the effects of interactions among the traps. Lebenhaft and Kapral (1979) first used a monopole expansion for spheres on simple and face-centered cubic lattices. They quantitatively determined the correct $c^{1/3}$ scaling (where c is the trap

volume fraction) for the first correction to the rate constant. Their results, however, incorrectly show the effective reaction rate diverging at $c \approx 0.17$, a physically unreasonable result. As we shall show, the divergence is due to the neglect of the average irreducible quadrupole and the source distribution in the fluid phase necessary for a steady-state formulation of the problem. Recently, Venema and Bedeaux (1989) have computed the exact effective reaction rate for cubic lattices using a spherical multipole expansion. At closest packing they found up to 50 moments were required to achieve accuracy to five significant figures.

Felderhof and Deutch (1976) used the multipole approach through the dipole level with two-particle ensemble averaging to determine the first correction to Smoluchowski's equation for a random dispersion of spherical particles. Most notably, they found the reaction rate scaled as $c^{1/2}$ rather than $c^{1/3}$ as seen in periodic systems. The $c^{1/2}$ correction can also be found by determining the flux into a single reactive sphere in the electrostatic analog of a Brinkman medium. Muthumukar & Cukier (1981) extended this work to include higher moments but for penetrable spheres. Muthumukar (1982) has also developed an effective medium theory for random systems.

Recently, direct numerical simulations have been used to determine the effective reaction reaction rate for infinite systems of spherical sinks. Lee, Kim, Miller, and Torquato (1989) and Zheng and Chiew (1989) calculate the reaction rate as the inverse of the average time for tracer particles representing the reactant to randomly walk to one of many randomly placed static traps. The arrival times are averaged over a number of initial starting positions and trap configurations. Both research groups' results compare quite well and are consistent with the lower bounds established by Torquato (1986). Miller and Torquato (1989) have performed similar numerical simulations for suspensions of bidispersed traps.

In this chapter we shall use our method on infinite random dispersions of spherical traps. Here, we shall only employ up to the quadrupoles in the multipole expansion but shall also directly include the exact near-field two-body interactions to see if this method is as successful for computing the effective reaction rate as it has

been for computing the conductivity in Chapters 2 and 3. In §5.2 we briefly outline the method and determine explicitly the form of the lower order corrections for cubic lattices. In §5.3 we apply the method to infinite, random dispersions modeled as periodically replicated cells of Monte Carlo generated configurations of a finite number of spheres. We then compare our results to some of the above referenced work and to Brinkman-like effective medium theories.

5.2. Method

We formulate the problem as an infinite dispersion of static, non-penetrable, spherical particles of radius a immersed in a matrix. A very fast reaction occurs on a sphere surface with a reactant whose concentration at a position $\mathbf{x}$ is denoted by $\phi(\mathbf{x})$. The reactant has diffusivity D in the matrix phase and D_p in the particle phase. Further, to ensure a steady-state, there is some reactant source distributed throughout the suspension. The effective reaction rate is then defined as the ratio of the total reactant consumed per unit volume by the traps (or produced per unit volume in the suspension) to the suspension average concentration of the reactant. The average rate of consumption of reactant, r, is thus given by $r = k_{eff}\langle\phi\rangle n$, where k_{eff} is the effective reaction rate, $\langle\phi\rangle$ is the volume average concentration of the mobile reactant, and n is the number density of particle traps.

Effectively, we must solve Poisson's equation in the matrix and particle phases with the usual continuity of concentration and flux at the particle surfaces. We need, however, only the average particle flux and the average concentration rather than the detailed concentration field. Because the Poisson equation is linear, there exists the exact relationship,

$$\begin{pmatrix} \mathbf{q} \\ \mathbf{S} \end{pmatrix} = \begin{pmatrix} \mathbf{C}_{q\Phi} & \mathbf{C}_{q\mathbf{G}} \\ \mathbf{C}_{\mathbf{S}\Phi} & \mathbf{C}_{\mathbf{SG}} \end{pmatrix} \cdot \begin{pmatrix} \mathbf{\Phi} \\ -\mathbf{G} \end{pmatrix} \tag{5.1}$$

among N particles. The vectors $\mathbf{q}, \mathbf{S}, \mathbf{\Phi}$, and $\mathbf{G}$ contain the N particle charges, the $3N$ components of the particle dipoles, the N particle relative concentrations at each particle reference point, $\mathbf{R}_\beta$ $(\phi(\mathbf{R}_\beta) - \langle\phi(\mathbf{R}_\beta)\rangle)$, and $3N$ components of the average potential gradient, respectively. The matrix in (5.1) is called the capacitance matrix, $\mathbf{C}$, in electrostatics and is a geometric quantity dependent only upon the trap configuration, D_p/D, and the form of the source distribution.

Here the particles will be assumed to have a uniform concentration of zero at their surfaces, so if the reactant source is distributed only in the matrix phase the particles are equivalent to electrostatic perfect conductors. If reactant is also distributed in the particle phase, and if $D_p/D \gg 1$, the particles are also equivalent to perfect conductors. The capacitance matrix's submatrices relate the charge to

the potential, $\mathbf{C}_{q\Phi}$, the charge to the gradient, $\mathbf{C}_{q\mathbf{G}}$, etc. The effective reaction rate is then the suspension average value of the $\mathbf{C}_{q\Phi}$ coupling when there is no potential gradient. In this case the effective rate constant, nondimensionalized by Smoluchowski's dilute trap rate constant, $k_s = 4\pi Da$, is

$$\frac{k_{eff}}{k_s} = \frac{\langle \mathbf{C}_{q\Phi} \rangle}{4\pi Da}. \tag{5.2}$$

Recall, in our method, which is described in detail in Chapter 2, we approximate the capacitance matrix by

$$\mathbf{C} \approx \mathbf{M}^{-1} + \mathbf{C}_{2b} - \mathbf{C}_{2b}^{\infty}. \tag{5.3}$$

The "potential" matrix, $\mathbf{M}^{-1}$, in its *exact* form is the inverse of the capacitance matrix. Here, we form an approximation to the potential matrix from a moment expansion about each particle derived from the integral representation of Poisson's equation. The moment expansion can be carried out to any level. If the expansion is done up to the quadrupole level, for example, the so-called grand potential matrix, $\hat{\mathcal{M}}$ can be written as

$$\begin{pmatrix} \mathbf{\Phi} \\ -\mathbf{G} \\ -\nabla\mathbf{G} \end{pmatrix} = \begin{pmatrix} \hat{\mathbf{M}}_{\Phi q} & \hat{\mathbf{M}}_{\Phi \mathbf{S}} & \hat{\mathbf{M}}_{\Phi \mathbf{Q}} \\ \hat{\mathbf{M}}_{\mathbf{G}q} & \hat{\mathbf{M}}_{\mathbf{GS}} & \hat{\mathbf{M}}_{\mathbf{GQ}} \\ \hat{\mathbf{M}}_{\nabla q} & \hat{\mathbf{M}}_{\nabla \mathbf{S}} & \hat{\mathbf{M}}_{\nabla \mathbf{Q}} \end{pmatrix} \cdot \begin{pmatrix} \mathbf{q} \\ \mathbf{S} \\ \mathbf{Q} \end{pmatrix}, \tag{5.4}$$

where $\nabla\mathbf{G}$ is the gradient of the average potential gradient and $\mathbf{Q}$ is the vector containing the N particle quadrupoles. For an unbounded statistically homogeneous suspension of particles $\nabla\mathbf{G} = \mathbf{0}$ because it is inconsistent to have a quadratic concentration field in the absence of boundaries. Since $\nabla\mathbf{G} = \mathbf{0}$, we can solve for $\mathbf{Q}$ in terms of $\mathbf{q}$ and $\mathbf{S}$ and form an approximate potential matrix $\mathbf{M}$. If additional moments are included, they can also be solved for in terms of $\mathbf{q}$ and $\mathbf{S}$ since all higher derivatives of the gradient must vanish for an infinite system of particles, and their effects can be included into $\mathbf{M}^{-1}$.

The accuracy of the potential matrix, and hence, the accuracy of the potential invert depend upon the number of moments retained in its formulation. The inversion of the potential matrix captures the many-body far-field particle interactions

since the inversion is equivalent to a many-body method of reflections solution. Note, care must be taken in forming the potential matrix for an infinite suspension because the particle interactions are long-ranged, giving rise to convergence difficulties, as discussed in Chapter 2.

Recall we are considering particles analogous to perfect conductors in the electrostatic problem. If two nearby particles have different concentrations the flux between them is logarithmically singular in gap width. To include these near-field effects all the moments would have to be included in the potential formulation. Rather than do this, the near-field interactions are included directly by addition of the exact two-body capacitance matrix, $\mathbf{C}_{2b}$, less the far-field two-body capacitance matrix, $\mathbf{C}_{2b}^{\infty}$, already included in the potential invert. The two-body capacitance matrices contain all the interactions between two particles alone in the matrix. The method proves very accurate for computing effective conductivities, which are determined by the average particle dipoles, and we wish to discover how helpful this approach is for the present problem.

Ignoring for the moment the addition of two-body interactions and using the moment scattering only, we may derive analytically the effective reaction rate for cubic arrays up to the quadrupole level. From equation (2.37), the relative concentration of a sphere at its reference point is given by,

$$\begin{aligned}\phi(\mathbf{R}_\alpha) - \langle\phi(\mathbf{R}_\alpha)\rangle = &\frac{q_\alpha}{4\pi D a} + \frac{na^2\langle q\rangle}{3D} \\ &+ \frac{1}{4\pi D}\sum_{\substack{\beta \\ \beta\neq\alpha}}(q_\beta\frac{1}{r} + \mathbf{S}_\beta\cdot\nabla_y\frac{1}{r} + \frac{1}{2}\mathbf{Q}_\beta : \nabla_y\nabla_y\frac{1}{r}) \\ &- \frac{1}{4\pi D}\int_V (n\langle q\rangle\frac{1}{r} + n\langle\mathbf{S}\rangle\cdot\nabla_y\frac{1}{r} + \frac{1}{2}n\langle\mathbf{Q}\rangle : \nabla_y\nabla_y\frac{1}{r})dV.\end{aligned} \tag{5.5}$$

The first term on the right-hand side contains the sphere self-term and the second term includes both the constant source distribution and the average irreducible quadrupole for the suspension. The summations are the moment expansion through the quadrupole level, and the integrals over all space V contain the effect of the average charge, dipole and quadrupole. It is these integrals that insure an absolutely convergent concentration difference since the diverging sums exactly cancel with

growing integrals for large r. Similar equations can be written for $\mathbf{G}$ and $\nabla\mathbf{G}$ for any particle α. Now for cubic lattices, the sphere quadrupole is zero due to the lattice symmetry, and further, there is no coupling between the concentration and dipoles, again because of cubic symmetry. So up to the quadrupole level the relative potential for a sphere in a cubic lattice is given by,

$$\phi(\mathbf{R}_\alpha) - \langle\phi(\mathbf{R}_\alpha)\rangle = \frac{q_\alpha}{4\pi Da}\Big[1 + c + \sum_{\substack{\beta \\ \beta\neq\alpha}} \frac{a}{r} - \int_V n\frac{a}{r}dV\Big] \tag{5.6}$$

where q_β and $\langle q\rangle$ have been replaced by q_α since all spheres are equivalent in the lattice. Using the method of Ewald sums, the sum and integral in (5.6) can be evaluated to yield,

$$\phi(\mathbf{R}_\alpha) - \langle\phi(\mathbf{R}_\alpha)\rangle = \frac{q_\alpha}{4\pi Da}\big[1 - mc^{1/3} + c\big], \tag{5.7}$$

where m is a constant and computed to be 1.7601, 1.7918, and 1.7919 for simple, body-centered, and face-centered cubic lattices, respectively. Because we assume the particle traps are analogous to perfect conductors with zero potential on their surfaces, $\phi(\mathbf{R}_\alpha) = 0$, and therefore, the effective reaction rate given by (5.2) is then

$$\frac{k_{eff}}{k_s} = \frac{1}{1 - mc^{1/3} + c}, \tag{5.8}$$

up to the quadrupole level. This is consistent with the results of Lebenhaft and Kapral and Venema and Bedeaux. Lebenhaft and Kapral's result does not include the c term in the denominator of (5.8) since they did not include the $\langle q\rangle$ term due to the irreducible quadrupole and the source distribution in the matrix phase in their analysis. Neglecting this term results in an aphysical divergence at $c \approx 0.17$. Venema and Bedeaux have continued the expansion in spherical harmonics to include in equation (5.8) additional terms of increasing powers of c in the denominator. Also, many investigators have considered the problem with the source distribution in the matrix phase only, in which case equation (5.8) is multiplied by $(1 - c)$. Within the context of our method, this can be shown explicitly after some tedious manipulations and is physically reasonable since the problem is linear and must scale with the

source strength; hence, if the source strength is reduced by $(1-c)$, the effective reaction rate must be reduced too.

The above results for periodic arrays show the known $O(c^{1/3})$ scaling of the first correction to the Smoluchowski result for small c. For a random medium the first correction to the rate is $O(c^{1/2})$ as can be shown by solving the electrostatic analog of the Brinkman equation for a single sphere with reactant concentration, ϕ, vanishing at its surface and $\phi = \langle\phi\rangle$ far from the sphere. The Brinkman-like equation is motivated physically as follows: The steady-state reaction-diffusion equation is given by,

$$D\nabla^2\phi + r = 0, \tag{5.9}$$

where r is the rate of production per unit volume of the species. The total flux into an isolated sphere in a matrix is gven by $q = 4\pi Da(\phi - \langle\phi\rangle)$, where here ϕ is the concentration of the diffusing species at the sphere's surface. If we imagine our Brinkman-like effective medium as a collection of spheres distributed randomly in space, the rate of production per unit volume is $-n4\pi Da(\phi - \langle\phi\rangle)$. Therefore, the Brinkman-like equation is

$$\nabla^2\phi - n4\pi a(\phi - \langle\phi\rangle) = 0. \tag{5.10}$$

Solving (5.10) with the aforementioned boundary conditions, we find the effective reaction rate is given by

$$\frac{k_{eff}}{k_s} = 1 + \sqrt{3c}, \tag{5.11}$$

which is precisely Felderhof and Deutch's first correction showing the $O(c^{1/2})$ scaling.

This Brinkman-like effective medium theory can be modified further to be "self-consistent" and include the effective diffusivity of the diffusing species in the dispersion. In this case we write the Brinkman-like equation as

$$D_{eff}\nabla^2\phi - k_{eff}n(\phi - \langle\phi\rangle) = 0, \tag{5.12}$$

where D_{eff} is the effective diffusivity for a random array of perfect spherical conductors and is a function of the trap volume fraction, and k_{eff} is the sought after

reaction rate. Solving (12) we find the implicit relation for the reaction rate,

$$\frac{k_{eff}}{k_s} = \sqrt{\frac{3ck_{eff}D_{eff}}{k_sD}} + \frac{D_{eff}}{D}. \tag{5.13}$$

5.3. Results for Random Dispersions of Spherical Traps

Several simulations were performed to determine the effective reaction rate for a random suspension of spherical traps. To simulate an infinite collection of traps, a finite number of spheres were randomly placed in a cubic box via Monte Carlo methods, and the box was periodically replicated throughout all space. Our previous work in Chapter 3 showed that 32 particles per cell is sufficient to obtain results independent of cell size. The mobility matrix was formed as described earlier and elsewhere taking advantage of the periodicity. Simulations were performed with and without the addition of the near-field two-body interactions. The results are illustrated in Figure 5.1 for a constant source distribution in the matrix phase only. Recall that for a constant source distribution in both the particle and matrix phases, these effective reaction rates must be divided by $(1 - c)$.

The non-analytic $c^{1/2}$ dependence at low volume fractions of the effective reaction rate constant is apparent in our results as observed in the decreasing slope up to 10 volume percent. The computed rate constant, however, exhibits a maximum at around $c = 0.4$, which is not a physically reasonable result. The rate constant should increase with the volume fraction of traps because the reactant will have less distance to diffuse in order to react with one of the traps. A maximum also occurs in our analytic result for the cubic lattices. Evidently many multipoles are necessary to compute the reaction rate constant accurately. The addition of two-body interactions produced negligible changes in the effective reaction rate constant; the two sets of results are indistinguishable.

In addition to our simulation results, we also plot the results of the random walker simulations of Lee, *et al.*, the lower bound of Torquato, and the theoretical results of Felderhof and Deutch. Our limited multipole expansion matches Lee, *et al.*'s simulations up to $c = 0.3$, after which it grossly underpredicts the effective reaction rate, indeed dropping below the lower bound for $c \approx 0.45$. Our simulation results compare quite well to the results of Felderhof and Deutch up to about $c = 0.08$, again indicating that the $c^{1/2}$ dependence is properly captured at low volume fractions with our method. Even at modest volume fractions Felderhof and

Deutch's results seem to over predict the reaction constant predicted by both our and Lee, *et al.*'s results.

The reaction rate computed from the Brinkman-like effective medium equation (5.13) using known results for D_{eff} computed in Chapter 3 is also shown in Figure 5.1. These results compare quite well to those of Lee, *et al.* for small and large volume fractions, although they are off by as much as 25% at intermediate values. The use of such an effective medium equation can perhaps provide a reasonable estimate of the reaction rate for non-spherical particles if effective conductivity data is available.

Based upon the results presented here and Venema and Bedeaux's work, it would appear that a very large number of many-body multipoles must be included to accurately compute the effective reaction rate. As mentioned earlier, Venema & Bedeaux reported 50 spherical moments were needed to compute the reaction rate for an fcc lattice accurate to five significant figures. Venema (1990) also found that when calculating the reaction rate for a regular array of cylinders, the rate would alternately exhibit a maximum or no maximum depending upon if an odd or even number of moments were used in the multipole scattering; this is consistent with our results. Unfortunately, adding exact near-field two-body interactions, which is very effective for approximating the neglected higher order moments for the effective conductivity problem, does not help in this case. Since there is no relative potential or concentration difference between particles, there is no near-field singular behavior dominating the effect of the neglected higher moments. It appears, therefore, that if a multipole scattering method is used to compute the effective reaction rate, many moments must be included in the formulation.

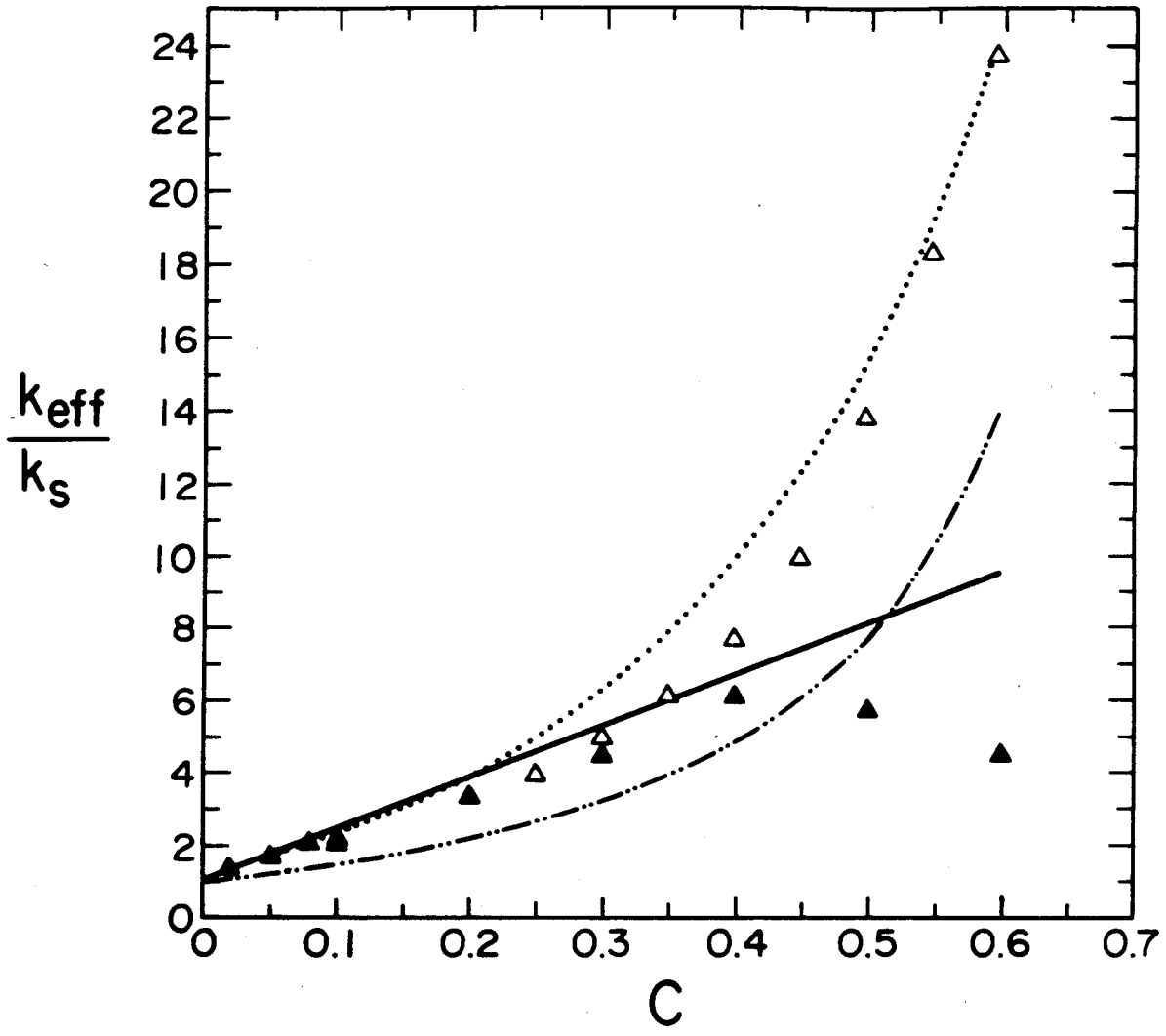

Figure 5.1 Effective reaction rate, nondimensionalized with the dilute, Smoluchowksi result of $4\pi Da$, versus volume fraction of spherical traps. The closed triangles are our simulation results, the open triangles are the random walker results of Lee, *et al.*, the lower dashed line is the lower bound of Torquato, the solid line is the theoretical result of Felderhof and Deutch, and the upper dotted line is reaction rate computed with the self-consistent Brinkman-like effective medium theory (equation (5.13)). All results here assume that a constant source distribution exists in the matrix phase only, except for the results of Felderhof and Deutch where it is not clear what assumptions were made to insure a steady-state.

CHAPTER 6

DYNAMIC SIMULATION OF ELECTRORHEOLOGICAL FLUIDS

6.1. Introduction

In the late 1930's Willis Winslow (Carlson, Sprecher, & Conrad 1990), an intrepid basement experimentalist, observed interesting phenomena when dielectric particles suspended in oil were subject to an electric field. He saw the electrically induced formation of fibrous particle chains aligned with the electric field, and, more interesting, Winslow found that the effective viscosity of the suspension could be varied by orders of magnitude by varying the applied electric field. In fact he observed that the viscosity increased with the square of the applied electric field. This electrorheological (ER) response is often referred to as the Winslow effect.

Winslow (1949) recognized the potential of these new fluids with their "tunable" viscosities and patented several electromechanical devices, such as clutches, brakes, and valves that could be controlled by varying the electric field. Although none of his machines were ever used commercially, there is now a renewed interest in designing controllable machines and devices using ER fluids, probably fueled by the electronics technology available today to quickly access and analyze system data. Figure 6.1 illustrates a few possible devices using ER fluids. The ER fluid clutch allows the fine control of the output rotation rate for any given input rotation by varying the applied electric field across the plates. Such a device has potential application in automobiles or assembly line robots. If an ER suspension is used in some fluid system, the flow may be regulated or stopped with an ER valve, which has the advantage of no moving parts. The vibration damping mount illustrated is a variation of the spring-dashpot viscous dampers. With an ER fluid the damping parameter can be dynamically varied to control mechanical vibrations of engines or perhaps even buildings during earthquakes. Of course, this is only a partial list of the possibilities, but even so, we see these fluids could profoundly change many aspects of present technology and industry from automotive design to robotics to

building construction.

Currently available ER fluids, however, do not have the necessary properties for practical application. For example, they tend to settle out of suspension, have poor tribological properties, and, most importantly, do not have a high enough range of effective viscosity for practical applications. Particularly for this latter problem, we must understand the underlying physics of the ER response in order to engineer better fluids. A detailed micromechanical model relating the bulk rheological properties to the suspension microstructure would be an excellent tool for this task.

In the remaining chapters we shall endeavor to understand ER fluids with a molecular dynamics-like simulation. In this chapter we develop the methodology for the simulation of dielectric particles forming an electrorheological fluid. The simulation accounts for both hydrodynamic forces due to an imposed shear flow and electrostatic forces due to the applied electric field. The simulation allows the observation of the time-evolved motions of the suspended particles and the instantaneous rheology of the suspension so we can directly relate the suspension bulk properties to its microstructure and gain insight into the processes involved. In addition the simulation method provides a means to test theories that describe ER suspensions, including constitutive models. But before modeling these fluids, we must have a clear idea of their characteristics.

Typical suspended materials in an ER fluid are 1-100μm size approximately spherical particles of cornstarch, silica, or even zeolites, while the suspending fluids are nonconducting solvents such as silica oil, chlorohydrocarbons, or corn oil. To minimize settling problems the fluids are blended so that the particles are close to neutrally buoyant, with densities in the range of 0.6 - 2.0 g/cm^3. The viscosities of the suspending fluids, at room temperature, are from 0.01 - 10 Pa-s (water is about 0.001 Pa-s). The zero field viscosity of the suspension with particle loadings ranging from 0.05 - 0.50 by volume fraction are up to an order of magnitude greater. The effective viscosity of the ER suspension can be 100,000 times greater for electric field strengths of about 1 kV/mm perpendicular to the shear flow. The dielectric constants relative to vacuum for the suspending fluid vary from 2 - 15 and those

of the particles from 2 - 40. The particle-to-fluid dielectric constant ratio typically varies from 2 - 10. The particle Reynolds number is less than 0.1 (maximum shear rates are about 0.1 $\sec^{-1}$), and the fluid Reynolds number is small enough so inertia is negligible. Also, the particle Peclét number is extremely large, in excess of 100,000 usually, so thermal forces are negligible. Indeed the thermal forces must be small otherwise the Brownian motion would disrupt the chains of particles that are key, as we shall see, to the ER response.

The key to observing the ER response, as noted by Winslow (1949) is the induced electrostatic polarization forces due to the dielectric mismatch between the particles and the fluid. As discussed in the first half of the thesis, when an uncharged particle is placed in an electric field, it develops an induced dipole if the surrounding fluid has a different dielectric constant. This dipole is further enhanced by the presence of other particles. The dipole, of course, can be thought of as a concentration of positive charge at one end of the particle and negative charge at the other end. With this simple picture and using the interactions of two particles as a paradigm, we can qualitatively explain why ER fluids form chains of particles aligned with the electric field.

Let us imagine two particles whose line of centers is parallel to the electric field, such as those in Figure 6.2. The force between point charges scales as $O(q_\alpha q_\beta / r^2)$, so there is attraction between the positive and negative charges at the surfaces nearest and furthest from each other and repulsion between charges of the same sign. There is then a net attraction of the particles along their line of centers so that they move toward each other. If we apply the same considerations to particles whose line of centers is perpendicular to electric field, we find there is a net repulsion moving the particles away from each other along their line of centers. For particles whose line of centers is neither parallel nor perpendicular to the electric field, the particles may experience both attraction and repulsion causing the pair to eventually translate and rotate into alignment with the electric field. Thus, the forces due to polarization interactions cause the formation of particle chains aligned with the electric field. As we shall see, the microstructure of a suspension is intimately related to its bulk

rheological properties, so the formation and strength of these chains strongly affect the viscosity of an ER fluid.

The microstructure and rheology of ferrofluids developed by Rosensweig (1985) also depend upon an applied field. However, there are fundamental differences between the ferrofluids and ER fluids. A ferrofluid is a suspension of *permanently* magnetized particles, and so there are polarization forces without an applied magnetic field. These suspensions would then settle out because of particle clumping, and so the particles are usually sufficiently small such that Brownian forces dominate in the zero-field limit to disperse the particles. As mentioned, Brownian forces are usually negligible for an ER suspension. Since the magnetic dipoles are permanent in a ferrofluid, the rheological properties scale linearly with the applied magnetic field in contrast to quadratic dependence on field strength observed in ER fluids since their particle dipoles are induced. There is also a torque on a ferrofluid particle given by the cross product of its dipole and the applied field which gives rise to an asymmetric stress tensor as shown by Batchelor (1970). In an ER fluid of practically spherical particles, the local electric field is aligned with the induced dipole, as shown from the Faxén law of Chapter 2, so there is no net torque on the particle. There are asymmetric stresses in ER fluids, but they exist because of the effective torque on the deformed or strained chains of particles.

It was almost two decades after Winslow (1949) published his observations that an extensive study of ER fluids was performed by Klass & Martinek (1967*a*, *b*) and Uejima (1972). They both confirmed many of Winslow's findings and performed limited experiments to test the effects of gap spacing (of which they found none) and solids volume fraction. Uejima also found that ER fluid rheology, at least for the shear stress, was fairly well modeled as a Bingham plastic with the shear stress τ given by,

$$\tau = \tau_B + \eta_B \dot{\gamma}, \tag{6.1}$$

where τ_B and η_B are the so-called Bingham yield stress and plastic viscosity, and $\dot{\gamma}$ is the shear rate. Uejima observed that the yield stress scaled with square of the electric field and the plastic viscosity was approximately constant.

Both groups tested the effect of particle water content on the ER response, and for silica particles they found the amount of water did affect the magnitude of the ER response. In fact they believe that water is an essential ingredient for the observation of the ER response. Unlike Winslow, Klass & Martinek and Uejima ascribed the interparticle forces to the interactions of polarized particle double layers of water and trace salts. Later experiments by Filisko & Radzilowski (1990) showed that the presence of water is not always necessary for the presence of electrorheological activity. They found that silica particles, indeed, must contain at least 1.5 wt% water in order to exhibit the ER response, and the suspension effective viscosity increases with water content above this critical value for fixed electric fields. Alumino-silicate or zeolite particles, however, are equally active from less than 0.02 wt% water to 0.8 wt%. Filisko & Radzilowski and Conrad, Chen, & Sprecher (1990) both propose that the natural mobile charge carriers in the zeolites, like sodium ions, migrate due to the electric field and create a particle dipole. The ER response does increase as the water content in the zeolites rises above 0.8 wt%, and so water can play an important role in some manner. In any of these suspensions, the particles effectively have a dielectric constant greater than the suspending fluid, so the induced polarization forces still exist, but the atomic scale mechanism for polarization is different in each case. These mechanisms are important in so far as the breakdown or saturation of the particle polarization is concerned. If the particle has reached polarization saturation, then the viscosity will no longer scale quadratically with the electric field but will scale linearly.

There was, and perhaps still is some dispute (Pool 1990) over the importance of water in observing the ER response. Zukoski (1989) has synthesized a "dry" ER fluid carefully prepared to contain no water and still observed the ER response. The simulation results of Klingenberg, Van Swol, & Zukoski (1989) and Klingenberg (1990) as well as our forthcoming simulation results also indicate that the polarization forces due to dielectric mismatch give rise to the ER response. Most researchers now agree with this model and do not believe small amounts of water are necessary (Pool 1990). That is not to say that water could or does not play a

role in the interparticle interactions, but that its presence is not necessary. In fact the presence of water is deleterious to ER fluids because it increases the conduction (these fluids ideally, but not practically, are pure dielectrics), increasing power consumption and causing unwanted resistance heating which reduces the ER response as pointed out by Gast & Zukoski (1989).

Marshall, Goodwin & Zukoski (1989) performed a thorough study of an ER fluid of silica particles, wet as mentioned above, in a chlorohydrocarbon suspending fluid. Their experiments covered a large range of field strengths, shear rates, and volume fractions. They found that the effective viscosity of the ER fluid could be correlated with a so-called Mason number, Ma, a measure of the viscous forces to electrostatic forces, named in honor of the late Dr. S. G. Mason and his work on electroviscous flows (for example, see the review by Arp, Foister, & Mason 1980). Marshall *et al.* also noted that yield stress was linear in the volume fraction range studied. Recent work by Klingenberg (1990) has shown that the yield stress in fact has a maximum at around 35-40 volume percent solids. There have also been several experimental studies on magnetorheological fluids, the magnetic analogs of ER fluids. Work by Mimouni, Bossis, Mathis, Meunier, & Paparoditis (1990) and Lemaire & Bossis (1991) indicate that these suspension behave quite similarly to ER fluids, and their physics is well described by interacting magnetically induced dipoles. Finally, we point out the excellent review by Gast & Zukoski (1989) that lists several other similar direct and related experimental studies of ER fluids.

There has been some effort to construct micromechanical models of ER fluids with dielectric mismatch as the cause of the electrostatic interactions. Adriani & Gast (1988) developed a perturbation theory to describe an ER fluid close to its equilibrium balance of Brownian and electrostatic interactions. They calculate the high frequency elastic modulus and dynamic viscosity of the ER suspension. However, they account for the hydrodynamic and electrostatic interactions from mean-field theories, so their results are not accurate for dense systems. Since the particles are always in close contact when a sufficient electric field is applied, their results are probably only qualitatively correct. Adriani & Gast (1989) have also

applied their model to predict the dependence of the dichroism and birefringence of an ER suspension on Ma for the correlation of rheo-optical experiments.

As mentioned earlier, Klingenberg, Van Swol, & Zukoski (1989) and Klingenberg (1990) have developed a dynamic simulation of ER fluids. Their method assumes simple Stokes drag for the hydrodynamic forces on the particles and simple induced point dipole electrostatic forces, so there are no many-body far-field interactions and no near-field lubrication-like interactions. To prevent particle overlap, a near-field repulsive force is included. Because of the simplicity of their method, they can simulate many particles, and indeed they capture many of the structural features observed in ER suspension. Their method, however, predicts only the large electric field limit of the effective viscosity, and even then underpredicts experimental results due to their *ad hoc* account of near-field electrostatic interactions. Their simulation also does not provide a good means to develop and test a constitutive model since it contains so many approximations. We also point out that recently Whittle (1990) has performed a study with a simulation similar to Klingenberg *et al.*, where he too does not account for the detailed hydrodynamic or electrostatic interactions.

As mentioned earlier, here we develop a dynamic simulation that accurately accounts for both the hydrodynamic and electrostatic interactions. The simulation captures the far- and near-field effects for both types of interactions. The simulation also allows for the prediction of the effective viscosity of the suspension and other rheological properties for any range of electric fields and shear rates.

In §6.2 we briefly describe "Stokesian dynamics" which is the basis of our simulation method. Stokesian dynamics simulates the motions of particles due to an imposed bulk shear flow, applied particle forces, and hydrodynamic interactions for zero-Reynolds-number or inertialess conditions. This technique captures both far- and near-field hydrodynamic interactions and is accurate over the entire volume fraction range. In addition to the particle motions, the bulk stress of the suspension is computed using Stokesian dynamics from which rheological parameters can be determined.

In order to implement Stokesian dynamics, we need the electrostatic interparticle forces, and in §6.3 we describe a method employing the techniques of Chapter 2 to determine them. This method computes the conservative interparticle force by way of a system electrostatic energy. The system energy includes the effects of both the applied electric field and interparticle interactions. The formulation of the energy using the results of the earlier chapters allows us to include both the far- and near-field particle interactions. Also, the energy approach developed in this section provides the foundation for computing the strain energy function of an idealized ER fluid and developing a model for the Bingham or dynamic yield stress in Chapter 7.

The complete simulation is applied in §6.4 to an unbounded monolayer of suspended spherical particles, with a particle-to-fluid dielectric constant ratio of 4, subject to a simultaneous shear flow and orthogonal electric field at an areal fraction of 0.4 for a large range of the Mason number, Ma, the ratio of viscous forces to electrostatic forces. The effective viscosities and first normal stress differences are presented as a function of Ma. Time traces of the viscosities are also presented along with "snapshots" of the particle configurations, and we discuss the relationship among the microstructure, Ma, and viscosity. The simulation results are also compared to the experimental data of Marshall *et al.* Finally, the effect of periodic boundary conditions is also tested, and we discuss their effect on the simulation of ER suspensions.

6.2. Simulation Method: Hydrodynamic Interactions and Rheology

6.2.1 Fundamentals of Stokesian Dynamics

The Stokesian dynamics method has been described in detail elsewhere (Brady & Bossis 1988, Durlofsky, Brady, & Bossis 1987, and Brady, Phillips, Lester, & Bossis 1988), so here we present an outline with special attention to the calculation of the rheology.

For N rigid neutrally buoyant particles suspended in an incompressible Newtonian fluid of viscosity η and density ρ, the motion of the fluid is governed by the Navier-Stokes equations, and the motion of the particles is described by the coupled evolution equation,

$$\mathbf{m}.\frac{d\mathbf{U}}{dt} = \mathbf{F}^{\mathbf{H}} + \mathbf{F}^{\mathbf{P}}, \tag{6.2}$$

which simply states: mass $\times$ acceleration equals the sum of the forces. In (6.2) $\mathbf{m}$ is a generalized mass/moment of inertia matrix of dimension $6N \times 6N$, $\mathbf{U}$ is the particle translational/rotational velocity vector of dimension $6N$, and the $6N$ force/torque vector $\mathbf{F}$ is represented by 1) the hydrodynamic forces $\mathbf{F}^{\mathbf{H}}$ exerted on the particles due to their motion relative to the fluid, 2) the deterministic non-hydrodynamic forces, $\mathbf{F}^{\mathbf{P}}$, which for an ER fluid are the interparticle electrostatic forces. A stochastic or Brownian force may also be included in (6.2), but is not important here since most ER suspensions are dominated by hydrodynamic and electrostatic forces.

When the motion of the particles and the fluid is on a scale such that viscous forces dominate inertial forces, the fluid dynamics is governed by Stokes equations. In this case, for a small particle Reynolds number ($Re = \rho\dot{\gamma}a^2/\eta \ll 1$), the hydrodynamic force exerted on a particle in a suspension undergoing a bulk shear flow is given by Brenner (1964) as

$$\mathbf{F}^{\mathbf{H}} = -\mathbf{R}_{FU} \cdot (\mathbf{U} - \mathbf{U}^{\infty}) + \mathbf{R}_{FE} : \mathbf{E}^{\infty}. \tag{6.3}$$

Here, $\mathbf{U}^{\infty}$ is the imposed flow at infinity evaluated at the particle center, $\mathbf{E}^{\infty}$ is the symmetric (and traceless, by virtue of continuity) part of the velocity gradient

tensor. The tensors $\mathbf{R}_{FU}$ and $\mathbf{R}_{FE}$ are the resistance matrices that relate the hydrodynamic force/torque on the particles to their motion relative to the fluid and to the imposed shear flow. There is a linear relationship between the hydrodynamic force and the velocity and rate of strain because Stokes equations and the boundary conditions are also linear. The resistance matrices are the hydrodynamic analogs of the capacitance matrices in Chapters 2-5. Like the capacitance matrices, the resistance matrices are geometric quantities completely determined by the instantaneous particle configurations. The resistance matrices here and below are formulated to include the long-ranged far-field interactions and the near-field lubrication interactions in an analogous fashion to the capacitance matrix formulation in Chapter 2. The near-field effects for the hydrodynamics are the lubrication forces that exist between two particles in relative motion. Two nearby particles moving toward each other, for example, must squeeze out the thin lubricating film of fluid in the small gap between them. This creates large pressures that generate singular hydrodynamic forces on the particles. These forces are $O(\xi^{-1})$ and $O(ln\xi)$ where ξ is the non-dimensionalized gap width. The near-field lubrication here is important for preventing particle overlap in the dynamic simulation as well as capturing the effects of percolating chains of particles which we expect to be common in ER fluids.

Since inertial forces are negligible in the limit of small Re, we may neglect the LHS of (6.2) and in combination with (6.3) yields,

$$\frac{d\mathbf{x}}{dt} = \mathbf{U} = \mathbf{U}^{\infty} + \mathbf{R}_{FU}^{-1} \cdot (\mathbf{F}^{\mathbf{P}} + \mathbf{R}_{FE} : \mathbf{E}^{\infty}). \tag{6.4}$$

Non-dimensionalizing (6.4) and integrating it over a time step Δt produces the evolution equation for the change in particle configuration $\mathbf{x}$ (with error of $O(\Delta t^2)$),

$$\Delta\mathbf{x} = \{\mathbf{U}^{\infty} + \mathbf{R}_{FU}^{-1} \cdot [Ma^{-1}\mathbf{F}^{\mathbf{P}} + \mathbf{R}_{FE} : \mathbf{E}^{\infty}]\}\Delta t. \tag{6.5}$$

Here, $\mathbf{x}$ has been nondimensionalized by the characteristic particle size, a; the time by the inverse shear rate, $\dot{\gamma}^{-1}$; the hydrodynamic forces by $6\pi\eta a^2\dot{\gamma}$; the interparticle electrostatic force by $12\pi\epsilon a^2(\beta E)^2$. $Ma = \eta\dot{\gamma}/2\epsilon(\beta E)^2$ the so-called Mason number, which measures the relative importance of the viscous shear forces to the

electrostatic forces. Here ϵ is the dielectric constant of the fluid, ϵ_p is the dielectric constant of the particle, $\beta = (\epsilon_p - \epsilon)/(\epsilon_p + 2\epsilon)$, and E is magnitude of the imposed electric field. Equation (6.5) clearly depends upon Ma, but it is also a function of the volume fraction of particles, c, and the electrostatic interparticle forces which are characterized by the dielectric mismatch, β. Note that up to this point no restrictions have been made on particle shape or size.

The suspension bulk stress, $\langle\boldsymbol{\Sigma}\rangle$, provides information about the rheology and can also be computed with Stokesian dynamics. The bulk stress is defined as the ensemble or equivalent volume average stress of a statistically homogeneous suspension of particles. For N particles in a volume V, Batchelor (1970, 1977) has found that,

$$\langle\boldsymbol{\Sigma}\rangle = \mathrm{IT} + 2\eta\mathbf{E}^{\infty} + \frac{N}{V}\{\langle\mathbf{S}^{\mathbf{H}}\rangle + \langle\mathbf{S}^{\mathbf{P}}\rangle - \langle\mathbf{x}\mathbf{F}^{\mathbf{P}}\rangle\}. \tag{6.6}$$

Note $N/V = n$ is the number density of particles and $\langle\cdot\rangle$ is an ensemble average. The IT stands for an isotropic term, of no interest for incompressible suspensions, and the second term is the fluids contribution to the stress. The presence of the particles makes the last three contributions to the bulk stress. The hydrodynamic and particle stresslets, $\mathbf{S}^{\mathbf{H}}$ and $\mathbf{S}^{\mathbf{P}}$, are the symmetric and traceless first moments of the force distribution on a particle due to the shear flow and the interparticle forces. The stresslet is precisely given by the integral over the particle surface,

$$\mathbf{S} = \int_{\partial\Omega} \left[(\mathbf{x}\sigma + \sigma\mathbf{x})\cdot\mathbf{n} - \frac{2}{3}\mathbf{I}(\mathbf{x}\cdot\sigma\cdot\mathbf{n}) - \eta(\mathbf{u}\mathbf{n} + \mathbf{n}\mathbf{u})\right] dA, \tag{6.7}$$

where $\mathbf{x}$ here is measured relative to some reference point in the particle, $\mathbf{n}$ is the outward facing normal, and σ and $\mathbf{u}$ are the stress and velocity on the boundary of the particle for either a shear flow or interparticle forces depending upon whether we are computing $\mathbf{S}^{\mathbf{H}}$ or $\mathbf{S}^{\mathbf{P}}$. The $\partial\Omega$ is the area of the particle surface. Again due to the linearity of Stokes equations, the stresslets can be written in terms of resistance tensors as,

$$\langle\mathbf{S}^{\mathbf{H}}\rangle = -\langle\mathbf{R}_{SU}\cdot\mathbf{R}_{FU}^{-1}\cdot\mathbf{R}_{FE} - \mathbf{R}_{SE}\rangle : \mathbf{E}^{\infty}, \tag{6.8a}$$

$$\langle\mathbf{S}^{\mathbf{P}}\rangle = -\langle\mathbf{R}_{SU}\cdot\mathbf{R}_{FU}^{-1}\cdot\mathbf{F}^{\mathbf{P}}\rangle, \tag{6.8b}$$

where $\mathbf{R}_{SU}$ and $\mathbf{R}_{SE}$ are the configuration dependent resistance matrices that relate the particle stresslets to particle velocities and rate of strain. Generally speaking, the stresslets are the added mechanical or contact stress due to the resistance of the rigid particles to the local deformation.

The $-\langle \mathbf{x}\mathbf{F}^{\mathbf{P}} \rangle$ derived by Batchelor (1977) from virtual strain arguments is the thermodynamic stress associated with the suspension. The ensemble average $\langle \mathbf{x}\mathbf{F}^{\mathbf{P}} \rangle$ for a statistically homogeneous suspension is precisely given by,

$$\langle \mathbf{x}\mathbf{F}^{\mathbf{P}} \rangle = \frac{1}{2N} \sum_{\alpha}^{N} \sum_{\beta}^{N} (\mathbf{x}_\alpha - \mathbf{x}_\beta)\mathbf{f}^{\alpha\beta}, \tag{6.9}$$

where

$$\mathbf{F}^{\alpha} = \sum_{\beta}^{N} \mathbf{f}^{\alpha\beta}. \tag{6.10}$$

The $\mathbf{f}^{\alpha\beta}$ is the force on particle α induced by particle β, and $\mathbf{F}^{\alpha}$ is the total force on particle α. When modeling the suspension rheology with a only finite number of particle interactions, the thermodynamic force is more simply,

$$\langle \mathbf{x}\mathbf{F}^{\mathbf{P}} \rangle = \frac{1}{N} \sum_{\alpha}^{N} \mathbf{x}_\alpha \mathbf{F}^{\alpha}. \tag{6.11}$$

The thermodynamic stress can be interpreted as a spring-like elastic restoring force. Recall that the particles prefer to be aligned with the electric field, so any deformation of that state will produce interparticle forces acting to realign the particle chains. These forces manifest themselves macroscopically as the bulk thermodynamic stress.

Equations (6.5) and (6.6) are the core of the dynamic simulation. Given an initial configuration, (6.5) is simply integrated in time to follow the dynamic evolution of the suspension microstructure, and (6.6) is evaluated to determine the rheological behavior of the suspension. Clearly from (6.5) and (6.6), the entire evolution and rheological properties are determined by the hydrodynamic interactions included in the resistance matrices and the electrostatic forces. Stokesian dynamics accurately

determines the hydrodynamic resistance matrices so all that is left is the computation of the electrostatic interparticle forces. Before proceeding to that presentation in §6.3, we shall describe in more detail the contributions to the bulk stress.

6.2.2 Contributions to the Bulk Stress

In order to better interpret the effective viscosities predicted by the simulation, it would help to better understand the three particle contributions to the bulk stress. The added hydrodynamic stress, $\mathbf{S^H}$, is quite sensitive to the suspension microstructure, and, for example, can be very large for rod-like chains. In a shear flow the hydrodynamic stresslet of a particle scales, roughly, as the cube of its largest length scale. So, an ER suspension of particle chains has a higher viscosity compared to the same well-dispersed suspension partially by virtue of the increased hydrodynamic stress. Also, relative motion between two nearby particles creates large stresses due to the singular lubrication interaction. This is the hydrodynamic analog of singularly large electrostatic dipoles for nearby perfectly conducting particles at different potentials increasing the effective conductivity of a suspension.

The particle stresslet, $\mathbf{S^P}$, is rather different in that its contribution to the viscosity is usually negative for an ER fluid. Consider, for example, two particles in a shear flow and orthogonal electric field as depicted in Figure 6.3(a). Now for a spherical particle its stresslet is given by the Faxén law,

$$\mathbf{S} = \frac{20}{3}\pi\eta a^3 \mathbf{e}(\mathbf{x}_\alpha), \tag{6.12}$$

where $\mathbf{e}(\mathbf{x}_\alpha)$ is the local rate of strain at the center of the particle that would exist in its absence. This is the hydrodynamic analog of the Faxén law for the electrostatic dipole in equation (2.19). Because Stokes equations are linear we can break the computation of $\mathbf{S}$ into that due to the bulk shear flow, $\mathbf{S^H}$, and that due to the interparticle forces, $\mathbf{S^P}$. From inspection the contribution of the appropriate component of $\mathbf{S^H}$ to the viscosity is always positive. To determine the contribution of $\mathbf{S^P}$, we must consider the velocity disturbance on one particle due to the force on another. Because of the relative positions of the particles in Figure 6.3a, the resultant electrostatic forces on particle α creates a velocity gradient opposite to that of the bulk flow on particle β, and likewise for β on α. So for this example microstructure, the appropriate component of $\mathbf{S^P}$ must be opposite to its counterpart of $\mathbf{S^H}$ from equation (6.12), and hence contributes a negative viscosity.

The particular geometry shown in Figure 6.3*a* is that one would typically expect in ER fluid, where the shear flow has distorted the alignment of a pair or chain of particles. Occasionally the suspension might have a microstructure that has the mirror image of that in Figure 6.3*a* where then $\mathbf{S^P}$ would contribute positively to the viscosity. This, however, occurs infrequently.

The $-\langle \mathbf{xF^P} \rangle$ piece for the system in Figure 6.3*a* contributes positively to the suspension viscosity, since it resists motion in the direction of the bulk shear flow. The effect of $\mathbf{S^P}$ appears then to be a reduction of the effect of the spring-like restoring force. This is perhaps clearer if we consider the situation in Figure 6.3*b*. The two particles are in contact with equal but opposite forces. The normal forces make no contribution to the stress of the system if there is no deformation of the particles. This is because the stress is concentrated at the point of contact, so the normal force contribution to the particle and thermodynamic stress is,

$$\langle \mathbf{S^P} \rangle = -\frac{1}{2}(\mathbf{x}_\alpha - \mathbf{x}_\beta)\mathbf{F}_n, \tag{6.13}$$

$$-\langle \mathbf{xF^P} \rangle = \frac{1}{2}(\mathbf{x}_\alpha - \mathbf{x}_\beta)\mathbf{F}_n, \tag{6.14}$$

and exactly cancel. The tangential forces do contribute to the stress, but depend upon the friction at contact. If we assume, for example, the frictional force to be the product of a friction coefficient μ and the normal force, the added stress is,

$$\langle \Sigma \rangle = \frac{1}{2}(\mathbf{x}_\alpha - \mathbf{x}_\beta)\mathbf{F}_\mathrm{t} - \frac{1}{2}(\mathbf{x}_\alpha - \mathbf{x}_\beta)\mu\mathbf{F}_\mathrm{n}. \tag{6.15}$$

The first term is our spring-like restoring force, and the second term is effectively the $-\langle \mathbf{R}_{SU} \cdot \mathbf{R}_{FU}^{-1} \cdot \mathbf{F^P} \rangle$ contribution, which is opposite in sign to the first term. In our case the hydrodynamic lubrication friction of the thin film of fluid between particles reduces the stress transfer from one sphere to another. From this example this reduction in the stress is clearly then not peculiar to just the hydrodynamic interactions of Stokes flow.

The important conclusion here is that the reduction of the stress will occur due to any balancing force preventing the spheres from overlapping or running through

each other in the simulation. If some near-field repulsive forces prevented particle overlap, then their contribution to the $-\langle \mathbf{x}\mathbf{F}^{\mathbf{P}} \rangle$ piece would reduce the stress like the hydrodynamic $\mathbf{S}^{\mathbf{P}}$. Similarly, if particles were allowed to touch and deformed under contact to arrest their motion, then this added deformation stress would play the role of $\mathbf{S}^{\mathbf{P}}$. Using the the strong lubrication forces as the means to prevent particle overlap is particularly convenient from the point of view of implementation since they already exist as part of the suspensions hydrodynamics and do not require the hypothesis of another interparticle force.

We also note here that the contribution of the thermodynamic stress is asymmetric. As pointed out by Batchelor (1970), the existence of body-couples on particles in a suspension create asymmetric stresses. The individual spherical particles of an ER suspension have no body-couple since the dipole moment and the electric field are aligned. The chain of particles, however, does have a net torque trying to realign the particles with the electric field. Considering each chain as a particle, there are then indeed body-couples, and thus there are asymmetric stresses. Close examination of $-n\langle \mathbf{x}\mathbf{F}^{\mathbf{P}} \rangle$ in the forthcoming simulations does show the stresses to be asymmetric. This is, however, not of much importance for an ER device where the simple shear flow is always perpendicular to the applied electric field.

6.3 Simulation Method: Electrostatic Interparticle Forces

The exact electrostatic interparticle forces in an ER suspension can be computed from the solution of the many-body potential problem and the integration of Maxwell stresses over each particle. This is practically impossible, however, for anything more than two spherical particles. There is an alternative method that avoids the need for detailed knowledge of the local potential field that is quite simple and elegant using the electrostatic energy of the system. Since the electrostatic interparticle force is conservative, the force on any particle is the negative of the gradient of the electrostatic energy with respect to the particle's position, and this energy can be written in terms of the system capacitance matrix.

Recall that the energy of a system of charged particles in the absence of an electric field is one-half the sum of the product of the particle charges and their potentials (Jackson 1975, Landau & Lifshitz 1984). For charge-free particles in an electric field, the electrostatic energy is analogously given by (Landau & Lifshitz),

$$\mathcal{U} = \frac{1}{2V}\sum_{\alpha}\mathbf{S}_{\mathrm{E}}^{\alpha}\cdot\mathbf{E} = \frac{1}{2V}\mathbf{S}_{E}\cdot\mathcal{E}. \tag{6.16}$$

Here $\mathcal{U}$ is the energy per unit volume for a system of N particles in a volume V. The induced dipole on particle α is $\mathbf{S}_{\mathrm{E}}^{\alpha}$ and $\mathbf{E}$ is the macroscopic applied electric field. The slightly more compact form on the RHS has $\mathbf{S}_E$ as the vector containing the $3N$ components of all the particle dipoles and $\mathcal{E}$ as the complementary $3N$ electric field vector.

Since Laplace's equation and the boundary conditions are linear in the electric field, we know that

$$\mathbf{S}_E = \hat{\mathbf{C}}(\mathbf{x})\cdot\mathcal{E}, \tag{6.17}$$

where $\hat{\mathbf{C}}(\mathbf{x})$ is the dipole-electric field capacitance matrix for charge-free particles and the $\mathbf{x}$ reminds us that, as we shall see, it is a function of the instantaneous particle positions. The capacitance matrix for charge-free particles can be determined directly from equation (2.25) as

$$\hat{\mathbf{C}}(\mathbf{x}) = \mathbf{C}_{S\varphi}\cdot(\mathbf{C}_{q\varphi})^{-1}\cdot\mathbf{C}_{qE} - \mathbf{C}_{SE}. \tag{6.18}$$

In Chapter 2 we described how the various submatrices can be accurately computed over the entire concentration range given the particle configuration, and thus we completely know $\hat{\mathbf{C}}(\mathbf{x})$ and the electrostatic energy. Then from classical physics, the force on particle α is

$$\mathbf{F}^{\alpha} = -\frac{\partial \mathcal{U}(\mathbf{x})}{\partial \mathbf{x}_{\alpha}} = -\frac{1}{2}\mathcal{E} \cdot \frac{\partial \hat{\mathbf{C}}(\mathbf{x})}{\partial \mathbf{x}_{\alpha}} \cdot \mathcal{E}, \tag{6.19}$$

and similarly the torque on the particle is

$$\mathbf{T}^{\alpha} = -\frac{\partial \mathcal{U}(\mathbf{x})}{\partial \psi_{\alpha}} = -\frac{1}{2}\mathcal{E} \cdot \frac{\partial \hat{\mathbf{C}}(\mathbf{x})}{\partial \psi_{\alpha}} \cdot \mathcal{E}, \tag{6.20}$$

where $\mathbf{x}_{\alpha}$ and ψ_{α} is the particle's position and Euler angle vectors. Here we see clearly that there is no torque on a spherical particle since its Euler angle is irrelevant to its dipole strength and the system electrostatic energy. Also note that both the energy and the interparticle force scales with the square of the electric field.

The capacitance matrix includes both the far- and near-field interactions, as do the interparticle forces. The near-field interactions are in fact quite strong and for perfect conductors ($\epsilon_p/\epsilon = \infty$) the interparticle force scales as $O(\xi^{-1})$ for nearby particles as shown by Jeffrey (1978). This singularity is captured by the energy formulation. Recall that the dipoles for two particles near contact in an electric field are $O(ln\xi)$. Thus from equation (6.16), the energy is also $O(ln\xi)$, and so the derivative of the energy with respect to separation or force is $O(\xi^{-1})$. The near-field interactions are smaller for the more modest dielectric constant ratios, but there is still an enhancement in the interparticle force over the many-body far-field effects.

It is interesting to know the form of the resulting force if no near-field interactions are included in the capacitance matrix. Using just the potential matrix of equation (2.24), we find that

$$\mathbf{S}_E = \mathbf{M}_{ES}^{-1} \cdot \mathcal{E}, \tag{6.21}$$

and thus

$$\mathbf{F}^{\alpha} = -\frac{1}{2}\mathcal{E} \cdot \frac{\partial \mathbf{M}_{ES}^{-1}}{\partial \mathbf{x}_{\alpha}} \cdot \mathcal{E}. \tag{6.22}$$

A similar expression can be written for the torque. Because we can determine $\mathbf{M}_{ES}$ more readily than its inverse, we rewrite equation (6.22) to remove the derivative of the invert using a matrix identity to yield,

$$\mathbf{F}^{\alpha} = \frac{1}{2}\mathcal{E} \cdot \mathbf{M}_{ES}^{-1} \cdot \frac{\partial \mathbf{M}_{ES}}{\partial \mathbf{x}_{\alpha}} \cdot \mathbf{M}_{ES}^{-1} \cdot \mathcal{E}. \tag{6.23}$$

Using equation (6.21) and the fact that $\mathbf{M}_{ES}^{-1}$ is symmetric, equation (6.23) becomes,

$$\mathbf{F}^{\alpha} = \frac{1}{2}\mathbf{S}_{E} \cdot \frac{\partial \mathbf{M}_{ES}}{\partial \mathbf{x}} \cdot \mathbf{S}_{E}. \tag{6.24}$$

Finally, using equation (2.38) we can expand (6.24) with a bit of algebra to yield,

$$\mathbf{F}^{\alpha} = \mathbf{S}_{\mathrm{E}}^{\alpha} \cdot \sum_{\substack{\beta=1 \\ \beta \neq \alpha}}^{N} \nabla\nabla\nabla \frac{1}{r} \cdot \mathbf{S}_{\mathrm{E}}^{\beta}, \tag{6.25}$$

where $r = |\mathbf{x}_{\alpha} - \mathbf{x}_{\beta}|$ is the center to center distance between particles α and β. Thus given the particle dipoles, computed from the potential invert, and the particle positions, we can compute the far-field approximation to the electrostatic interparticle force with equation (6.25).

It is also interesting to see how our method for computing the force compares to the methods employed by Klingenberg, Van Swol, & Zukoski (1989) and Whittle (1990). The basis of their method is a multipole expansion of the particle forces. From Jackson (1975) the force on a particle with some charge distribution is approximately given by,

$$\mathbf{F}^{\alpha} = q_{\alpha}\mathbf{E}(\mathbf{x}_{\alpha}) + \mathbf{S}_{\mathrm{E}}^{\alpha} \cdot \nabla\mathbf{E}(\mathbf{x}_{\alpha}) + \ldots, \tag{6.26}$$

where $\mathbf{E}(\mathbf{x}_{\alpha})$ is the local electric field evaluated at the center of particle α. Equation (6.26) neglects higher order moments of the charge distribution and higher order variations in the local electric field. For N charge free particles, the local gradient of the electric field is approximately given by equation (2.36),

$$\nabla\mathbf{E}(\mathbf{x}_{\alpha}) = \sum_{\substack{\beta=1 \\ \beta \neq \alpha}}^{N} \nabla\nabla\nabla \frac{1}{r} \cdot \mathbf{S}_{\mathrm{E}}^{\beta} + \ldots, \tag{6.27}$$

Equation (6.27) also ignores the higher multipoles of the charge distribution and higher order variations in the local electric field. Thus combining equation (6.26) with (6.23) yields the force on a charge free particle, namely,

$$\mathbf{F}^{\alpha} = \mathbf{S}_{\mathrm{E}}^{\alpha} \cdot \sum_{\substack{\beta=1 \\ \beta \neq \alpha}}^{N} \nabla\nabla\nabla \frac{1}{r} \cdot \mathbf{S}_{\mathrm{E}}^{\beta} + \ldots, \tag{6.28}$$

which is exactly what we derived in equation (6.25). We see that our method, using only the potential matrix invert, is equivalent to a moment expansion of the force up to the dipole level. The addition of the two-body interactions into the capacitance matrix then includes the effects of the infinite sum of the remaining higher moments and captures the near-field effects that are important for high dielectric constant particles near contact.

Klingenberg *et al.* employ equation (6.28) but use the induced dipole of an isolated particle in an electric field, so all the particles have the identical dipole strength. Hence, they neglect many-body far-field interactions as well as the near-field interactions. Klingenberg (1990) has recently augmented his method to include a few higher moments in equations (6.28) to capture some of the near-field interactions. Whittle (1990) uses a method similar to Klingenberg *et al.* as the basis to compute the interparticle forces, however, he includes an *ad hoc* force field to capture the near-field interactions.

Unfortunately, there are limited results available to compare against the many-body electrostatic force computed from the energy formulation via the capacitance matrix. In fact the only results for modest dielectric constant ratios (10 or less) are the forces for two identical spherical particles in an electric field computed by Klingenberg and presented in Gast & Zukoski (1989). The force is represented by three functions $f_{\|}, f_{\perp}$, and f_{Γ}, of center to center separation, r, in the equation

$$\mathbf{F}^{\alpha} = 12\pi\epsilon_p(\beta E)^2 a^2 \left(\frac{a}{r}\right)^4 \left\{(2f_{\|}\cos^2\theta - f_{\perp}\sin^2\theta)\mathbf{e}_{\mathrm{r}} + f_{\Gamma}\sin 2\theta \mathbf{e}_{\theta}\right\}. \tag{6.29}$$

Here θ is the angle between the sphere line of centers and the applied electric field, $\mathbf{e}_{\mathrm{r}}$ is the unit vector along the sphere line of centers, and $\mathbf{e}_{\theta}$ is the azimuthal unit

vector. Table 6.I lists the results using the energy formulation with and without the addition of near-field effects with those of Klingenberg for $\epsilon_p/\epsilon = 2$ and 10. The energy method results are in excellent agreement with Klingenberg's data with the near-field interactions. Without the near-field interactions the predicted forces are (within 15%) for separations as close as 2.2 sphere radii. The error is greater for the higher dielectric constant ratio as the near-field interactions become more important. When the particles are near contact the error is approximately 25% for $\epsilon_p/\epsilon = 2$ and 71% for $\epsilon_p/\epsilon = 10$. However, the absence of near-field effects is still superior to that of point dipoles. For point dipoles the force functions are unity for all particle separations, while (6.25) gives the correct result in the far-field since the many-body interactions are still included.

With the electrostatic interparticle forces, we can now implement the dynamic simulation and do so in the next section to study the dynamics and rheology of an ER suspension

6.4 Rheology and Microstructure of a Monolayer

6.4.1 Introductory Remarks

We applied the simulation outlined in the preceding section to an unbounded monolayer of dielectric spheres with the electric field in the y direction and the shear flow in the x direction as illustrated in Figure 6.4. A monolayer is studied for a few reasons. The microstructure is more easily visualized with video animations and instantaneous "snapshots" of the particle configurations. Using the monolayer system also reduces the computation time by almost a factor of eight compared to a full three-dimensional simulation. It still, however, retains much of the underlying physics of the problem as we shall see. Also, although the particle centers are confined to a two-dimensional plane (not by applied forces but simply by the symmetry of the hydrodynamic interactions), the interactions are those of three-dimensional spheres. To simulate an unbounded infinite suspension, we apply periodic boundary conditions to a periodic cell containing N particles. Note that in order to sum the three-dimensional interactions, the sheet of particles must also be replicated in the z direction as well. The sheets are placed far enough apart such that the measured effective viscosities are no longer a function of the separation. A distance 16 particle radii between the sheets was more than sufficient.

From equation (6.6), in order to compute a viscosity for the monolayer, we need the number density of particles, which requires a volume for the N particles in the sheet of a periodic cell. We choose this volume to be the product of the area of the periodic cell and twice the particle radius, or the thickness of the monolayer. The bulk shear is in the xy-plane ($\mathbf{U}^\infty = \dot{\gamma} y \mathbf{e}_x$), so the total relative viscosity, η^T, the viscosity of the suspension divided by the viscosity of the fluid, is the proportionality between the yx components of the strain and the bulk stress, *i.e.*,

$$\eta^T = \eta^H + \eta^{S^P} + \eta^{XF}, \tag{6.30}$$

where,

$$\eta^H = 1 + \frac{5}{3} c_A \frac{1}{N} \sum_{\alpha=1}^{N} (\mathbf{S}_\alpha^H)_{yx}, \tag{6.31a}$$

$$\eta^{S^P} = \frac{5}{3} c_A \frac{1}{MaN} \sum_{\alpha=1}^{N} (\mathbf{S}_\alpha^P)_{yx}. \tag{6.31b}$$

$$\eta^{XF} = \frac{5}{3} c_A \frac{1}{Ma2N} \sum_{\alpha}^{N} \sum_{\beta}^{N} [(\mathbf{x}_\alpha - \mathbf{x}_\beta)\mathbf{f}^{\alpha\beta}]_{yx}. \tag{6.31c}$$

The areal fraction of the monolayer is c_A. We shall call η^H the hydrodynamic viscosity, which includes the fluid contribution of unity in equation (6.31a), η^{S^P} the particle viscosity, and η^{XF} as the $\mathbf{xF^P}$ viscosity. Note both the particle and $\mathbf{xF^P}$ viscosity are proportional to Ma^{-1}, and we shall sometimes refer to their combination as η^{ER}, the ER viscosity. The stresslet in equation (6.31) has been non-dimensionalized such that an isolated sphere in the monolayer gives a hydrodynamic contribution to the relative viscosity of $\frac{5}{3}c_A$, which is the monolayer equivalent of the Einstein viscosity.

6.4.2 Sphere Ordering in an Electric Field

An initial test of the simulation was to see if particle chaining was observed and to compare the predicted chaining time to experimental observations. The spheres were placed randomly within the periodic cell monolayer and allowed to order under the action of an applied electric field. Figure 6.5 illustrates the progressive development of a microstructure for 25 particles at an areal fraction of 0.4, and the $Ma = 10^{-3}$. Since there is no shear flow, the choice of Ma is arbitrary in so far as the time scales as $\dot{\gamma}^{-1} = Ma^{-1}\eta/(2\epsilon(\beta E)^2)$ in the simulation. The drawn square is the outline of the periodic cell. By $t = 0.1$ at least two complete chains have formed and aligned with the electric field. In comparing Figures 6.5*a* to 6.5*b*, we see the aggregation of nearest neighbors as described in the introduction. Particles G-K-P have rotated and aligned with the electric field, and particles W-V-U-Y have formed an aligned cluster as well. By $t = 0.2$ particle I has connected the two complete chains of the previously illustrated time, and particles W and Q have connected to form a third percolating chain. Continuing for longer times, we see at $t = 2.5$ that the third chain on the left of the periodic box has moved toward the larger chain doublet, and by $t = 2.7$ the three chains have formed a chain triplet with one or

two particle bridges. Note that the third chain moves down as well.

At first we might think this counter to the arguments made in the introduction that particles whose line of centers is perpendicular to the electric field repel one another. While this is true for particles directly apart from each other, a particle in one chain also experiences attractive forces from the particles above and below its direct opposite in the other chain. In fact there is then a net attraction that causes the chains to approach one another. The time for approach, as we see, is much slower than initial chain formation because the hydrodynamic resistance is much larger for this long rod-like body while the electrostatic forces are no greater.

From our simulation we can estimate the chaining time in an ER fluid. The dimensional chaining time is the simulation chaining time multiplied by $Ma^{-1}\eta/2\epsilon(\beta E)^2$. Marshall, Goodwin, & Zukoski (1989) used an ER fluid with $\eta \approx 0.01$ Pa-s, $\epsilon = 8 \times 8.854 \times 10^{-2}$ farad/m, and an electric field of about 1kV/mm. For a simulation chaining time of 0.1, the dimensional chaining time is about 0.03 seconds. Marshall *et al.* report that the ER suspension "sets up" in less than 0.1 seconds which is consistent with our simulation results. Further we estimate the dimensional aggregation time of two chains to be approximately 0.8 seconds or about 26 times longer than the chaining time, no doubt due to the greater hydrodynamic resistance of the chains.

Experimentally, Conrad, Fisher, & Sprecher (1990) have observed chains of multiple particle thickness. After a short time, though, the chains do not grow in thickness. It is observed that the particles near the electrodes are practically forever attached to the metal surface while there is an electric field. This is probably due to both the strong electrostatic forces with the metallic surface and surface roughness of both the particles and electrodes. The simulation chains will grow no thicker since the periodic boundary conditions preclude the addition of any other chains.

6.4.3 Dynamic Simulation Results: Effective Viscosity

Several dynamic simulations were performed on an infinite, unbounded monolayer of spherical particles with a particle to the fluid dielectric constant ratio of 4. The periodic cell was square in shape, and there were 25 particles per cell. The simulations were performed with and without the addition of the near-field electrostatic interactions, though near-field hydrodynamic interactions were always included since they are necessary to prevent particle overlap. The simulation times, T, were typically 10.0 (non-dimensionalized by the shear rate) but were sometimes less. In all cases the reported average of the effective viscosities had reached steady-state values. The summary of the effective viscosities are presented in Figure 6.6 and Table 6.II. The 95% confidence limits on the effective viscosities are presented in Table 6.III. Simulations were also performed on 49 particles in a square periodic cell as listed in Table 6.II. There is little difference in the predicted effective viscosities between 25 and 49 particles.

The total viscosity increases with decreasing Ma with and without the addition of near-field electrostatic interactions. In fact the viscosity scales as the inverse of Ma for small Ma, or, equivalently, the viscosity scales with the square of the applied electric field as observed experimentally. The hydrodynamic viscosity, the contribution due to the resistance to deformation of the particles, increases with decreasing Ma up until about $Ma = 2 \times 10^{-4}$ where it appears to reach a plateau value of about 100. The ER viscosity steadily increases with decreasing Ma over the entire range presented here. At high Ma, when the viscous forces dominate, the viscosity is practically entirely the hydrodynamic contribution. Note the total viscosity is approximately equal to the $Ma = \infty$ limit (pure shear, no electrostatics) at about $Ma = 10^{-1}$. As the Ma decreases, the ER viscosity contribution to the total viscosity steadily increases and eventually dominates at $Ma = 2 \times 10^{-4}$. The difference in the effective viscosities computed with and without the near-field electrostatic interactions is only about 20% at the smallest Ma of 1×10^{-4}. At this Ma the hydrodynamic viscosity is about the same independent of the addition of near-field electrostatic interactions, so the entire increase is due to the increased

electrostatic interactions and not to any fundamental changes to the microstructure. This rather small difference is due to the modest dielectric constant ratio here, which is actually typical of an ER fluid. It is expected that for higher dielectric constant ratios, the addition of the near-field interactions would become more important, especially since the interactions are singular for $\epsilon_p/\epsilon = \infty$. The importance of the dielectric constant ratio on the rheology is examined in greater detail in Chapter 7.

The total viscosities are converted into the shear stresses in Figure 6.7 by multiplying them by the appropriate Ma. This shear stress-shear rate plot has the asymptotic features of the Bingham plastic model for the shear stress. The shear stress approaches a constant value or Bingham yield stress at small Ma or shear rates. At high Ma or shear rates the viscosity increases linearly, as a Newtonian fluid. Here the shear stress is non-dimensionalized by $2\epsilon(\beta E)^2$, and we see the Bingham yield stress scales with the square of the electric field as observed by Uejima (1972) and Marshall *et al.* (1989).

Although the shear stress-shear rate plot has the asymptotic features of a Bingham plastic, the Bingham shear stress model does not match the rheological data well for all Ma. The Bingham model plotted in Figure 6.7 assumes a yield stress of 0.12 and a plastic viscosity of 2.85, the infinite Ma limit of the viscosity. This model underestimates the shear stress in the intermediate Ma region of 10^{-1} to 10^{-3}. From the data in Figure 6.7, the ER stress ($\eta^{ER}Ma$) is effectively the dynamic yield stress as Ma vanishes, and the hydrodynamic viscosity is the plastic viscosity. This plastic viscosity, however, is not independent of Ma. It has two different plateau values at the extremes and is shear thinning in the intermediate region. The value of the plastic viscosity is inconsequential at low Ma where the dynamic yield stress dominates the stress and at high Ma the hydrodynamic viscosity times the shear rate dominates the stress, so the stress at the extremes is modeled well by a Bingham shear stress model with the above parameters. However, since the plastic viscosity shear thins in the intermediate region, the true plastic viscosity of the Bingham model actually increases in the intermediate region increasing the viscosity compared to the Bingham model. The actual shear stress equation should

be

$$\tau = \tau_B + \eta_B(\dot{\gamma})\dot{\gamma}, \tag{6.32}$$

to take account of the varying behavior of the plastic viscosity.

Figures 6.8-6.11 are time traces of the four different viscosities of the suspension at $Ma = \infty, 10^{-2}, 10^{-3}$, and 10^{-4}. The heavy dotted lines are the average or running average viscosity up to that particular time. For all but the last Ma, near-field electrostatic interactions are not included. The time traces are actually qualitatively similar at identical Ma irrespective of the addition of electrostatic interparticle forces. For $Ma \geq 10^{-3}$ the initial particle configuration was randomly selected by Monte Carlo methods. For the smaller Ma the configuration in Figure 6.5*c* was the initial position of the particles.

For the infinite Ma there is only the hydrodynamic viscosity as seen in Figure 6.8. The viscosity slowly increases and mildly fluctuates about its mean of 2.85. It takes about 7 time units to reach this steady state as the initial random microstructure is distorted into the shear configuration. (See Figure 6.12.) As the Ma decreases, the magnitude of the four viscosities increases. The fluctuations of the four viscosities increase dramatically as well. These large excursions are mostly due to large excursions in the hydrodynamic viscosity, but there are also large variations in the other viscosities at these times as well. The time to reach steady state appears to be much smaller for the lower Ma and is about 3 or 4 time units.

The hydrodynamic viscosity, η^H, is, of course, always positive, but the particle viscosity, η^{S^P}, is mostly negative as expected from the discussion in §6.2.2. The $\mathbf{xF^P}$ viscosity, η^{XF}, is mostly positive, though it too is negative sometimes, particularly near the rapid fluctuations. The net or total viscosity is positive for most of the time. These occasionally negative total viscosities, η^T, and large excursions reflect the limitation of the finite number of particles in the simulation. A real system would sample several thousand particles and the net fluctuations would be much smaller. The average values, however, are still reasonable, especially in light of the forthcoming comparison to experimental results.

To best interpret these time traces, we must examine the microstructure of the

suspension. A video animation of the dynamic simulations is the best visual aid to see how the microstructure changes with Ma and to correlate the motion of the particles to the viscosities. Such a video animation has been made in conjunction with Dr. Andrew Kraynik at the Sandia National Laboratories and has been extremely helpful in understanding ER fluids. Here we present only selected snapshots of the suspension microstructure to describe the dynamics of the suspension and relate it to the rheology, though we shall refer to observations from the video as well. In the snapshots the average electric field extends from the bottom to the top of the page and the shear flow is from left to right. Again, the outlined box is the periodic cell which is sometimes distorted due to the shear motion. In the simulations the periodic cell is arbitrarily reset at a strain or, equivalently, a time of unity.

Figure 6.12*a* is the initial Monte Carlo generated configuration for $Ma = \infty$. The particles are fairly randomly dispersed throughout the periodic cell. Figure 6.12*b* depicts the microstructure after a time of 10. There is a bit more structure in this ending configuration, and it is readily apparent from the video animation. Particles tend to be driven toward each other along the axis of compression of the shear flow (top left corner to the lower right corner) and away from each other along the axis of extension of the flow (bottom left corner to the upper right corner). This suspension, however, is relatively structureless compared to those with an applied electric field. Recall, the viscosity is about 2.85.

Figures 6.13($a - d$) are snapshots of the microstructure for $Ma = 10^{-2}$. In Figure 6.13*a* at $t = 1.4$, we see the chain structure roughly aligned with the electric field. It is slightly distorted off the axis of the electric field due to the shear flow. At this point the total viscosity is about 25 and, as seen in Figure 6.9, is mostly due to the hydrodynamic viscosity of about 20, with the total ER contribution of about 5. Based upon the rheology, the hydrodynamic forces are still substantial compared to the electrostatic forces despite the rather small Ma. The electrostatics, however, have altered the microstructure as seen by comparing Figure 6.13*a* to Figure 6.12*b*, especially in the formation of percolating clusters that span the periodic cell, and thus increase the hydrodynamic viscosity. Since the particles are perfectly rigid,

they are extremely good conductors of stress. Since viscosity can be interpreted as the ability to transmit stress across a velocity gradient, it is not surprising that the hydrodynamic viscosity, which measures this contribution, is large when there are the efficient stress transmission paths provided by the percolating clusters. The hydrodynamic viscosity excursions seen in all the time traces are in fact correlated to the formation of these percolating structures with the particles in very close contact. The lubrication forces that prevent overlap also generate extremely large stresses for particles near contact and in relative motion. These stresses increase with decreasing particle spacing which decreases with Ma.

From the microstructure the electrostatic forces here are still rather weak compared to the hydrodynamic forces. In Figure 6.13*b* at $t = 2.0$, the chain B-I-C-S-V has dislodged the Q-A-N-K chain (think of the U particle as stationary) due to the hydrodynamic forces of the shear flow. Electrostatics still play a role in the general chain-like structure and the alignment of dangling chains as seen in Figure 6.13*c* at $t = 2.50$. Here chain segment X-P-T has aligned with the electric field and connected to its periodic image. The viscosity here has dropped since particle M and U are not in contact and the chain of cluster no longer percolates across the shear flow of the periodic cell. By $t = 3.6$ as shown in Figure 6.13*d* the structure again percolates, and the viscosity increases to about 25. Note that the deviation of the chains from alignment with the electric field is fairly constant. As mentioned in §6.2, the ER viscosity is due to torque on the chains trying to realign themselves with the electric field.

Probably the most dramatic change in the microstructure occurs at $Ma \leq 2 \times 10^{-4}$. At these Ma there are two distinct kinds of deformation of the suspension microstructure. For initially aligned chains the suspension is rigid and appears to deform like an elastic body. Figures 6.14$(a - b)$ show the configuration of the suspension for $Ma = 1 \times 10^{-4}$ at $t = 4.5$ and 4.6. Although not well represented here, the motion of the chains is almost affine. As the deformation continues, the effective viscosity increases because of the increasing η^{XF} due to the straining of the chains as seen in Figure 6.11*d*. At a critical strain, here occurring at about

$t = 4.95$, there is a second type of motion. The chain breaks in half or "snaps" in two and rapidly translates through the fluid until it runs into its periodic image as shown in Figures 6.14$(c-d)$ at times $t = 4.95$ and 5.00. This time scale is much shorter than that of the inverse shear rate and is proportional to the $\dot{\gamma}^{-1}Ma$ since it is motion driven by the electrostatic forces on the particles. Note also that η^{XF} has dropped dramatically as well since the chain has gone from a highly strained state to an almost aligned state. The other viscosities also fluctuate dramatically during this rapid reconfiguration. At $t = 4.95$ η^{H} increases because now the particles at the breaking point can move rapidly by one another in a shear-like motion unlike during the elastic-body-like deformation when relative motion was impossible since the particles were all packed tightly together. The hydrodynamic viscosity drops back down when the chain reforms and the particles can no longer move relative to one another again. The η^{S^P} also changes and actually increases and decreases rapidly at this point. The increases in the particle stress at this point can be attributed to the rapid translation of the chain counter the bulk shear flow which resists the bulk motion.

This interchain rearrangement is actually one of three types of rapid microstructural rearrangements observed in the simulation of the ER fluids at small Ma. The other two, both preceded by the slow, elastic-body like deformation, are intrachain rearrangements and network rearrangements. The intrachain rearrangement is depicted in Figures 6.15$a-c$. The microstructure has slowly deformed and from Figures 6.15$a-b$, particle H has rolled over particle Q, increasing the η^{XF} as seen in Figure 6.11. Then between $t = 6.55$ and 6.60 the chain rapidly jumps over so now particles C and Q are in contact. The η^{XF} has also dropped precipitously at this point. Note that there is also the rapid delta function-like increases of the other viscosities. The network rearrangement is illustrated by the sequence of snapshots in Figure 6.16$a-c$. The strained microstructure in Figure 6.16a at $t = 7.25$ is strained to the point where it forms a network illustrated in Figure 6.16b at $t = 7.30$. After a short while, again on a much faster time scale determined not by the shear rate but by $\dot{\gamma}^{-1}Ma$, the network breaks or snaps as particles L and B-C break free from

one another as seen in Figure 6.16*c* at $t = 7.30$. There is also the dramatic drop in η^{XF} and the fluctuations of the other viscosities. Thus we see that all three rapid microstructural reconfigurations – interchain, intrachain, and network rearrangement – all have similar manifestations in the instantaneous viscosities. From here on out all three rearrangements will be sometimes referred to as "snapping" of the microstructure.

Although not readily apparent from the time traces of the viscosities for 25 particles (but from the video animations) these rapid reconfigurations are not dramatic (i.e., very fast) until about $Ma \leq 2 \times 10^{-4}$, which is about the Ma where the hydrodynamic viscosity plateaus. Similar microstructural reconfigurations as shown in Figures 6.14 to 6.16 are also seen at $Ma = 2 \times 10^{-4}$. Since the average microstructure is here independent of Ma, then the average hydrodynamic viscosity is also independent of Ma as observed by its upper plateau value. Thus the shear thinning of the hydrodynamic or plastic viscosity at intermediate Ma is the shear induced breakdown or melting of the average microstructure for low Ma.

We also note here that the slow straining and rapid reconfigurations are exceptionally dramatic and well portrayed in the video animations of nine particles. This is due to the fact that nine particles form shorter chains that translate more quickly when they break in half. The effect of chain length on the time scale for the snapping of the microstructure might explain why such a low Ma is needed to observe an ER response, i.e., viscosity growing as the square of the electric field. The Ma number is a ratio of the viscous forces to the electrostatic forces, and the length scale for characterizing the hydrodynamic resistance is the radius of a sphere making up the particle chains. In fact the hydrodynamic resistance should be characterized by some function appropriate for a rod-like chain that increases with the length of the chain and its aspect ratio. This will be, of course, greater than the sphere radius. This new Ma would be much larger and closer to the $O(1)$ value expected at the transition point rather than the $O(0.01)$ value observed in Figure 6.6.

Finally, it is worthwhile to examine the electrostatic energy of the suspension

$\mathcal{U}$ for the different Ma. Figure 6.17 illustrates the time trace of the energy for $Ma = 10^{-2}, 10^{-3}, 2 \times 10^{-4}$, and 10^{-4}. For the largest Ma number the energy rises and falls in a rather smooth fashion. As Ma decreases, the energy drops more rapidly after slowly increasing. By the smaller values of the Ma numbers, the energy drops are quite dramatic. In fact the time trace of the energy is probably the best lumped representation of the dynamics of the microstructure at low Ma. The slowly increasing energy of the system corresponds to the relatively slow elastic-body-like deformation, and the precipitous drop in the electrostatic energy occurs when the microstructure rapidly reconfigures or snaps. This connection between the macroscopic energy and the microstructure's dynamics implies that energy is being stored during the elastic-body-like deformation and viscously dissipated during the snapping process.

The behavior of the microstructure and the energy also makes us suspect that the energy jumps and the Bingham or dynamic yield stress are related. The rapid reconfigurations and the dominance of the ER viscosity or stress on the rheology both occur at $Ma \leq 2 \times 10^{-4}$. The yield stress although often interpreted as a force per unit area is also an energy per unit volume as is $\mathcal{U}$. Further, both the yield stress and the energy jumps scale as $2\epsilon(\beta E)^2$. At this point it is only supposition, but in Chapter 7 we show through a total energy balance that indeed the yield stress is proportional to the energy jumps and the proportionality is given by the frequency of the snapping of the microstructure.

6.4.4 Dynamics Simulation Results: First Normal Stress Difference

In addition to the shear viscosity, the first normal stress difference of the suspension can be computed from the bulk stress. Like the shear viscosity, the total first normal stress difference, χ^T is given by,

$$\chi^T = \chi^H + \chi^{ER}, \tag{6.33}$$

where

$$\chi^T = \langle \Sigma_{xx} \rangle - \langle \Sigma_{yy} \rangle, \tag{6.34}$$

so

$$\chi^H = \frac{5}{3} c_A \frac{1}{N} \sum_{\alpha=1}^{N} [(\mathbf{S}_\alpha^H)_{xx} - (\mathbf{S}_\alpha^H)_{yy}], \tag{6.35a}$$

$$\chi^{ER} = \frac{5}{3} c_A \frac{1}{MaN} \sum_{\alpha=1}^{N} [(\mathbf{S}_\alpha^P)_{xx} - (\mathbf{S}_\alpha^P)_{yy}] - \frac{5}{3} c_A \frac{1}{Ma2N} \sum_{\alpha}^{N} \sum_{\beta}^{N} [(\mathbf{x}_\alpha - \mathbf{x}_\beta)\mathbf{f}^{\alpha\beta}]_{xx} - [(\mathbf{x}_\alpha - \mathbf{x}_\beta)\mathbf{f}^{\alpha\beta}]_{yy}. \tag{6.35b}$$

The hydrodynamic normal stress difference is χ^H, and here the particle stress and thermodynamic contributions have been lumped into a single ER normal stress difference, χ^{ER}. Since the electrostatic forces in the z direction are not needed for the dynamic simulation, they are not computed, so the second normal stress difference is not known. The first normal stress differences for different Ma are listed in Table 6.IV and plotted in Figure 6.18. Note that the normal stress difference is nondimensionalized by $\eta\dot{\gamma}$. From Figure 6.18 the first normal stress difference is practically zero for no electric field, as expected for a hard-sphere suspension of force-free particles. As Ma decreases, χ^T becomes increasingly negative, and in fact grows in magnitude with the square of the electric field or as Ma^{-1}. The χ^H is on average positive while the χ^{ER} is on average negative. The existence of the first normal difference indicates the anisotropic character of the ER fluid.

This negative normal stress difference is not surprising in light of the strong attractive forces holding the chains together. The normal stress due to the electrostatic forces in the x direction is practically zero since the chains are far apart. The

normal stress due to electrostatics in the y direction is very large since the particles in the chains are attracted to one another along the y axis. Thus the difference between the xx and yy normal stresses, χ^{ER}, is negative, and since they are driven by the electrostatic forces, they scale with the square of the electric field. The positive χ^{H} is due to the lubricating film pressures countering the motion of the particles. The χ^{ER} normal stress difference, however, dominates. From the table note that the fluctuations are extremely large.

Time traces of the first normal stress difference for $Ma = 10^{-2}$ and 10^{-4} are plotted in Figures 6.19 and 6.20. The large fluctuations are readily apparent from these time traces. Like the effective viscosities, the dramatic fluctuations at $Ma = 10^{-4}$ are due to the rapid microstructural reconfigurations. At the larger Ma, the fluctuations are less dramatic since the electrostatic forces are not so large compared to the hydrodynamic forces.

The normal stresses can be quite large for an ER device, however, the actual mechanical requirements are quite modest, so normal stress differences are probably not key design considerations.

6.4.5 Comparison to Experimental Results

We compare the simulation effective viscosity to the experimental results of Marshall, Goodwin, & Zukoski (1989). Their ER fluid consists of hydrated poly (methacrylate) particles in a chlorinated hydrocarbon oil, and the effective viscosities were measured over a large range of Ma numbers. To compare the simulation results to their experimental results, the monolayer areal fraction is converted to a volume fraction by multiplying c_A by two-thirds. This "two-thirds" rule is correct in the dilute limit where the Einstein viscosity correction is $\frac{5}{2}c$ in three-dimensions and $\frac{5}{3}c_A$ in a monolayer. It is approximately correct in the limit of closest packing where two-thirds of the maximum packing areal fraction of a two-dimensional lattice is very close to the maximum packing volume fraction for the three-dimensional analog lattice. For a two-dimensional square lattice, for example, the maximum areal fraction is $\frac{\pi}{4}$, and the maximum volume fraction for simple cubic lattice is $\frac{\pi}{6}$. Here the ratio of maximum areal fraction to volume fraction is exactly two-thirds. The simulation data then corresponds to an approximate volume fraction of $c = 0.27$. The closest volume fraction from the data reported was $c = 0.23$.

Figure 6.21 compares the simulation results, with and without near-field electrostatic interactions, to the experimental results. The comparison between the two is extremely good at both extremes of the Ma number. At the intermediate values of Ma, the simulation viscosities very slightly underpredict the experimental viscosities. The experimental suspensions, even in the absence of the electric field, has a yield stress at low shear rates due to some other interparticle colloidal forces. At low Ma these colloidal forces are unimportant where the electrostatic forces dominate. At the intermediate Ma numbers these colloidal forces might be as important as the electrostatic forces in altering the microstructure and changing the hydrodynamic viscosity as well as making their own contribution to the particle and thermodynamic viscosities as well. In any event the comparison is exceptionally good, and it appears that the simulation captures both the qualitative and quantitative features of an ER suspension.

6.4.6 Effects of Periodic Boundary Conditions

The successful comparison to experimental data is quite satisfying, but we wonder what effect periodic boundary conditions has on the effective viscosities computed with the simulation and why in spite of them the results are in such good quantitative agreement. From the video animations the periodic boundary conditions have a clear effect on the evolution of the microstructure. The interchain rearrangement or chain snapping occurs roughly with a period of one time unit or a strain of one periodic cell. When the chain snaps, it connects to its periodic image and the process, roughly speaking, repeats itself. The effective viscosities and especially the energy time traces also exhibit a periodicity of one or so for each slow deformation and chain snapping episode in the microstructure.

Klingenberg & Zukoski (1990) have experimentally observed the microstructure in an ER suspension by using a microscope and have made observations that are similar to those discussed in this chapter. They observed percolating chains of particles spanning the electrode gap, much like the percolating structures spanning the periodic cell. With the shear flow induced by the moving upper electrode, they observed that the chains do deform much like a elastic body until a critical strain at which point they snap in half. The upper broken chain then reconnects with the nearest forward lower half chain and the process repeats itself on a fairly regular frequency. Thus the periodic breaking and snapping of chains observed in the simulation is completely realistic. The critical strain observed by Klingenberg & Zukoski, however, varied from 0.4 to 0.6, unlike the critical strain of unity in the simulations. Clearly, here the periodic boundary conditions have had an influence on the critical strain and the snapping frequency. We show later in Chapter 7 that the exact value of the critical strain is not important for modest conductivity ratios which explains why the comparison between the experiments and the simulation is so good despite the difference.

Because of the periodic boundary conditions, the number of chains per periodic cell is only one. This is because initially distinct chains are brought near one another due to the shear flow, and chains coalesce due to the attraction discussed in §6.4.2.

This is seen for 25 particles and $Ma = 10^{-4}$ where the initial configuration is shown in Figure 6.5*c* with two chains, but later on in Figures 6.14-6.16, there is a single chain in the periodic cell. In the experiments the chains are observed to be almost permanently stuck to the walls due to the strong electrostatic force between the particles and the perfectly conducting metal plate. The chains will always coalesce into a single chain in the simulations since there are no walls pinning the chains. This also is confirmed for simulations in rectangular periodic cells. A few simulations were performed with 50 particles in a cell as high as the periodic cell for 25 particles but twice as long. The initially two percolating chains clumped together after only a time or strain of one. This clumping lowers the effective viscosity of the suspension compared to the 25 particle simulations as shown in Table 6.II. The difference increases as the Ma decreases. This is not surprising since the dynamics of the chains are not important except at the lower Ma. The decrease in the viscosity is caused by the decrease in the snapping frequency of the rapid reconfigurations of the chains which in Chapter 7 we show is proportional to the yield stress. The 50 particle chain is twice as far apart from its periodic image as the 25 particle chain, since the periodic cell is twice as long for the former than the latter. Thus, the snapping frequency is half as great, as is, in fact, the effective viscosity at $Ma = 10^{-4}$ for 50 particles compared to 25 particles. The reduction in the effective viscosity due to the chain clumping is also seen in the time trace of the 25 particle simulation at $Ma = 1 \times 10^{-4}$. Recall that here the initial starting configuration is that of Figure 6.5*c* with two separate chains. These chains clump together as we have discussed, and the running average viscosity actually decreases a small amount.

In using the simulation with periodic boundary conditions at low Ma, we have effectively modeled the ER fluid as a single chain surrounded by periodic images of itself. Evidently this captures the essential physics since the agreement between the simulation and experimental viscosities is extremely good. If the slow chain deformation and rapid reconfiguration are the most important dynamics, this is not surprising since the near-field interactions within the chain are accounted for

accurately, and the surrounding microstructure is basically chains like the periodic images. Thus the periodic boundary conditions used in the simulation are not unreasonable and in fact reflect the qualitative behavior of a real ER suspension between two metal plates. The simulations, however, should be interpreted as single chain simulations for low Ma.

6.5 Conclusions

We have presented a method for the dynamic simulation of an ER suspension subject to a simultaneous shear flow and orthogonal electric field. The Stokesian dynamics methodology accurately accounts for both the far- and near-field hydrodynamic interactions among the particles due to the electrostatic forces and the bulk shear flow. The conservative electrostatic interparticle forces were computed from a system electrostatic energy that was determined with the capacitance matrix developed in Chapter 2 for determining the effective conductivity of a suspension. Because the capacitance matrix contains both far- and near-field electrostatic interactions, the electrostatic forces do too. With the complete simulation the time evolved motion and the bulk rheology of the ER suspension were determined as a function of the Ma. The effective viscosity was found to scale as Ma^{-1} or with the square of the electric field for low Ma as observed in experiments. The material behaves approximately as a Bingham plastic except with a shear thinning plastic viscosity at Ma between 2×10^{-4} and 10^{-1}. The effective viscosities compared extremely well to experimental data which indicate the simulation effectively captures the physics qualitatively and quantitatively.

The dynamics of the motion were correlated with rheology and it was found that at $Ma \leq 2 \times 10^{-4}$ the microstructure began to exhibit two distinct motions, namely a slow elastic-body-like deformation and a rapid reconfiguration or snapping of the microstructure. This snapping of the microstructure coincides with a precipitous drop of η^{XF} and the electrostatic energy of the system. We suppose at this point that the slow strain and rapid snapping episodes are the key to the ER response and Bingham yield stress. How these microstructural changes and the jumps in the electrostatic energy are related to the Bingham or dynamic yield stress are developed in Chapter 7. This theory of the dynamic yield stress will be tested using the dynamic simulation described in this chapter.

Table 6.I

Comparison of Two-Sphere Force Functions

$\epsilon_p/\epsilon = 2.0$

		$f_{\|\|}$			$f_\perp$			f_r	
r/a	K	NF	FF	K	NF	FF	K	NF	FF
3.0	1.09	1.09	1.06	0.97	0.97	0.97	1.01	1.01	1.01
2.5	1.11	1.11	1.08	0.94	0.96	0.96	1.03	1.03	1.01
2.2	1.27	1.27	1.11	0.88	0.88	0.95	1.05	1.05	1.02
2.0	1.50	1.50	1.14	0.82	0.82	0.93	1.08	1.08	1.04

$\epsilon_p/\epsilon = 10.0$

		$f_{\|\|}$			$f_\perp$			f_r	
r/a	K	NF	FF	K	NF	FF	K	NF	FF
3.0	1.18	1.18	1.14	0.92	0.92	0.92	1.04	1.04	1.03
2.5	1.45	1.45	1.22	0.83	0.83	0.90	1.10	1.10	1.05
2.2	2.09	2.09	1.35	0.72	0.72	0.87	1.20	1.20	1.10
2.0	5.20	5.17	1.51	0.62	0.63	0.83	1.46	1.44	1.15

The Klingenberg data from Gast & Zukoski (1989) are under the heading "K." The "NF" and "FF" headings are for the energy formulation of the force with near-field interactions and with only far-field interactions.

Table 6.II

Dynamic Simulation Effective Viscosities

$N = 25$, No Near-Field Electrostatic Interactions

Ma	$\langle \eta^T \rangle$	$\langle \eta^H \rangle$	$\langle \eta_{SP} \rangle$	$\langle \eta^{XF} \rangle$	$\langle \eta^{ER} \rangle$	T
∞	2.85	2.85	0.0	0.0	0.0	10.1
10^{-1}	3.68	3.48	-0.10	0.30	0.20	10.1
5×10^{-2}	5.20	4.78	-0.24	0.66	0.42	6.0
2×10^{-2}	9.03	6.78	-2.16	4.41	2.25	10.1
10^{-2}	17.33	11.84	-4.40	9.89	5.49	10.1
5×10^{-3}	23.20	14.03	-8.04	17.21	9.17	3.0
2×10^{-3}	85.13	49.08	-12.09	48.14	36.05	10.1
10^{-3}	109.6	55.79	-23.67	77.43	53.76	10.1
2×10^{-4}	452.7	120.8	-14.61	346.5	331.9	5.1
10^{-4}	1055	90.26	-310.8	1275	964.2	10.1

$N = 25$, Near-Field Electrostatic Interactions

Ma	$\langle \eta^T \rangle$	$\langle \eta^H \rangle$	$\langle \eta_{SP} \rangle$	$\langle \eta^{XF} \rangle$	$\langle \eta^{ER} \rangle$	T
∞	2.85	2.85	0.0	0.0	0.0	10.1
10^{-1}	3.77	3.43	-0.19	0.53	0.34	10.1
10^{-2}	22.10	15.51	-12.89	19.48	6.59	10.1
10^{-3}	120.3	61.32	-29.74	88.68	58.94	10.1
2×10^{-4}	544.4	120.0	-344.6	769.0	424.4	4.1
10^{-4}	1248	102.7	-1593	2738	1145	8.85

Table 6.II, Continued

$N = 49$, No Near-Field Electrostatic Interactions

Ma	$\langle\eta^T\rangle$	$\langle\eta^H\rangle$	$\langle\eta_{SP}\rangle$	$\langle\eta^{XF}\rangle$	$\langle\eta^{ER}\rangle$	T
10^{-2}	13.15	8.42	-2.31	7.04	4.73	8.0
10^{-3}	114.0	52.06	-26.70	88.64	61.94	2.0

$N = 50$ (Rectangular Box), No Near-Field Electrostatic Interactions

Ma	$\langle\eta^T\rangle$	$\langle\eta^H\rangle$	$\langle\eta_{SP}\rangle$	$\langle\eta^{XF}\rangle$	$\langle\eta^{ER}\rangle$	T
10^{-2}	16.82	14.70	-1.84	3.96	2.12	22.0
10^{-3}	93.22	56.04	-12.00	49.18	37.18	10.0
10^{-4}	444.1	96.74	-123.7	471.1	347.4	2.6

All viscosities reported are relative to the suspending fluid viscosity, η. The time T is the time of the simulation and is non-dimensionalized with the shear rate, $\dot{\gamma}$. The time steps for each simulation varied from 10^{-3} for $Ma = \infty$ to 2×10^{-5} for $Ma = 1 \times 10^{-4}$. The smaller time steps are needed to resolve the rapid reconfigurations that occur on a much shorter time scale.

Table 6.III

95% Confidence Limits for Viscosities in Table 6.II

$N = 25$, No Near-Field Electrostatic Interactions

Ma	$\langle \eta^T \rangle$	$\langle \eta^H \rangle$	$\langle \eta_{S^p} \rangle$	$\langle \eta^{XF} \rangle$
∞	0.10	0.10	0.0	0.0
10^{-1}	0.11	0.11	0.05	0.10
5×10^{-2}	0.11	0.13	0.13	0.09
2×10^{-2}	0.22	0.18	0.08	0.11
10^{-2}	0.68	0.59	0.19	0.18
5×10^{-3}	1.01	1.14	0.93	0.43
2×10^{-3}	5.48	4.85	1.54	0.84
10^{-3}	11.76	12.35	-3.48	2.20
2×10^{-4}	49.1	37.9	23.25	13.0
10^{-4}	84.4	41.22	61.00	29.27

$N = 25$, Near-Field Electrostatic Interactions

Ma	$\langle \eta^T \rangle$	$\langle \eta^H \rangle$	$\langle \eta_{S^p} \rangle$	$\langle \eta^{XF} \rangle$
∞	0.11	0.11	0.0	0.0
10^{-1}	0.16	0.15	0.04	0.09
10^{-2}	1.09	0.96	0.37	0.41
10^{-3}	20.10	18.40	4.44	3.52
2×10^{-4}	29.79	22.00	23.20	13.75
10^{-4}	60.79	52.46	23.92	16.72

Table 6.III, Continued

$N = 49$, No Near-Field Electrostatic Interactions

Ma	$\langle \eta^T \rangle$	$\langle \eta^H \rangle$	$\langle \eta_{S^p} \rangle$	$\langle \eta^{XF} \rangle$
10^{-2}	1.30	1.55	0.98	1.83
10^{-3}	19.00	10.50	6.88	5.19

$N = 50$ (Rectangular Box), No Near-Field Electrostatic Interactions

Ma	$\langle \eta^T \rangle$	$\langle \eta^H \rangle$	$\langle \eta_{S^p} \rangle$	$\langle \eta^{XF} \rangle$
10^{-2}	1.22	1.20	0.63	0.14
10^{-3}	15.62	15.17	-6.81	2.39
10^{-4}	58.18	14.27	40.15	53.13

Table 6.IV

Dynamic Simulation First Normal Stress Difference

$N = 25$, No Near-Field Electrostatic Interactions

Ma	χ^T	χ^H	χ^{ER}
∞	0.03 ± 0.02	0.03 ± 0.02	0.0 ± 0.0
10^{-1}	-0.09 ± 0.05	0.04 ± 0.04	-0.13 ± 0.06
2×10^{-2}	-3.36 ± 0.21	1.35 ± 0.18	-4.71 ± 0.14
10^{-2}	-5.42 ± 0.71	3.58 ± 0.53	-9.00 ± 0.36
2×10^{-3}	-29.70 ± 6.17	21.22 ± 5.58	-50.92 ± 2.14
10^{-3}	-4.95 ± 15.30	64.20 ± 14.72	-69.15 ± 8.01
2×10^{-4}	-164 ± 79.2	133 ± 50.6	-297 ± 52.2
10^{-4}	-535 ± 115	87.4 ± 30.7	-622 ± 119

$N = 25$, Near Field Electrostatic Interactions

Ma	χ^T	χ^H	χ^{ER}
10^{-2}	-10.80 ± 2.97	1.44 ± 2.92	-12.24 ± 0.36
10^{-3}	-11.76 ± 11.48	15.30 ± 7.93	-27.06 ± 9.87
2×10^{-4}	-250 ± 61.3	158 ± 33.4	-408 ± 51.2
10^{-4}	-352 ± 62.0	78.30 ± 23.90	-430 ± 58.5

Note the numbers following the $\pm$ are the 95% confidence limits of the first normal stress difference. The times of the simulations are identical to the equivalent Ma viscosity data in 6.II.

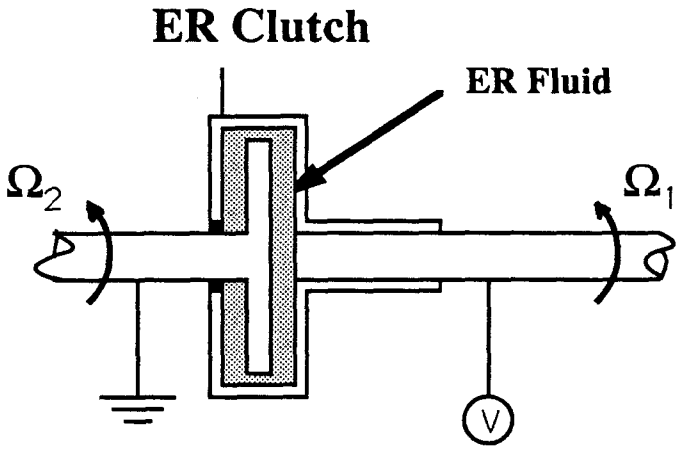
ER Clutch
ER Fluid
Ω_2
Ω_1
V

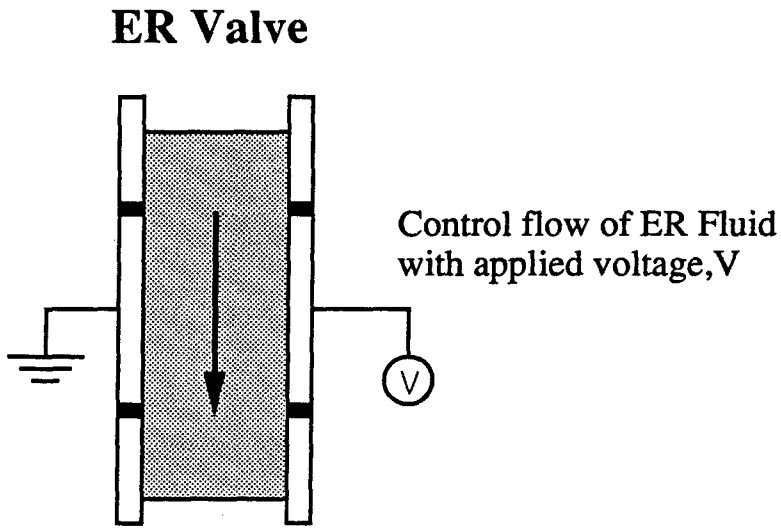
ER Valve
Control flow of ER Fluid
with applied voltage,V
V

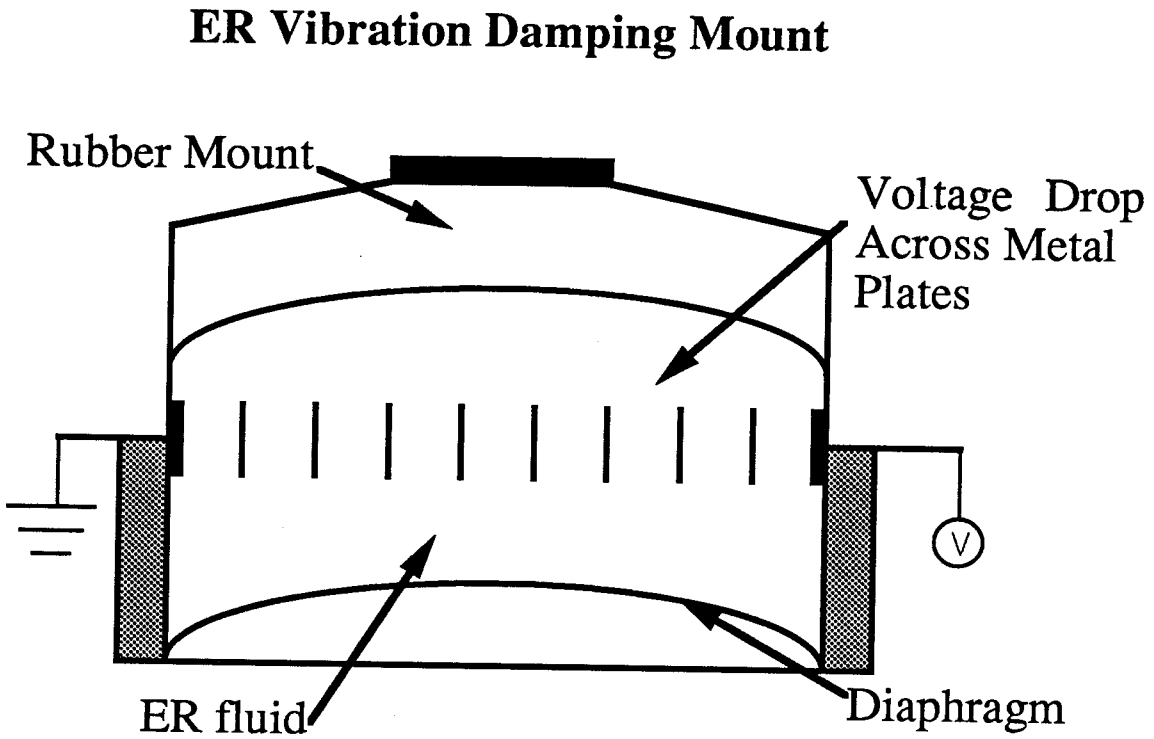

Figure 6.1. Some possible applications of ER fluids in electromechanical devices. The ER clutch allows the fine control of the output rotation rate for some input rotation with applications to automobiles or assembly line robots. An ER fluid valve controls the flow without any moving parts. The vibration damping mount is a specific example of spring-dashpot-type shock absorber which allows dynamic control of mechanical vibration from an engine or perhaps even a building.

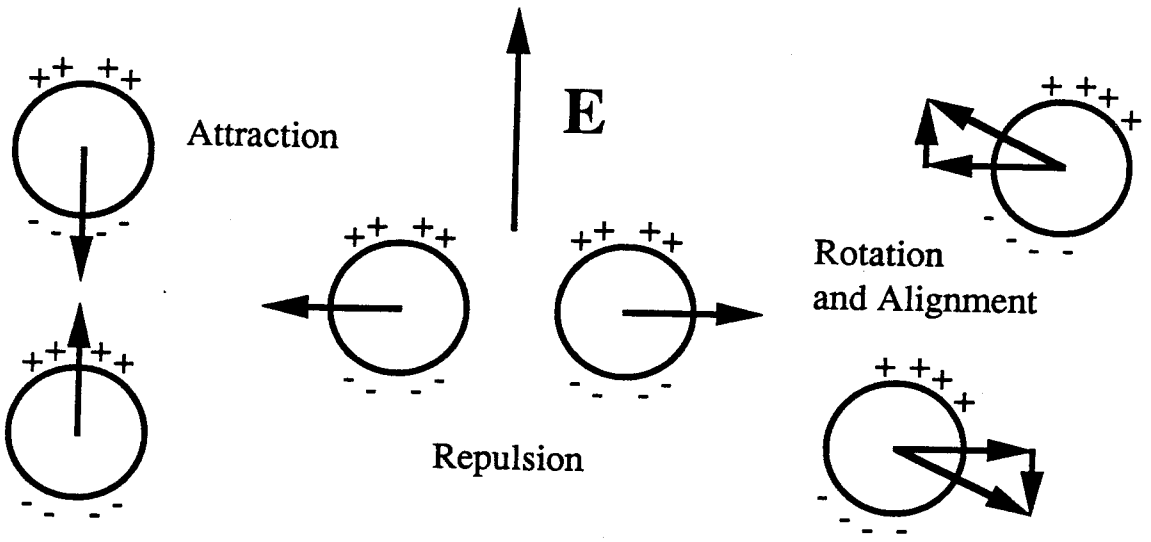

Figure 6.2. Mechanism of fibration and alignment of dielectric particles. Due to the dielectric mismatch between the particles and the fluid, the particles have an induced dipole as illustrated. The interaction of these dipoles cause attraction, repulsion, rotation, and alignment of particles, creating chains that align with the applied electric field.

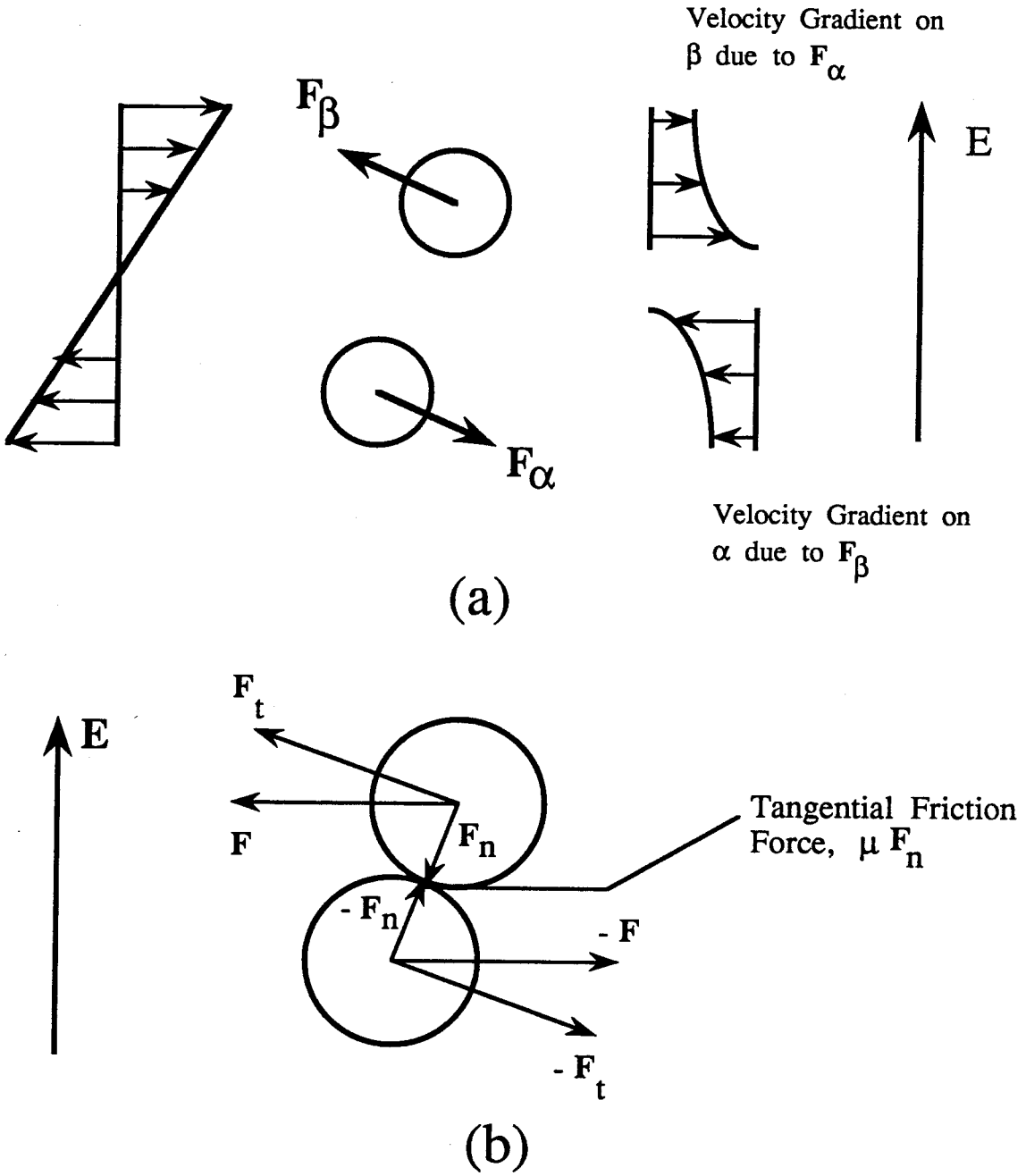

Figure 6.3. The effects of stress in a suspension due to electrostatic interparticle forces. While the $-\langle \mathbf{xF^P} \rangle$ due to chain deformation increases the stress of the suspension, the velocity gradients (*a*) due to the interparticle forces act counter to the bulk shear flow and reduce the total stress in the suspension. This reduction is not atypical and is also seen, for example, for contact friction forces as depicted in (*b*).

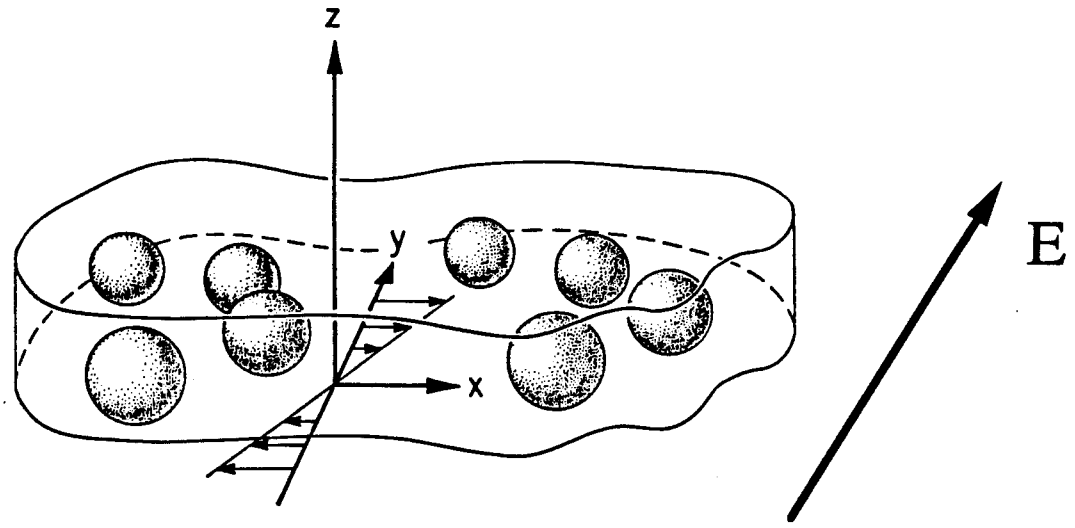

Figure 6.4. Illustration of monolayer of spheres used in dynamic simulation. The shear flow in the x direction is orthogonal to the applied electric field in the y direction. To simulate an unbounded suspension, periodic boundary conditions are applied to the N particles in the cell.

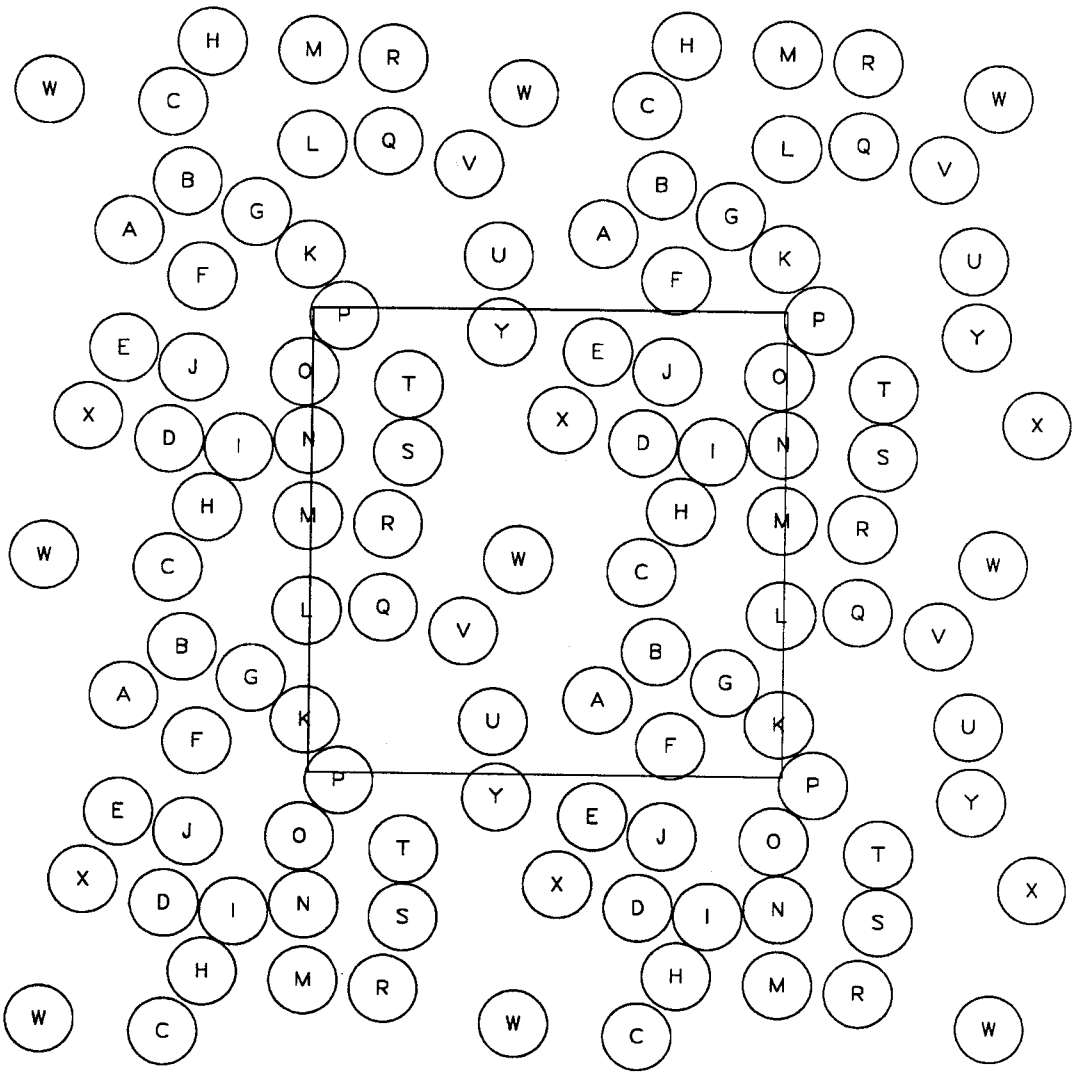

Figure 6.5*a*. Instantaneous "snapshot" of the suspension microstructure for sphere ordering with no shear flow and $Ma = 10^{-3}$ at $t = 0.0$. With no shear rate here time scales as $Ma^{-1}\eta/(2\epsilon(\beta E)^2)$. The outlined square is the periodic cell.

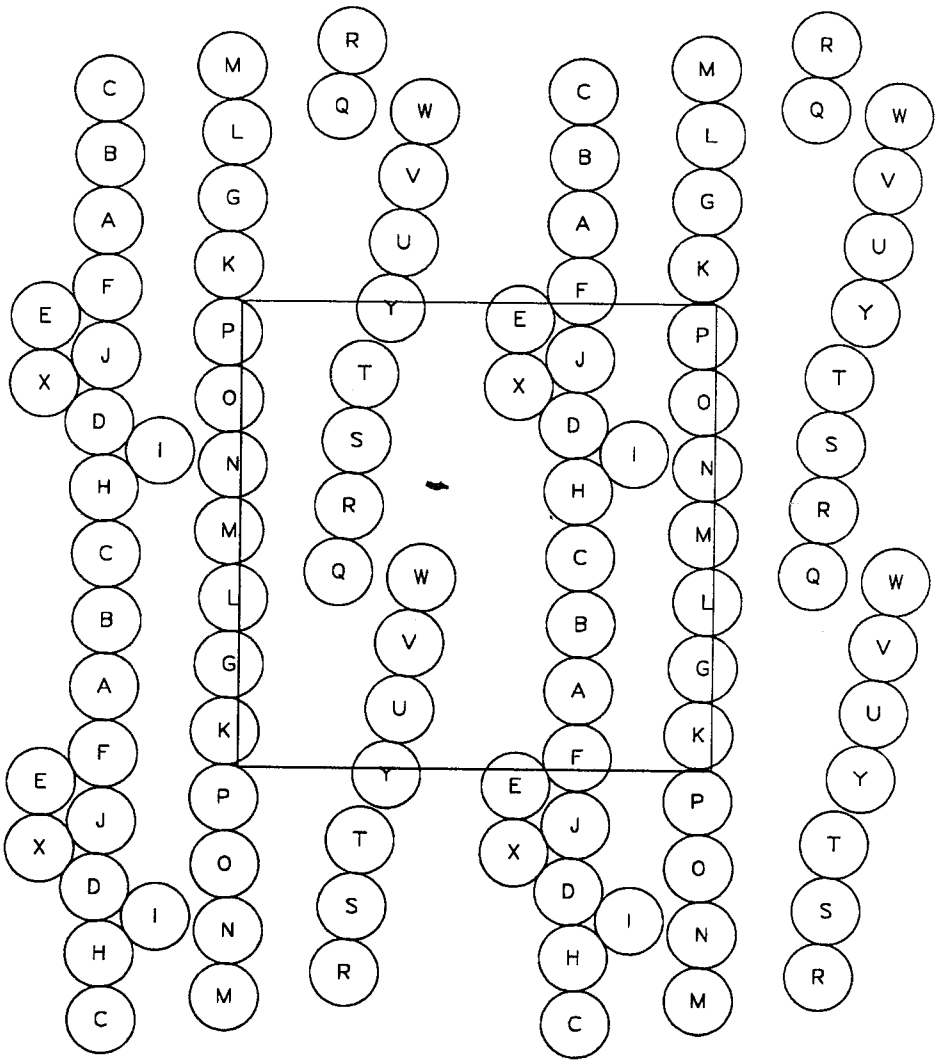

Figure 6.5*b*. As before for $t = 0.1$.

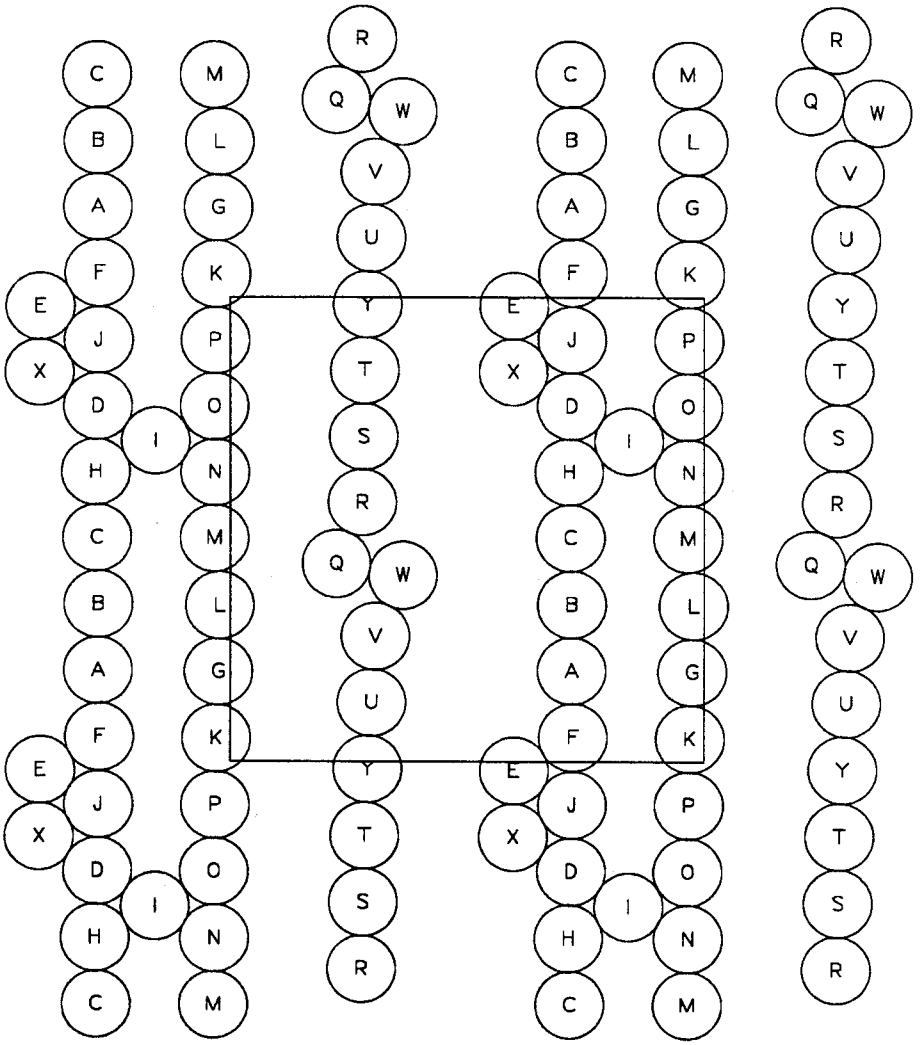

Figure 6.5c. As before for $t = 0.2$.

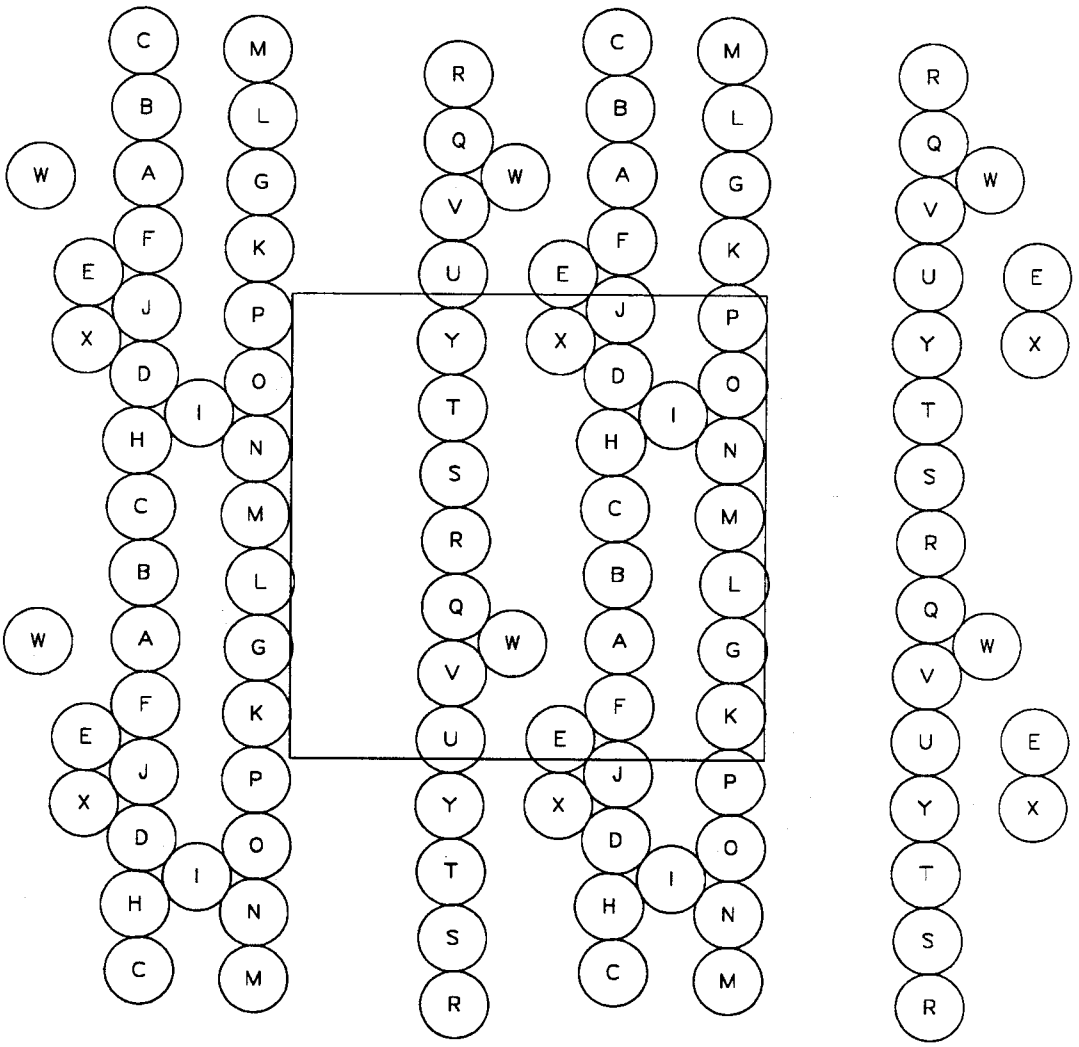

Figure 6.5*d*. As before for $t = 2.5$.

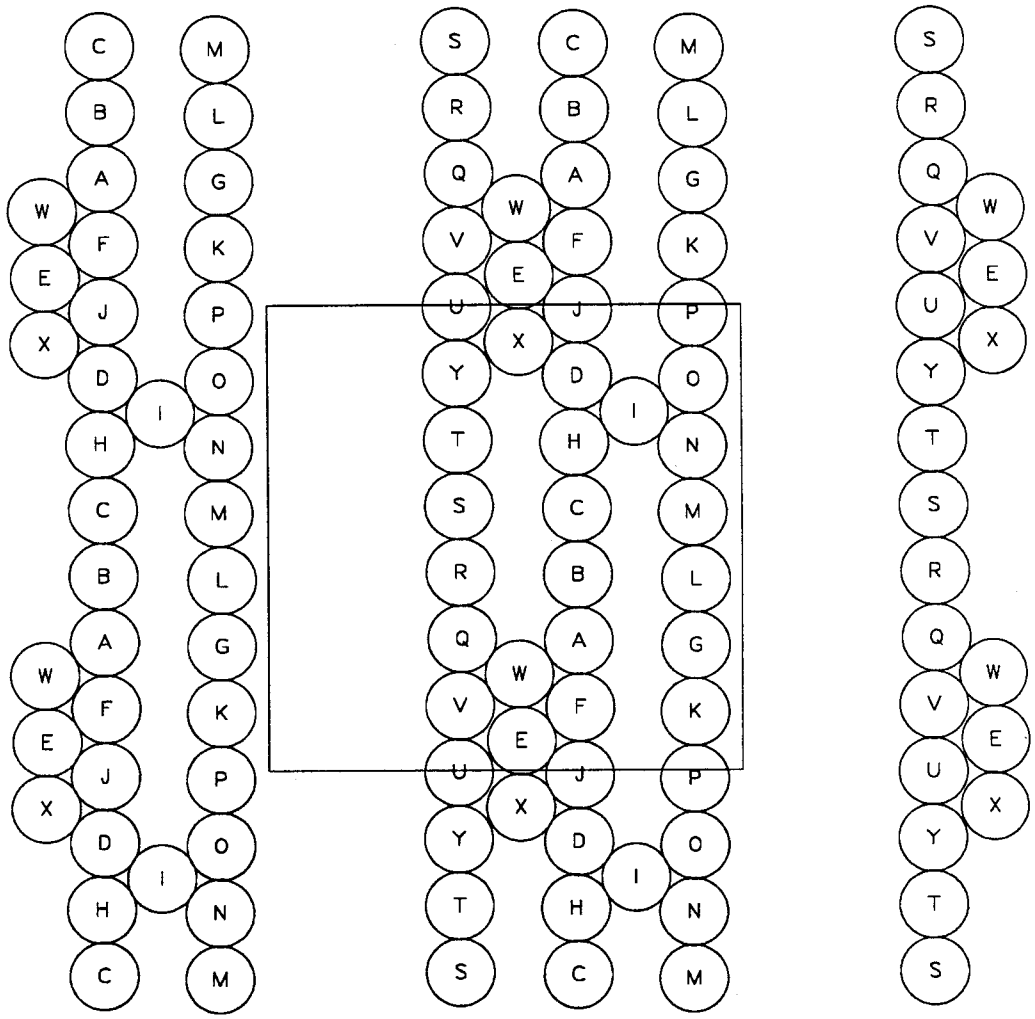

Figure 6.5*e*. As before for $t = 2.7$.

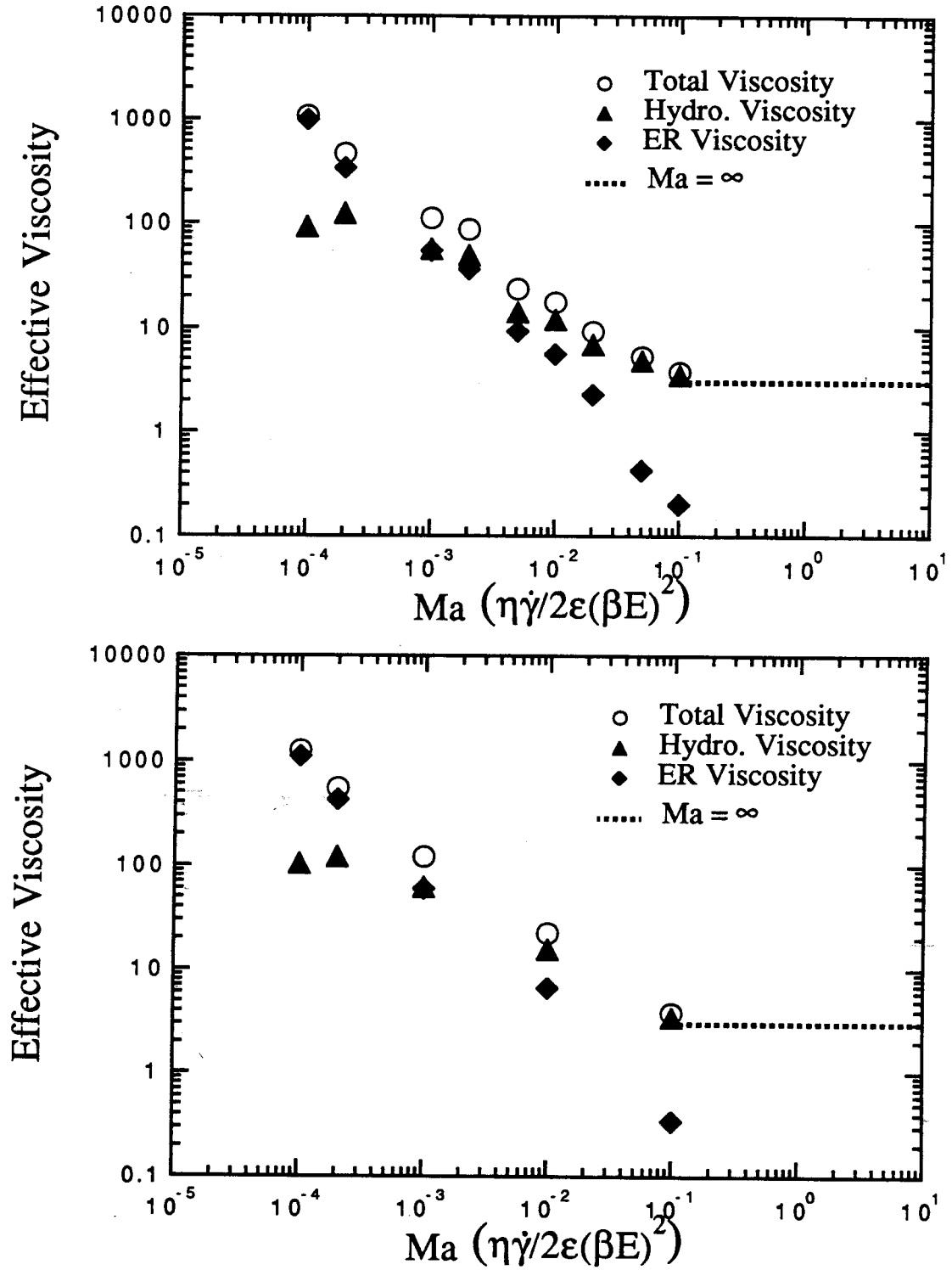

Figure 6.6. Total, hydrodynamic, and ER viscosities for monolayer simulations without (*a*) and with (*b*) the addition of near-field electrostatic interactions. The viscosities are relative to the suspending fluid. The dotted line corresponds to the no electric field viscosity.

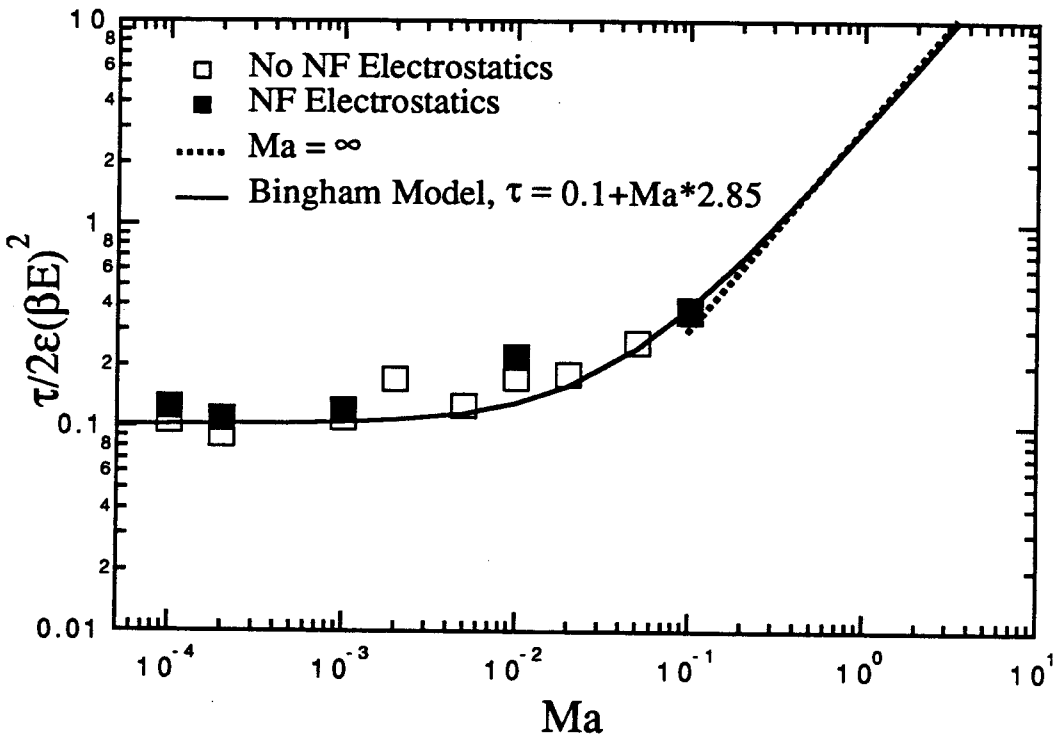

Figure 6.7. Shear stress for the monolayer simulations. The shear stress is normalized by electrostatic forces per unit area rather than the viscous forces. The solid line is a Bingham shear stress model assuming a constant plastic viscosity.

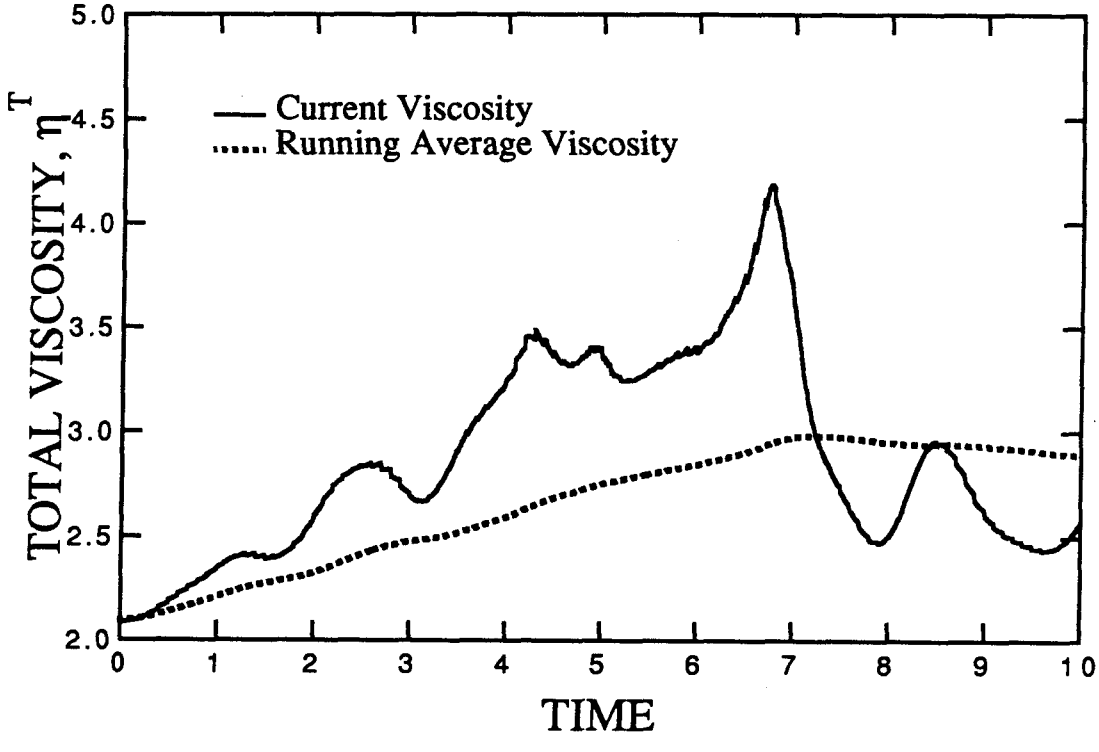

Figure 6.8. Time trace for total viscosity for $N = 25$ and $Ma = \infty$ (no electric field). Both the current and running average effective viscosity are illustrated.

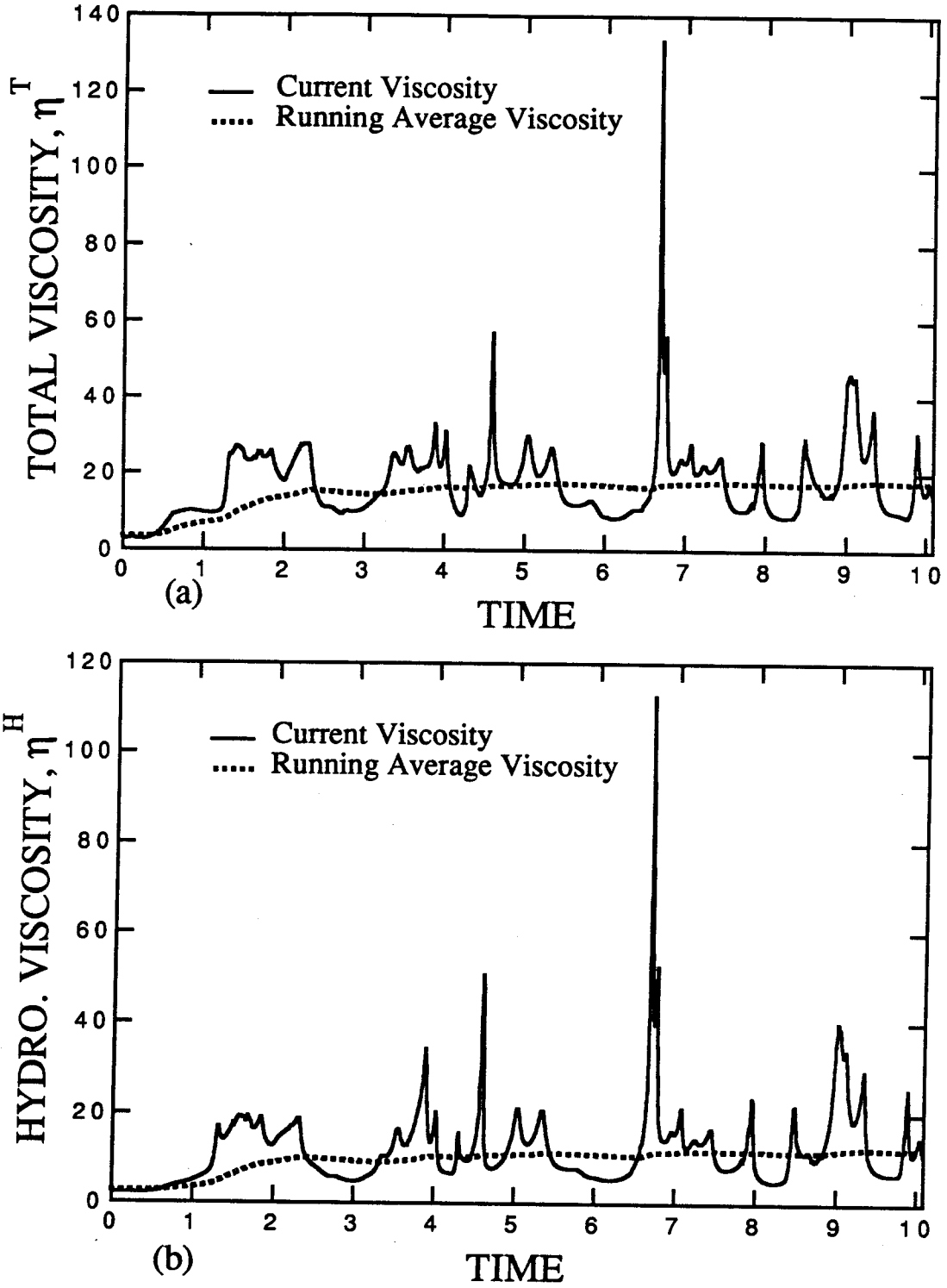

Figure 6.9*a*, *b*. Time traces of the total (*a*) and the hydrodynamic (*b*) viscosity for $N = 25$ and $Ma = 10^{-2}$.

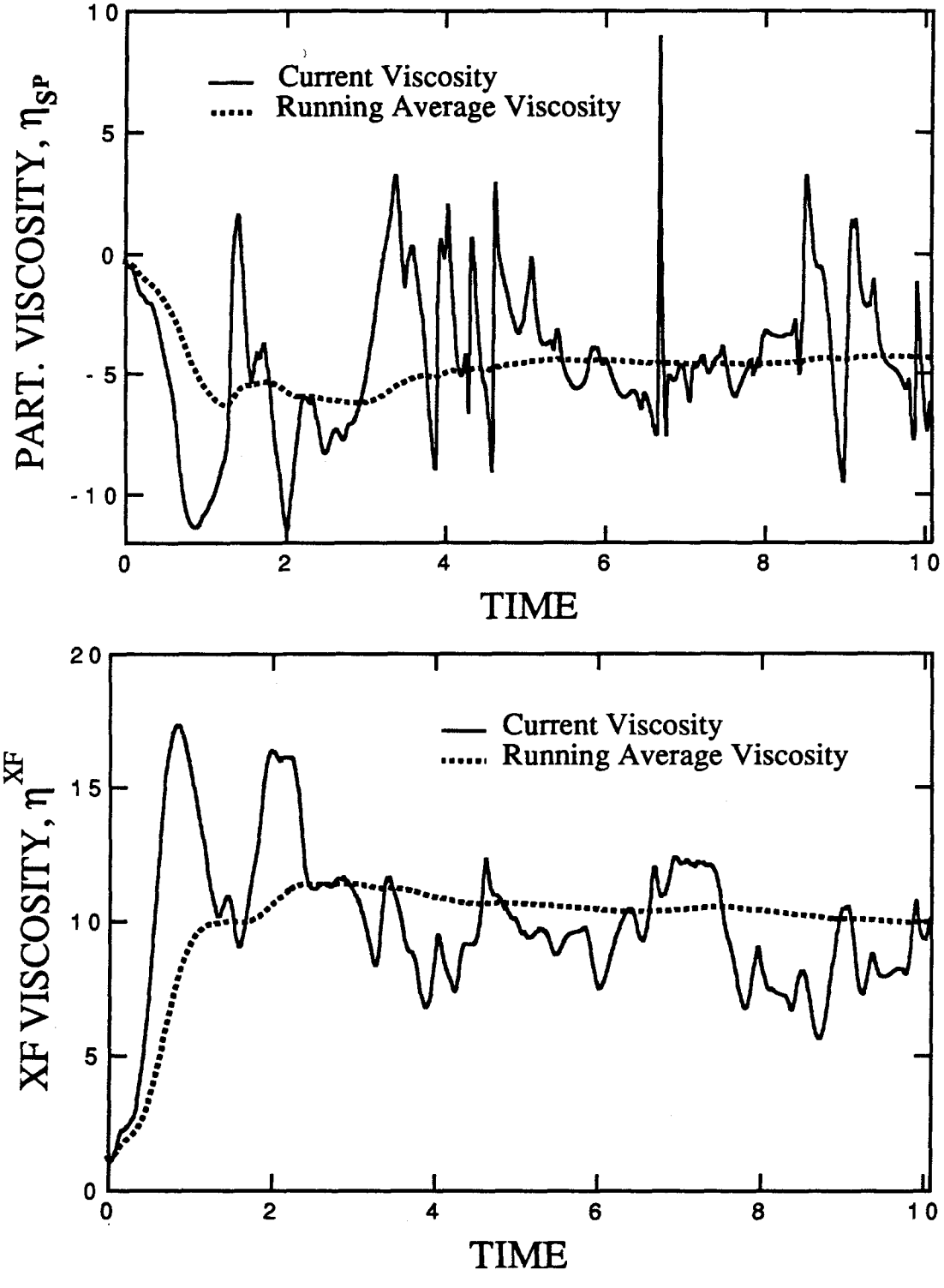

Figure 6.9*c*, *d*. Time traces of the particle (*c*) and the $\mathbf{xF^P}$ (*d*) viscosity for $N = 25$ and $Ma = 10^{-2}$.

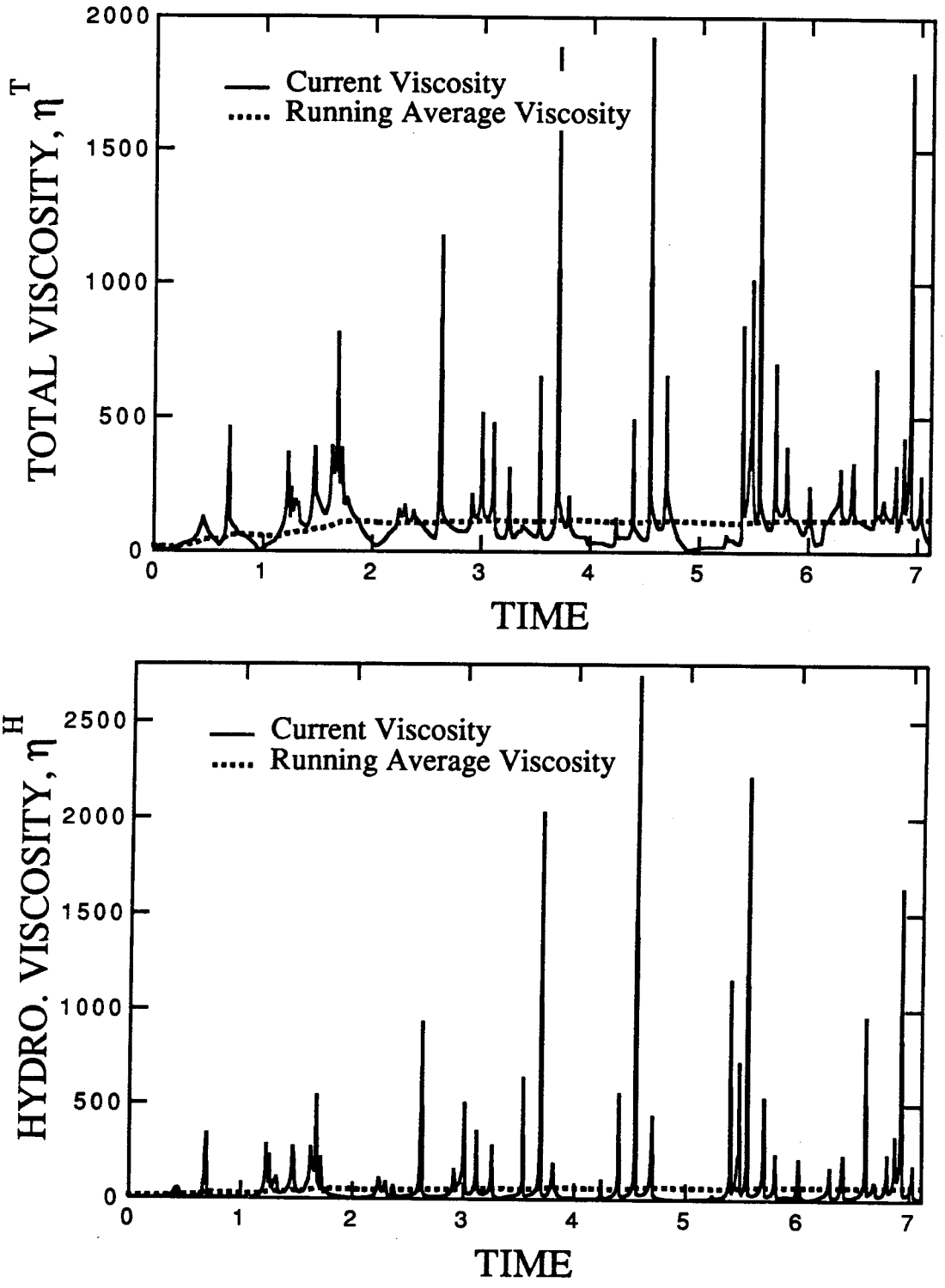

Figure 6.10*a, b*. Time traces of the total (*a*) and the hydrodynamic (*b*) viscosity for $N = 25$ and $Ma = 10^{-3}$.

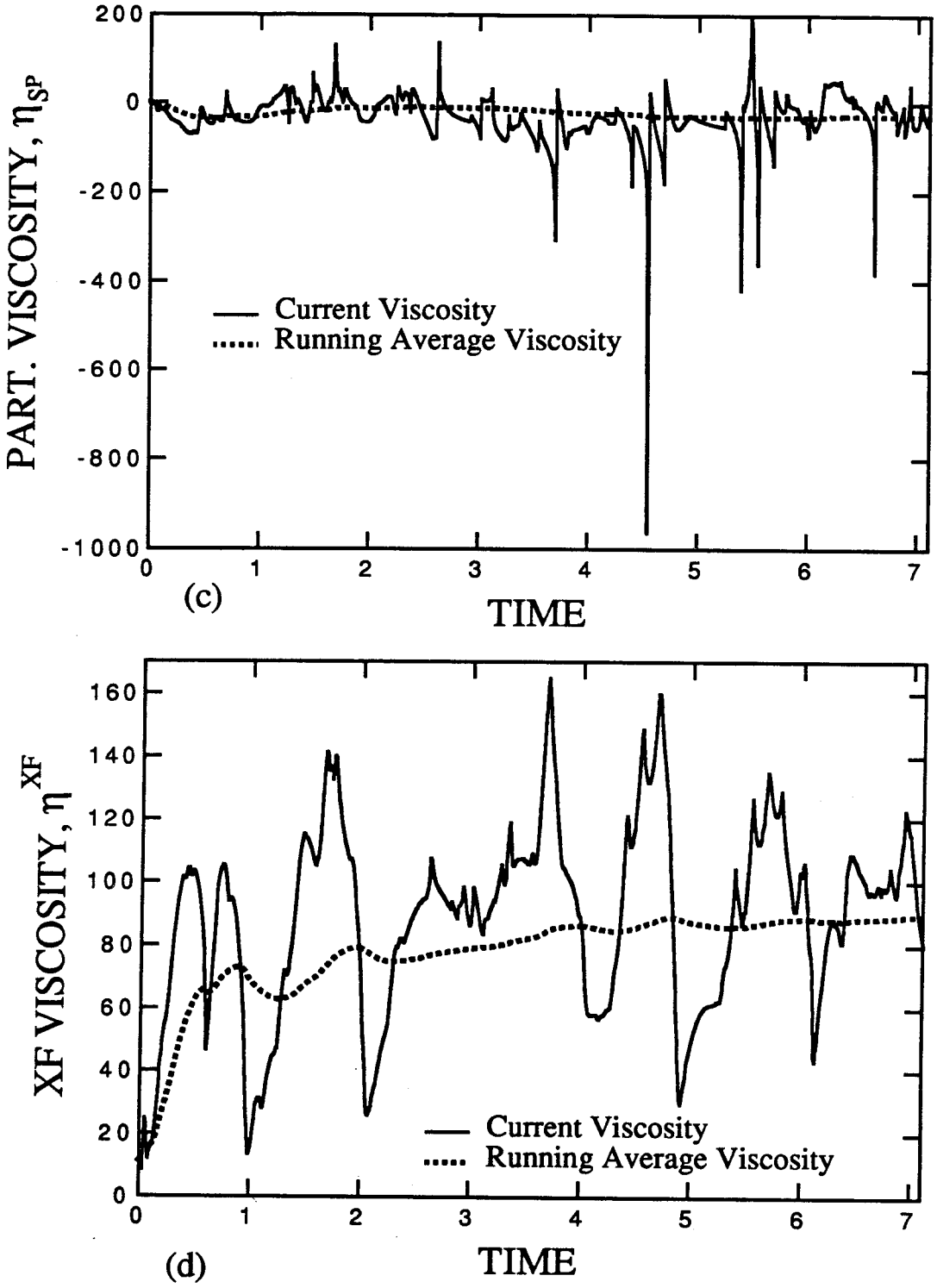

Figure 6.10*c, d*. Time traces of the particle (*c*) and the $\mathbf{xF^P}$ (*d*) viscosity for $N = 25$ and $Ma = 10^{-3}$.

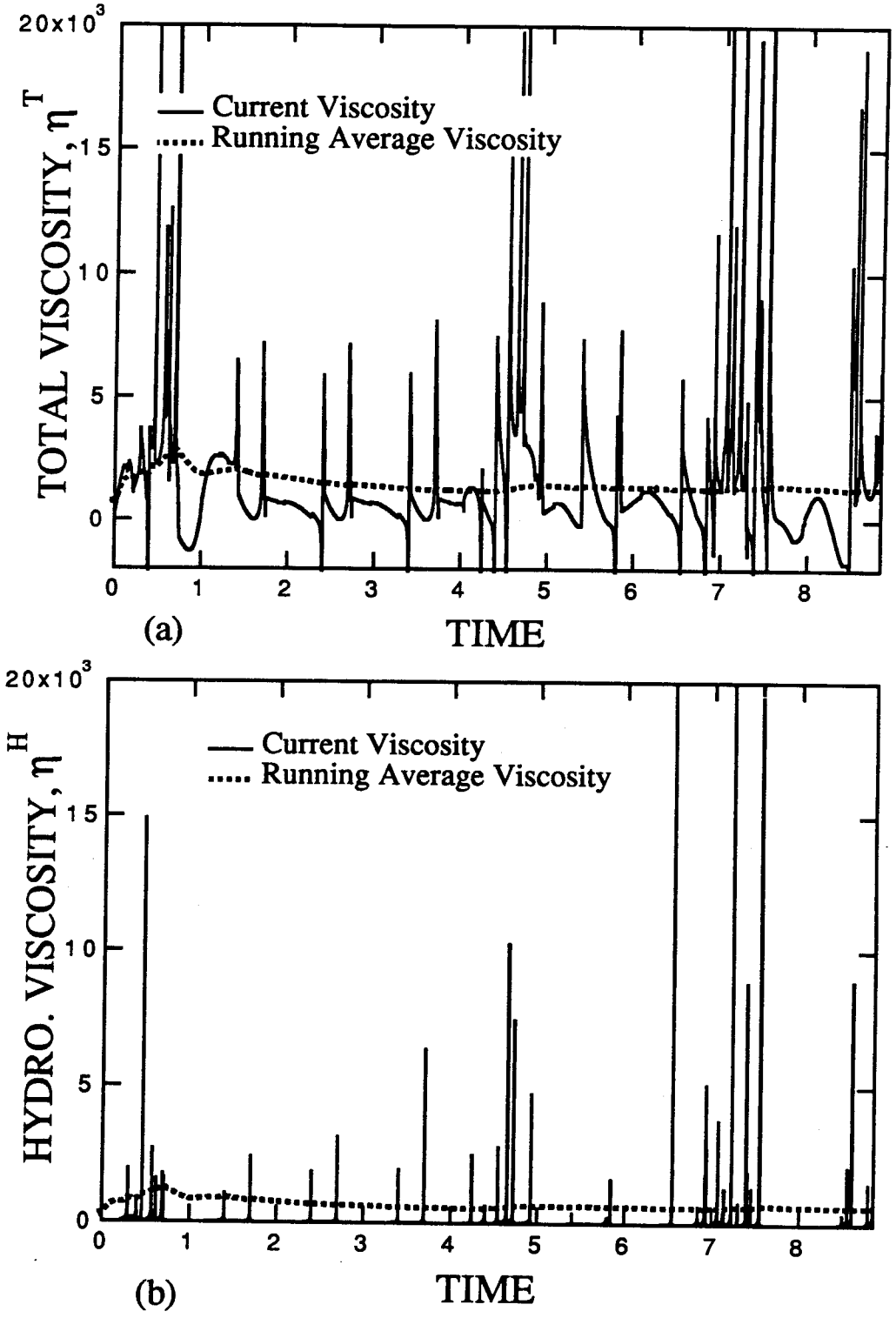

Figure 6.11*a, b*. Time traces of the total (*a*) and the hydrodynamic (*b*) viscosity for $N = 25$ and $Ma = 10^{-4}$. Large viscosity excursions sometimes exceed 2×10^4, but are clipped in order to concentrate on the more basic features.

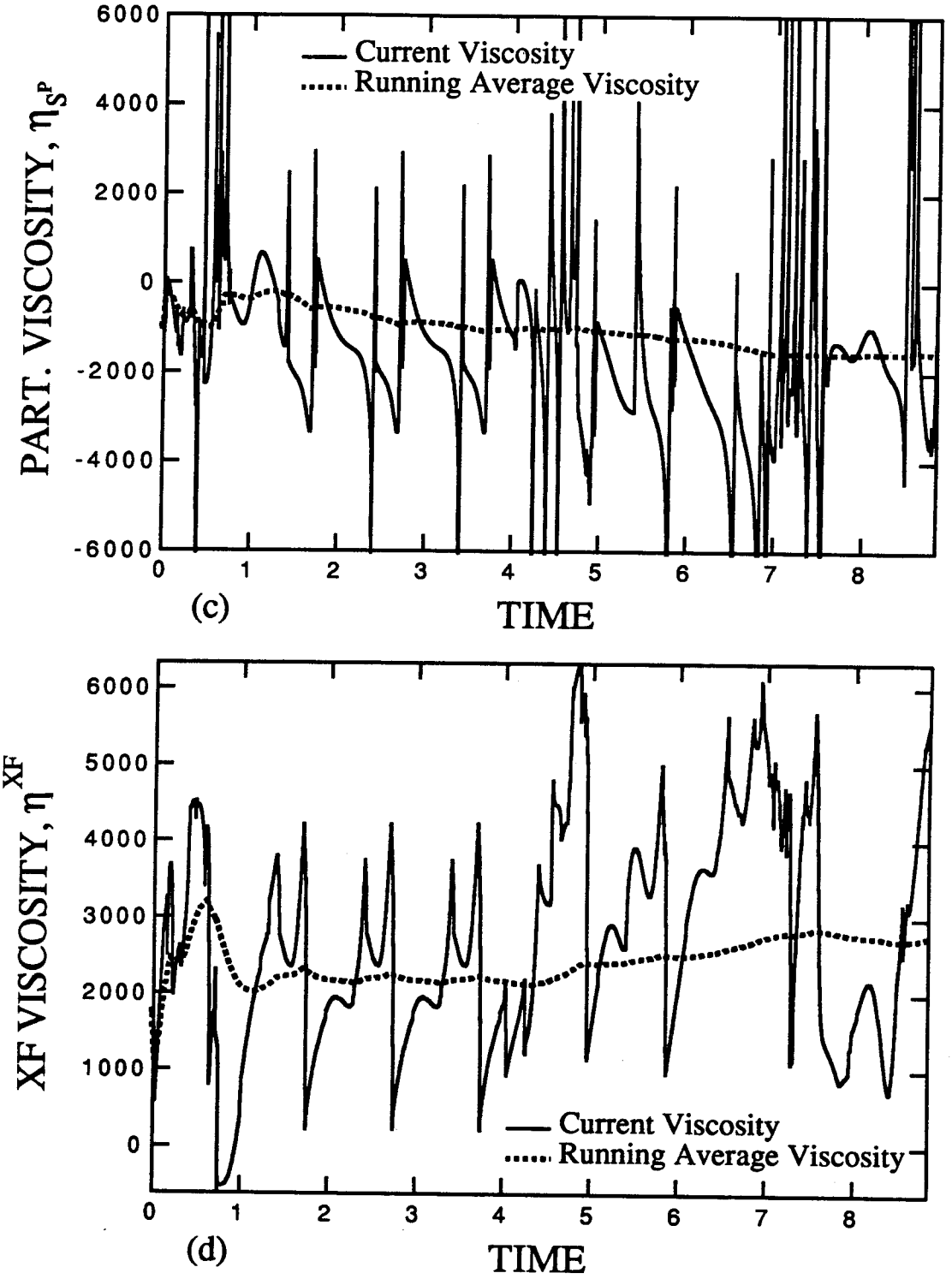

Figure 6.11*c*, *d*. Time traces of the particle (*c*) and the hydrodynamic (*d*) viscosity for $N = 25$ and $Ma = 10^{-4}$. Large viscosity excursions sometimes exceed 2×10^4, but are clipped in order to concentrate on the more basic features.

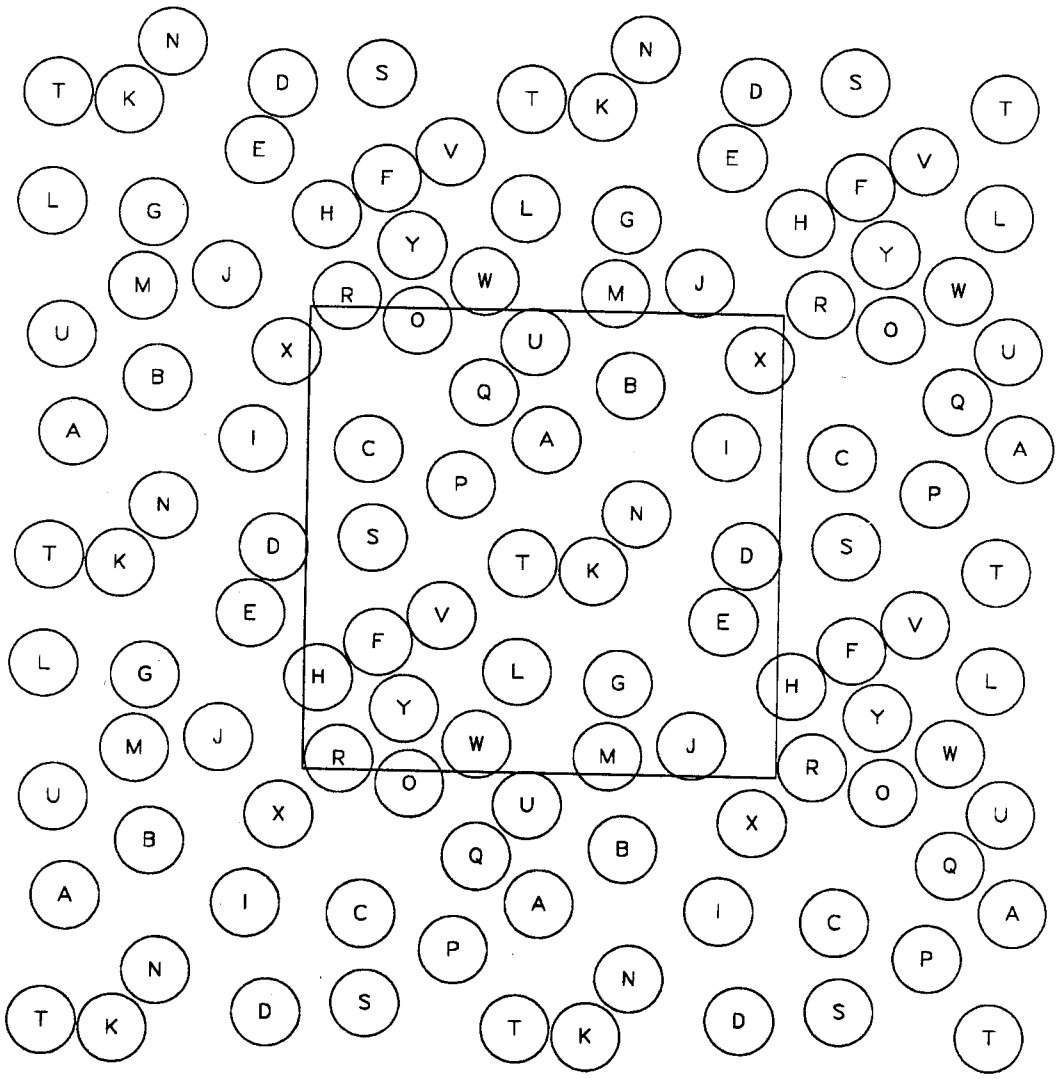

Figure 6.12*a*. Instantaneous snapshot of the suspension microstructure for flowing system at $Ma = \infty$ for $t = 0.0$. This starting configuration was generated by Monte Carlo methods. The shear flow is from left to right and the electric field is from bottom to top.

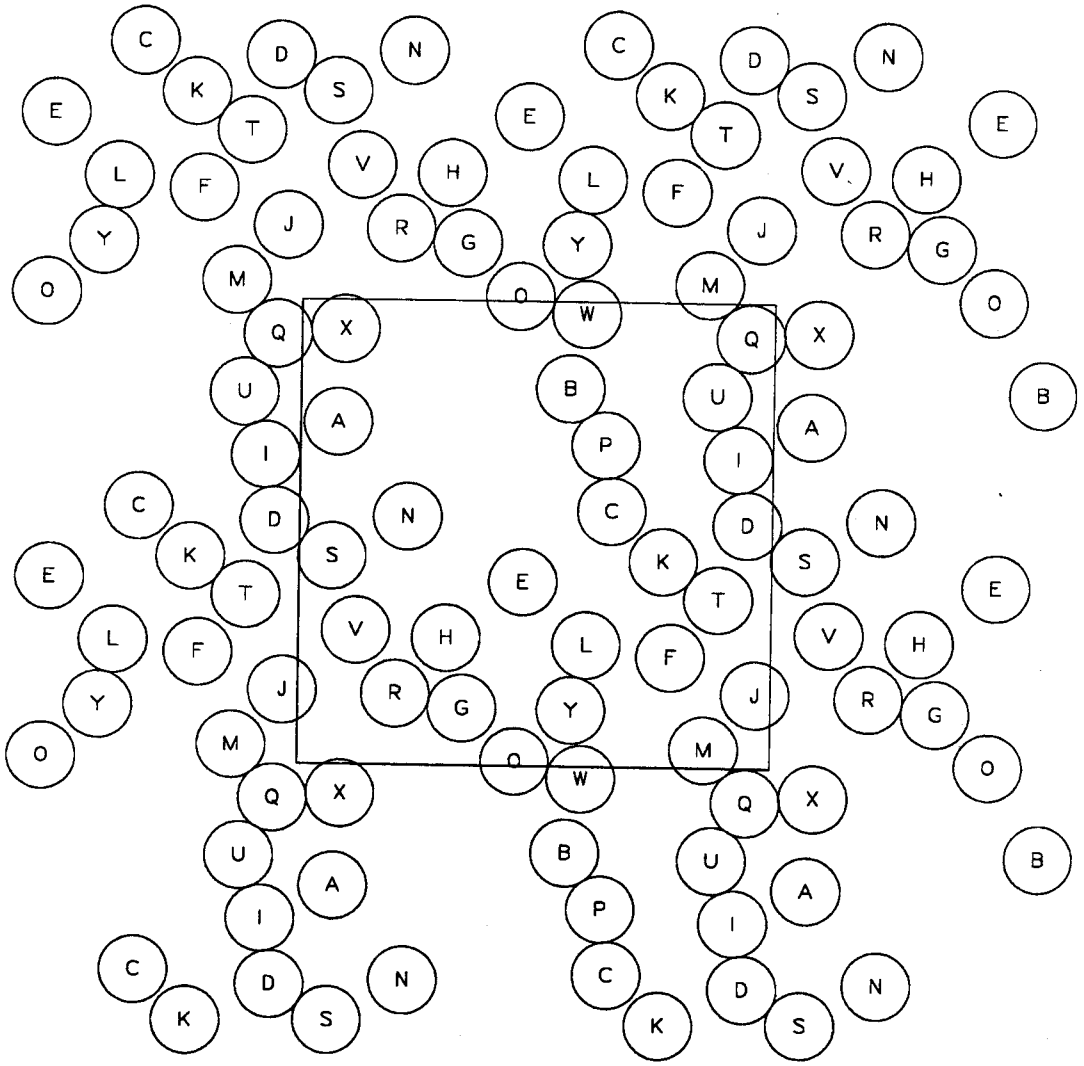

Figure 6.12*b*. As before for $t = 10.0$ (the end of the simulation). For this Ma particles tend to be driven toward each other along the axis of compression of the shear flow (top left to bottom right) and pulled apart along the axis of extension (bottom left to top right).

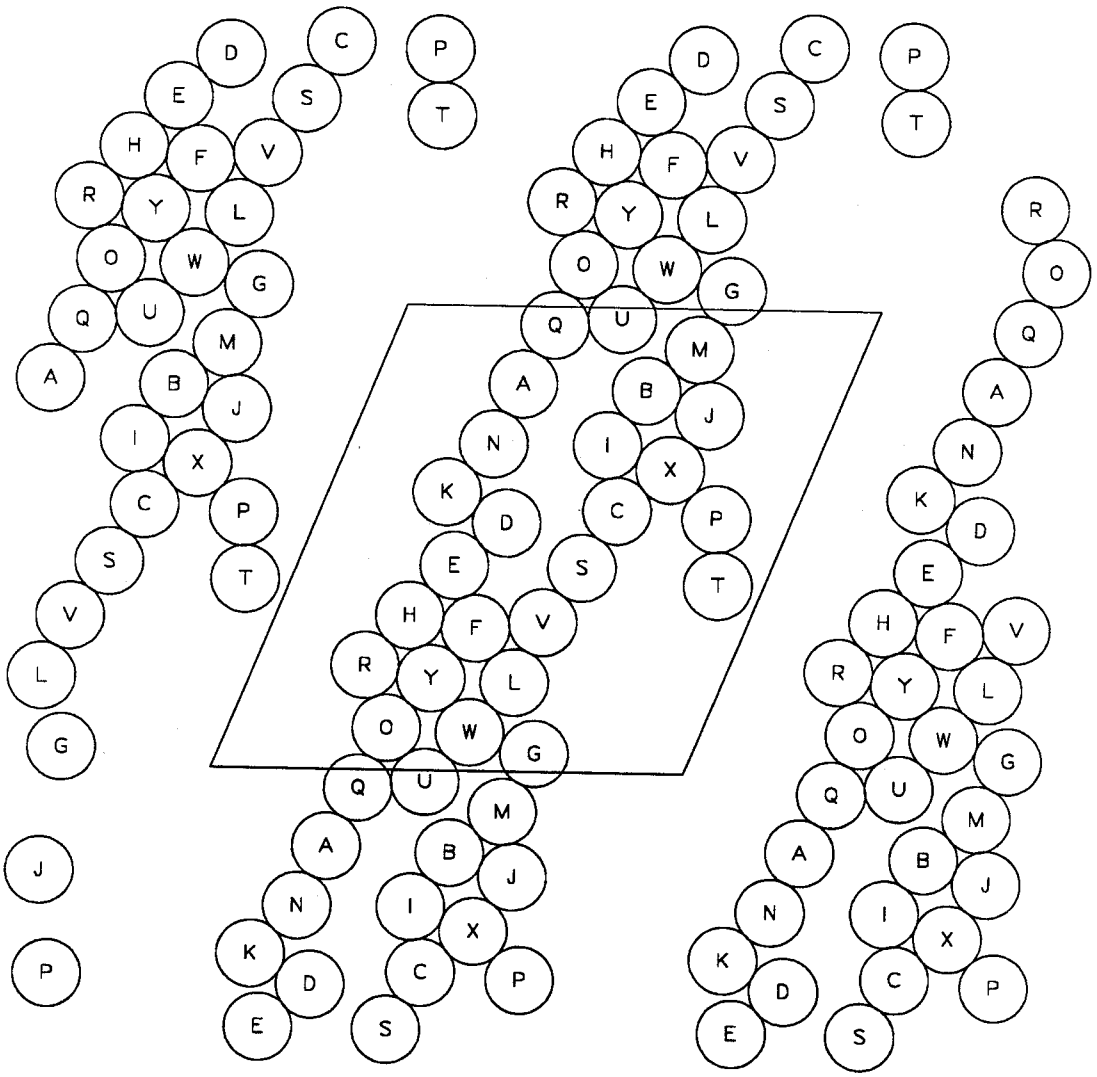

Figure 6.13*a*. Instantaneous snapshot of the suspension microstructure for flowing system at $Ma = 10^{-2}$ for $t = 1.4$. The original starting configuration was generated by Monte Carlo methods. Note the percolating chain of particles in sharp contrast to the relatively structureless flow in Figure 6.12*b*. The outlined rhombus is the strained periodic cell and is arbitrarily reset to a square at a strain of unity.

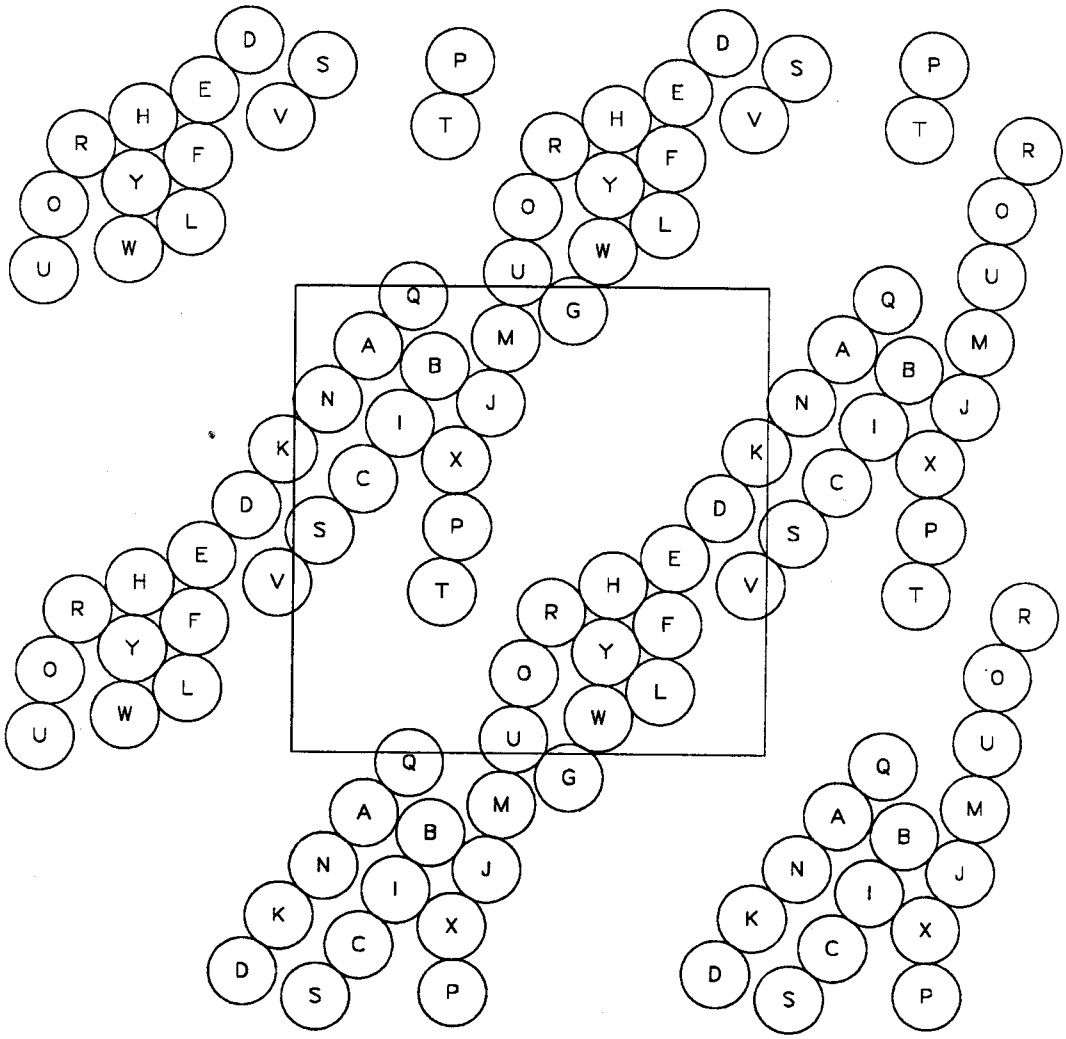

Figure 6.13*b*. As before for $t = 2.0$. Note the disruption of the chain from the previous figure due to hydrodynamic forces.

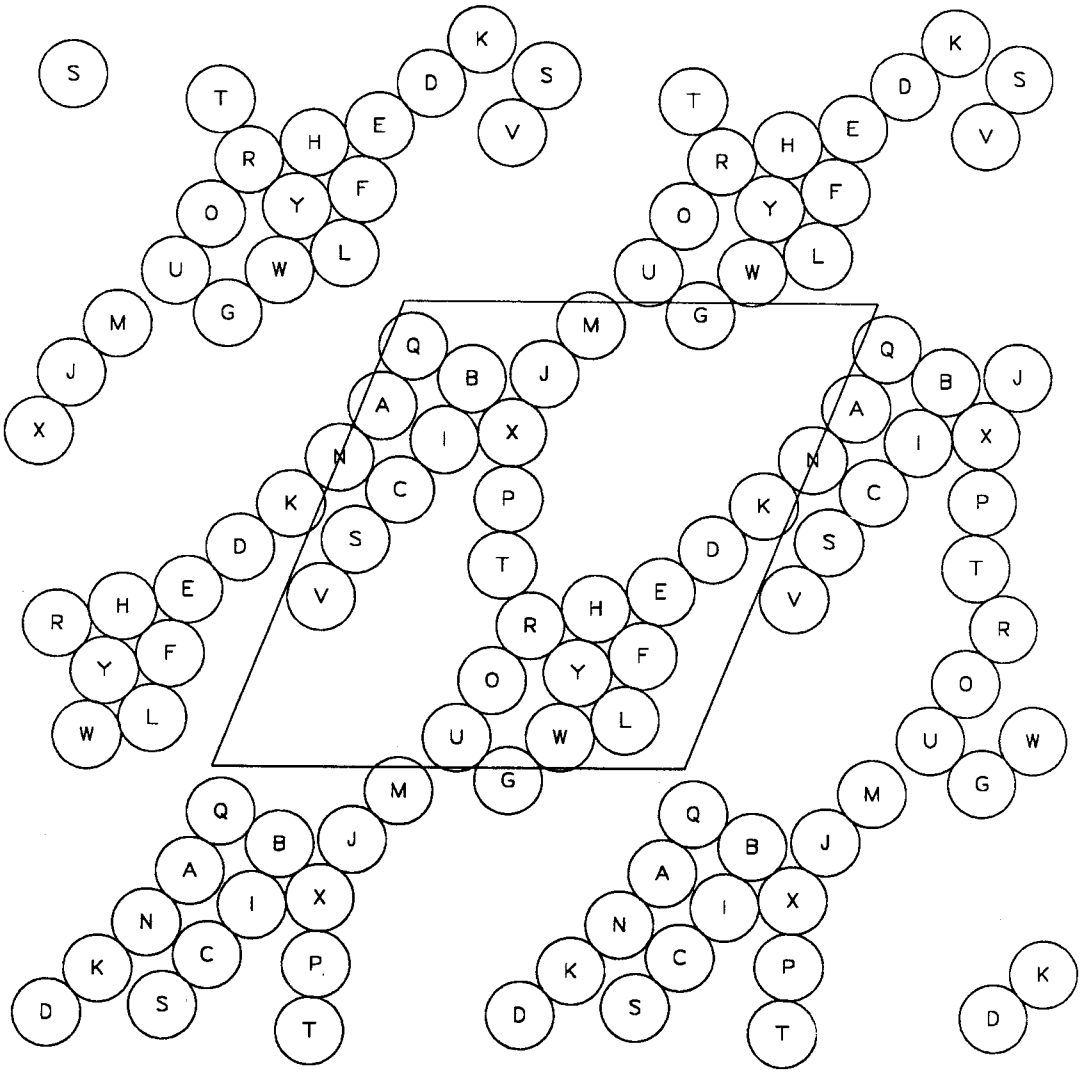

Figure 6.13c. As before for $t = 2.5$. Note the absence of the percolating chain spanning the periodic cell perpendicular to the shear flow.

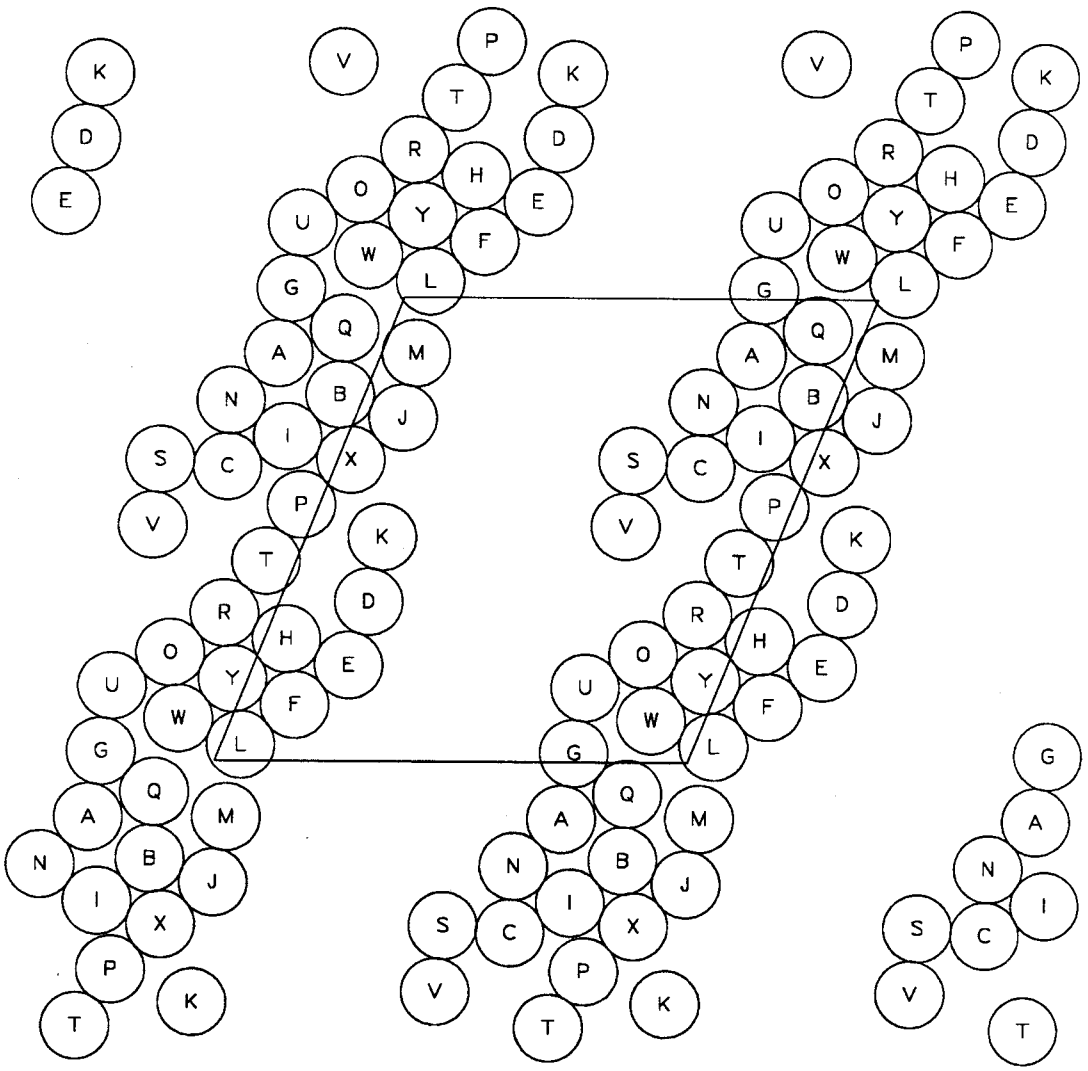

Figure 6.13*d*. As before for $t = 3.6$. Note the reformation of the percolating cluster perpendicular to the direction of the shear flow.

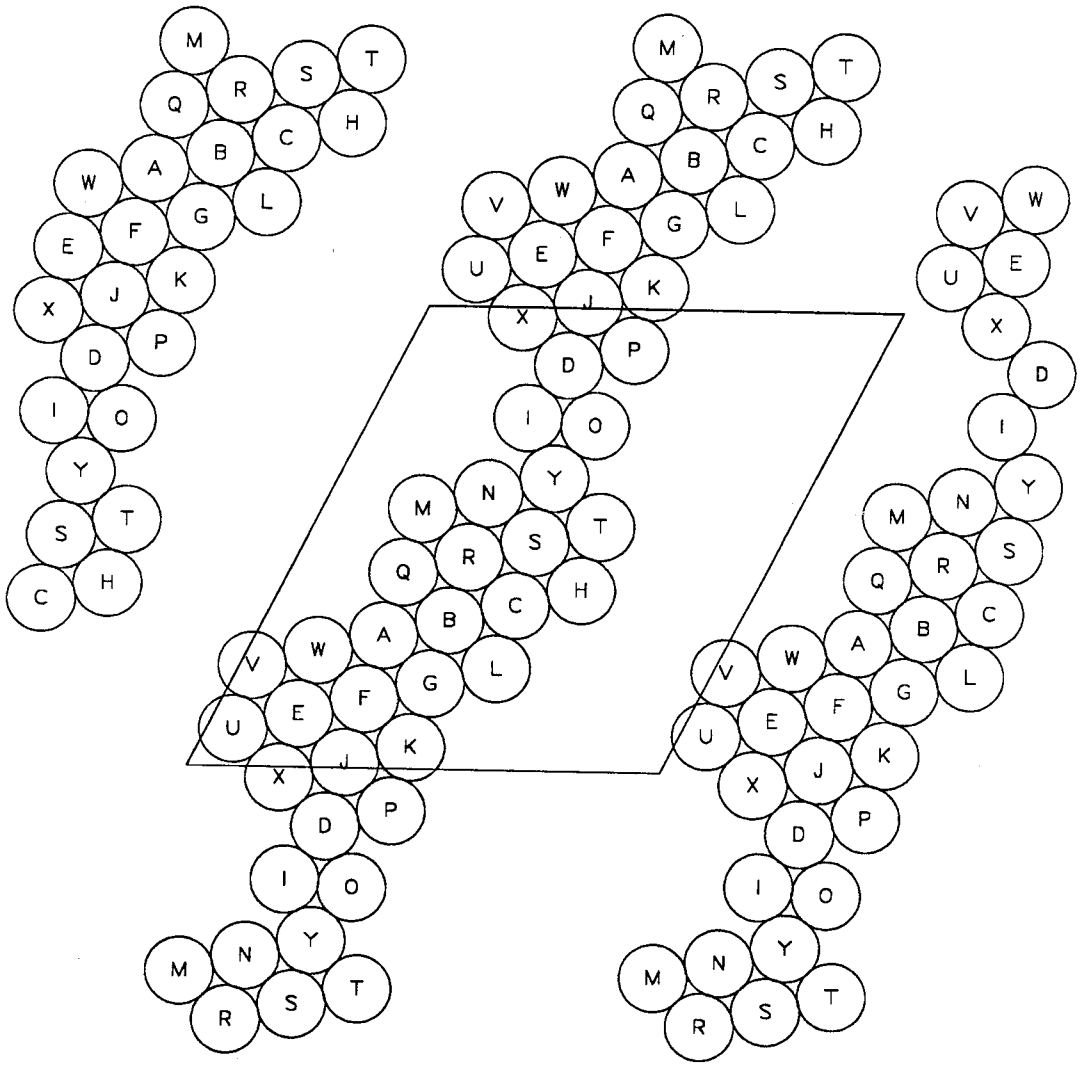

Figure 6.14*a*. Instantaneous snapshot for $N = 25$ and $Ma = 10^{-4}$ at $t = 4.5$. This sequence of configurations illustrates rapid interchain microstructural rearrangements. The original starting configuration is illustrated in Figure 6.5*b*.

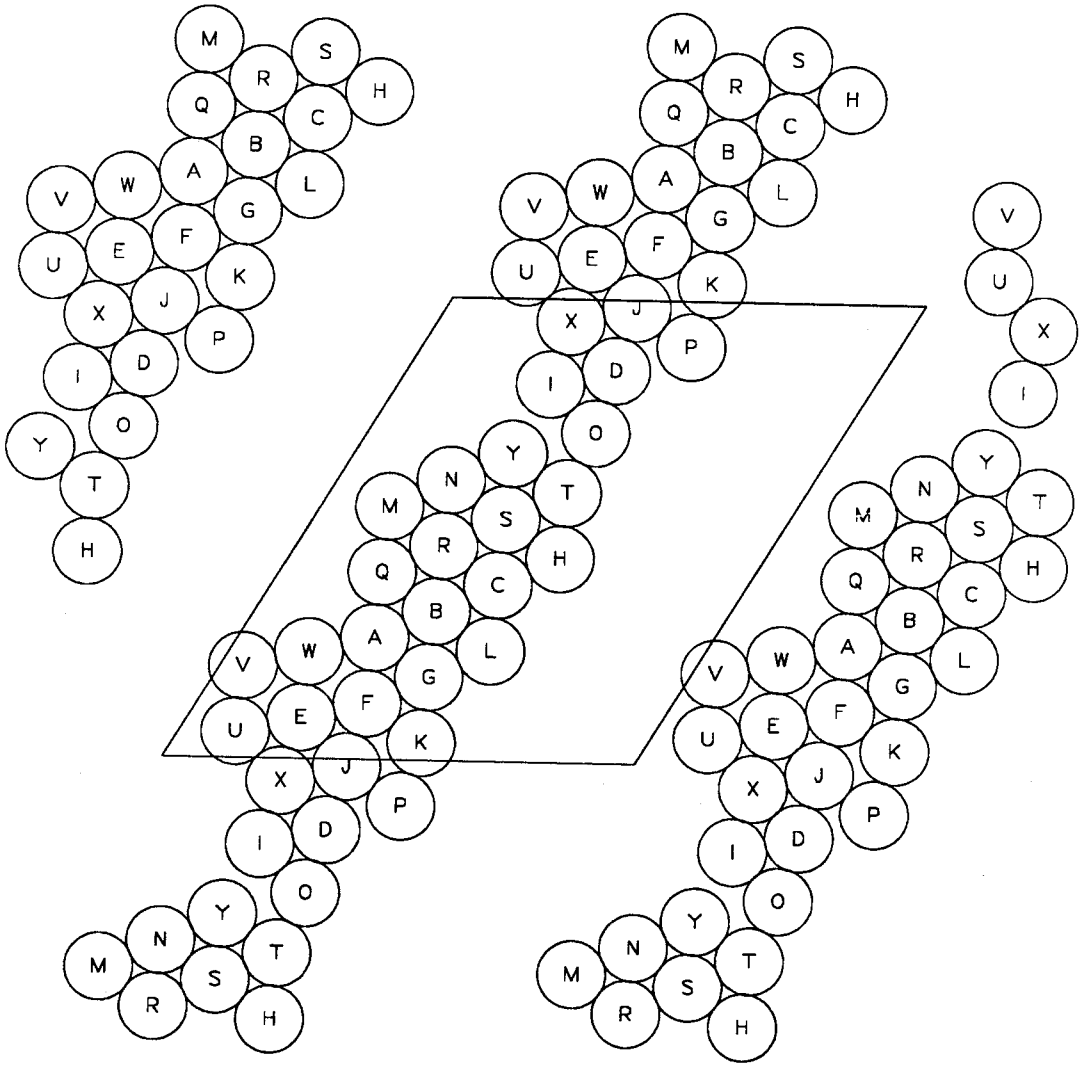

Figure 6.14*b*. As before for $t = 4.6$.

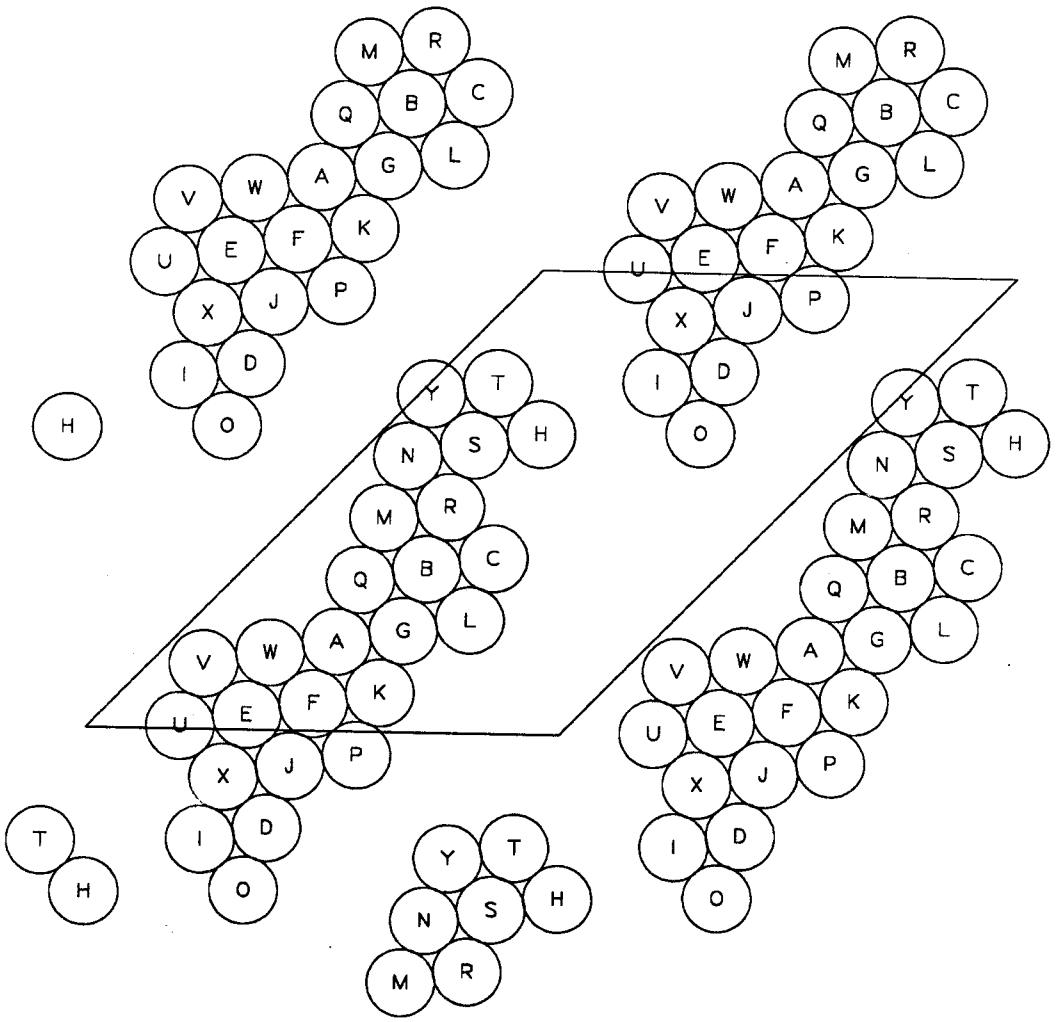

Figure 6.14*c*. As before for $t = 4.95$.

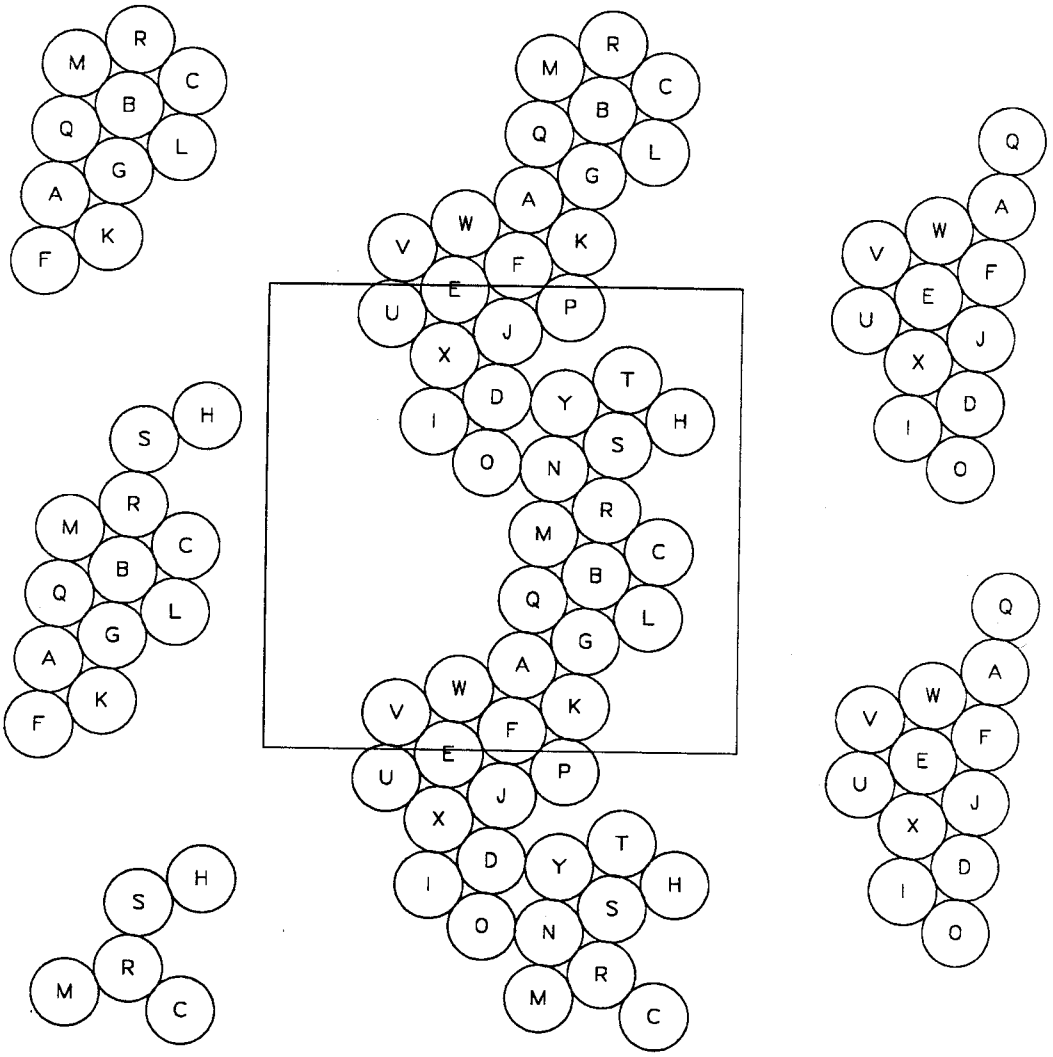

Figure 6.14*d*. As before for $t = 5.0$. Note the chain strained slowly until $t = 4.95$ at which point it snapped and rapidly reformed with its periodic image.

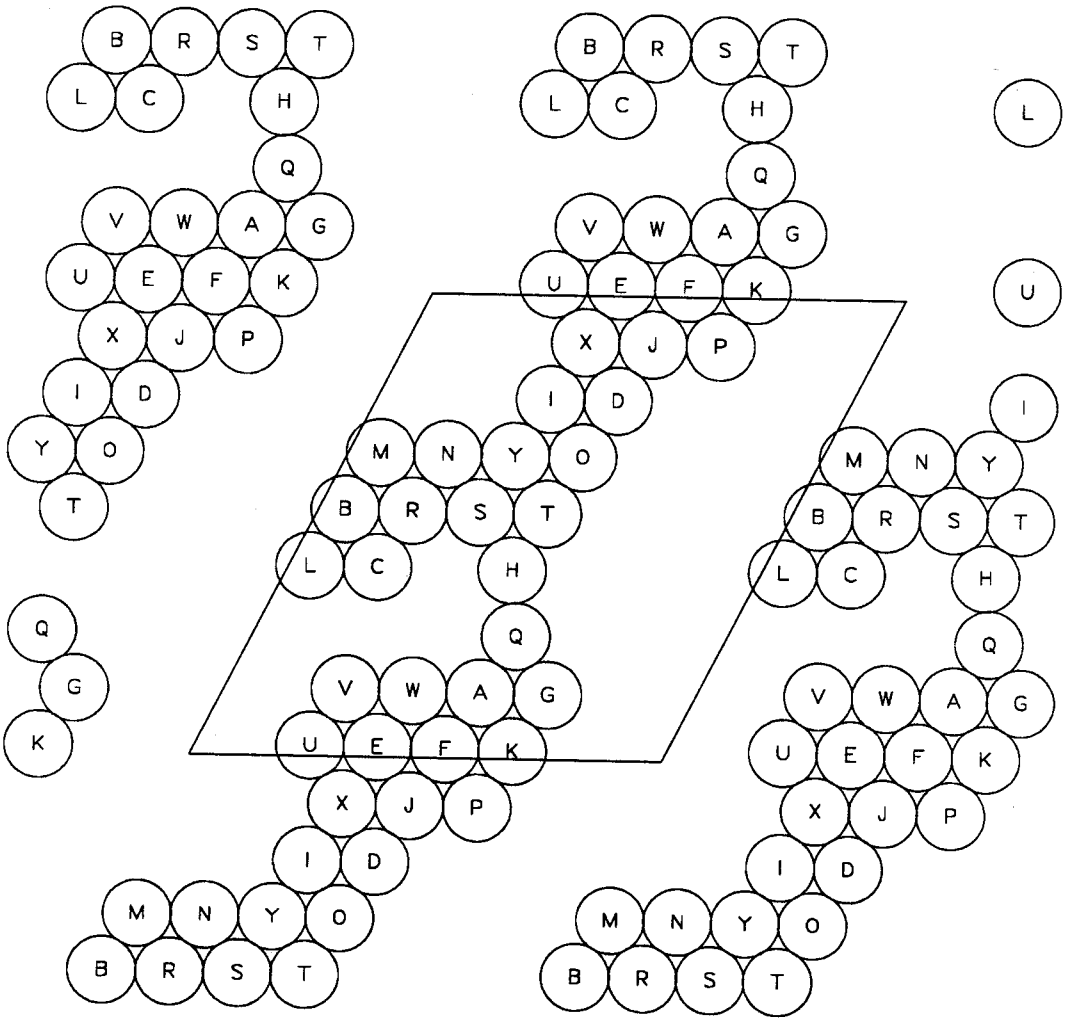

Figure 6.15*a*. Instantaneous snapshot for $N = 25$ and $Ma = 10^{-4}$ at $t = 6.5$. This sequence of configurations illustrates rapid intrachain microstructural rearrangements.

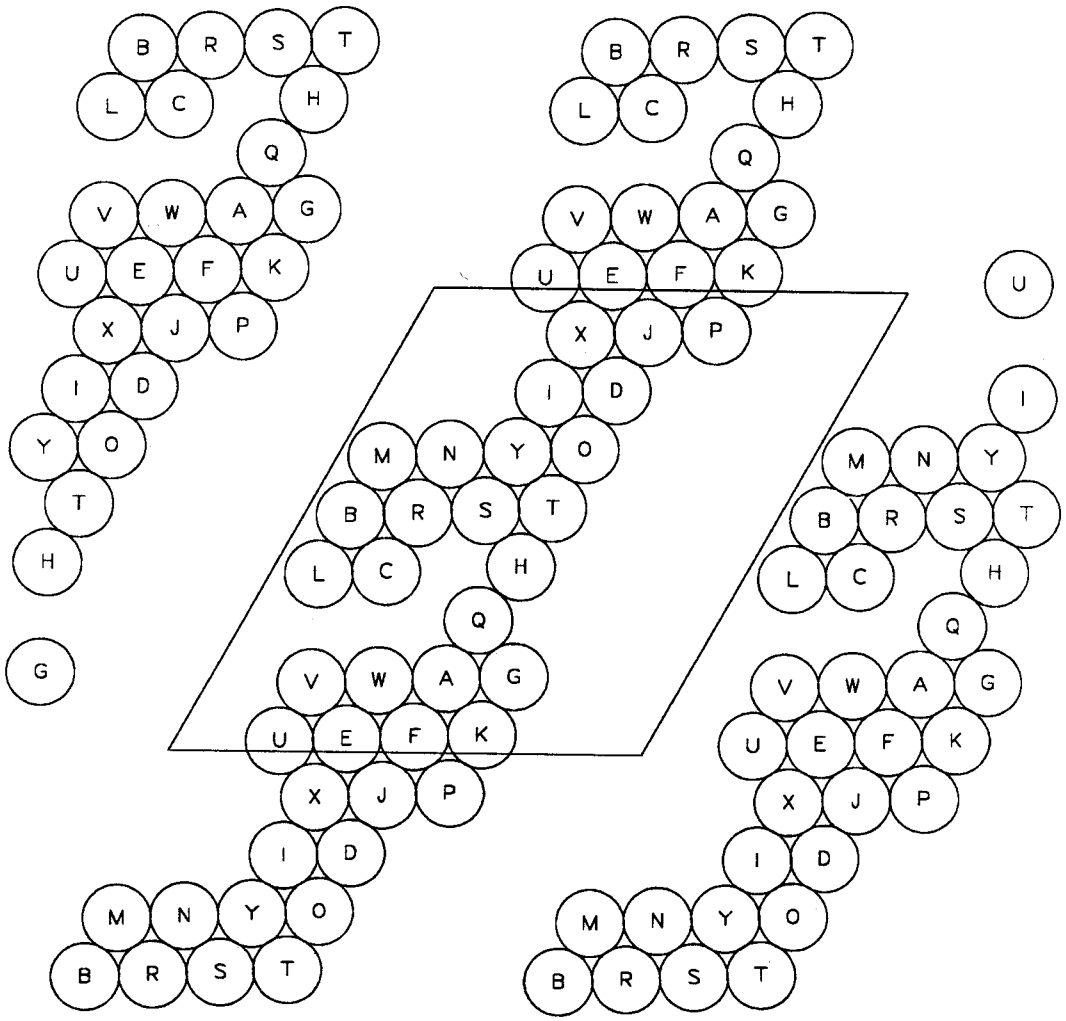

Figure 6.15*b*. As before for $t = 6.55$.

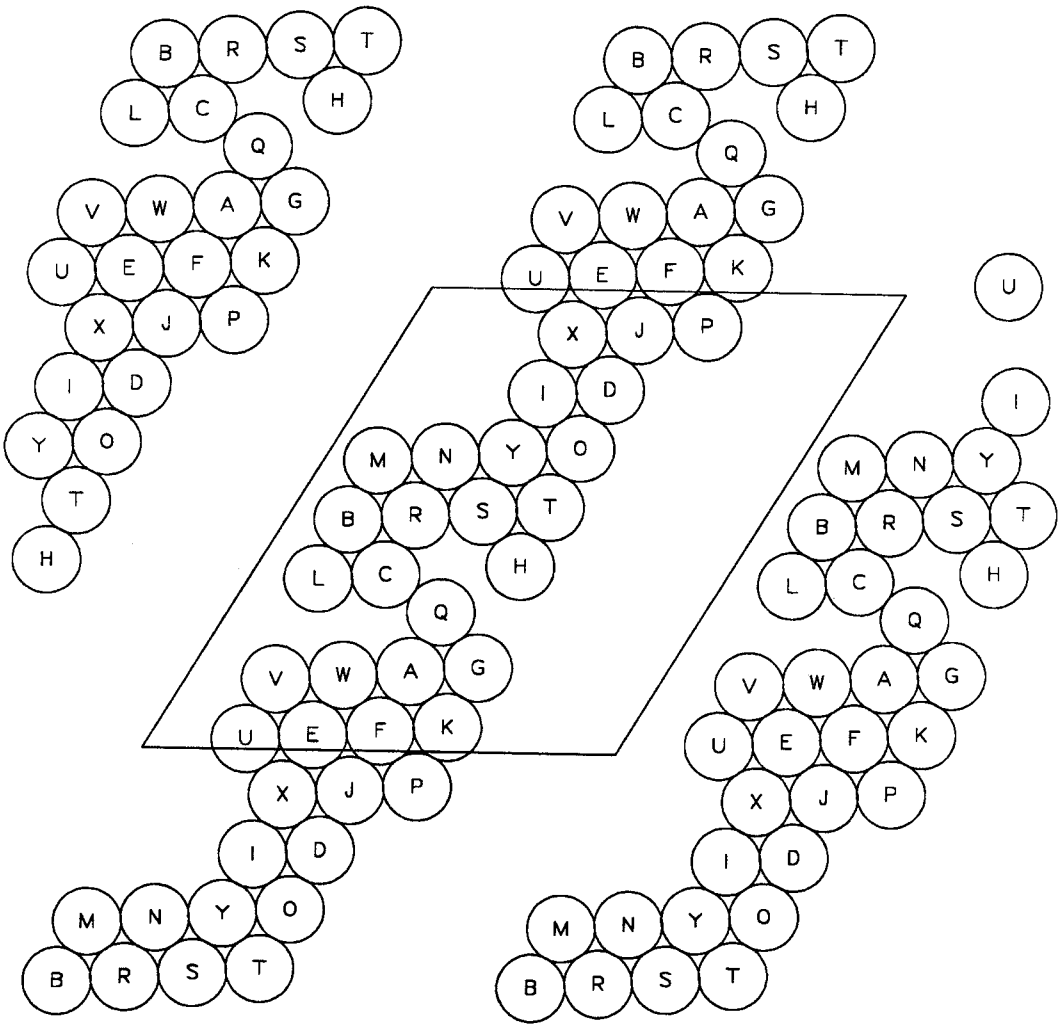

Figure 6.15*c*. As before for $t = 6.6$. Note the rapid jump made by particle C to Q.

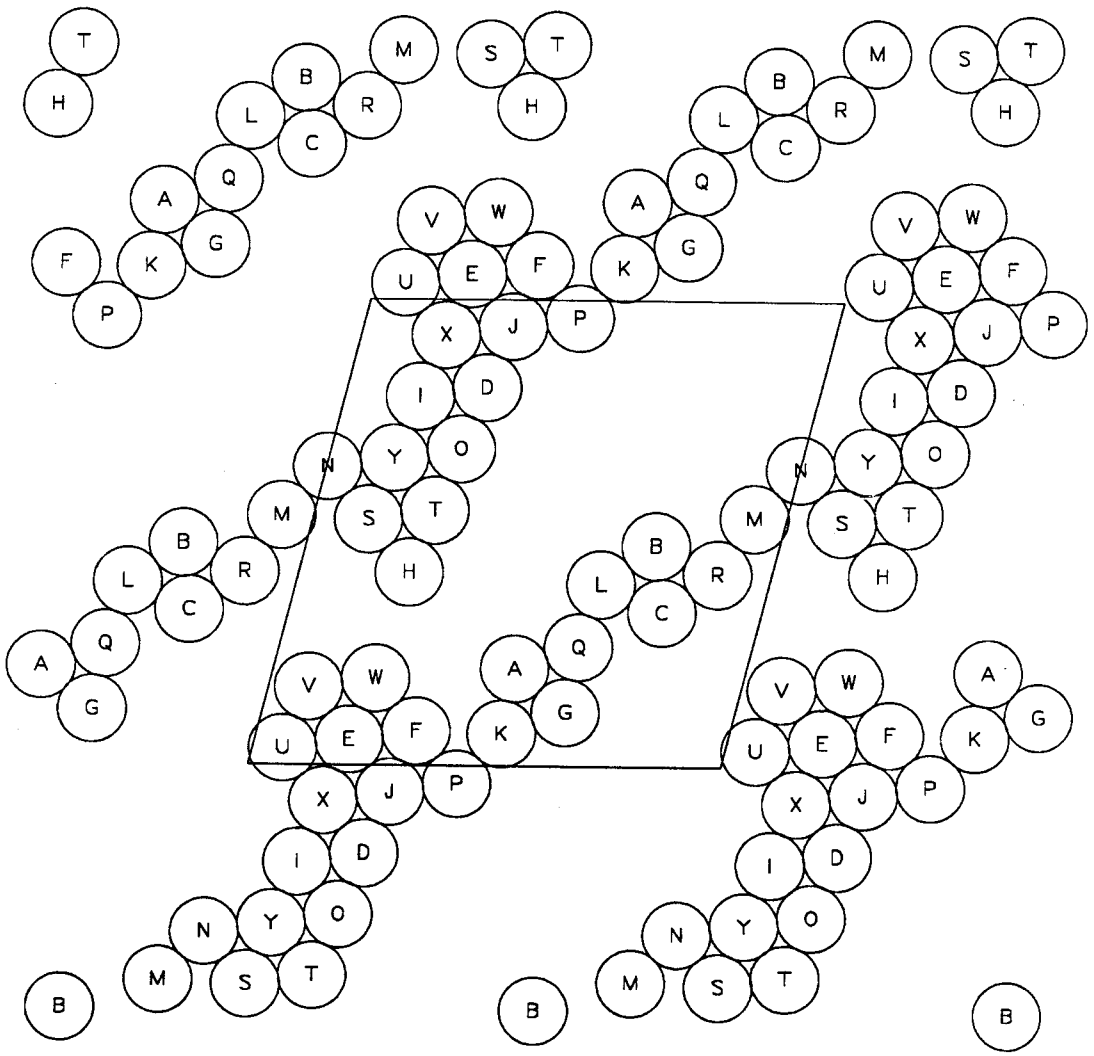

Figure 6.16*a*. Instantaneous snapshot for $N = 25$ and $Ma = 10^{-4}$ at $t = 7.25$. This sequence of configurations illustrates rapid network rearrangements.

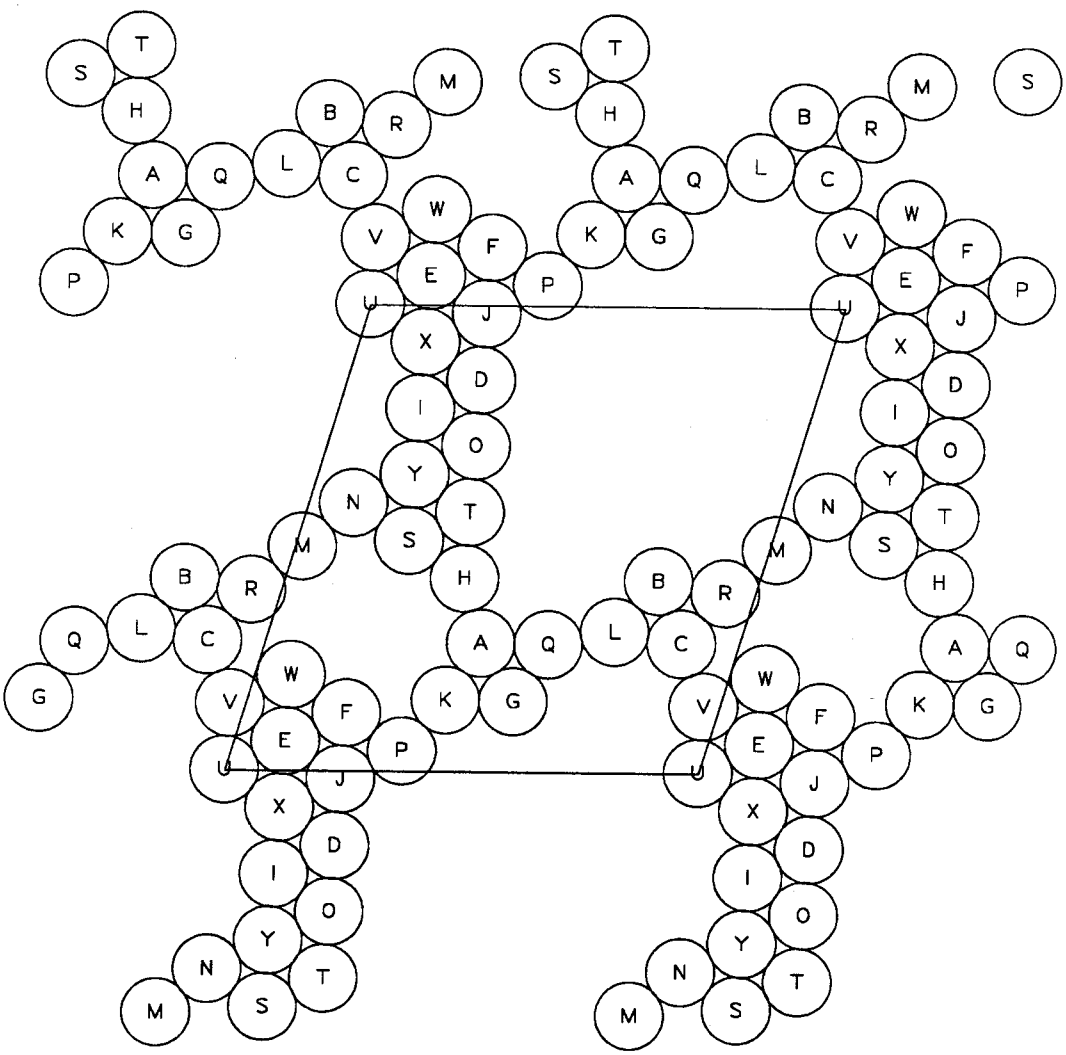

Figure 6.16*b*. As before for $t = 7.30$. Note the formation of an interconnecting network.

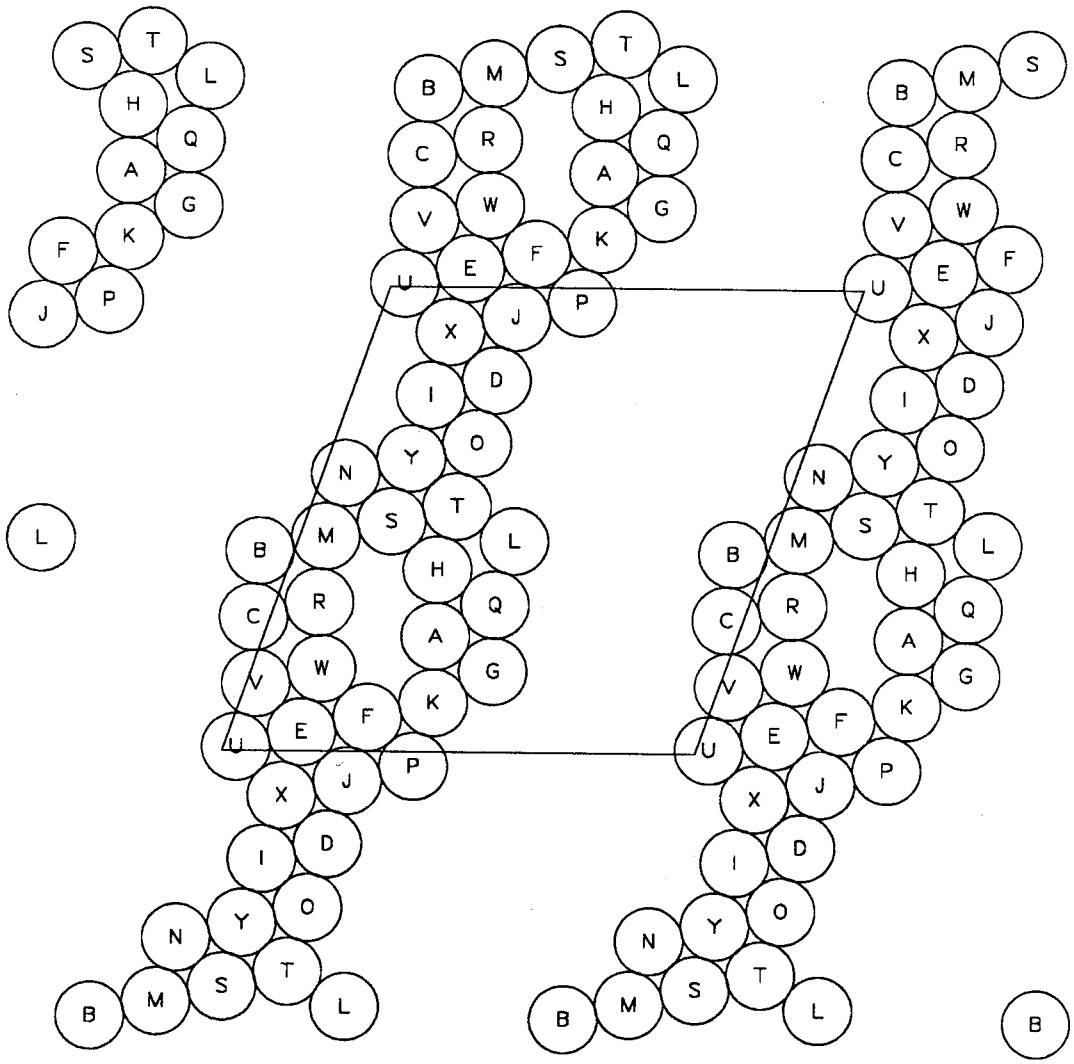

Figure 6.16c. As before for $t = 7.35$. Note the rapid contraction of the network into peroclating chains.

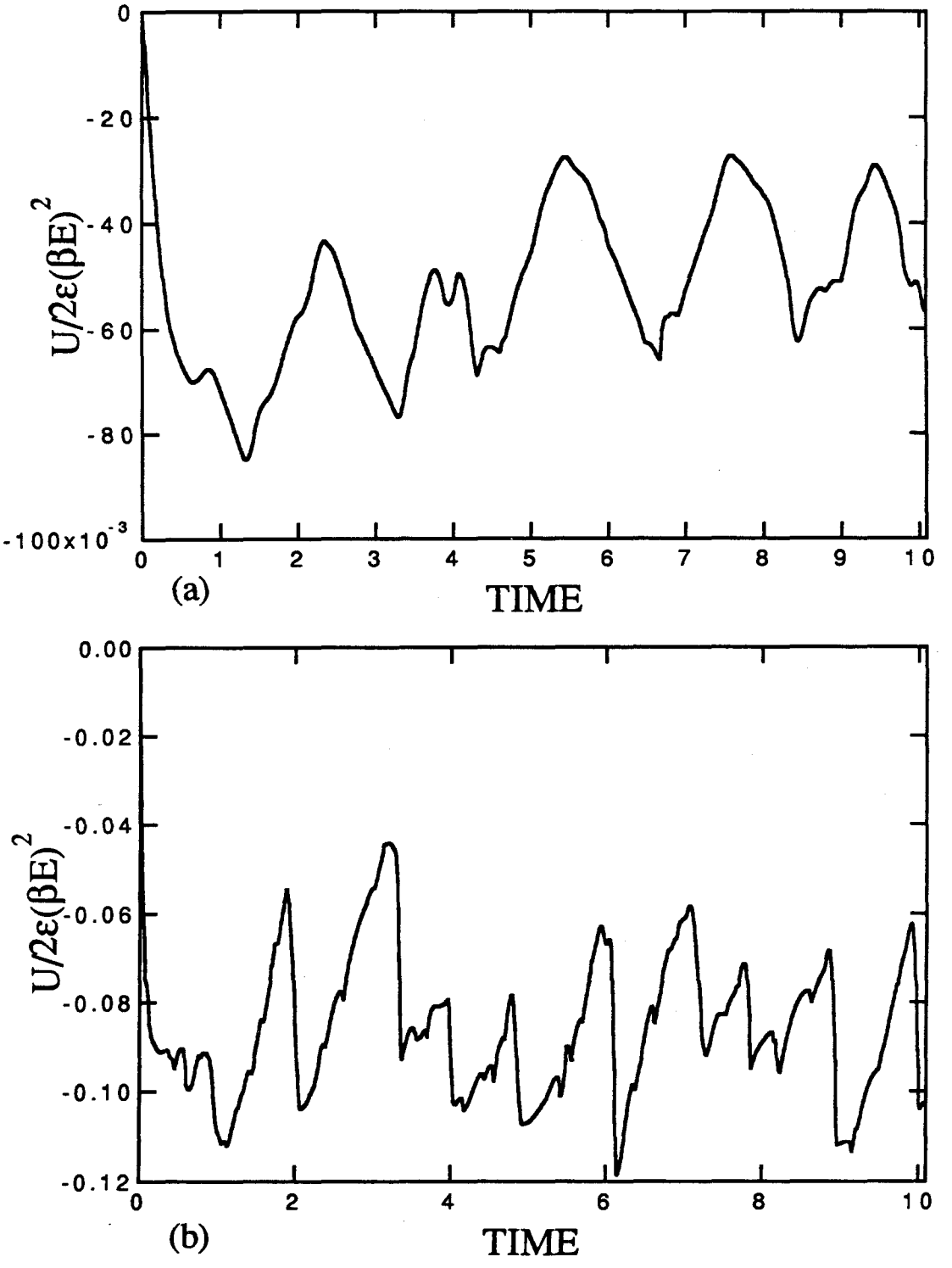

Figure 6.17*a, b.* Time traces of the electrostatic energy for $Ma = 10^{-2}$ (*a*) and $Ma = 10^{-3}$ (*b*).

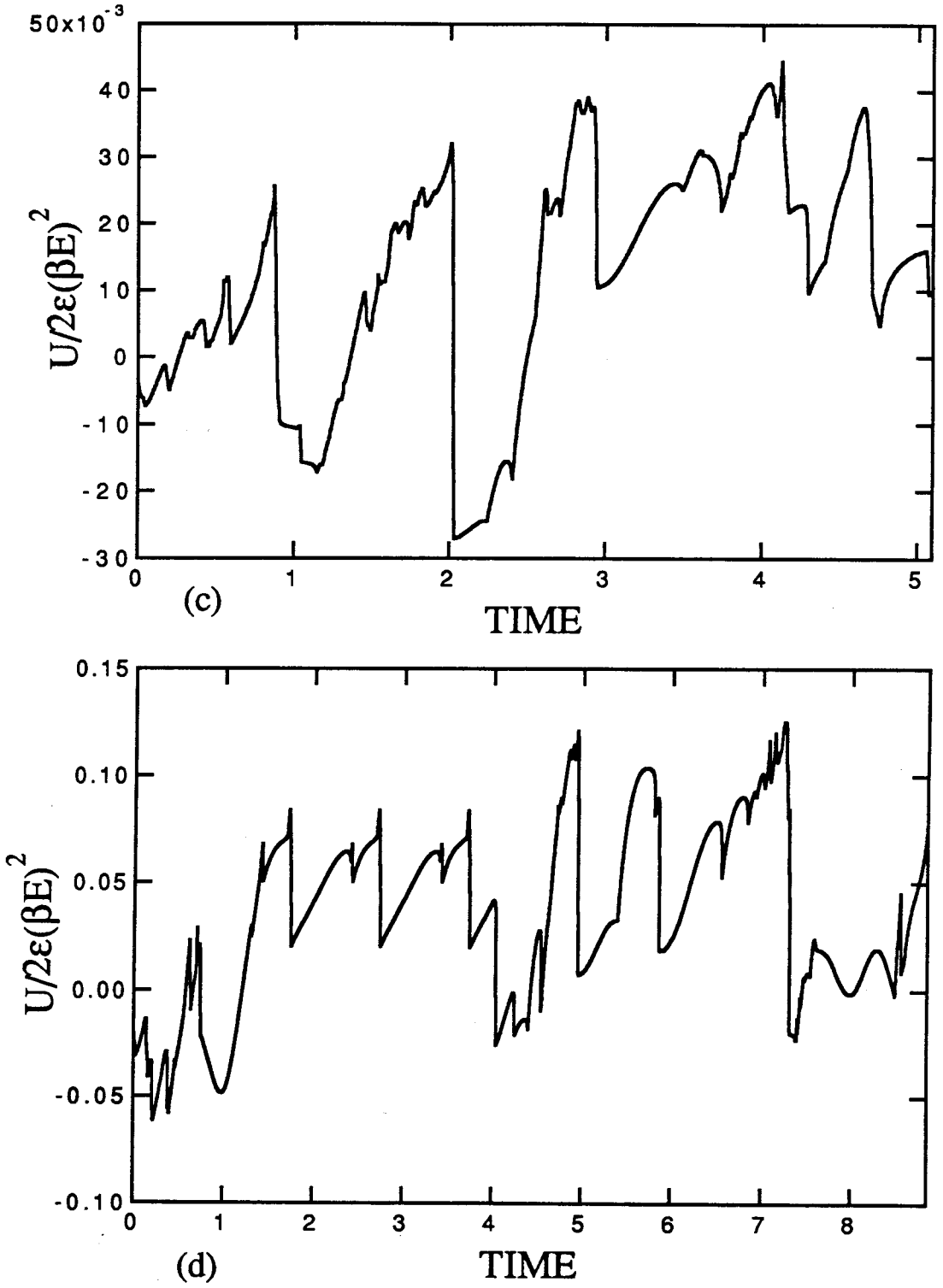

Figure 6.17*c*, *d*. Time traces of the electrostatic energy for $Ma = 2 \times 10^{-4}$ (*c*) and $Ma = 10^{-4}$ (*d*).

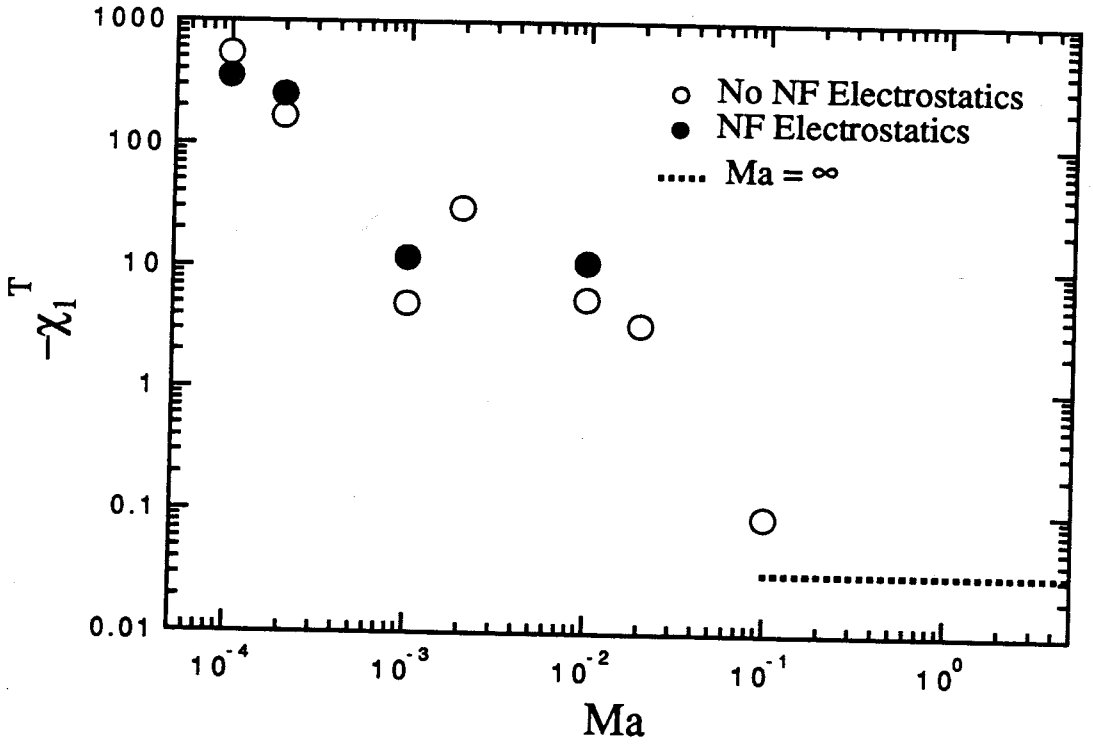

Figure 6.18. The negative of the first normal stress differences $\Sigma_{xx} - \Sigma_{yy}$ nondimensionalized by $\eta\dot{\gamma}$. Simulation results with and without the addition of near-field electrostatics are illustrated. The $Ma = \infty$ result is practically zero especially considering the fluctuations reported in Table 6.IV.

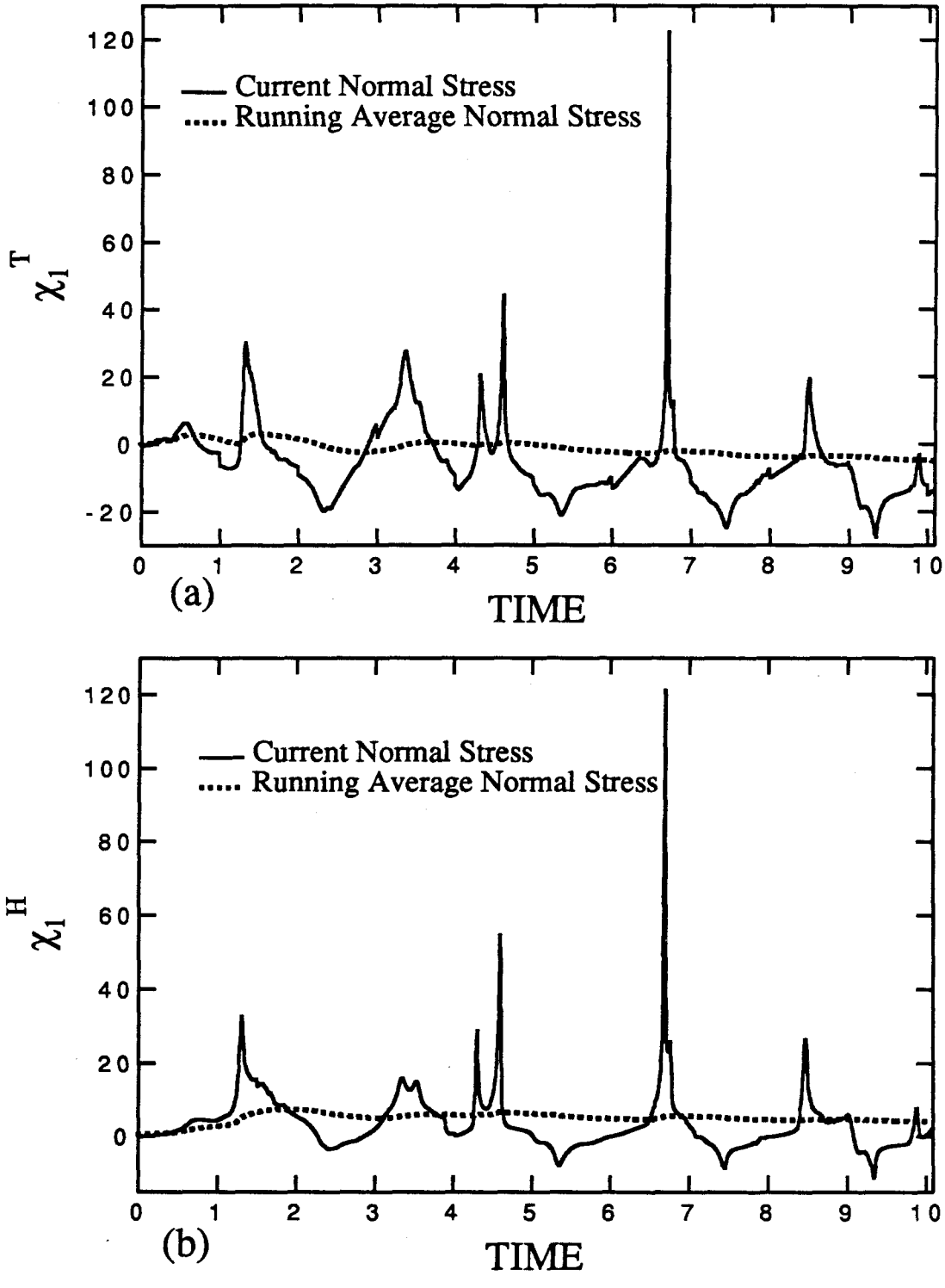

Figure 6.19*a, b.* Time traces of the total (*a*) and hydrodynamic (*b*) first normal stress difference for $Ma = 10^{-2}$.

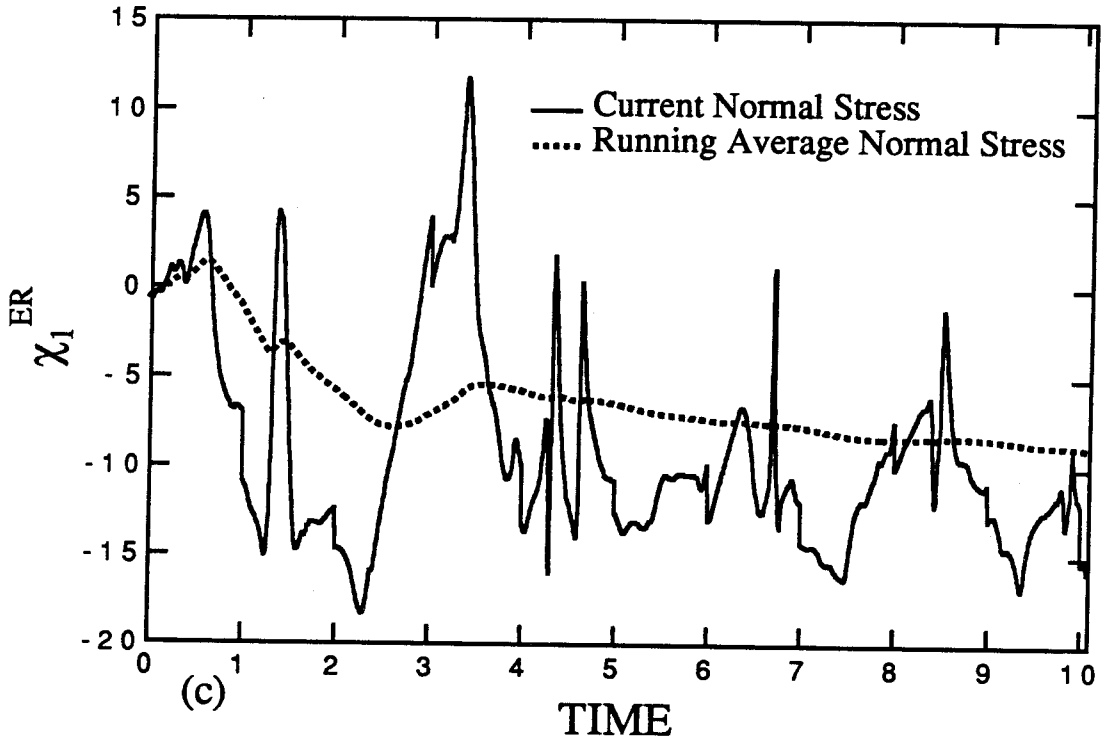

Figure 6.19*c*.Time trace of the ER (c) first normal stress difference for $Ma = 10^{-2}$.

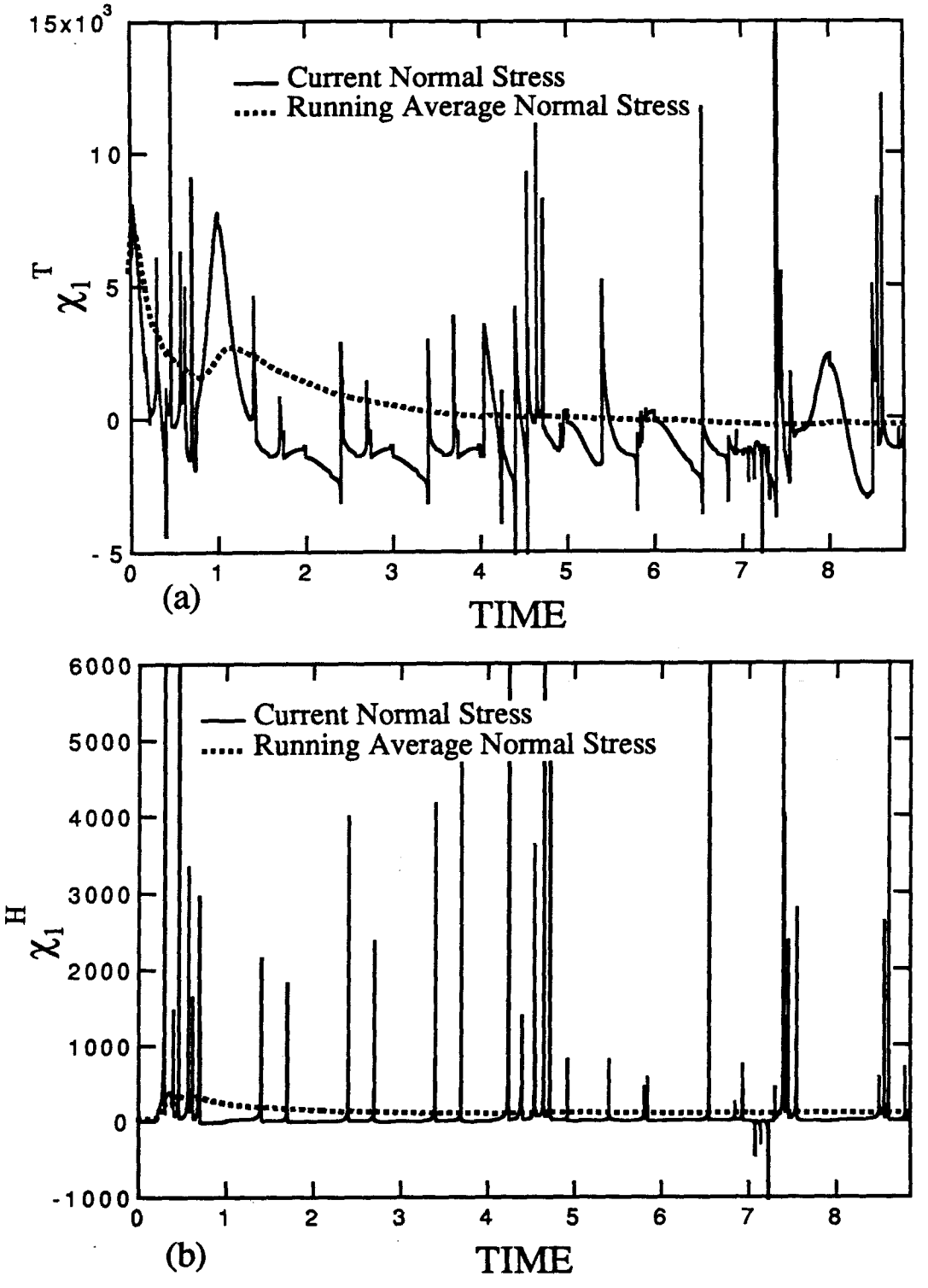

Figure 6.20*a, b.* Time traces of the total (*a*) and hydrodynamic (*b*) first normal stress difference for $Ma = 10^{-4}$. There are excursions exceeding 6000 but are clipped to concentrate on the basic features.

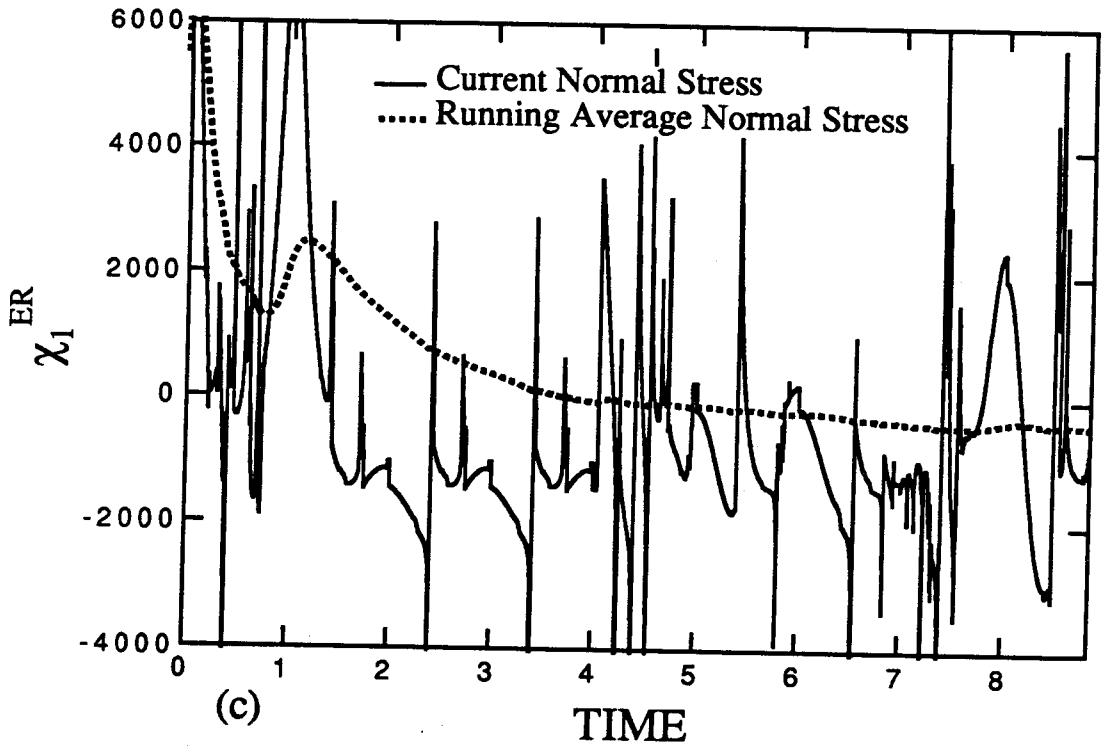

Figure 6.20*c*.Time trace of the ER (c) first normal stress difference for $Ma = 10^{-4}$.

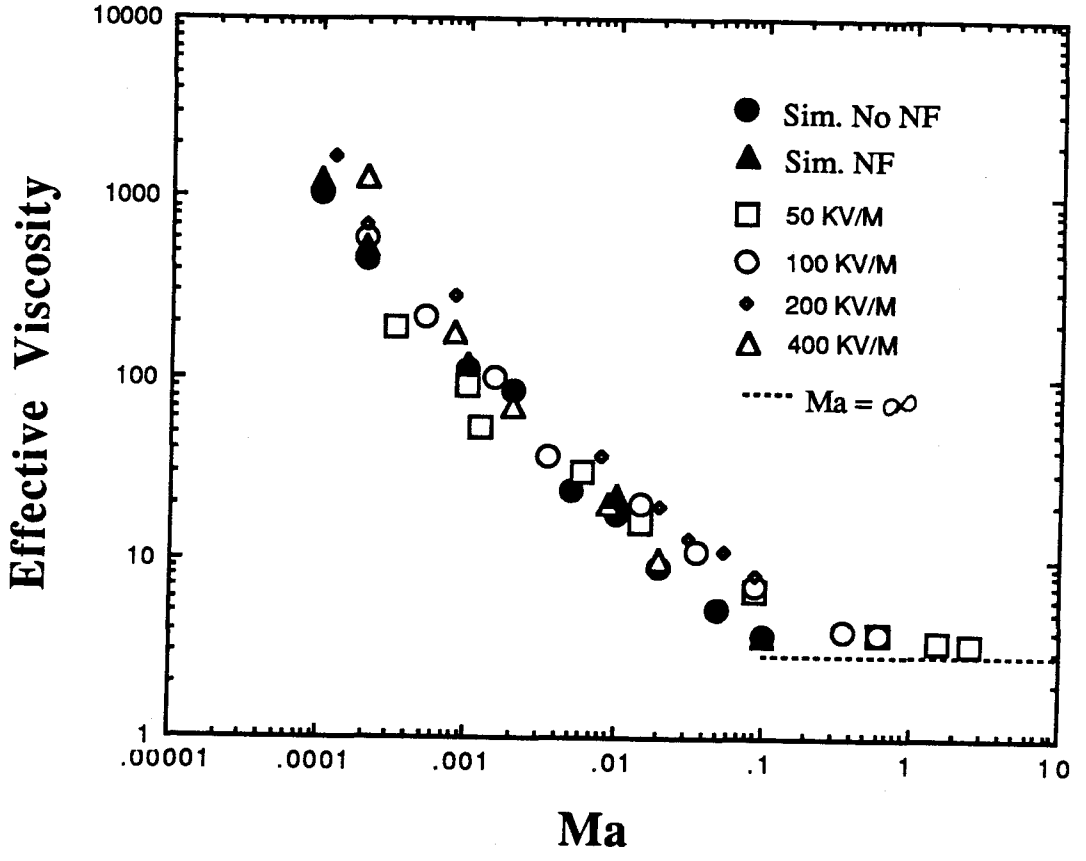

Figure 6.21 Comparison of simulation results to the experimental results of Marshall *et al.* illustrated with the open symbols and the applied field used. The equivalent volume fraction of the monolayer from the "two-thirds" rule is 0.27, and the experimental volume fraction is 0.23.

CHAPTER 7

YIELD STRESSES IN ELECTRORHEOLOGICAL FLUIDS

7.1 Introduction

From the simulations of the last chapter, the shear rheology of an electrorheological fluid apparently can be modeled reasonably well as a Bingham plastic with a Bingham yield stress. It is often concluded by extrapolation to zero-shear rate that the stress must exceed this dynamic yield stress in order for the material to flow and that the material can support a stress less than this critical value. Indeed an ER suspension can support a stress with no flow. For example, after a pair of electrodes is dipped in an ER suspension and an electric field is applied across them, the electrodes may be removed and the ER suspension trapped between the metal plates essentially is solidified. The ER suspension supports the gravitational stresses and does not flow. This behavior is the basis of operation for the ER valve.

The minimum stress required to cause the ER fluid to flow in the above example, however, is not necessarily the dynamic yield stress but the *static yield stress.* As pointed out by Kraynik (1990), there are three yield stresses characterizing the rheological behavior of a material, and they are illustrated with the hypothetical shear stress-shear strain curve in Figure 7.1 for a quasistatic deformation. The first is the elastic-limit yield stress τ_y which is most commonly used in solid mechanics. Upon complete removal of a stress exceeding τ_y, the material never fully recovers and suffers a permanent strain γ_e. The strain at the elastic-limit is the transition between elastic and plastic deformation. The maximum stress on the plot is the static yield stress τ_s, and it is the minimum stress necessary for the unbounded strain or deformation of the material. In the case of the solidified ER suspension between the electrodes, the gravitational stresses do not exceed the static yield stress. Finally, the plateau stress for large strains is the dynamic yield stress τ_d. Equivalently, it is the extrapolated stress in the limit of zero-shear rate on a shear stress-shear rate plot, which of course is the Bingham yield stress.

This schematic is just one example of the behavior of a viscoelastic material

meant to illustrate the three yield stresses. It is possible that there is no maximum stress, and that the static and dynamic yield stresses coincide. Also, the elastic-limit yield strain may occur below the strain at the static yield stress. The static yield stress shown in Figure 7.1 occurs in the elastic deformation region of the material, but it could arise from some plastic deformation behavior. Note for a Newtonian fluid the shear stress is zero for all strains since it cannot support a stress without flow.

Clearly, an ER suspension has a non-zero static yield stress as demonstrated by the dipped electrode experiment and the viability of the ER valve, but the existence of non-zero elastic-limit and dynamic yield stresses is not so transparent. There have been very few experiments studying the elastic-limit yield of an ER suspension. Filisko (1990) has performed some frequency response experiments where the electrified suspension is subjected to a small oscillating strain and has measured the resulting stresses for the fluid. For small deformations he observed a linear elastic response with a constant storage modulus, which indicates that the suspension is within the elastic region and hence has a non-zero elastic-limit yield stress. It is still not known if the elastic-limit yield strain occurs below or above the static yield strain.

The existence of the dynamic yield stress for any material, let alone an ER suspension, is still controversial. Barnes & Walters (1985) contend that the dynamic yield stress is nothing more than an empirical constant that depends on the experimental conditions and is thus not a real physical quantity. Their claim is based on the fact that as lower shear rates become measurable with better constant shear stress rheometers, they have observed that many materials continue to flow below the yield stresses previously determined with less accurate instruments. In essence the previous experiments were not carried out for a sufficient time to reliably measure a shear rate. Note that from their claim, the quasistatic stress-strain curve in Figure 7.1 would have zero dynamic yield stress plateau. For the few examples Barnes & Walters present, their argument is fairly convincing. Hartnett & Hu (1989), in an attempt to disprove Barnes & Walter's claim, performed an ex-

periment where they placed a ball in a less dense viscoelastic fluid and found from very accurate measurements that after several months the ball had not moved at all. While one might interpret this experiment as a falling ball rheometer and proof of a dynamic yield stress, it actually may only be demonstrating the existence of a static yield stress. Barnes & Walters, of course, would argue the experiment had not been carried out for a long enough time. In any event rheologists agree, including Barnes & Walters, that the yield stress concept is an invaluable engineering tool for modeling rheological behavior, but the question still remains whether it is a true physical quantity independent of the measuring apparatus.

In this chapter we shall describe and determine both the static and dynamic yield stress of an ER suspension from a microstructural point of view. In particular both descriptions will connect these yield stresses to the electrostatic energy determined from the suspension configuration. This relationship between energy and stress might not be surprising to those familiar with solid mechanics, where the strain-energy determines the stress of elastic (or hyperelastic) materials. Although we could use our simulation to study the elastic-limit yield stress, that project is post-poned to future work since the elastic-limit yield stress is of secondary importance compared to the other yield stresses.

In §7.2 we briefly outline the theory of elastic materials and explain how it can be applied to determine the non-linear elastic stress-strain relationship for the quasistatic deformation of an idealized model of an ER suspension. From its non-linear response we shall determine the static yield stress and the small strain elastic modulus of the material as functions of the volume fraction and the particle-to-fluid dielectric constant ratio. Also, since we compute the effective dielectric constant tensor for the suspension, we can calculate the zero-frequency birefringence with the strain of the material. The birefringence is an optical parameter used to probe the microstructure of a material. The birefringence is often linearly correlated to the stress in the material through a so-called stress optical rule. (Fuller 1990). We find that the relationship between the stress and the birefringence is highly non-linear and explain why this is so in terms of the electrostatic energy.

The dynamic yield stress is also related to the electrostatic energy of the suspension, but in a rather unique way due to the rapid reconfigurations of the microstructure or "chain snapping" observed in the previous chapter. In §7.3 we develop a theory for the dynamic yield stress using a total energy balance to relate the stress and the energy of the flowing system. We demonstrate for an ER fluid that the dynamic yield stress is indeed a real physical quantity counter to the claim of Barnes & Walters. This microstructural theory of the dynamic yield stress is then successfully proven by testing it with the dynamic simulation.

In §7.4 the theory is applied to a model microstructure that allows the relatively simple determination of the dynamic yield stress as a function of volume fraction and particle-to-fluid dielectric constant ratio. In the model, the dynamic yield stress exhibits a maximum at an optimal volume fraction for modest dielectric constant ratios. We also show that for our model microstructure the static yield stress is always greater than the dynamic yield stress. Finally, in §7.5 we make some concluding remarks.

7.2 Non-Linear Elastic Behavior of an ER Fluid

7.2.1 Theory of Stress in Non-Linear Elastic Materials

As we have described, the ER suspension appears to behave like a solid and exhibits some elastic behavior. The stress of a linear elastic material is proportional to the strain or deformation, and it is a reasonable approximation for small deformations of any elastic material. The electrostatic interactions that give rise to the forces among the particles in an ER suspension are highly non-linear as we have seen, so we suspect that beyond small deformations, the ER suspension has a non-linear elastic response. It is convenient to describe the stress response of a non-linear elastic material with its strain-energy $\mathcal{U}$, which is sometimes referred to as the strain energy function. There has been a rigorous mathematical development of the stress in terms of the strain energy for elastic materials, and this is explained in some detail in Gurtin (1981). Here we shall employ a few of the final results for our application.

From Gurtin the Piola-Kirchhoff stress $\boldsymbol{\sigma}$, in terms of the strain energy, is

$$\boldsymbol{\sigma} = \frac{\partial \mathcal{U}}{\partial \mathbf{G}^T}, \tag{7.1}$$

where $\mathbf{G}$ is the deformation tensor of the material. Note here we have $\mathbf{G}^T$ instead of $\mathbf{G}$ in equation (7.1) since our stress is the transpose of that used by Gurtin. The deformation tensor is the gradient of the final position of a particle $\mathbf{y}$ in the material or body with respect to its initial position $\mathbf{x}$, or

$$\mathbf{G} = \nabla_{\mathbf{x}}\mathbf{y}(\mathbf{x}). \tag{7.2}$$

A typical deformation is illustrated in Figure 7.2. The Piola-Kirchhoff stress corresponds to the force-per-unit area with respect to a reference configuration of the body in question. The reference configuration, for example, could be the originally undeformed body. The Piola-Kirchhoff stress is particularly useful in solid mechanics where the final deformation is usually not known, and so it is more convenient to describe the stress with respect to the known reference configuration.

The Cauchy stress $\boldsymbol{\tau}$ is the more common stress to fluid mechanics, and it is related to the Piola-Kirchhoff stress by,

$$\boldsymbol{\tau} = \frac{1}{\det \mathbf{G}} \mathbf{G} \cdot \boldsymbol{\sigma}, \tag{7.3}$$

where again we have transposed Gurtin's actual definition to be consistent with our convention for the definition of the stress. For an isochoric deformation, such as in an incompressible ER suspension, the determinant of the deformation tensor is unity. Now in terms of the strain for an isochoric deformation, the Cauchy stress is

$$\boldsymbol{\tau} = \mathbf{G} \cdot \frac{\partial \mathcal{U}}{\partial \mathbf{G}}. \tag{7.4}$$

The bulk stress $\boldsymbol{\Sigma}$ is also the Cauchy stress for the sheared suspension. The question is, how are the two stresses related and under what restrictions. We suspect that $\boldsymbol{\tau}$ is just the spring-like or thermodynamic stress $-n\langle \mathbf{x}\mathbf{F}^{\mathbf{P}} \rangle$ since both are elastic stresses. We demonstrate this and determine under what restrictions it is true in the following way.

Recall from equations (6.16) and (6.17) that the electrostatic energy $\mathcal{U}$ of the ER suspension is given by

$$\mathcal{U} = \frac{n}{2V} \mathcal{E} \cdot \langle \mathbf{C} \rangle \cdot \mathcal{E}. \tag{7.5}$$

From Chapter 2 the ensemble average capacitance matrix $\langle \mathbf{C} \rangle$ is a function of the instantaneous relative positions between particle pairs, and since the N-particle average electric field vector $\mathcal{E}$ is constant, $\mathcal{U}$ also must be only a function of the instantaneous relative particle positions. Then using the chain rule to evaluate equation (7.1), we find

$$\boldsymbol{\sigma} = \frac{n}{2} \sum_{\alpha} \sum_{\beta} \frac{\partial (\mathbf{y}_\alpha - \mathbf{y}_\beta)}{\partial \mathbf{G}} \cdot \frac{\partial \mathcal{U}}{\partial (\mathbf{y}_\alpha - \mathbf{y}_\beta)}, \tag{7.6}$$

where $\mathbf{y}_\alpha$ and $\mathbf{y}_\beta$ are the instantaneous or current positions of particles α and β, and the sums are over the N particles. The RHS of equation (7.6) is divided by $\frac{1}{2}$ to not double count interactions. For an homogeneous deformation, the deformation

tensor is constant so the current position $\mathbf{y}$ of each particle is proportional to its initial position $\mathbf{x}$ and is given by,

$$\mathbf{y} = \mathbf{G} \cdot \mathbf{x}, \tag{7.7}$$

and so

$$\frac{\partial(\mathbf{y}_\alpha - \mathbf{y}_\beta)}{\partial \mathbf{G}} = (\mathbf{x}_\alpha - \mathbf{x}_\beta)\mathbf{I}. \tag{7.8}$$

The Piola-Kirchhoff stress then becomes

$$\boldsymbol{\sigma} = \frac{n}{2} \sum_\alpha \sum_\beta (\mathbf{x}_\alpha - \mathbf{x}_\beta) \frac{\partial \mathcal{U}}{\partial(\mathbf{y}_\alpha - \mathbf{y}_\beta)}. \tag{7.9}$$

Using equation (7.3) for an isochoric deformation, we convert equation (7.9) into the Cauchy stress

$$\boldsymbol{\tau} = \frac{n}{2} \sum_\alpha \sum_\beta \mathbf{G} \cdot (\mathbf{x}_\alpha - \mathbf{x}_\beta) \frac{\partial \mathcal{U}}{\partial(\mathbf{y}_\alpha - \mathbf{y}_\beta)} \tag{7.10}$$

or

$$\boldsymbol{\tau} = \frac{n}{2} \sum_\alpha \sum_\beta (\mathbf{y}_\alpha - \mathbf{y}_\beta) \frac{\partial \mathcal{U}}{\partial(\mathbf{y}_\alpha - \mathbf{y}_\beta)}. \tag{7.11}$$

This is precisely equation $-n\langle \mathbf{x}\mathbf{F}^{\mathbf{P}} \rangle$ in equation (6.9) except for the change of xs for ys since $\mathbf{f}^{\alpha\beta} = -\frac{\partial \mathcal{U}}{\partial(\mathbf{y}_\alpha - \mathbf{y}_\beta)}$.

Thus, the strain energy Cauchy stress is equal to the bulk stress if the hydrodynamic stress $\langle \mathbf{S}^{\mathbf{H}} \rangle$ and the particle stress $\langle \mathbf{S}^{\mathbf{P}} \rangle$ vanish for the homogeneous deformation. For a quasistatic deformation of the ER suspension, or in limit of vanishing shear rate or Ma, the hydrodynamic stress vanishes since it is proportional to the shear rate. The particle stress is zero when the net electrostatic force on each particle is zero. This requirement on the force seems to eliminate the $-n\langle \mathbf{x}\mathbf{F}^{\mathbf{P}} \rangle$ stress altogether, but recall that equation (7.11) has pairwise forces between particles α and β since $\mathbf{f}^{\alpha\beta} = -\frac{\partial \mathcal{U}}{\partial(\mathbf{y}_\alpha - \mathbf{y}_\beta)}$. So while the sum of the pairwise forces over a particle is zero, each pairwise force does not necessarily vanish. In fact each individual particle on a periodic lattice has no net electrostatic interparticle force due to symmetry but each particle-particle pairwise force is non-zero. Further, certain

deformations of certain periodic lattices are homogeneous, satisfying the other requirement equating $\boldsymbol{\tau}$ and $-n\langle \mathbf{x}\mathbf{F}^{\mathbf{P}} \rangle$. Spheres on a simple cubic array, for example, subject to a shear strain or shear flow at zero-Reynolds number, deform or translate with the bulk deformation of the suspension.

Indeed most deformations in an ER suspension are simple shear strains with the deformation tensor

$$\mathbf{G} = \begin{pmatrix} 1 & \gamma & 0 \\ 0 & 1 & 0 \\ 0 & 0 & 1 \end{pmatrix}, \tag{7.12}$$

where γ is the amount of strain. Then from equations (7.1) and (7.4), the Cauchy shear stress on the plane parallel to the shear flow is

$$\tau = \frac{\partial \mathcal{U}}{\partial \gamma}. \tag{7.13}$$

In the next section this equation for the shear stress is applied to determine the stress-strain relation for an idealized ER suspension.

7.2.2 Non-Linear Elastic Simulations

The simplest microstructure that satisfies the requirements of an homogeneous deformation in a shear flow, a vanishing $\langle \mathbf{S}^{\mathbf{P}} \rangle$, and is physically reasonable is the rectangular lattice in Figure 7.3. This lattice looks like chains of particle aligned with the electric field like that seen in an ER fluid. Although depicted in two-dimensions, the lattice is actually three-dimensional, extending into and out of the page. As the structure strains, one layer of particles slides relative to the other by an amount depending on the strain. Eventually, due to the periodic nature of the microstructure, the initial configuration repeats itself at some shear strain γ_p which decreases with increasing volume fraction since the chains then start out closer together. Note that particles do actually move apart from neighbors in the same chain after one cycle.

Several simulations were performed on the microstructure in Figure 7.3 for volume fraction c from 0.1 to 0.5 and particle-fluid dielectric constant ratios, ϵ_p/ϵ, of 2, 4, and 10. The energy was computed at each configuration with equation (7.5), and then the periodic suspension was deformed some small strain (0.01 was found to be

sufficiently small). The energy was then recomputed at the new configuration. The shear stress was determined by numerically differentiating the energy with respect to the strain from equation (7.13). When checked against the bulk stress, the strain energy stress is indeed the $-n\langle \mathbf{x}\mathbf{F}^{\mathbf{P}} \rangle$ for the quasistatic deformation. Computationally, the stress determined with the energy method is much faster than using the bulk stress method since the energy requires only computing the capacitance matrix, while the bulk stress requires computing the complicated derivative of the capacitance matrix.

Figure 7.4 illustrates the energy and stress versus strain plots for $c = 0.2$ and is qualitatively typical of all the volume fractions. The starting configuration at zero strain is all particles aligned with the electric field as in the top sketch in Figure 7.3. This configuration is arbitrarily assigned the zero-energy state. As the material is strained, the energy of the suspension increases at first, reaches a maximum at $\frac{1}{2}\gamma_p$, and then decreases back to zero as the microstructure repeats itself. As we see, the changes in energy increase with increasing dielectric constant ratio. The broadness of the energy maximum decreases for increasing volume fraction as the periodic strain decreases as depicted in Figure 7.6.

The energy increases as the material strains because the particle dipoles increase as the particles move away from each other. Recall the energy is the sum of the dot product of the particle dipoles and electric field and that the dipoles are in opposite sense to the electric field. When the particles are nearby one another the *magnitude* of the dipoles is large due to the many-body far-field inductions and the near-field lubrication-like singularity discussed in Chapter 2. The magnitude decreases as the particles move apart, and since the dipole sign is negative relative to the electric field, the energy actually increases relatively. The strength of these far- and near-field interactions increases with increasing dielectric constant ratio, hence increasing the energy changes for equal deformations.

From the shear stress plot in Figure 7.4*b*, we see that the ER suspension is a highly non-linear elastic material that in fact does exhibit a static yield stress. As the suspension is strained from its initial configuration, the stress progressively in-

creases and becomes more non-linear with the strain. Eventually, the stress reaches the static yield stress τ_s, after which it decreases, reaches zero at half the period, becomes negative, reaches a minimum, and then returns to zero as the microstructure repeats itself. We can imagine straining the suspension requires ever more stress, and then after the static yield stress, the material strain softens and requires less stress to strain. In fact after $\frac{1}{2}\gamma_p$, we have to hold the suspension back to maintain a quasistatic deformation. Clearly, the stress must exceed the static yield stress in order for the unbounded strain of the material. The static yield stress increases with increasing dielectric constant ratio, and the static yield strain γ_s, decreases with increasing dielectric constant ratio. The negative stresses are a result of the periodic nature of the microstructure. After straining past $\frac{1}{2}\gamma_p$, the sphere chains can more easily realign themselves by moving forward in the direction of strain rather than counter to it, so the stress is negative. The increasing static yield stresses with dielectric constant ratio are again due to the increasing interparticle interactions with increasing dielectric constant ratios. Finally, since the deformation near zero-strain is asymptotically linearly elastic, we can assign a modulus in this region as the proportionality between the shear stress and the shear strain. This slope also increases with increasing dielectric constant ratio due to the increased electrostatic interactions.

Table 7.I and Figure 7.5 summarize the results for the static yield stress and modulus for the range of volume fractions and dielectric constants listed earlier. Interestingly, the static yield stress increases linearly with c for low c and approaches saturation or even exhibits a maximum for large c. The energy of the suspension is effectively the product of the number density of chains n_c and the energy per chain $\mathcal{U}_c$. Then $\tau = n_c \frac{\partial \mathcal{U}_c}{\partial \gamma}$. At low volume fractions the chains are too far apart to interact with one another so the energy per chain and the change in energy per chain with strain does not depend on volume fraction. That is, the intrachain interparticle interactions dominate the interchain interparticle interactions. Since n_c scales linearly with c, the static yield stress increases linearly with volume fraction. This is illustrated in Figure 7.6 where the energy and stress, normalized by the number

density of spheres, is plotted versus strain for $\epsilon_p/\epsilon = 4.0$ As the volume fraction increases, however, the chains begin to interact electrostatically. As the material strains, although particles move away from other particles within their own chain, particles in the nearby chains are now close, so the change in energy at similar strains is less than that at lower volume fractions. In fact the change in energy per chain decreases faster than c^{-1} for $\epsilon_p/\epsilon \leq 4$ resulting in a maximum in the static yield stress at about $c = 0.4$. Qualitatively similar results are seen for the modulus G in Figure 7.5*b*, and similar arguments as those used for the yield stress can be applied to explain them.

Recall that the electrostatic energy is $(ln\xi)$ and that the interparticle force is $O(\xi^{-1})$ for perfect conductors $(\epsilon/\epsilon = \infty)$ near contact where ξ is the non-dimensionalized separation distance between particle surfaces. Thus, it is expected that the energy and stress would be quite large for a suspension of perfect conductors. Stress-strain simulations at $c = 0.1-0.5$ were performed on perfect conductors with an assumed particle interface separation distance of 1×10^{-5}. This corresponds to a 1nm steric layer separating 100μm particles. Klingenberg (1990) has proposed this separation as the lower limit of gap spacing attainable for perfectly conducting particles with steric layers, and thus provides a maximum bound on the yield stress in an ER fluid. The energy and stress for $c = 0.2$ are illustrated in Figure 7.7. The strain is only plotted out to 0.2 to resolve the static yield stress which is very sharp and occurs at a strain of 0.003. The remaining part of the curve is qualitatively like Figure 7.4. The static yield stress and the modulus are depicted in Figure 7.8. Both curves are practically linear. Since the particles are perfect conductors, the near-field interactions completely dominate, so interchain interactions are unimportant for determining the elastic properties.

In assigning the maximum of the non-linear elastic stress as the static yield stress, we are assuming that the material does not reach its elastic-limit at this point. Certainly, this is true for our idealized microstructure, but, unfortunately, we cannot compare our predicted static yield stresses to experimental values for lack of data. Our modulus corresponds to the low frequency storage modulus, and when

experimental data such as that of Filisko (1990) is published, a comparison can be made. Of course a real ER suspension confined between two plates quasistatically deformed does not exhibit the complete stress-strain behavior shown in Figure 7.4. As shown in the previous chapter, the suspension microstructure undergoes rapid microstructural rearrangements at some particular strain. The perfect periodicity of the microstructure precludes this "snapping" of the chains. It is possible, however, that the ER fluid might behave as in Figure 7.4 up until that critical strain, and ER suspension behaves qualitatively, at least as we have shown.

7.2.3 Birefringence of a Slowly Deforming ER Suspension

The measurement of optical parameters, such as the birefringence or dichroism, is often used to determine the microstructure in a suspension (see Fuller 1990 and Doi & Edwards 1986). Usually, the stress is not measured independently, but it is assumed that the stress is proportional to the optical parameter with a linear stress-optical rule. The stress and microstructure of the suspension can then be correlated, for example, under flow conditions or states of strain.

Any material is birefringent if plane polarized light travels through it at different speeds, depending upon the angle of the plane relative to some axis on the material face. The birefringence, roughly speaking, measures the difference in the speed of light for two particular plane polarized beams. The birefringence is precisely defined as the difference between the two principal eigenvalues of the index of refraction tensor $\mathbf{N}$ (Fuller 1990). From Doi & Edwards (1986) the index of refraction tensor at low frequency or long-wavelength is the square root of the effective dielectric constant tensor $\mathbf{\Lambda}$ of the suspension introduced in the earlier chapters, or

$$\mathbf{N} \cdot \mathbf{N} = \mathbf{\Lambda}. \tag{7.14}$$

In terms of two of the three principal eigenvectors of $\mathbf{\Lambda}$, ϵ_{11} and ϵ_{22}, the birefringence, ΔN, is

$$\Delta N = \sqrt{\epsilon_{22}} - \sqrt{\epsilon_{11}}, \tag{7.15}$$

Here we assume that the light travels perpendicular to the plane of two of the three eigenvectors. This is usually realized experimentally when the light beam travels

parallel to the axis of the cylinders in a Couette device. In this approximately two-dimensional flow the annular planes of the device are the planes of two of the principal eigenvalues.

Using the simulation, we can compute the zero-frequency or long-wavelength limit of the birefringence from the effective dielectric constant tensor with equation (7.15) for the quasistatic stress-strain experiments. Figure 7.9*a* is a plot of the birefringence versus strain for $c = 0.2$ and $\epsilon_p/\epsilon = 10$. The birefringence is highest at the initial configuration when the particles are all aligned. The effective dielectric constant is highest for all strains along the eigenvector of the axis of the particle chains and lowest along the eigenvector perpendicular to that axis. Since the particles are closest at the initial configuration, the maximum eigenvalue difference or birefringence occurs here. As the suspension is deformed, the birefringence decreases since the dielectric tensor becomes more isotropic as the microstructure becomes more isotropic (see Figure 7.3). In fact the birefringence almost vanishes at $\frac{1}{2}\gamma_p$ where the microstructure is almost perfectly isotropic. As the microstructure returns to it initial configuration so does the birefringence.

Compared to the stress in Figure 7.4*b* and repeated in Figure 7.9*b*, the birefringence is not linearly proportional to the stress, even at small strains. Apparently, there is no linear stress-optical rule. The birefringence, however, looks like an inverted energy versus strain curve, so we might suspect that the negative derivative of the birefringence might be the optical parameter for a linear stress-optical rule. Actually, the derivative of the square of the birefringence turns out to be the correct optical parameter, and the explanation, not surprisingly, is based upon the energy.

The energy of the suspension in terms of the ensemble average capacitance matrix $\langle \mathbf{C} \rangle$ is

$$\mathcal{U} = \frac{1}{2} n \mathbf{E} \cdot \langle \mathbf{C} \rangle \cdot \mathbf{E}, \tag{7.16}$$

where n is the number density of particles. From Chapter 2 the effective dielectric constant tensor is

$$\mathbf{\Lambda} = \mathbf{I} + n\langle \mathbf{C} \rangle. \tag{7.17}$$

The energy and the dielectric constant are both proportional to $\langle \mathbf{C} \rangle$. Since the

birefringence roughly scales with the square root of the magnitude of $\mathbf{\Lambda}$, then $\Delta N \sim \mathcal{U}^{1/2}$ or $\mathcal{U} \sim \Delta N^2$. Because shear stress is the derivative of the energy with respect to strain, we conclude that

$$\tau = -\xi \frac{\partial (\Delta N)^2}{\partial \gamma}, \tag{7.18}$$

where ξ is some constant and the negative sign ensures the right sign for the stress.

Figure 7.9*b* compares the birefringence function in equation (7.18) to the stress for $\epsilon_p/\epsilon = 10$ and $c = 0.2$. The constant $\xi = 8.1$ was chosen to give the best comparison, which is extremely good. Any discrepancy is due to the fact that our scaling argument relies on comparing the magnitude of scalars to tensors which is not exactly direct, but is certainly reasonable in light of the results. The results for other volume fraction and dielectric constant ratios are similar. The offering here is foremost a formula for experimentalists to correlate the quasistatic stress-strain with birefringence function of equation (7.18). It is also one example of the power of these simulations as a tool to test a microstructural theory for a measurable macroscopic property. In the next section, we shall apply the simulation to help develop and test a theory for the dynamic yield stress.

7.3 Theory of the Dynamic Yield Stress

In the previous section we saw how the non-linear elastic properties of an ER suspension, particularly the static yield stress, are related to the electrostatic energy of the system. We might wonder if the dynamic yield stress is also related to the electrostatic energy. There is, in fact, compelling evidence from the dynamic simulations of Chapter 6 in favor of such a relationship. Although the dynamic yield stress is typically thought of as a force per unit area, it can also be interpreted as an energy per unit volume, as is $\mathcal{U}$. Also, the dynamic yield stress scales with the square of the electric field, for small enough Ma, as does the electrostatic energy. Further, the dynamic yield stress begins to follow this dependence at the Ma where the rapid reconfigurations of the microstructure begin to occur. It is then not unreasonable to suppose that the energy jumps we saw associated with the rapid reconfigurations are related to the dynamic yield stress. In this section we shall prove this conjecture by deriving the exact relationship between the energy jumps and the dynamic yield stress.

In order to connect the stress and the electrostatic energy of an ER suspension, we use the total energy balance applied to the control volume illustrated in Figure 7.10. The ER suspension is confined between two plates a distance l apart across which there is an electric field. The lower plate is immobile and the upper plate translates steadily with a velocity such that the shear rate in this Couette flow is $\dot{\gamma}$. The areal average shear stress on the top plate is τ. The total integral energy balance of this flowing system is (Whitaker 1984),

$$\int_{A_{upper}} \mathbf{n} \cdot \boldsymbol{\tau}'(t) \cdot \mathbf{v} dA = \int_V \Phi'(t) dV + \frac{d}{dt} \int_V \mathcal{U}'(t) dV, \tag{7.19}$$

where $\boldsymbol{\tau}'(t)$ is the local instantaneous stress on the upper plate, $\Phi'(t)$ is the local instantaneous dissipation rate per unit volume, and $\mathcal{U}'(t)$ is the local instantaneous electrostatic energy per unit volume. The area of the upper plate is A_{upper} and the volume of the system is V. The energy balance basically states that the rate of work done on the fluid by the moving plate is equal to the rate of energy dissipated by the fluid plus the rate of increase in the electrostatic energy of the system. Because

the flow is a steady shear and the control volume does not change shape or size, several terms have been eliminated, such as the kinetic energy of the system and the rate of energy flux into and out of the control volume.

Since the top plate moves steadily, its velocity $\mathbf{v} = \dot{\gamma} l \mathbf{e}_x$. The energy balance then becomes,

$$\int_{A_{upper}} \tau'(t)\dot{\gamma} l dA = \int_V \Phi'(t) dV + \frac{d}{dt}\int_V U'(t) dV, \tag{7.20}$$

where $\tau'(t)$ is the instantaneous local shear stress on the wall. To evaluate the LHS of equation (7.20), the instantaneous pointwise shear stress is replaced by the instantaneous areal averaged shear stress $\tau(t)$. Further, Batchelor (1970) has shown that for a statistically homogeneous suspension, such as the one in the control volume, $\tau(t)$ is constant throughout the control volume and so is equal to the instantaneous volume averaged shear stress. Thus the areal stress or work integral can be replaced by a volume integral with $\tau(t)$, and so the energy balance becomes

$$\int_V \tau(t)\dot{\gamma} dV = \int_V \Phi'(t) dV + \frac{d}{dt}\int_V U'(t) dV. \tag{7.21}$$

Replacing $\Phi'(t)$ and $U'(t)$ by the volume averaged dissipation rate and energy, $\Phi(t)$ and $U(t)$, we derive the volume averaged energy balance

$$\tau(t)\dot{\gamma} = \Phi(t) + \frac{dU(t)}{dt}. \tag{7.22}$$

All these terms, of course, fluctuate in time. The average stress and the energy decrease rapidly upon snapping, and, as we shall see, the dissipation increases dramatically at this point. The dynamic yield stress, however, is a time average quantity since it is the plateau stress for large strains, and so it is associated with several of these strain-snapping episodes during deformation. The time average of equation (7.22) is,

$$\frac{1}{T}\int_0^T \tau\dot{\gamma} dt = \frac{1}{T}\int_0^T \Phi(t) dt + \frac{1}{T}\int_0^T \frac{dU(t)}{dt} dt, \tag{7.23}$$

where T is a time period that includes many rapid reconfiguration events. Evaluating the last integral and replacing the time averaged stress integral by the time

averaged stress, $\langle\tau\rangle$, we find that

$$\langle\tau\rangle\dot{\gamma} = \frac{1}{T}\int_0^T \Phi(t)dt + \frac{U(T) - U(0)}{T}. \tag{7.24}$$

All that is left is to evaluate the dissipation integral. In the above same paper Batchelor (1970) also determined the volume average dissipation rate per unit volume for a statistically homogeneous suspension, and found that

$$\Phi(t) = [2\eta\mathbf{E}^\infty + n\langle\mathbf{S^H}\rangle + n\langle\mathbf{S^P}\rangle] : \mathbf{E}^\infty + \frac{1}{V}\mathbf{F^P}\cdot(\mathbf{U} - \mathbf{U}^\infty). \tag{7.25}$$

As a reminder, $\mathbf{E}^\infty$ is the bulk rate of strain, $\mathbf{S^H}$ and $\mathbf{S^P}$ are the hydrodynamic and particle stresses, and $\mathbf{U} - \mathbf{U}^\infty$ is the N-relative particle velocity vector. The first term is the dissipation due to the bulk stress without the $-n\langle\mathbf{xF^P}\rangle$ multiplied by the strain rate. The elastic stress is not included since it is not associated with dissipation. The second term is the power consumed moving a particle through a force field, and it is, as expected, invariant to the motion of the observer. Equation (7.25) can be simplified if we recall from equation (6.3) that

$$\mathbf{U} - \mathbf{U}^\infty = \mathbf{R}_{FU}^{-1}\cdot\mathbf{F^P} + \mathbf{R}_{FU}^{-1}\cdot\mathbf{R}_{FE} : \mathbf{E}^\infty, \tag{7.26}$$

and from equation (6.8*b*) that

$$\langle\mathbf{S^P}\rangle = -\langle\mathbf{R}_{SU}\cdot\mathbf{R}_{FU}^{-1}\cdot\mathbf{F^P}\rangle. \tag{7.27}$$

Using equations (7.26) and (7.27) in the energy dissipation rate yields,

$$\begin{aligned}\Phi(t) = {} & [2\eta\mathbf{E}^\infty + n\langle\mathbf{S^H}\rangle] : \mathbf{E}^\infty - n\langle\mathbf{R}_{SU}\cdot\mathbf{R}_{FU}^{-1}\cdot\mathbf{F^P}\rangle : \mathbf{E}^\infty \\ & + \frac{1}{V}\mathbf{F^P}\cdot\mathbf{R}_{FU}^{-1}\cdot\mathbf{F^P} + n\langle\mathbf{F^P}\cdot\mathbf{R}_{FU}^{-1}\cdot\mathbf{R}_{FE}\rangle : \mathbf{E}^\infty,\end{aligned} \tag{7.28}$$

where the last term has been written in ensemble average form. Because $\mathbf{R}_{FU}^{-1}$ is symmetric and $\mathbf{R}_{SU}$ is the transpose of $\mathbf{R}_{FE}$,

$$\langle\mathbf{R}_{SU}\cdot\mathbf{R}_{FU}^{-1}\cdot\mathbf{F^P}\rangle = \langle\mathbf{F^P}\cdot\mathbf{R}_{FU}^{-1}\cdot\mathbf{R}_{FE}\rangle, \tag{7.29}$$

and so

$$\Phi(t) = \eta^H\dot{\gamma}^2 + \frac{1}{V}\mathbf{F^P}\cdot\mathbf{U^P}, \tag{7.30}$$

where $\mathbf{U^P} = \mathbf{R}_{FU}^{-1} \cdot \mathbf{F^P}$ is the particle velocities due to the interparticle forces. We shall call $\frac{1}{V}\mathbf{F^P} \cdot \mathbf{U^P}$ the particle dissipation rate. The $\eta^H \dot{\gamma}^2$ is the dissipation rate for a simple shear flow, and it has the form of the dissipation rate for a Newtonian fluid.

If we insert this result into equation (7.24), the time average energy balance becomes,

$$\langle \tau \rangle \dot{\gamma} = \langle \eta^H \rangle \dot{\gamma}^2 + \frac{1}{T}\int_0^T \frac{1}{V}\mathbf{F^P} \cdot \mathbf{U^P} dt + \frac{\mathcal{U}(T) - \mathcal{U}(0)}{T}, \tag{7.31}$$

where $\langle \eta^H \rangle$ is the time averaged hydrodynamic viscosity of the suspension. It is interesting to determine the scaling of the integral of the particle dissipation rate. The force vector, $\mathbf{F^P}$ is $O(2\epsilon(\beta E)^2 a^2)$ and the particle velocity, $\mathbf{U^P} = \mathbf{R}_{FU}^{-1} \cdot \mathbf{F^P}$ is $O[2\epsilon(\beta E)^2 a^2/(\eta a)]$ (the electrostatic particle force divided by the hydrodynamic resistance), so it first appears that the time averaged particle dissipation is $O(na^3 \eta \dot{\gamma}^2 Ma^{-2})$. Note that the na^3 arises from taking the dot product of the vectors effectively summing N interactions and then dividing by the volume V. From experiments and the simulations, the shear stress in an ER fluid scales with the square of the electric field or as $O(\eta \dot{\gamma} Ma^{-1})$, so $\langle \tau \rangle \dot{\gamma}$ is $O(\eta \dot{\gamma}^2 Ma^{-1})$ aside from some volume fraction dependence. At first there appears to be an inconsistency, but in fact, as we shall argue, the particle dissipation is smaller than $O(na^3 \eta \dot{\gamma}^2 Ma^{-2})$ most of the time except during the rapid reconfigurations of the microstructure.

We may also estimate this reconfiguration or snapping time t_s from scaling arguments. At some critical strain, a chain snaps and must translate a distance comparable to its length l due to electrostatic forces. The velocity of a single particle with no shear flow is $O[2\epsilon(\beta E)^2 a^2/(\eta a)]$, so the velocity of the chain is $O[g_l 2\epsilon(\beta E)^2 a^2/(\eta a)]$, where g_l accounts for the increased electrostatic force and hydrodynamic resistance for the chain of particles. The snapping time is then $O[(l/a) g_l^{-1} \dot{\gamma}^{-1} Ma]$. The net contribution of the particle dissipation integral to the stress is $O(na^3 (l/a) g_l^{-1} \eta \dot{\gamma} Ma^{-1})$, or more simply $O(\eta \dot{\gamma} Ma^{-1})$ aside from the number density and chain length correction. This is completely consistent with the observed scaling for the shear stress.

With this in mind, we can evaluate the particle dissipation integral approximately. The integral is broken up into a sum of integrals over intervals each with a slow strain and a rapid reconfiguration or snapping,

$$\frac{1}{T}\int_0^T \frac{1}{V}\mathbf{F}^{\mathbf{P}}\cdot\mathbf{U}^{\mathbf{P}}dt = \frac{1}{T}\sum_i^{N_s}\int_{T_{i-1}}^{T_i}\frac{1}{V}\mathbf{F}^{\mathbf{P}}\cdot\mathbf{U}^{\mathbf{P}}dt. \tag{7.32}$$

T_i is the ending time of the i^{th} strain-snapping episode and N_s is the number of such episodes during the time T. Note that $T_0 = 0$. Each of these episodes can be further sub-divided into the time intervals of the solid body-like slow strain from T_{i-1} to $T_i - t_s$ and the rapid snapping from $T_i - t_s$ to T_i, or

$$\int_{T_{i-1}}^{T_i}\frac{1}{V}\mathbf{F}^{\mathbf{P}}\cdot\mathbf{U}^{\mathbf{P}}dt = \int_{T_{i-1}}^{T_i-t_s}\frac{1}{V}\mathbf{F}^{\mathbf{P}}\cdot\mathbf{U}^{\mathbf{P}}dt + \int_{T_i-t_s}^{T_i}\frac{1}{V}\mathbf{F}^{\mathbf{P}}\cdot\mathbf{U}^{\mathbf{P}}dt, \tag{7.33}$$

where, of course, t_s is the snapping time. This time may actually vary from episode to episode, but as we shall see its exact value is not as important as that it is small compared to $T_i - T_{i-1}$. During the slow strain, the integrand is very small, in fact practically zero during the deformation. Physically, the particles are so close together that they are relatively immobile with respect to one another, and so although $\mathbf{F}^{\mathbf{P}}$ may be large, $\mathbf{U}^{\mathbf{P}}$ is basically zero. Mathematically, $\mathbf{F}^{\mathbf{P}}\cdot\mathbf{U}^{\mathbf{P}} = \mathbf{F}^{\mathbf{P}}\cdot\mathbf{R}_{FU}^{-1}\cdot\mathbf{F}^{\mathbf{P}}$, and the eigenvalues of the mobility tensor, $\mathbf{R}_{FU}^{-1}$ are very near zero when all the particles are near contact. (They are positive since the matrix is always positive-definite.) Thus the particle dissipation integrand is almost zero, and the contribution during this period to the integral in equation (7.33) is also small. This is in fact justified in the forthcoming test with the simulation.

During the rapid reconfiguration of the microstructure, however, the chain breaks free and now the particles can move relative to one another beyond the bulk flow. The forced particle velocity at any time is

$$\mathbf{U}^{\mathbf{P}} = \frac{d\mathbf{x}}{dt} - \mathbf{U}^{\mathbf{E}}, \tag{7.34}$$

where

$$\mathbf{U}^{\mathbf{E}} = \mathbf{R}_{FU}^{-1}\cdot\mathbf{R}_{FE} : \mathbf{E}^{\infty} + \mathbf{U}^{\infty}, \tag{7.35}$$

and is velocity due to the bulk shear flow. Then using equation (7.34) in the last integral of equation (7.33) and assuming the first integral on the RHS of (7.33) is zero from the arguments above, the dissipation rate over an interval becomes,

$$\int_{T_{i-1}}^{T_i} \frac{1}{V}\mathbf{F}^{\mathbf{P}} \cdot \mathbf{U}^{\mathbf{P}} dt = \int_{T_i - t_s}^{T_i} -\frac{\partial \mathcal{U}}{\partial \mathbf{x}} \cdot \frac{d\mathbf{x}}{dt} dt - \int_{T_i - t_s}^{T_i} \frac{1}{V}\mathbf{F}^{\mathbf{P}} \cdot \mathbf{U}^{\mathbf{E}} dt. \tag{7.36}$$

Here the particle force has been replaced by its energy form. The first integral can be easily evaluated by the chain rule to convert equation (7.36) to

$$\int_{T_{i-1}}^{T_i} \frac{1}{V}\mathbf{F}^{\mathbf{P}} \cdot \mathbf{U}^{\mathbf{P}} dt = \Delta \mathcal{U}_i - \Phi_i^E, \tag{7.37}$$

where

$$\Delta \mathcal{U}_i = \mathcal{U}(T_i - t_s) - \mathcal{U}(T_i), \tag{7.38}$$

and

$$\Phi_i^E = \int_{T_i - t_s}^{T_i} \frac{1}{V}\mathbf{F}^{\mathbf{P}} \cdot \mathbf{U}^{\mathbf{E}} dt. \tag{7.39}$$

The energy dissipated in an interval is the change in energy from the critically strained state and the state immediately after the rapid reconfiguration. The Φ_i^E is the dissipation error made by assuming that the translation of the chain is completely dominated by the velocity due to interparticle forces. From the scalings of the snapping time and the force on a particle, the contribution of this dissipation error is $O(\eta\dot{\gamma})$ aside from some correction due to the chain length. Since the energy scales as the square of the electric field, we see that this term becomes negligible as $Ma \to 0$. So neglecting this error term, we finally find that the particle dissipation integral is

$$\frac{1}{T}\int_0^T \frac{1}{V}\mathbf{F}^{\mathbf{P}} \cdot \mathbf{U}^{\mathbf{P}} dt = \frac{1}{T}\sum_{i=1}^{N_s} \Delta \mathcal{U}_i. \tag{7.40}$$

We now have completed the evaluation of the total energy balance and determined that

$$\begin{aligned} \langle \tau \rangle \dot{\gamma} &= \langle \eta^H \rangle \dot{\gamma}^2 + \frac{1}{T}\sum_i^{N_s} \Delta \mathcal{U}_i + \frac{\mathcal{U}(T) - \mathcal{U}(0)}{T}, \\ &= \langle \eta^H \rangle \dot{\gamma}^2 + \frac{N_s}{T}\langle \Delta \mathcal{U} \rangle + \frac{\mathcal{U}(T) - \mathcal{U}(0)}{T}, \end{aligned} \tag{7.41}$$

in the limit of vanishing Ma. Here the $\langle \Delta \mathcal{U} \rangle$ is the time averaged energy jump. Now since the microstructure presumably reconfigures at a rate proportional to the shear rate, the snapping frequency N_s/T is $\xi(c)\dot{\gamma}$ where $\xi(c)$ is some parameter that may be a function of the volume fraction. Further for long times the difference in energy between the final and initial configurations is bounded, and so as $T \to 0$, $[\mathcal{U}(T) - \mathcal{U}(0)]/T \to 0$. Then inserting the presumed form for the snapping frequency into equation (7.41) and dividing by the shear rate, the average shear stress is

$$\langle \tau \rangle = \langle \eta^H \rangle \dot{\gamma} + \xi(c) \langle \Delta \mathcal{U} \rangle. \tag{7.42}$$

This is exactly the form of the shear stress proposed in equation (6.32)! We see explicitly that the plastic viscosity is the average hydrodynamic viscosity, as we inferred from the bulk stress equation in Chapter 6. More importantly, it is clear now that the dynamic yield stress is indeed proportional to the average energy jumps, and that the constant of proportionality is the snapping frequency divided by the shear rate, or

$$\begin{aligned} \tau_d &= \frac{1}{\dot{\gamma}} \frac{N_s}{T} \Delta \mathcal{U} \\ &= \xi(c) \langle \Delta \mathcal{U} \rangle \end{aligned} \tag{7.43}$$

Also, we can see that the dynamic yield stress is a real physical quantity. No matter how slow the deformation, the ER fluid will always exhibit a dynamic yield stress.

With our simulation we can test the theory developed here for the dynamic yield stress. Figure 7.11 illustrates results for a simulation of nine particles at $Ma = 2 \times 10^{-4}$. As we mentioned in Chapter 6, nine particles show the slow strain and snapping quite dramatically. Figure 7.11*a* is the time trace for the ER stress of the suspension non-dimensionalized by the electric field strength. There are several rapid changes in the stress associated with the snapping of the chains. The energy trace of the simulation in Figure 7.11*b* shows the distinctive energy jumps as the suspension reconfigures itself. Figure 7.11*c* is a semi-log plot of the instantaneous particle dissipation, $\frac{1}{V}\mathbf{F}^{\mathbf{P}} \cdot \mathbf{U}^{\mathbf{P}}$. Note that it varies over several orders of magnitude throughout the simulation. In particular during the slow straining

periods when the energy is increasing slowly, the particle dissipation is quite small, as we argued based on the immobility of the particles. This justifies our neglect of the particle dissipation during this period. The particle dissipation increases dramatically during the energy jumps, also as we claimed. This is quite obvious in the linear plot of the particle dissipation rate time trace. The dissipation now looks like delta functions that exactly coincide with the energy jumps in Figure 7.11*b*. The dotted curve in Figure 7.11*d* is the instantaneous dissipation error, $\frac{1}{V}\mathbf{F}^{\mathbf{P}} \cdot \mathbf{U}^{\mathbf{E}}$. The theory assumes that this dissipation error is small compared to the particle dissipation *only during snapping.* This is clearly the case, since the delta functions are clearly larger than the dissipation error. During the slow straining period, however, no assumption is made about the relationship between the two terms, and indeed the dissipation error is often greater in magnitude than the particle dissipation during these times. Note since the dissipation error is not a real dissipation, it sometimes is aphysically negative.

We need to sum the energy jumps to test our theory and for the most part it is clear where the jumps begin and end. When it is not so apparent, the particle dissipation time trace is extremely useful. The criterion used here is counting energy jumps associated with dissipations greater than 2.0×10^3, or basically all but the smallest delta function in Figure 7.11*d*. Also, here there is a net rate of energy increase, $(\mathcal{U}(T) - \mathcal{U}(0))/T$, albeit small, which should be added to the energy jumps when comparing the computed ER shear stress to the dynamic yield stress from equation (7.41). Table 7.II lists the comparison for the simulation in Figure 7.11 and for simulations of 9 and 25 particles with the near-field electrostatic interaction included. The predicted dynamic yield stresses are in very good agreement with the ER shear stress predicted by the bulk stress. Any errors are due to the neglect of the particle dissipation during the slow-straining period and the dissipation error Φ^E. These small errors are expected to decrease with decreasing Ma.

In summary we have demonstrated that the electrostatic energy and the dynamic yield stress are related, and in fact, the dynamic yield stress is proportional to the energy jumps associated with the rapid reconfiguration of the microstructure

or chain snapping. Note that although the theory was developed in the context of ER fluids, it is generally applicable to any material whose microstructure exhibits the potential to store energy on a slow time scale and then rapidly release and viscously dissipate that energy on a much faster time scale. Kraynik, Bonnecaze, & Brady (1991) generalize the theory to include other materials including foams as an example. Kraynik (1988) has observed in simulations of foams that the interfacial area slowly increases with a quasistatic deformation and thus increases the interfacial energy of the system. When the foam reaches a critical strain, determined by an instability of a particular convergence of film boundaries, the cells of the foam rapidly rearrange and viscously dissipate the stored energy in the fluid between the film boundaries. With this general theory, microstructural models can be developed for any fluid that has the required characteristics in order to study the effects of system parameters on the dynamic yield stress. In the next section such a microstructural model is developed to understand the volume fraction and dielectric constant ratio dependence of the dynamic yield stress of ER fluids.

7.4 Dynamic Yield Stress for a Model ER Fluid

With the theory developed in the previous section, we would like to learn something about the volume fraction dependence and the effect of the dielectric constant ratio on the dynamic yield stress and then hopefully use the knowledge to guide the synthesis of future ER fluids. Basically, to apply the theory we must evaluate,

$$\tau_d = \frac{1}{\dot{\gamma}} \frac{N_s}{T} \langle \Delta U \rangle. \tag{7.44}$$

In this section a simple microstructural model of an ER fluid is proposed so we can easily determine the snapping frequency and the average energy jump and thereby gain some insight into the important factors of the dynamic yield stress.

It was observed in our simulations that the chains strained affinely up until a critical strain γ_c of about unity, when the chains broke in half and reconnected with their periodic image. This critical strain, as discussed in Chapter 6, is an artifact of the periodic boundary conditions, but is qualitatively correct in that each chain does undergo a rapid reconfiguration at fairly regular strains. Klingenberg & Zukoski (1990) have observed in visual experiments of sheared ER fluids that the chains snapped at strains of about 0.4 to 0.6. These chains, of course, were of varying particle thickness and randomly spaced in the suspension, but from this picture, we can abstract the idealized microstructure in Figure 7.12, which has also been proposed by Klingenberg & Zukoski. It consists of single particle diameter chains spanning the electrode and periodically replicated throughout the gap width. The upper electrode moves so as to deform the chains affinely up until the critical strain. At this point the chains snap, and the upper chain half reconnects with the forward lower chain half. Thus, the microstructure repeats itself and the process continues. The snapping frequency is then simply $\dot{\gamma}/\gamma_c$, and the energy jump is the energy difference between the critically strained and initial configurations.

The periodic structure is a reasonable assumption for lumping the average chain spacing. The single particle here, though, represents several particles that make up the chain, since the chain is really one or several particle diameters wide. This assumption is near in spirit to the bead-spring models used in polymer studies

where the bead includes many monomer units of the polymer and the spring represents the collection of chemical bonds. Using these single particle wide strands is convenient since then the energy jump can be determined from the energy-strain curves computed in the non-linear elastic deformation simulations. Since the initial configuration energy is zero, the dynamic yield stress is

$$\tau_d = \frac{1}{\gamma_c} U(\gamma_c). \tag{7.45}$$

Table 7.I lists the energy and dynamic yield stress using the critical strain of 0.5, as observed by Klingenberg & Zukoski (1990). The dynamic yield stress is also plotted in Figure 7.13. Most striking is the qualitative similarity to the static yield stress in Figure 7.5*a*. The static yield stress, though, is about twice as large as the dynamic yield stress for the modest dielectric constant ratios of $\epsilon_p/\epsilon \leq 10.0$.

The dynamic yield stress increases with increasing dielectric constant ratio. At low volume fractions, the dynamic yield stress scales linearly with the c, and has a maximum at $c = 0.4$ for $\epsilon_p/\epsilon \leq 10$. For the perfect conductors, the linear relationship with c continues up to $c = 0.5$. Evidently, the extent of the linear region increases with increasing dielectric constant ratio. The explanation for this behavior is much like that for the static yield stress. The energy at the critical strain is the product of the number density of chains, n_c, and the energy per chain, $U_c(\gamma_c)$, and so then $\tau_d = n_c U_c(\gamma_c)/\gamma_c$. At low volume fractions the electrical intrachain interactions among particles dominate since the chains are far apart, and so $U_c(\gamma_c)$ is independent of volume fraction. Since $n_c \sim c$ then $\tau_d \sim c$. At the higher volume fractions and the more modest dielectric constant ratios, the chains interact electrically so much so that energy per chain does not increase much during the strain. In fact $U_c(\gamma_c)$ decreases faster than c^{-1} for $c \geq 0.4$ since there is a maximum in the dynamic yield stress. For perfect conductors with $\xi = 10^{-5}$, intrachain interactions dominate the energy so there is no yield stress maximum. In his experiments Klingenberg (1990) has observed a maximum in the dynamic yield stress at a volume fraction of 0.35, which is extremely close to the predicted volume fraction of 0.4.

Also included in Figure 7.13 is the dynamic yield stress data of Marshall, Goodwin, & Zukoski (1989) presented earlier in viscosity form. Recall, their dielectric

constant ratio was 3.8. The comparison is extremely good at the larger volume fractions, but the model appears to fail at smaller volume fractions. At the lower volume fractions the chains might be erratically spaced so that when a chain snaps, it has no nearby chain with which to reconnect. These dangling chains then do not strain and break again until they run into another free chain. This lowers the snapping frequency, hence reducing the dynamic yield stress.

To test the sensitivity of the model, the dynamic yield stress was determined with the static yield strain, γ_s, as the critical strain. Recall that the static yield strain is fairly constant for a given dielectric constant, but decreases with increasing dielectric constant ratio. The dynamic yield stress for the perfect conductors was not computed since a critical strain of 0.003 is not realistic. Instead, the dynamic yield stress was calculated for an arbitrary critical strain of 0.25. Also, the maximum value of $\Delta\mathcal{U}(\gamma)/\gamma$ was computed. This provides an upper bound on the dynamic yield stress for the model microstructure with no adjustable parameters. The maximum dynamic yield stress and its critical strain, γ_m, and the other dynamic yield stresses are listed in Table 7.I. For $\epsilon_p/\epsilon \leq 10$, the three different dynamic yield stresses are found to be quite similar and so are not very sensitive to the choice of the critical strain. This explains why there is such good agreement between the dynamic simulation effective viscosities and Marshall *et al.*'s data despite the fact that the simulation critical strain of unity was probably greater than the experimental critical strain. Note that the critical strains for the maximum dynamic yield stresses, γ_m, are within the range of critical strains observed by Klingenberg & Zukoski. For the perfect conductors, however, the dynamic yield stress is very sensitive to the choice of critical strain. From Table 7.I the dynamic yield stresses computed at critical strains of 0.25 and 0.5 differ by almost a factor of two, though qualitatively they both are linear in volume fraction. The maximum dynamic yield stress for the perfect conductors occurs for a critical strain of 0.0065 which is completely unrealistic for any rheometer or ER device. This resultant unattainable dynamic yield stresses are about ten times greater than the other two yield stresses for perfect conductors and on the order of magnitude with static yield stress.

The explanation of the sensitivity or lack thereof is best explained with the schematic of the energy versus strain in Figure 7.14 drawn for the more modest dielectric constant ratios. The energy increases with strain rapidly at first, and then more slowly after the inflection point. The strain at the inflection point is the static yield strain, and the slope of the energy curve there is the static yield stress. The straight dashed line drawn in the figure passes through the energy curve twice; once at the inflection point and again at a higher energy and strain, γ_c. The slope of this dashed line is the dynamic yield stress assuming a critical strain of either γ_s or γ_c, since $\tau_d = \Delta\mathcal{U}(\gamma_c)/\gamma_c$. From this schematic, if the critical strain was lesser or greater than the γ_c indicated in the figure, the slope of the dashed line or the dynamic yield stress still would be about the same, provided the static yield strain were of the same order of magnitude. The energy for a perfect conductor, as seen in Figure 7.7*b*, is much more slowly increasing at the critical strains of 0.25 and 0.5, so it is roughly constant. Thus in this region, halving the critical strain doubles the dynamic yield stress for these suspensions as we saw in Table 7.I.

The schematic also indicates that the static yield stress is always greater than the dynamic yield stress. The dynamic yield stress is the average stress, $\langle\tau\rangle_\gamma$, over the strain γ_c since

$$\begin{aligned}\langle\tau\rangle_\gamma &= \frac{1}{\gamma_c}\int_0^{\gamma_c}\frac{d\mathcal{U}}{d\gamma}d\gamma \\ &= \frac{\Delta\mathcal{U}(\gamma_c)}{\gamma_c}.\end{aligned} \tag{7.46}$$

Now from the mean value theorem,

$$\langle\tau\rangle_\gamma = \tau_d \leq max\frac{d\mathcal{U}}{d\gamma}, \tag{7.47}$$

over the interval $[0, \gamma_c]$. The equality is true only if over the interval the energy is a linear function of strain. In fact the energy must be a quadratic function of the strain at small deformations in order to recover linear elastic behavior. Also, since $\frac{d\mathcal{U}(\gamma_s)}{d\gamma}$, the static yield stress, is the maximum stress possible, then

$$\tau_d < \tau_s. \tag{7.48}$$

Thus, the static yield stress is strictly greater than the dynamic yield stress in an ER suspension for the idealized microstructure assumed in our model. This is as expected from the original hypothetical stress-strain curve assumed in Figure 7.1 and the definition of the static yield stress.

The dynamic yield stress for the perfect conductors with the steric layers can be interpreted as an upper bounds for the dynamic yield stress, at least for our idealized model. Using the critical strain of 0.5, for a suspending fluid of dielectric constant ratio 2 relative to vacuum, the dynamic yield stress at $c = 0.4$ is about 200 Pa-$(\text{mm/kV})^2 \times E^2$. Thus for a for a field strength of 1 kV/mm, the dynamic yield stress is 200 Pa. The dynamic yield stress would be about twice this for the critical strain of 0.25. This formula can at least provide an estimate of whether an ER device is appropriate for a particular mechanical application.

Since our lumped model of the particle spacings and chain size still predicted experimental data well, the exact nature of the chain structure is not very important. Apparently, the volume fraction of particles and the dielectric constant ratio are the two most important factors determining the dynamic yield stress. Clearly when synthesizing an ER fluid the volume fraction of particles should not exceed the optimal value of about 40% for dielectric constant ratios of 10 or less. Perhaps the simplest way to improve the dynamic yield stress of an ER fluid is to increase the dielectric constant ratio. This option, however, involves other aspects of a commercially viable ER fluid. Ideally, the fluids are perfect capacitors and pass no charge, but in practice they are leaky dielectrics with a finite conductivity. Thus energy is consumed with passing current in the suspension, and is an important consideration for the power requirements of an ER fluid. This power consumption increases with the dielectric constant ratio, so then there is a "trade-off" between increased dynamic yield stress and greater power requirements for a particular electromechanical device. The added conduction also contributes to the detrimental heating of the material. Using perfectly conducting particles increases the conductivity greatly since the particles form percolating clusters spanning the electrode gap even with the steric layers if the fluid is slightly conductive as observed in Chapter

4. One possibility to reduce the conductivity and benefit from the large dielectric mismatch is to coat perfectly conducting particles with an insulating sheath. Even if the suspending fluid were slightly conductive, the particles would be isolated from the flow of charge, reducing the conductivity but still retaining the singular electrostatic interactions between one another. Since the perfectly conducting material would probably be a dense metal, the particles should be hollow or plastic filled to maintain near neutral particle buoyancy and reduce any potential settling problems.

7.5 Conclusions

In this chapter the static and dynamic yield stresses of an ER fluid have been connected to the electrostatic energy of the suspension. The static yield stress was directly related to the electrostatic energy from the theories of non-linear elasticity. The static yield stress was found to increase with increasing dielectric constant ratio due to the increased electrostatic interactions. Also, the static yield stress apparently exhibits a maximum at $c = 0.4$ for modest dielectric constant ratios of 10 or less. Thus, if such a fluid is to be used in an ER valve, the concentration of particles should not exceed 40 volume percent.

It was discovered that the dynamic yield stress is also related to the energy of the suspension through the sudden energy changes associated with the rapid reconfiguration of the suspension microstructure. The theory equating the dynamic yield stress to these energy jumps was developed in the context of ER fluids and successfully proven by testing the proposed formula with the dynamic simulation. As mentioned, the theory applies not just to ER fluids, but to any material capable of storing energy on one time scale and rapidly dissipating it on a much smaller time scale. Foams (Kraynik, *et al.*) are but one example of other possible materials. The theory presented here also showed that the dynamic yield stress is a true physical quantity for an ER fluid and, contrary to Barnes & Walters (1985), is not dependent on the time of the experiment.

Using the theory of the dynamic yield stress, a simple model was developed to predict the dynamic yield stress as a function of volume fraction and dielectric constant ratio. Like the static yield stress, it increases with the dielectric constant ratio and exhibits a maximum at 40 volume percent particles for dielectric constant ratios of 10 or less. Clearly when synthesizing an ER fluid with these modest dielectric constant ratios, the volume fraction of particles should not exceed this critical value. Suspensions of perfect conductors, however, have yield stresses that vary linearly with the volume and are much larger due to the singular nature of the electrostatic interactions. Although increasing the dielectric constant ratio is perhaps the simplest way to improve the ER response of the fluid, other consider-

ations, such as conductivity and energy consumption make this alteration perhaps less tenable as discussed in the previous section.

The dynamic simulation was exceptionally important for the development of the theory of the dynamic yield stress. The visual effect of the video animations of the simulations along with the time traces of the electrostatic energy and the viscosities (or stress) hinted at the connection between the yield stress and the energy jumps. Then once a theory was developed from the ideas seeded by the simulation, the dynamic simulation was used to test the theory. The real power and practical application of dynamic simulations is this ability to offer physical insights into phenomena that allow simple theories to be developed, and then the opportunity to test these ideas.

Table 7.I

Elastic and Dynamic Properties of Model ER Fluid

$\epsilon_p/\epsilon = 2.0$

c	γ_s	τ_s	G	$\mathcal{U}(0.5)$	$\tau_d(0.5)$	$\mathcal{U}(\gamma_s)$	$\tau_d(\gamma_s)$	γ_m	$\tau_d(\gamma_m)$
0.1	0.35	0.082	0.40	0.031	0.062	0.014	0.041	0.58	0.063
0.2	0.34	0.157	0.79	0.059	0.118	0.035	0.103	0.56	0.119
0.3	0.32	0.213	1.10	0.080	0.160	0.044	0.138	0.53	0.160
0.4	0.29	0.229	1.30	0.084	0.168	0.043	0.149	0.45	0.170
0.5	0.27	0.199	1.30	0.066	0.132	0.032	0.124	0.38	0.146

$\epsilon_p/\epsilon = 4.0$

c	γ_s	τ_s	G	$\mathcal{U}(0.5)$	$\tau_d(0.5)$	$\mathcal{U}(\gamma_s)$	$\tau_d(\gamma_s)$	γ_m	$\tau_d(\gamma_m)$
0.1	0.29	0.125	0.77	0.048	0.096	0.024	0.083	0.51	0.096
0.2	0.29	0.243	1.50	0.094	0.188	0.047	0.162	0.50	0.188
0.3	0.29	0.345	2.20	0.132	0.264	0.068	0.234	0.47	0.265
0.4	0.26	0.402	2.70	0.148	0.297	0.069	0.257	0.42	0.305
0.5	0.23	0.389	2.90	0.129	0.258	0.059	0.223	0.36	0.291

$\epsilon_p/\epsilon = 10.0$

c	γ_s	τ_s	G	$\mathcal{U}(0.5)$	$\tau_d(0.5)$	$\mathcal{U}(\gamma_s)$	$\tau_d(\gamma_s)$	γ_m	$\tau_d(\gamma_m)$
0.1	0.21	0.236	2.20	0.095	0.190	0.034	0.163	0.38	0.188
0.2	0.20	0.468	4.40	0.185	0.369	0.064	0.318	0.38	0.371
0.3	0.20	0.687	6.50	0.258	0.516	0.094	0.470	0.37	0.544
0.4	0.20	0.860	8.30	0.307	0.614	0.119	0.597	0.34	0.675
0.5	0.19	0.932	9.30	0.304	0.608	0.115	0.608	0.30	0.731

Table 7.I, Continued

Elastic and Dynamic Properties of Model ER Fluid

$\epsilon_p/\epsilon = \infty$

c	γ_s	τ_s	G	$\mathcal{U}(0.5)$	$\tau_d(0.5)$	$\mathcal{U}(0.25)$	$\tau_d(0.25)$	γ_m	$\tau_d(\gamma_m)$
0.1	0.003	23.69	31800	0.741	1.483	0.654	2.614	0.0065	19.09
0.2	0.003	47.37	63600	1.480	2.961	1.307	5.227	0.0065	38.18
0.3	0.003	71.06	95400	2.211	4.423	1.958	7.950	0.0065	57.27
0.4	0.003	94.75	127200	2.901	5.801	2.596	10.38	0.0065	76.36
0.5	0.003	118.4	159000	3.491	6.982	3.205	12.82	0.0065	95.45

The stresses, τ, modulus, G, and the energy $\mathcal{U}$ are non-dimensionalized by $2\epsilon(\beta E)^2$. The parenthetical values are the strains at which the functions are evaluated. For $\epsilon_p/\epsilon = \infty$, the gap width between particles is 10^{-5} relative to the sphere radius.

Table 7.II

Confirmation of Dynamic Yield Stress-Energy Model

$\epsilon_p/\epsilon = 4.0$

N	T	Ma	NF	$\sum \Delta \mathcal{U}$	$\sum \Delta \mathcal{U}/T$	τ^{ER}	Error
9	10.1	2×10^{-4}	No	0.4429	0.0438	0.0436	0.5%
9	10.1	2×10^{-4}	Yes	0.4901	0.0475	0.0462	2.8%
25	8.85	1×10^{-4}	Yes	1.0437	0.1179	0.1145	3.0%

The column NF indicates whether the near-field effects were included in computing the electrostatic interparticle forces. The sum of the energy changes includes the difference between the energy of the final and initial configurations. The $\Delta \mathcal{U}$ and τ^{ER} are non-dimensionalized by $2\epsilon(\beta E)^2$.

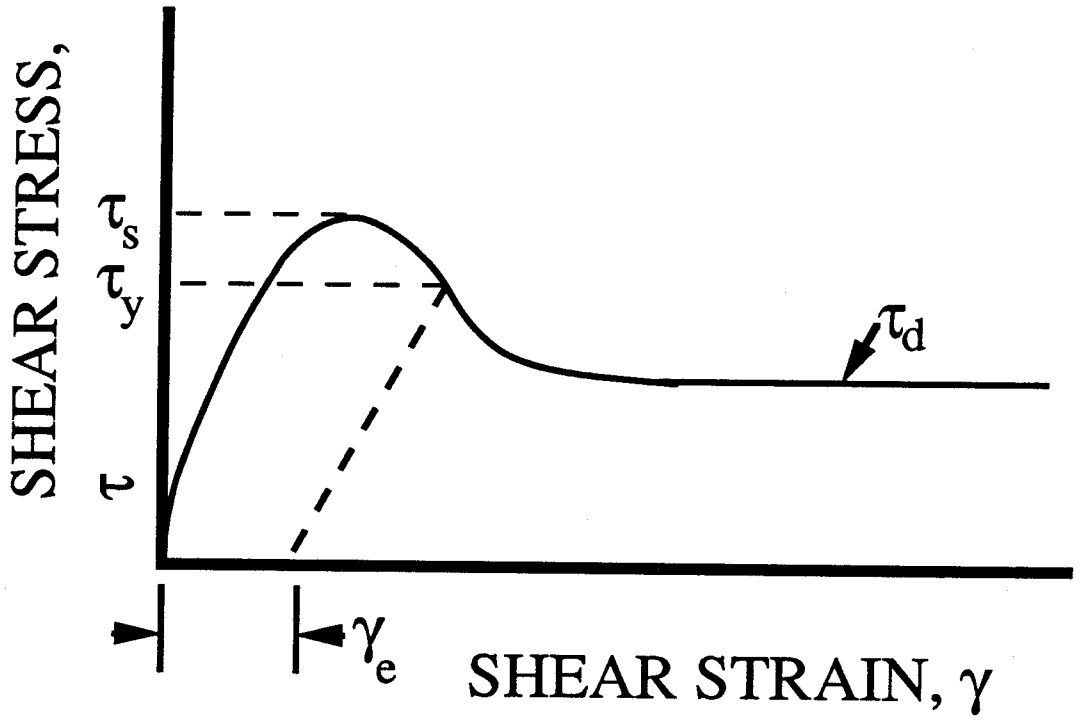

Figure 7.1. Hypothetical stress-strain curve for a quasistatic shear deformation illustrating the elastic-limit yield stress, τ_y, static yield stress, τ_s, and the dynamic yield stress, τ_d.

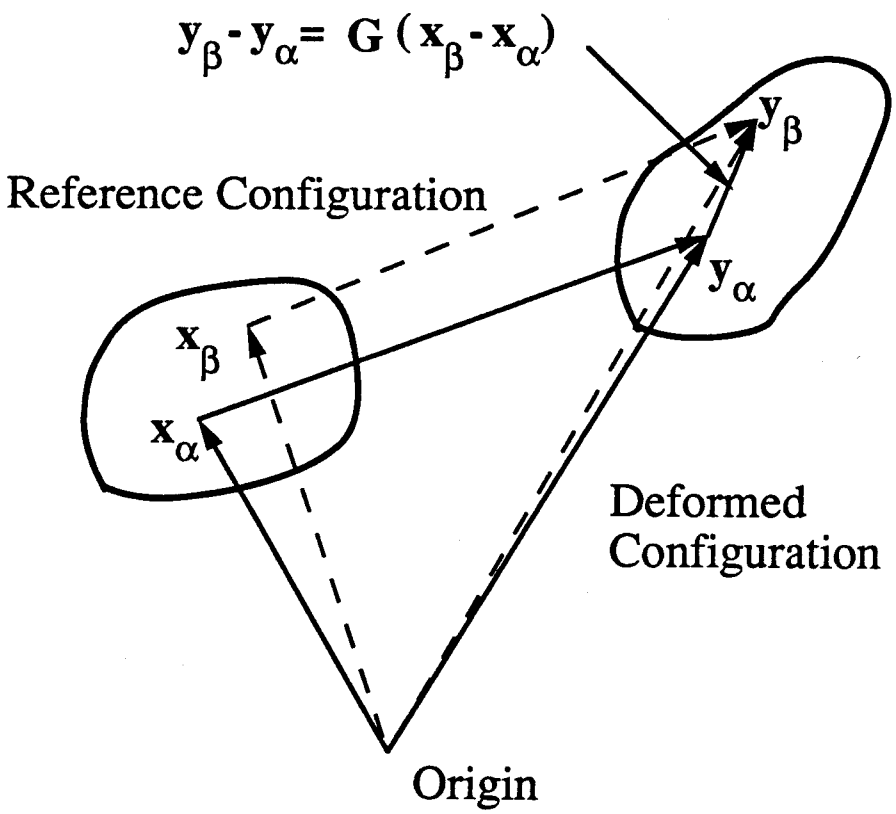

Figure 7.2. Body configuration diagram. Here the positions of particles in the deformed configuration are determined from the initial configuration and the homogeneous deformation tensor, G.

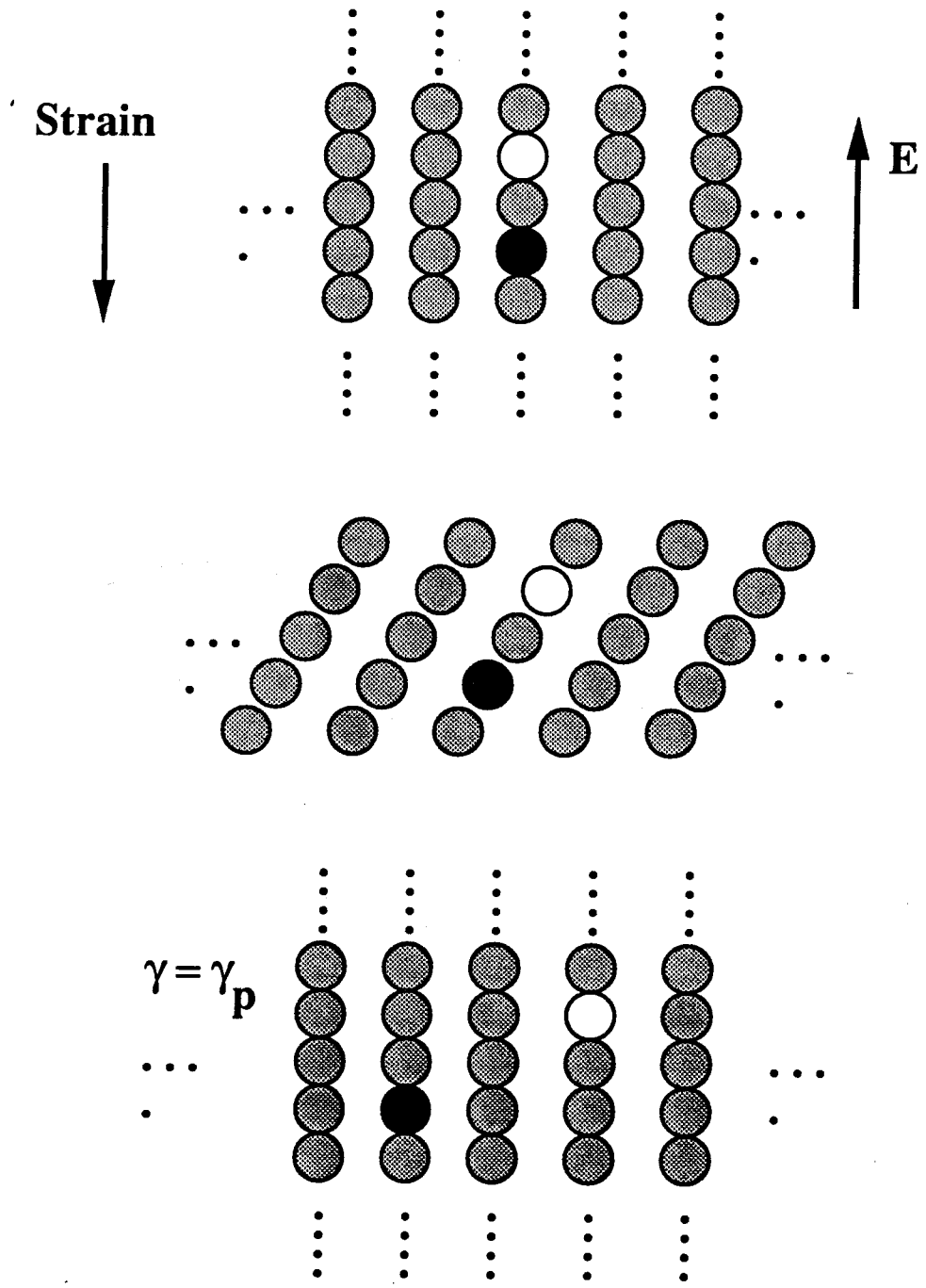

Figure 7.3. Model microstructure for quasistatic shear stress‹shear strain simulation of an ER fluid. Note the configuration repeats itself at a period of γ_p.

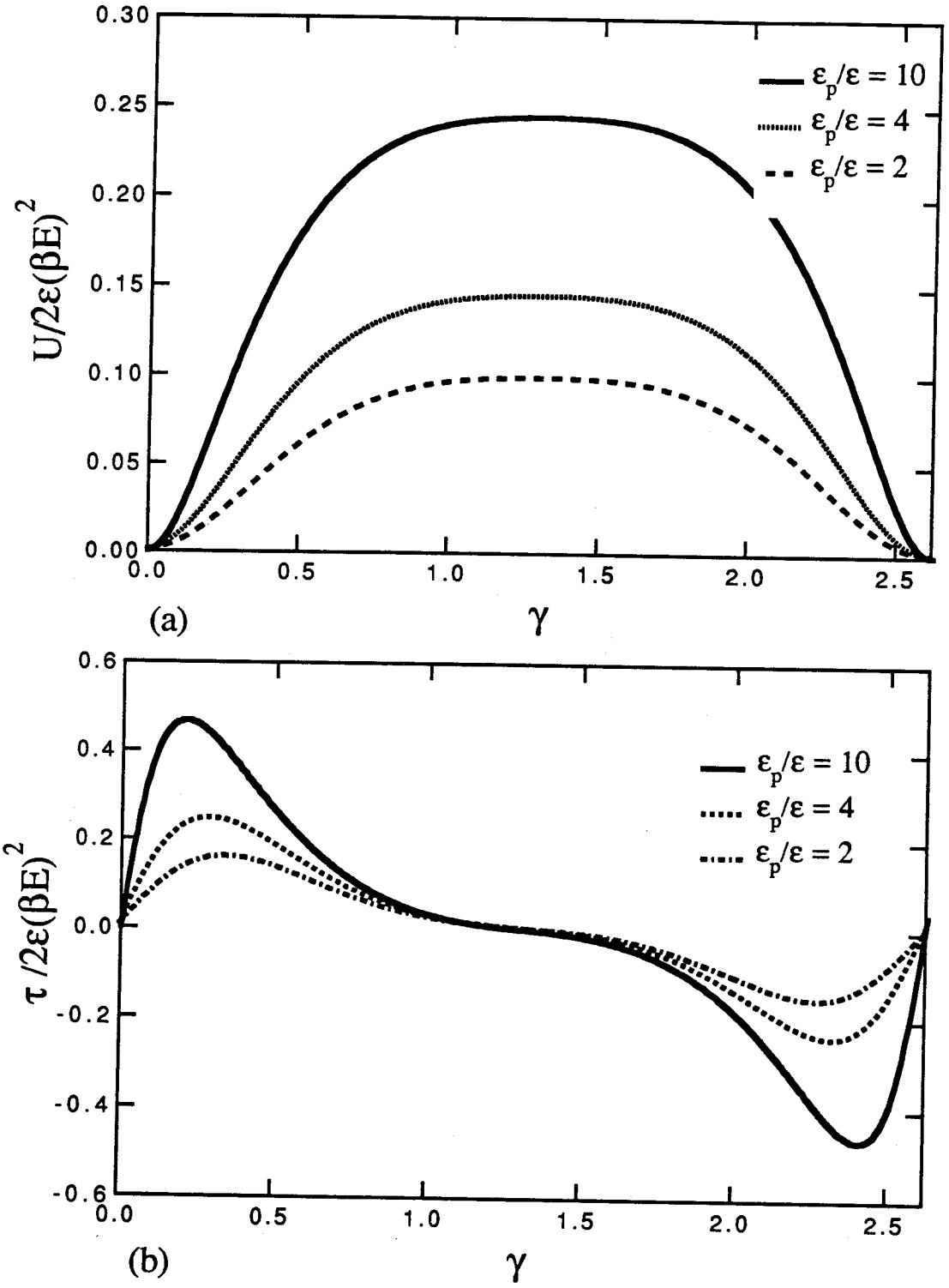

Figure 7.4*a*, *b*. Strain traces of the electrostatic energy (*a*) and stress (*b*) for $c = 0.2$ and $\epsilon_p/\epsilon = 2, 4$, and 10. Due to the periodic nature of the model microstructure, the curves repeat themselves after $\gamma_p \approx 2.6$.

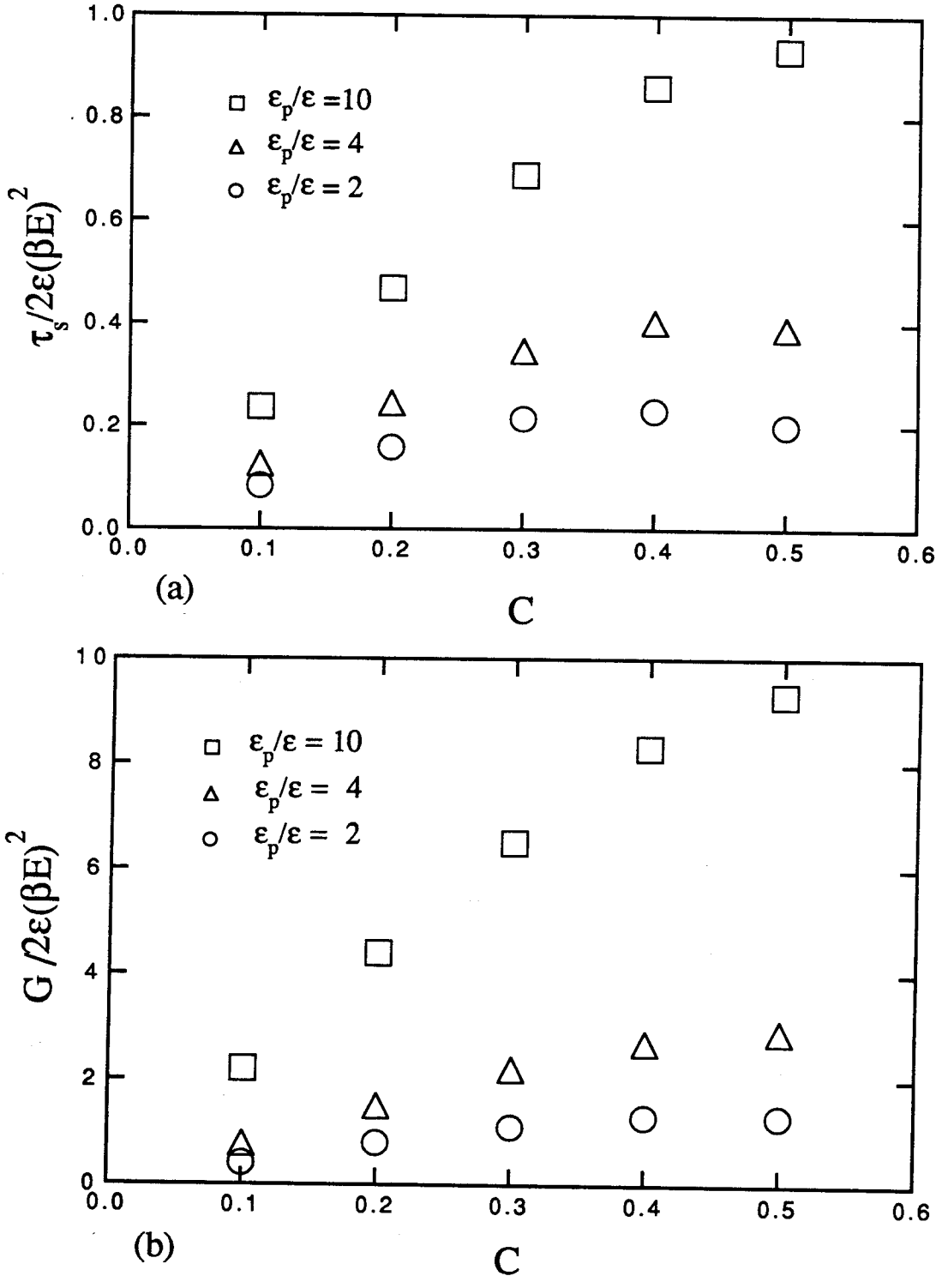

Figure 7.5*a, b*. Static yield stress, τ_s, and the linear elastic-limit modulus, G , as a function of volume fractions and $\epsilon_p/\epsilon = 2, 4$, and 10.

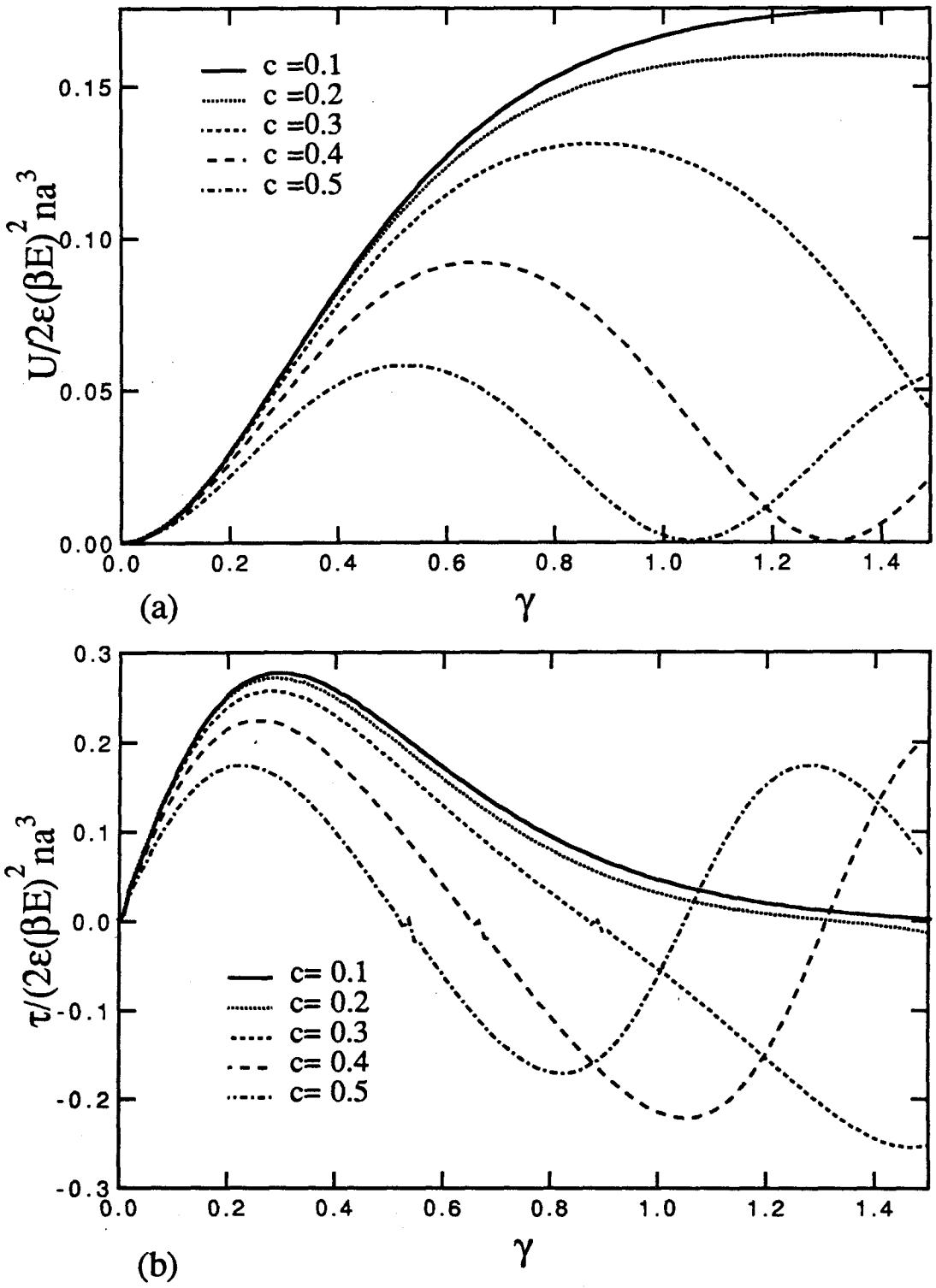

Figure 7.6*a*, *b*. Strain traces of the electrostatic energy (*a*) and stress (*b*) for $c = 0.2$ and $\epsilon_p/\epsilon = 2, 4$, and 10 here normalized by the number density of particles. Note the relative insensitivity of the energy and stress to strain at small volume fractions.

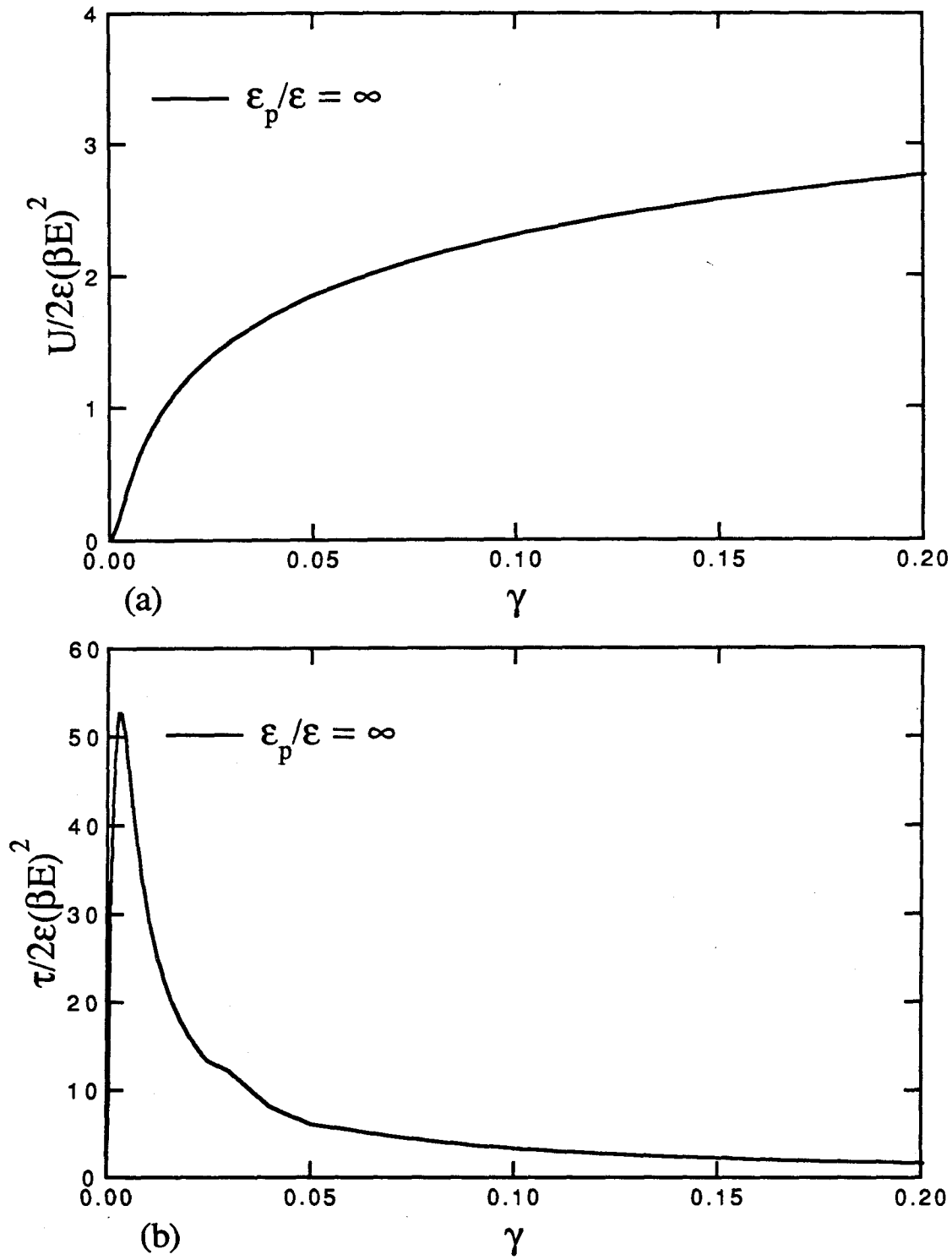

Figure 7.7*a, b.* Strain traces of the electrostatic energy (*a*) and stress (*b*) for $c = 0.2$ and $\epsilon_p/\epsilon = \infty$ for an initial non-dimensionalized particle gap width of 10^{-5}. The strain is only plotted out to 0.2 to resolve the sharp static yield stress. Qualitatively, the full figure looks much like Figure 7.4.

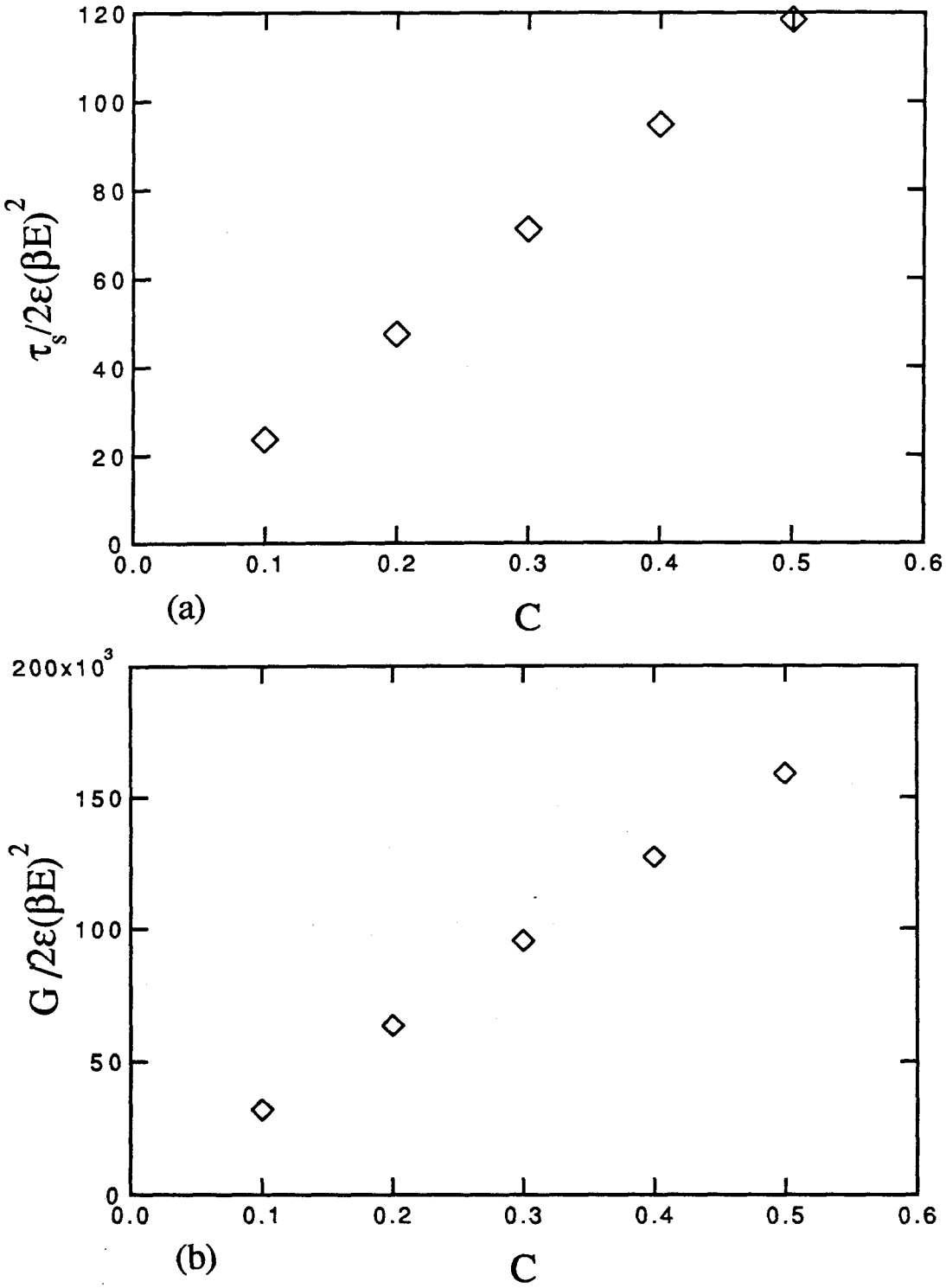

Figure 7.8*a*, *b*. Static yield stress, τ_s, and the linear elastic-limit modulus, G , as a function of volume fractions for $\epsilon_p/\epsilon = \infty$ with a non-dimensionalized particle gap width of 10^{-5}.

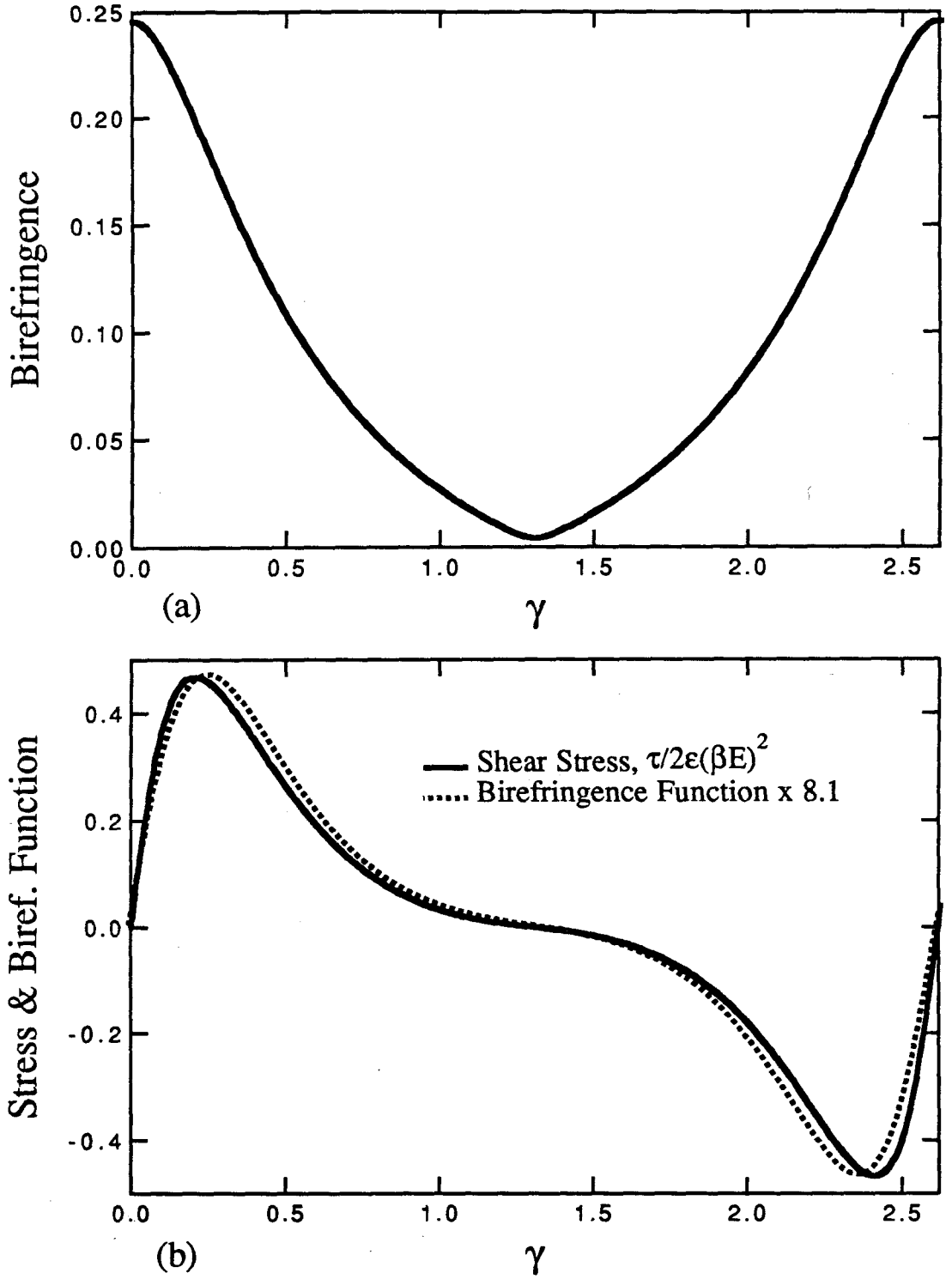

Figure 7.9*a, b*. Birefringence (*a*) and the proposed birefringence function in equation (7.18) with the shear stress (*b*) for $c = 0.2$ and $\epsilon_p/\epsilon = 10$. A constant of 8.1 was chosen for the birefringence function to give the best comparison between it and the stress.

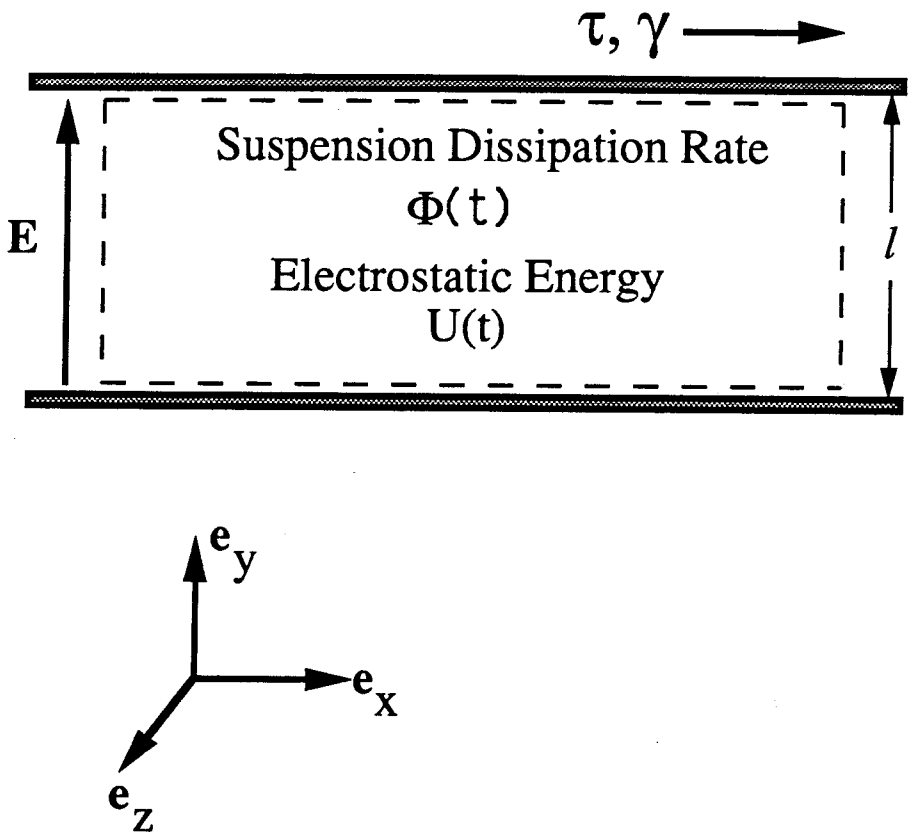

Figure 7.10. Control volume for total energy balance.

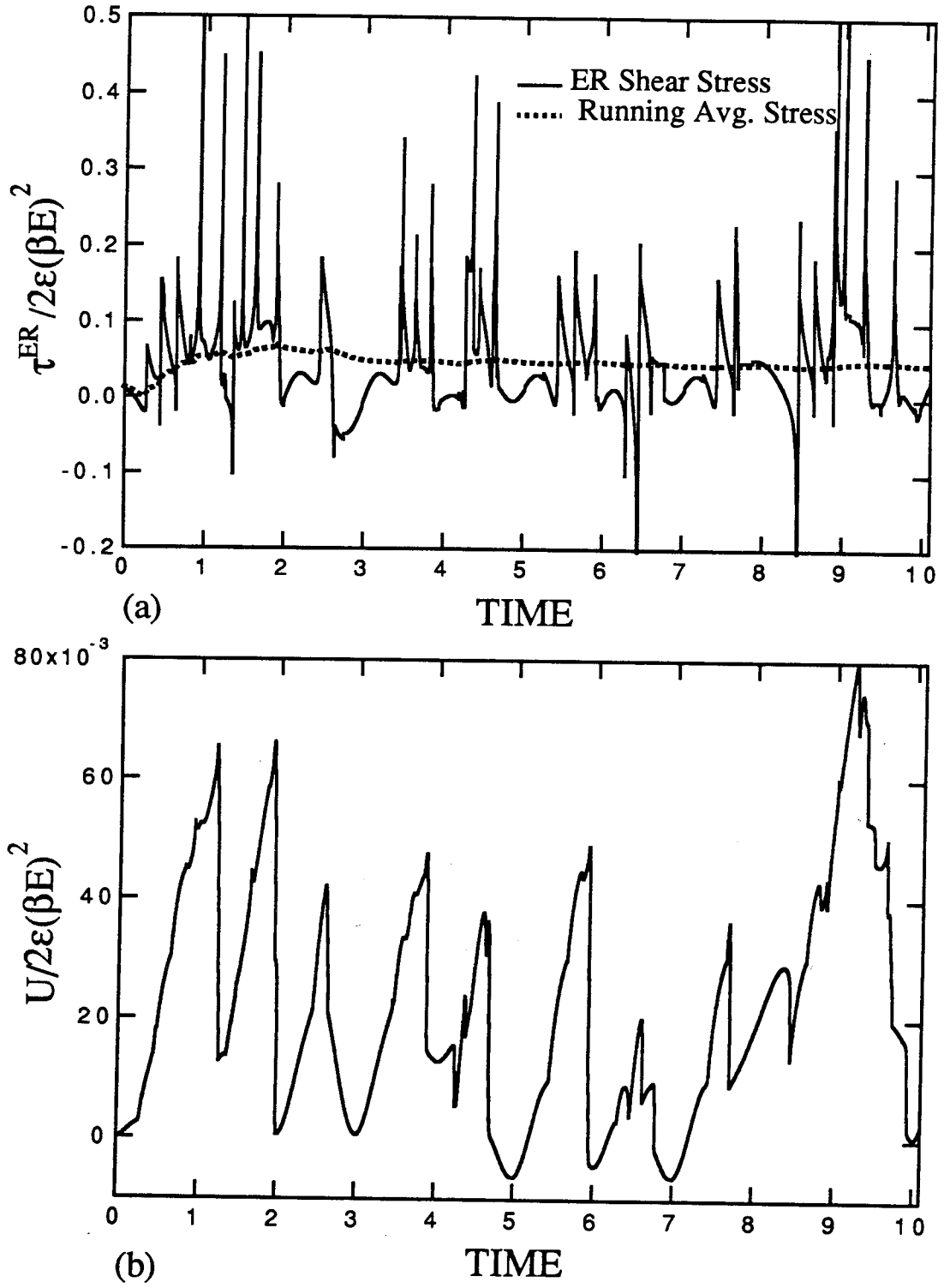

Figure 7.11*a, b*. Time traces of the ER stress (*a*) and the electrostatic energy (*b*) for $N = 9$ and $Ma = 2 \times 10^{-4}$.

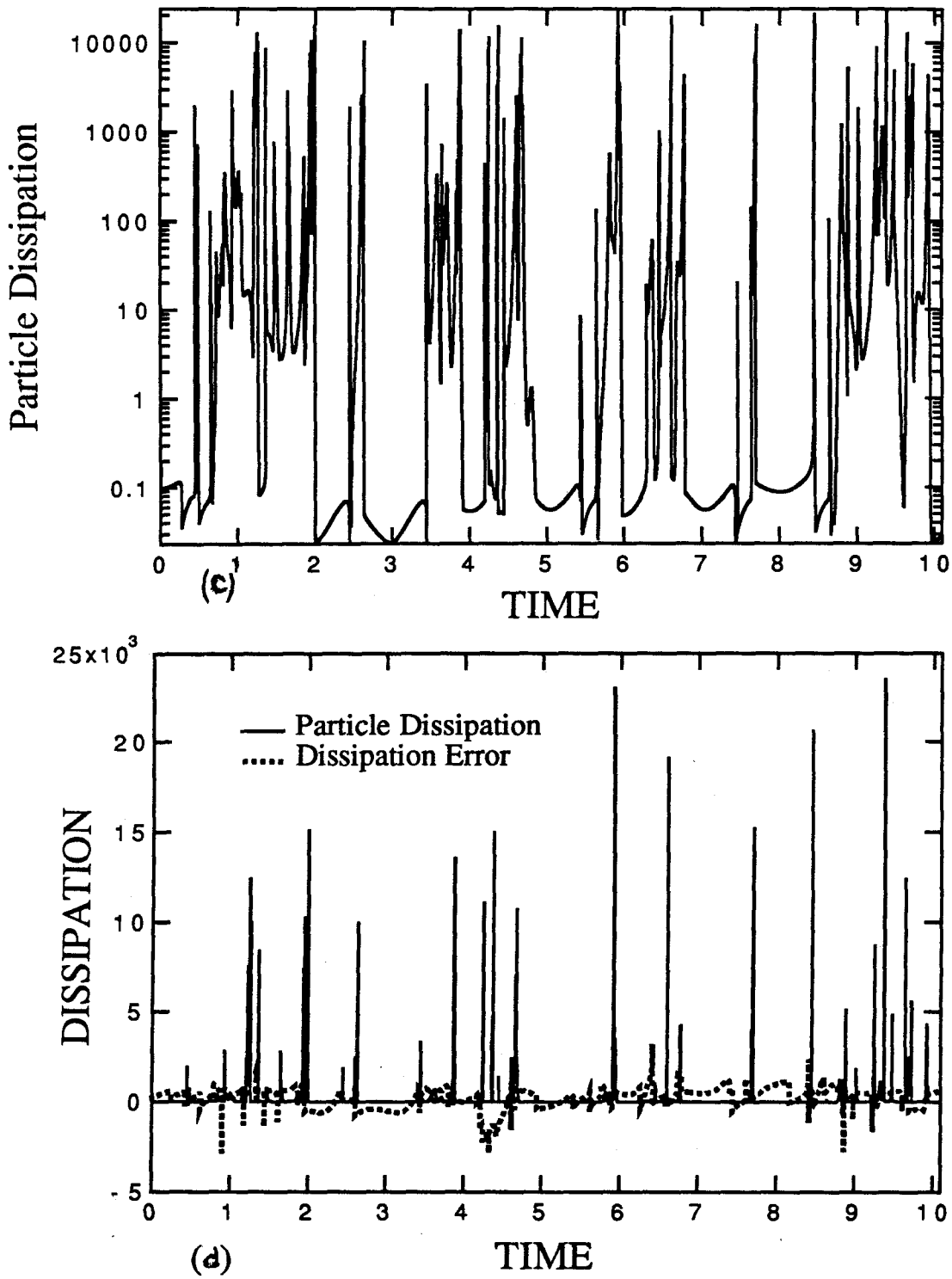

Figure 7.11*c*, *d*. Time traces of the particle dissipation alone (*c*) and with the dissipation error (*d*) for $N = 9$ and $Ma = 2 \times 10^{-4}$.

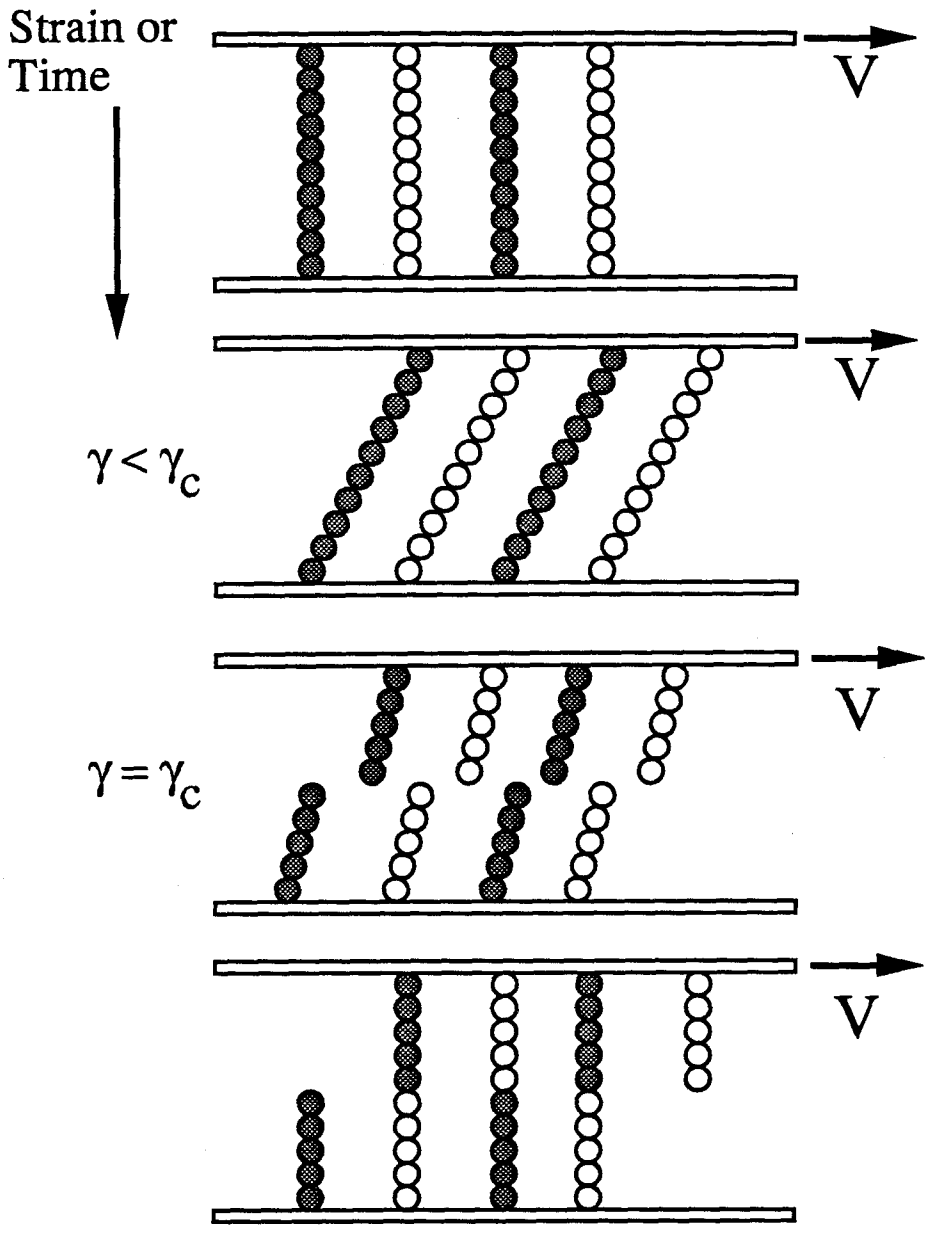

Figure 7.12. Idealized microstructural configurations in an ER for the dynamic yield stress model. The single particle chains deform affinely with the motion of the top plate, and then at a critical strain γ_c, the chains break or snap in half and rapidly reconfigure to their original microstructure. This process then repeats itself.

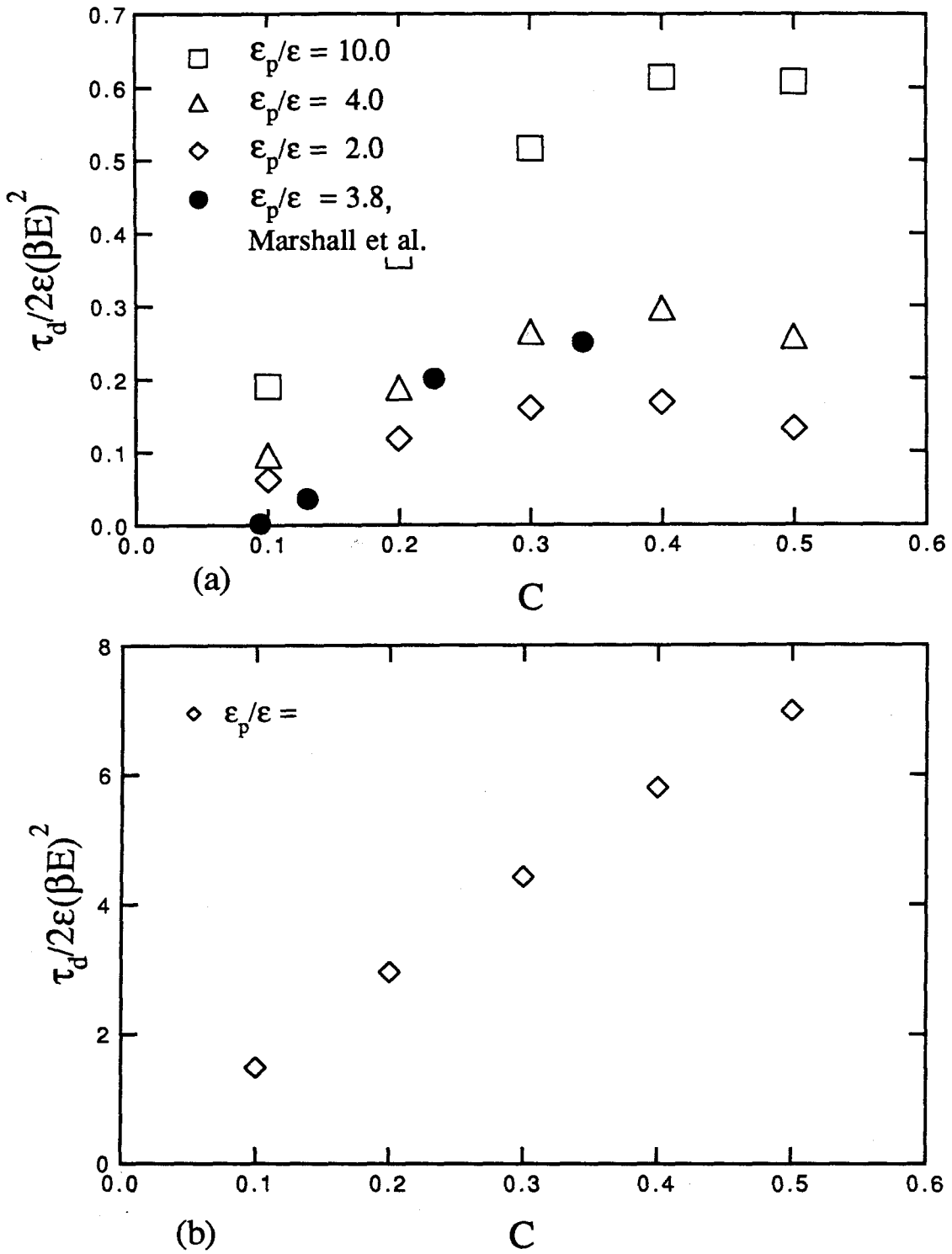

Figure 7.13*a, b*. Estimated dynamic yield stress from the idealized microstructural model for $\epsilon_p/\epsilon = 2, 4$, and 10 (*a*) and $\epsilon_p/\epsilon = \infty$ for a non-dimensionalized particle gap width of 10^{-5} (*b*). Included for comparison is the yield stress data of Marshall, *et al.*

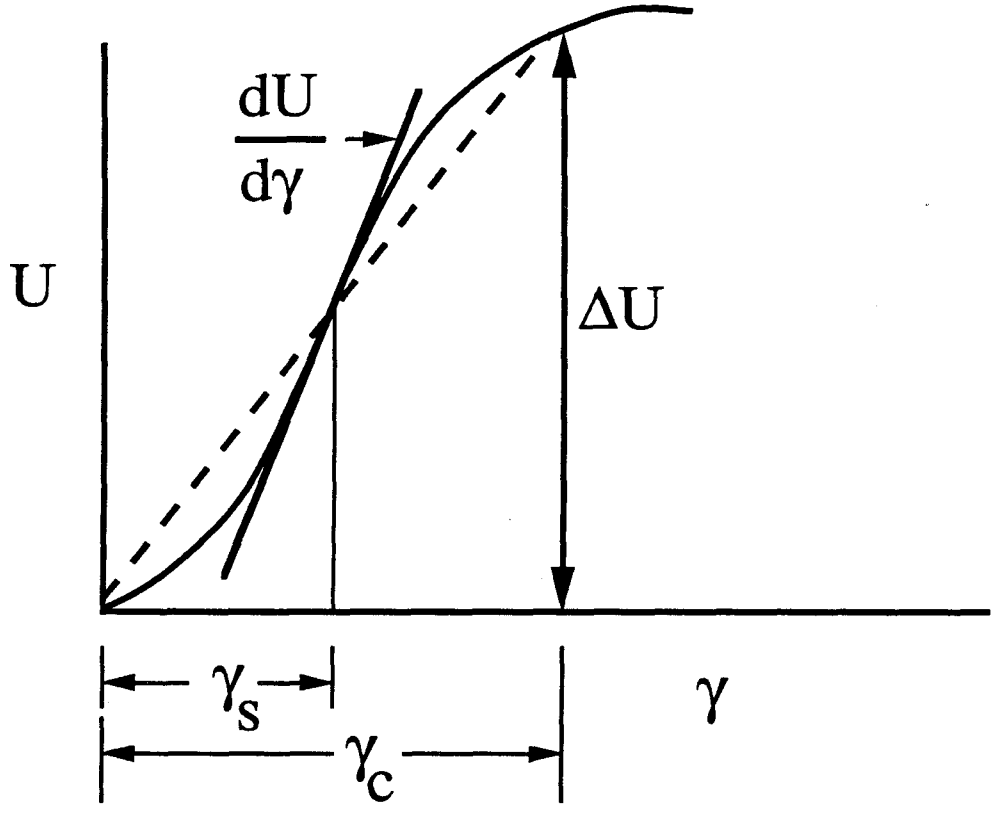

Figure 7.14. Schematic of energy-strain curve for modest dielectric constant ratio materials.

REFERENCES

Adriani, P.M. & Gast, A.P. 1988 A microscopic model of electrorheology. *Phys. Fluids* **31**, 2757.

Adriani, P.M. & Gast, A.P. 1989 Prediction of birefringence and dichroism of hard-sphere suspensions in combined electric and shear fields. *J. Chem. Phys.* **91**, 6282.

Arp, P.A., Foister, R.T., & Mason, S.G. 1980 Some electrohydrodynamic effects in fluid dispersions. *Adv. Coll. Int. Sci.* **12**, 295.

Barnes, H.A. & Walters, K. 1985 The yield stress myth? *Rheol. Acta.* **24**, 323.

Batchelor, G.K. 1970 The stress system in a suspension of force-free particles. *J. Fluid Mech.* **41**, 545.

Batchelor, G.K. 1972 Sedimentation in a dilute suspension of spheres. *J. Fluid Mech.* **52**, 245.

Batchelor, G.K. 1974 Transport properties of two-phase materials with random structure. *Ann. Rev. Fluid Mech.* **6**, 227.

Batchelor, G.K. 1977 The effect of Brownian motion on the bulk stress in a suspension of spherical particles. *J. Fluid Mech.* **83**, 97.

Batchelor, G.K. & Green J.T. 1972 The determination of the bulk stress in a suspension of spherical particles to $O(c^2)$. *J. Fluid Mech.* **56**, 401.

Batchelor, G.K. & O'Brien, R.W. 1977 Thermal or electrical conduction through a granular material. *Proc. Roy. Soc.* A **355**, 313.

Brady, J.F. & Bossis, G. 1988 Stokesian dynamics. *Ann. Rev. Fluid Mech.* **20**, 111.

Brady, J.F., Phillips, R.J., Lester, J.C., & Bossis, G. 1988 Dynamic simulation of hydrodynamically interacting suspensions. *J. Fluid Mech.* **195**, 257.

Brenner, H. 1964*a* The Stokes resistance of an arbitrary particle III. Shear fields *Chem. Eng. Sci.* **19**, 631.

Brenner, H. 1964*b* The Stokes resistance of an arbitrary particle IV. Arbitrary fields of flow. *Chem. Eng. Sci.* **19**, 703.

Carlson, J.D., Sprecher, A.F., & Conrad, H. (eds.) 1990 Electrorheological fluids. *Proceedings of the Second International Conference on ER Fluids* Technomic Publishing Co., Inc. Lancaster, PA.

Chen, H.S. & Acrivos, A. 1978 On the effective elastic moduli of composite materials containing spherical inclusions at non-dilute concentrations. *Int. J. Solids Struc.* **14**, 349.

Conrad, H., Chen, Y., & Sprecher, A.F. 1990 Electrorheology of suspensions of zeolite particles in silicone oil. *Proceedings of the Second International Conference on ER Fluids* Carlson, J.D., Sprecher, A.F., & Conrad, H. (eds.) Technomic Publishing Co., Inc. Lancaster, PA.

Dahler, J.S. & Scriven, L.E. 1963 Theory of structured continua 1. General consideration of angular momentum and polarization. *Proc. Roy. Soc.* A **275**, 504.

Davis, M.H. 1964 Two charged spherical conductors in a uniform electric field: Forces and field strength. *Quart. Journ. Mech. and Applied Math.* **17**, 499.

De Leeuw, S.W., Perram, J.W., & Smith, E.R. 1983 Simulation of electrostatic systems in periodic boundary conditions. III. Further theory and applications. *Proc. Roy. Soc.* A **388** 177.

Doi, M. & Edwards, S.F. 1986 *The theory of polymer dynamics.* Clarendon Press, Oxford.

Durlofsky, L., Brady, J.F., & Bossis, G. 1987 Dynamic simulation of hydrodynamically interacting particles. *J. Fluid Mech.* **180**, 21.

Ewald, P.P. 1921 Die Berechnung optischer und elektrostatischer Gitterpotentiale. *Ann. Phys.* **64**, 253.

Felderhof, B.U. & Deutch, J.M. 1976 Concentration dependence of the rate of diffusion-controlled reactions. *J. Chem. Phys.*, **64**, 455.

Filisko, F.E. 1990 Work presented at the 62nd meeting of the Society of Rheology (Santa Fe, Oct. 1990).

Filisko, F.E. & Radzilowski, L.H. 1990 An intrinsic mechanism for the activity of alumino-silicate based electrorheological materials. *J. Rheol.* **34**, 539.

Fricke, H. 1924 A mathematical treatment of the electric conductivity and capacity of disperse systems. I. The electric conductivity of a suspension of homogeneous spheroids. *Phys. Rev.* **24**, 575.

Fuller, G.G. 1990 Optical rheometry *Ann. Rev. Fluid Mech.* **22**, 387.

Gast, A.P., & Zukoski, C.F. 1989 Electrorheological fluids as colloidal suspensions. *Adv. Coll. Int. Sci.* **30**, 153.

Glendinning, A.B. & Russel, W.B. 1982 A pairwise additive description of sedimentation and diffusion in concentrated suspensions of hard spheres. *J. Colloid and Interface Science.* **89**(1), 124.

Gurtin, M.E. 1981 *An introduction to continuum mechanics.* Academic Press Inc., New York.

Hartnett, J.P. & Hu, R.Y.Z. 1989 The yield stress-an engineering reality. *J. Rheology* **33**, 671.

Hashin, Z. & Shtrikman, S. 1962 A variational approach to the theory of the effective magnetic permeability of multiphase materials. *J. Appl. Phys.* **33**(10), 3125.

Jackson, J.D. 1975 *Classical electrodynamics* 2nd ed., John Wiley & Sons.

Jeffrey, D.J. 1973 Conduction through a random suspension of spheres. *Proc. Roy. Soc.* A **338**, 503.

Jeffrey, D.J. 1978 The temperature field and electric potential around two almost touching spheres. *J. Ind. Maths. Applics.* **22**, 337.

Keller, J.B. 1963 Conductivity of a Medium Containing a Dense Array of Perfectly Conducting Spheres or Cylinders or Nonconducting Cylinders *J. Appl. Phys.* **34**(4), 991.

Kim, I.C., & Torquato, S. 1990 Effective conductivity of hard spheres by brownian motion simulation *to appear in J. Appl. Phys.*

Kirkpatrick, S. 1971 Classical transport in disordered media: Scalings and effective medium theories. *Phys. Rev. Letters.* **27**, 1722.

Kittel, C. 1976 *Introduction to solid state physics.* 5th ed., John Wiley & Sons, New York.

Klass, D.L & Martinek, T.W. 1967*a* Electroviscous Fluids. I. Rheological Properties. *J. Applied Phys.* **38**, 67.

Klass, D.L & Martinek, T.W. 1967*b* Electroviscous Fluids. II. Electrical Properties. *J. Applied Phys.* **38**, 75.

Klingenberg, D.J 1990 Ph.D. Thesis, University of Illinois.

Klingenberg, D.J, van Swol, F., & Zukoski, C.F. 1989 Dynamic simulation of electrorheological suspensions. *J. Chem. Phys.* **91**, 7888.

Klingenberg, D.J. & Zukoski, C.F. 1990 Studies on the steady-shear behavior of electrorheological suspensions. *Langmuir* **6**, 15.

Kraynik, A.M. 1988 Foam flows *Ann. Rev. Fluid Mech.* **20**, 325.

Kraynik, A.M. 1990 ER Fluid Standards: Comments on ER Fluid Rheology. *Proceedings of the Second International Conference on ER Fluids* Carlson, J.D., Sprecher, A.F., & Conrad, H. (eds.) Technomic Publishing Co., Inc. Lancaster, PA.

Kraynik, A.M., Bonnecaze, R.T., & Brady, J.F. 1991 *Work in progress.*

Landau, L.D. & Lifshitz, E.M. 1984 *Electrodynamics of continuous media.* 2nd ed., Pergamon Press, New York.

Lebenhaft, J.R. & Kapral, R. 1979 Diffusion-controlled processes among partially absorbing stationary sinks. *J. Stat. Phys.*, **20**, 25.

Lee, S.B. & Torquato, S. 1986 Porosity for the penetrable-concentric-shell model of two-phase disordered media: Computer simulation results. *J. Chem. Phys.* **85**, 7178.

Lee, S.B., Kim, I.C., Miller, C.M., & Torquato, S. 1989 Random-walk simulation of diffusion-controlled processes among static traps. *Phys. Rev.* B, **39**, 11833.

Lemaire, E. & Bossis, G. 1991 Yield stresses and wall effects in magnetic colloidal suspensions. *to appear in J. of Phys.* D.

Marshall, L., Goodwin, J.W., & Zukoski, C.F. 1989 Effects of electric-fields on the rheology of non-aqueous concentrated suspensions. *J. Chem. Soc. Faraday I*, **85**, 2785.

Maxwell, J.C. 1873 *Electricity and magnetism.* 1st ed., Clarendon Press.

McKenzie, D.R., McPhedran, R.C., & Derrick, G.H. 1978 The conductivity of lattices of spheres II. The body-centered and face-centered cubic lattices. *Proc. Roy. Soc.* A **362**, 211.

McPhedran, R.C. & McKenzie, D.R. 1978 The conductivity of lattices of spheres I. The simple cubic lattice. *Proc. Roy. Soc.* A **359**, 45.

Meridith, R.E. & Tobias, C.W. 1960 Resistance to potential flow through a cubic array of spheres. *J. Appl. Phys.* **31**, 1270.

Meredith, R.E. & Tobias, C.W. 1961 Conductivities in emulsions. *J. Electrochem. Soc.* **108**, 286.

Miller, C.M. & Torquato, S. 1989 Diffusion-controlled reactions among spherical traps: Effect of polydispersity in trap size. *Phys. Rev.* B, **40**, 7101.

Mimouni, Z., Bossis, G., Mathis, C., Meunier, A., & Paparoditis, C. 1990 Field induced structure in a colloidal suspension. *Progress in Coll. & Polymer Sci.*, **81**, 120.

Muthukumar, M. & Cukier, R.I. 1981 Concentration dependence of diffusion controlled processes among stationary reactive sinks. *J. Stat. Phys.*, **26**, 453.

Muthukumar, M. 1982 Concentration dependence of diffusion controlled processes among static traps. *J. Chem. Phys.*, **76**, 2667.

Nijboer, B.R.A., & De Wette, F.W. 1957 On the calculation of lattice sums. *Physica* A **23**, 309.

O'Brien, R.W. 1979 A method for the calculation of effective transport properties of suspensions of interacting particles. *J. Fluid Mech.* **91**, 17.

Ottavi, H., Clerc, J., Giraud, G., Roussenq, J., Guyon, E., & Mitescu, C.D. 1978 Electrical conductivity of a mixture of conducting and insulating spheres: an application of some percolation concepts. *J. Phys.* C. **11**, 1311.

Perry, P. & Throop, G.J. 1972 Decay of pair correlations in hard-sphere fluids. *J. Chem. Phys.* **57**, 1827.

Phillips, R.J., Brady, J.F., and Bossis, G. 1988 Hydrodynamic transport properties of hard-sphere dispersions. I. Suspensions of freely mobile particles. *Phys. Fluids* **31**, 3462.

Pool, R. 1990 The fluids with a case of split personality. *Science* **247**, 1180.

Lord Rayleigh 1892 On the influence of obstacles arranged in rectangular order on the properties of the medium. *Phil. Mag.* **34**, 481.

Rosensweig 1985 *Ferrohydrodynamics* Cambridge University Press, Cambridge UK.

Russakoff, G. 1970 A derivation of the macroscopic maxwell equations. *Am. J. Phys.* **38** 10, 1188.

Sangani, A.S. & Acrivos, A. 1982 The effective conductivity of a periodic array of spheres. *Proc. Roy. Soc.* A **386**, 263.

Scher, H. & Zallen, R. 1970 Critical Density in Percolation Processes. *J. Chem. Phys.* **53**, 3759.

Smith, W.R. & Henderson, D. 1970 Analytical representation of the Percus-Yevick hard-sphere radial distribution function. *Mol. Phys.* **19**, 411.

Smoluchowski, M. 1916 *Phys. Z.*, **17**, 557.

Stauffer, D. 1985 *Introduction to percolation theory.* Taylor & Francis, Inc.

Torquato, S. 1986 Concentration dependence of diffusion-controlled rections among static reactive sinks. *J. Chem. Phys.*, **85**, 7178.

Torquato, S. & Lado, F. 1986 Evaluation of bounds on the conductivity and bulk modulus of dispersions of impenetrable spheres. *Phys. Rev.* B **33**(9), 6428.

Turner, J.C.R. 1976 Two phase conductivity: The electrical conductance of liquid-fluidized beds of spheres. *Chem. Eng. Sci.* **31**, 487.

Uejima, H. 1972 Dielectric mechanism and rheological properties of electro-fluids. *Japanese J. of Appl. Phys.* **11**, 319.

Venema, P. 1990 Reaction-diffusion on a regular array of perfectly absorbing cylindrical sinks. *Physica* A, **162**, 317.

Venema, P. & Bedeaux, D. 1989 Reaction-diffusion on a periodic array of penetrable spherical sinks. *Physica* A, **156**, 835.

Winslow, W.M. 1949 Induced vibration of suspensions. *J. Applied Phys.*, **20**, 1137.

Whitaker, S. 1984 *Introduction to fluid mechanics.* Robert E. Krieger Publishing Co., Malabar, Florida.

Whittle, M. 1990 Computer simulation of an electrorheological fluid. *J. Non-Newt. Fluid Mech.*, **37**, 233.

Zheng, L.H. & Chiew, Y.C. 1989 Computer simulation of diffusion-controlled reactions in dispersions of spherical sinks. *J. Chem. Phys.*, **90**, 322.

Zukoski, C.F. 1989 *Personal communication.*

Zuzovski, M. & Brenner, H. 1977 Effective conductivities of composite materials composed of cubic arrangements of spherical particles embedded in an isotropic matrix. *J. Appl Math. Phys.* (ZAMP) **28**, 979.

APPENDIX

COMPUTATION OF THE TWO-BODY CAPACITANCE MATRIX FOR SPHERICAL PARTICLES

The two-body capacitance matrix is necessary for several of the simulations in this thesis. It can be constructed completely for perfect spherical conductors from the work of Davis (1964) and Jeffrey (1973, 1978). Although Jeffrey's first paper provides the relationship between the particle dipoles and the electric field for charge-free particles of arbitrary conductivity ratio, the complete two-body capacitance matrix can not be constructed without the other relationships for charged particles of arbitrary conductivity ratio. Since the work of Davis is only for perfect conductors, here we shall outline the solution for the potential field for two charged, equasized spherical particles of arbitrary conductivity ratio. It turns out to be easier to solve the exact two-body potential matrix problem, and invert it to determine the capacitance matrix.

To solve Poisson's equation inside and outside the spheres, we shall employ the method of twin multipole expansions developed by Ross (1968) and used by Jeffrey (1973). The potential satisfying the governing equations is given by the expansion of spherical harmonics

$$\phi_i = \phi(R_i) - \frac{q_i}{8\pi a^3 \lambda_p} r^2 + \frac{q_i}{4\pi a \lambda_p} \sum_{s=1}^{\infty} d_s^i \left(\frac{r_i}{a}\right)^s P_s(\cos\theta_i), \qquad (A1)$$

$$\phi_o = \frac{1}{4\pi\lambda}\left(\frac{q_1}{r_1} + \frac{q_2}{r_2}\right) + \frac{1}{4\pi\lambda a} + \sum_{s=1}^{\infty}\sum_{i=1}^{2} g_s^i q_i \left(\frac{a}{r_i}\right)^{s+1} P_s(\cos\theta_i), \qquad (A2)$$

where ϕ_i is the potential in sphere $i = 1$ or 2 and ϕ_o is the potential outside the spheres. The position of the centers and charges of the spheres are R_i and q_i. The radius of each sphere is a. The twin multipole spatial coordinates are r_i, measured from the centers of the spheres, and θ_i, their azimuthal angles. The matrix and particle conductivities are λ and λ_p, respectively. The constants d_s^i and g_s^i are now to be determined by the usual boundary conditions of continuity of potential and flux at the boundaries. Note that the first two terms of (A1) are the solution for an isolated uniformly charged sphere. Any charge distribution is acceptable exchanging

only these two terms for the appropriate isolated charged sphere solution. Such an alteration would not change the value of the coefficients in (A1) and (A2).

When applying the boundary conditions, it is advantageous to make use of two identities. First, when on the surface of sphere i, for example, it is best to rewrite (A2) completely in terms of r_i and θ_i with

$$\frac{P_n(\cos\theta_{3-i})}{r_{3-i}^{n+1}} = \left(\frac{1}{R}\right)^{n+1} \sum_{m=0}^{\infty} \binom{m+n}{n} \left(\frac{r_i}{R}\right)^m P_m(\cos\theta_i), \qquad (A3)$$

where R is the radial separation between the two spheres. Second, once we apply boundary conditions, we can use the orthogonality property of Legendre polynomials,

$$\int_o^\pi P_s(\cos\theta) P_n(\cos\theta) \sin\theta \mathrm{d}\theta = \begin{cases} 0 & s \neq n \\ \frac{2}{2s+1} & s = n, \end{cases} \qquad (A4)$$

to rewrite the coefficients as sums of one another. Then after a bit of algebra we find that,

$$d_n^i = \alpha_n g_n^i \qquad (A5)$$

$$\alpha_n \left(\frac{q_2}{q_1}\right)\left(\frac{a}{R}\right)^{n+2} = g_n^1 \left(\frac{a}{R}\right) - \left(\frac{q_2}{q_1}\right) \sum_{m=1}^{\infty} \alpha_n P_{n,m} g_m^2, \qquad (A6)$$

$$\alpha_n \left(\frac{q_1}{q_2}\right)\left(\frac{a}{R}\right)^{n+2} = g_n^2 \left(\frac{a}{R}\right) - \left(\frac{q_1}{q_2}\right) \sum_{m=1}^{\infty} \alpha_n P_{n,m} g_m^1, \qquad (A7)$$

where

$$\alpha_n = \frac{1 - \lambda_p/\lambda}{\lambda_p/\lambda + (1 + 1/n)}, \qquad (A8)$$

$$P_{n,m} = \binom{m+n}{n} \left(\frac{a}{R}\right)^{m+n+2}. \qquad (A9)$$

It is inconvenient to determine the g_n^i for arbitrary q_i. It is far easier to solve the general problem by determining the coefficients for the two sub-problems of *a*) two charged spheres of equal magnitude and sign and *b*) two charged spheres of equal magnitude and opposite sign. Thus the solution for arbitrary sphere charges can be formed from the sum of these two sub-problems since the governing equations are linear. Solving the sub-problems has the additional merit that then $g_n^1 = g_n^2 = g_n$ and likewise for d_n.

The equations (A6) and (A7) suggest, and it has indeed been proven by Ross, that g_n can be written as a power series of the radial separation between the spheres of the form

$$g_n^a = \alpha_n \left(\frac{a}{R}\right)^{n+1} \sum_{s=o}^{\infty} a_{ns} \left(\frac{a}{R}\right)^s, \tag{A10}$$

$$g_n^b = \alpha_n \left(\frac{a}{R}\right)^{n+1} \sum_{s=o}^{\infty} b_{ns} \left(\frac{a}{R}\right)^s, \tag{A11}$$

where the superscripts a and b refer to the subproblems. Using the infinite series and equations (A8) and (A9) we find that

$$a_{ns} = \sum_{m=1}^{\frac{1}{2}(s+1)} \alpha_m \binom{n+m}{m} a_{m(s-2m-1)}, \qquad a_{n0} = 1, \tag{A12}$$

$$b_{ns} = \sum_{m=1}^{\frac{1}{2}(s+1)} \alpha_m \binom{n+m}{m} b_{m(s-2m-1)}, \qquad b_{n0} = -1, \tag{A13}$$

Thus, the complete solution to the potential problem for two charged spheres is known, although it is not particularly elegant. There is no closed form solution for g_n^a or g_n^b.

The potential-charge coupling of the potential matrix is

$$\begin{pmatrix} \phi(R_1) \\ \phi(R_2) \end{pmatrix} = \begin{pmatrix} P_{11} & P_{12} \\ P_{12} & P_{11} \end{pmatrix} \cdot \begin{pmatrix} q_1 \\ q_2 \end{pmatrix}, \tag{A14}$$

where

$$P_{11} = \frac{1}{4\pi\lambda a}\left[1 + \frac{1}{2}\frac{\lambda}{\lambda_p} + \frac{1}{2}\sum_{s=1}^{\infty}(g_s^a - g_s^b)\left(\frac{a}{R}\right)^{s+1}\right], \tag{A15}$$

$$P_{12} = \frac{1}{4\pi\lambda a}\left[\frac{a}{R} + \sum_{s=1}^{\infty}(g_s^a + g_s^b)\left(\frac{a}{R}\right)^{s+1}\right], \tag{A16}$$

As mentioned before the two-body charge-potential capacitance matrix is constructed from simply inverting the above potential matrix.

The dipole-potential coupling of the capacitance matrix can also be constructed from the solutions of the above problems. The 2×6 matrix coupling is

$$\begin{pmatrix} \mathbf{S}_1 \\ \mathbf{S}_2 \end{pmatrix} = \begin{pmatrix} p_1\hat{\mathbf{r}} & -p_2\hat{\mathbf{r}} \\ p_2\hat{\mathbf{r}} & -p_1\hat{\mathbf{r}} \end{pmatrix} \cdot \begin{pmatrix} \phi(R_1) \\ \phi(R_2) \end{pmatrix}, \tag{A17}$$

where

$$p_1 = \frac{1}{2}\left(\frac{g_1^a}{P_{11}+P_{12}} + \frac{g_1^b}{P_{11}-P_{12}}\right), \tag{A18}$$

$$p_2 = \frac{1}{2}\left(\frac{g_1^b}{P_{11}-P_{12}} - \frac{g_1^a}{P_{11}+P_{12}}\right), \tag{A19}$$

and $\hat{\mathbf{r}}$ is the unit normal vector between particles 1 and 2. Now coupled with Jeffrey's solution (1973) we have the complete two-body capacitance matrix for equasized spheres of arbitrary conductivity ratio.